Contribution to the Inner Tracker Design and Penguin Sensitivity Studies for the Measurement of sin 2β in LHCb

THÈSE N^{O} 4234 (2008)

PRÉSENTÉE LE 28 NOVEMBRE 2008
À LA FACULTÉ SCIENCES DE BASE
LABORATOIRE DE PHYSIQUE DES HAUTES ÉNERGIES 1
PROGRAMME DOCTORAL EN PHYSIQUE

ÉCOLE POLYTECHNIQUE FÉDÉRALE DE LAUSANNE

POUR L'OBTENTION DU GRADE DE DOCTEUR ÈS SCIENCES

PAR

Aurélie PERRIN

acceptée sur proposition du jury:

Prof. R. Schaller, président du jury
Dr M. T. Tran, directeur de thèse
Dr F. Ronga, rapporteur
Prof. L. Villard, rapporteur
Dr H. Voss, rapporteur

ÉCOLE POLYTECHNIQUE
FÉDÉRALE DE LAUSANNE
Suisse
2008

Abstract

LHCb is one of the four large experiments hosted at the Large Hadron Collider (LHC) at CERN in Geneva. It will start taking data in september 2008, and will then operate for several years. It consists of a single-arm forward spectrometer dedicated to precise measurements of CP violation and rare decays in the B sector, with the aim of testing the Standard Model and possibly of discovering the first signatures of New Physics.

Building such a large experiment as LHCb is a challenge, and many contributions are needed. The Lausanne lab is responsible for the design and the production of the Silicon Inner Tracker (IT) of LHCb. This detector is made of Silicon sensors which need to be cooled to avoid thermal runaway. We present here a contribution to the design of this sub-detector and a description of the production steps. In particular, a study of the cooling of the Inner Tracker is described. It is shown that the cooling abilities of the IT can avoid thermal runaway.

CP violation in B meson decays was first observed in the measurement of the so-called "golden channel", in which a B_d^0 meson decays into a J/ψ and a K_s^0. The time-dependent CP asymmetry in $B_d^0 \to J/\psi K_s^0$ allows to measure the angle β of the (d,b) unitary triangle. This parameter is now known with 4% accuracy at B factories. However, this determination of $\sin 2\beta$ is made under the assumption that there is only a single amplitude present in this decay : this means that penguin diagrams which might be present have been neglected. In 1999, Robert Fleischer [29] proposed a theoretical method to access those penguin diagrams in the $B_d^0 \to J/\psi K_s^0$ decay, using the $B_s^0 \to J/\psi K_s^0$ channel. This method relies on U-Spin symmetry and also allows to determine the γ angle of the (d,b) unitary triangle.

We have developed a selection method for the $B_d^0 \to J/\psi K_s^0$ channel in order to strongly suppress the background and to allow the separation of the B_s^0 and B_d^0 peaks. We obtained mass resolution of $8\,\mathrm{MeV/c^2}$ and a B/S ratio for the channel $B_d^0 \to J/\psi K_s^0$ estimated to belong to [0, 0.039] at 90% confidence level in a $\pm 2\sigma$ mass window around the B_d^0 mass, after the first level of trigger (L0). For the channel $B_s^0 \to J/\psi K_s^0$, the B/S ratio is calculated from the result for $B_d^0 \to J/\psi K_s^0$ assuming known branching fractions. It lies in the interval [0, 3.33] at 90% CL. The annual yield is expected to be around 300 events for an integrated luminosity of $2\,\mathrm{fb}^{-1}$. We have simulated with fast Monte Carlo the $B_s^0 \to J/\psi K_s^0$ signal using the parametrization proposed in [29] and taking as input the results of selection obtained for $B_d^0 \to J/\psi K_s^0$. The simulation has been repeated several times for different integrated luminosities and B/S ratios. We conclude that after 5 years of normal running, LHCb will be able to determine the penguin contribution in the $B_d^0 \to J/\psi K_s^0$ decay with a sensitivity of (0.172 ± 0.004) using this method based on U-spin symmetry.

Keywords: High Energy Physics, CERN, LHC, Standard Model, b physics, CP violation, LHCb, silicon tracker, cooling.

Résumé

LHCb est l'une des quatre grande expériences du grand collisionneur de hadrons (LHC) au CERN à Genève. Elle entrera en fonction en septembre 2008 et continuera à prendre des données pendant plusieurs années. Le détecteur LHCb est un spectromètre à un seul bras dédié à la mesure précise de la violation CP et des désintégrations rares des mesons B, le but étant de tester le Modèle Standard et peut-être de découvrir les premières évidences d'une nouvelle physique.

Construire une expérience aussi grande que LHCb est un vrai défi et de nombreuses contributions sont nécessaires. Le laboratoire de Lausanne est responsable de la conception et de la production du détecteur à trace au Silicium "Inner Tracker" (IT) de LHCb. Ce détecteur est constitué de capteurs en Silicium, qui doivent être refroidis afin d'éviter un emballement thermique. Nous présentons ici une contribution à la conception du détecteur et une description des étapes de production. En particulier, l'étude du refroidissement de l'Inner Tracker est développée. Les essais montrent que la capacité de refroidissement du détecteur est suffisante pour éviter l'emballement thermique.

La violation CP dans le système des mésons B a été observée pour la première fois dans l'assymétrie en fonction du temps de la désintégration $B_d^0 \rightarrow J/\psi K_s^0$. Cette assymétrie permet de mesurer l'angle β du triangle d'unitarité (d, b). Ce paramètre est mesuré avec une précision de 4% dans les usines à B, mais une amélioration de la précision de la mesure est nécessaire. La connaissance de l'importance de la contribution des diagrammes pingouins, jusqu'à present négligée, est aussi très importante. En 1999, Robert Fleischer [29] propose une méthode théorique d'accéder aux diagrammes en pingouin de $B_d^0 \rightarrow J/\psi K_s^0$, en utilisant la désintégration $B_s^0 \rightarrow J/\psi K_s^0$. Cette méthode est fondée sur la symétrie U-Spin et permet aussi de déterminer l'angle γ du triangle d'unitarité (d, b).

Nous avons développé une sélection de $B_d^0 \rightarrow J/\psi K_s^0$ qui permet de fortement réduire le bruit de fond et qui permet la séparation des pics de B_s^0 et de B_d^0. Nous avons obtenu une résolution en masse de $8\,\mathrm{MeV/c^2}$ et un rapport B/S pour la désintégration $B_d^0 \rightarrow J/\psi K_s^0$ compris dans l'intervalle [0, 0,039] avec un niveau de confiance de 90% dans une fenêtre de masse de $\pm 2\sigma$ autour de valeur nominale de la masse du B_d^0, après le premier niveau de trigger (L0). Pour le cannal $B_s^0 \rightarrow J/\psi K_s^0$, le rapport B/S est déduit des résultats de $B_d^0 \to J/\psi K_s^0$. Il appartient à l'intervalle [0, 3.33] à un niveau de confiance de 90%. Un nombre d'événements annuel de 300 est attendu avec une luminosité intégrée de $2\,\mathrm{fb}^{-1}$. Nous avons simulé avec un Monte Carlo rapide le signal $B_s^0 \to J/\psi K_s^0$ en utilisant le paramétrage proposé dans [29] et les résultats de la sélection de $B_d^0 \to J/\psi K_s^0$ comme paramètres d'entrée. La simulation a été reproduite plusieurs fois pour différentes luminosités intégrées et différents rapports B/S. Après 5 ans de fonctionnement normal, LHCb pourra déterminer la contribution des diagrammes en pingouin de la désintégration $B_d^0 \to J/\psi K_s^0$ avec une sensibilité de (0.172 ± 0.004) en utilisant la méthode basée sur la symétrie U-Spin.

Mots-clés: Physique des hautes énergies, CERN, LHC, Modèle Standard, physique du quark b, violation de CP, LHCb, déctecteur trace au silicium, refroidissement.

Remerciements

J'aimerais tout d'abord remercier mon directeur de thèse Docteur Minh Tâm Tran qui m'a permis de mener à bien ce travail jusqu'au bout en me donnant une grande liberté d'action tant dans ma thèse à proprement parler que dans mon organisation de travail.

Je remercie Olivier Schneider et Aurelio Bay de m'avoir permis de réaliser cette thèse dans leur laboratoire et toute la collaboration LHCb du CERN avec qui j'ai eu grand plaisir à travailler.

Mes remerciements vont aussi à toutes les personnes du Laboratoire des Hautes Energies de Lausanne qui, tout au long de ces quatre ans et demi, ont cru en moi et qui m'ont aid à finaliser ce projet. Je remercie tout particulirement Helge Voss avec qui j'ai essuyé de nombreuses fuites, Frédérique Blanc qui m'a permis de comprendre mon analyse dans les moindres détails, Jeroen Van Hunen et Tagir Aushev pour leur aide au combien précieuse, Kim Vervink pour m'avoir aide et soutenue comme une amie qu'elle restera.

Mes remerciement vont aussi pour Nicolas Zwahlen, Jérémie Borel, Marc-Oliver Betler, Peter Faulen, Céline Terranova et tous mes autres collègue sans oublier Erika Luthi et Esther Hoffman nos deux secrétaires préférées, Alain Pinard, Bernard Howald, Monsieur Hertig, Raymond Frey pour m'avoir appris à me servir de mes mains autant que de ma tête et Monsieur Gailloud pour m'avoir beaucoup aidé à comprendre la théorie de la violation CP.

Cette thèse je l'adresse tout particulièrement aux trois hommes de ma vie, mon père tout d'abord qui m'a transmis sa passion pour l'univers, mon mari qui m'a soutenue toutes ces années et qui m'a donné le plus beau cadeau qu'il soit, et enfin mon fils, Matéo, qui me rempli de fierté et d'amour quotidiennement. Je remercie profondément ma mère qui a su m'apprendre à faire des choix et m'a transmis les valeurs qui gouvernent ma vie et ma soeur pour toute l'énergie positive qu'elle sait m'apporter. Enfin je tiens à remercier mes amis, Adeline, Lucie, Frère, Binôme, Colombe, Olive et tous les acolytes de l'Arcadie qui me donnent la force d'avancer dans la vie.

Contents

Introduction

One of the open questions which links particle physics and cosmology is related to the non-observation of galaxies made of anti-matter. A tiny difference between particles and antiparticles has been discovered in 1964 in an experiment with K mesons [1]. This phenomenon is called "CP asymmetry" or CP violation and, according to Andrei Sakharov, is one of the three necessary conditions to explain the dominance of matter over anti-matter in the Universe [2]. Despite a long history, CP violation is still not a very well understood phenomenon. It is observed in the neutral K meson decays and since 2001 in neutral B meson decays.

The theoretical description of this phenomenon is related to the mass generation of the quarks. In the Standard Model, this mass generation results in a set of parameters grouped in a matrix named the "Cabibbo-Kobayashi-Maskawa matrix" (CKM) [3, 4]. CP violation finds its origin in the presence of a phase among the elements of the CKM matrix. A detailed study of the elements of the CKM matrix, particularly the ones involving the third generation of quarks, is therefore needed to:

- study the violation of the CP symmetry and test the Standard Model,
- look for a "New Physics" which should manifest itself in case of a discovery of a flaw in the predictions of the Standard Model.

Since 2001, two experiments, BaBar at SLAC (USA) and Belle at KEK (Japan), both working at asymmetric e^+e^- colliders at a center-of-mass (CM) energy corresponding to the formation of the $\Upsilon(4S)$, have established the existence of mixing-induced CP violation by observing the time-dependence of B^0 meson decays to a few specific CP eigenstates of the type $b \to c\bar{c}s$ (dominated by a single weak phase), like the "gold plated channel" $B_d^0 \to J/\psi K_s^0$ or $c\bar{c}b$, $s\bar{q}q$ and $u\bar{u}d$. They obtained significant measurements of $\sin(2\beta)$ [5, 6, 7], 2β being the weak CP-violating phase of the $B_d^0 - \overline{B}_d^0$ mixing amplitude and also twice one of the angles of the unitary angle (d, b). Since then they have extended thier studies to many more channels and refined their analyses of time-dependent or time-integrate CP asymmetries, including B^0 decays to non-CP final states and charged B mesons decays.

In addition to a precise measurement of the angle β of the unitary triangle of the CKM matrix (which is known with an error of about 1 degree), BaBar and Belle started to

measure the angles α and γ in various ways, though with limited precision, especially for γ. So far all measurements of CP violation as well as other observables in hadronic flavour physics are consistent whithin the Standard Model: the CKM picture appears to give a coherent view of CP violation.
In the extraction of the CKM β angle, it was assumed that there is no CP violation in mixing or in the decay amplitudes. This latter hypothesis relies on the fact that $B_d^0 \to J/\psi K_s^0$ decays are highly dominated by the tree diagram and that penguin diagrams can be neglected. However, in view of the high accuracy which will be reached in the (near) future, the importance of the penguin diagrams must be assessed.

In 1999, Robert Fleischer [29] proposed a theoretical way to access the penguin diagrams of the $B_d^0 \to J/\psi K_s^0$, using the $B_s^0 \to J/\psi K_s^0$ channel. This method relies on U-Spin symmetry and also allows to determine the γ angle of the (d, b) unitary triangle.

The LHCb detector is a single arm spectrometer especially designed for the B mesons studies. The "Inner Tracker" is a subdetector of the Tracking System. The first part of my work was devoted to the Inner Tracker design, production and cooling tests. The second part of my thesis is focused on the study of the sensitivity to the penguin contribution in the measurement of $\sin 2\beta$ in LHCb. In order to estimate its sensitivity, the $B_d^0 \to J/\psi K_s^0$ selection at LHCb is first studied to allow the separation of the B_s^0 and B_d^0 peaks. Results of this selection is used in a fast simulation of the $B_s^0 \to J/\psi K_s^0$ decay in LHCb to estimate the LHCb sensitivity to the penguin contribution in the measurement $\sin 2\beta$.

This dissertation is divided into three parts. Part I presents an overview of the theoretical context (Chapter 1), a description of the detector and subdetectors of LHCb (Chapter 2) and its simulation tools (Chapter 3). Part II is devoted to the Inner Tracker design, production and cooling tests (Chapter 4). Finally, part III is divided into two chapters. Chapter 5 describes the $B_d^0 \to J/\psi K_s^0$ selection and its performances. Chapter 6 covers the simulation of the $B_s^0 \to J/\psi K_s^0$ decay and the estimation of the sensitivity of LHCb to the parameters which give the penguin contribution in the $B_d^0 \to J/\psi K_s^0$ decay.

Part I

Overview

Chapter 1

Theoretical Overview: CP violation

The violation of the CP symmetry was discovered through the observation of $K_2^0 \to \pi\pi$ decay in 1964 [1]. This observation showed that weak interactions are not invariant under CP transformations. In 2001, CP violation was also observed in decays of neutral B mesons [5, 7]. In the Standard Model (SM), the CP violation is found in the flavour structure of weak charged-current interactions. In this chapter[1], we will first describe the CP violation in the B meson system and in a second part, the study of $B_{d,s}^0 \to J/\psi K_s^0$ decays will be developped. The second decay, $B_s^0 \to J/\psi K_s^0$, will allow us to control the penguin diagrams in $B_d^0 \to J/\psi K_s^0$ and eventually to extract the unitary triangle γ angle.

1.1 CP violation in the Standard Model

In the Standard Model (SM) fermions are grouped in three families consisting of a doublet of left-handed particles (weak isospin ± 1/2) and singlets of right-handed particles (weak isospin 0). The charged weak interaction concerns only the left-handed particles. The three families of quarks which are eigenstates of the weak interaction are :

$$\begin{pmatrix} \mathrm{u} \\ \mathrm{d'} \end{pmatrix}_{\mathrm{L}} \quad \begin{pmatrix} \mathrm{c} \\ \mathrm{s'} \end{pmatrix}_{\mathrm{L}} \quad \begin{pmatrix} \mathrm{t} \\ \mathrm{b'} \end{pmatrix}_{\mathrm{L}}$$

1.1.1 Weak interaction

Whithin the framework of the SM, CP violation (see Section 1.3) has its origin in the Cabibbo-Kobayashi-Maskawa (CKM) matrix [4, 3, 14] which connects the electroweak

---

[1] This chapter is based on references [8, 9, 10, 11, 12, 13]

eigenstates (d', s', b') to their mass eigenstates (d, s, b) through a unitary transformation:

$$\begin{pmatrix} \mathrm{d'} \\ \mathrm{s'} \\ \mathrm{b'} \end{pmatrix} = \begin{pmatrix} V_{ud} & V_{us} & V_{ub} \\ V_{cd} & V_{cs} & V_{cb} \\ V_{td} & V_{ts} & V_{tb} \end{pmatrix} \cdot \begin{pmatrix} \mathrm{d} \\ \mathrm{s} \\ \mathrm{b} \end{pmatrix} = V_{CKM} \cdot \begin{pmatrix} \mathrm{d} \\ \mathrm{s} \\ \mathrm{b} \end{pmatrix} \tag{1.1}$$

The CKM matrix elements describe charged current couplings in the non-leptonic charged current interaction Lagrangian:

$$\mathcal{L}_{int}^{CC} = -\frac{g}{\sqrt{2}} \left(\overline{u}, \overline{c}, \overline{t}\right)_L \gamma^\mu V_{CKM} \begin{pmatrix} \mathrm{d} \\ \mathrm{s} \\ \mathrm{b} \end{pmatrix}_L W^{\mu\dagger} + h.c., \tag{1.2}$$

where g is the weak coupling constant related to the gauge group $SU_L(2)$ and the W^μ field describes the charged W bosons. The transition from one quark i to another quark j is proportional to the square of each element of the CKM matrix $|V_{ij}|^2$. The value of the CKM elements are not predicted by the SM and need to be determined by measurements. The above Lagrangian is invariant under charge conjugaison and parity transformations, i.e. under CP, provided that the CKM matrix is real. A $n \times n$ complex matrix possesses $2n^2$ real parameters. The unitarity of the CKM matrix implies the condition:

$$\sum_j V_{ij} V_{jk}^* = \delta_{ik} \tag{1.3}$$

For $i = k$, there is n constraints and for $i \neq k$, $2\frac{1}{2}n(n-1) = n^2 - n$ constraints. Therefore, an unitary complex matrix has n^2 independent parameters. Since one deals with $2n$ quark fields, $2n-1$ relative phases can be fixed arbitrarely. Therefore, the number of independent parameters in the V_{CKM} matrix is:

$$n^2 - (2n-1) = (n-1)^2 \tag{1.4}$$

With $n = 3$, the CKM matrix can be parametrized by three Euler angles and a single complex phase δ [12], which represents the genuine CP violation in SM.

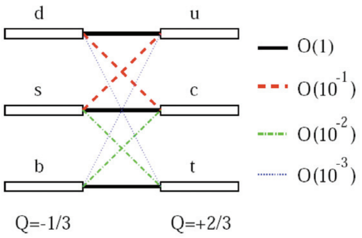

Figure 1.1: Hierarchy of the quark transitions mediated through charged-current processes.

1.1.2 CKM matrix parametrizations

There are several parametrizations of the CKM matrix in the litterature. The Particle Data Group [15] uses most of the time the Chau-Keung [16] parametrization:

$$V_{CKM} = \begin{pmatrix} c_{12}c_{13} & s_{12}c_{13} & s_{13}e^{-i\delta_{13}} \\ -s_{12}c_{23} - c_{12}s_{23}s_{13}e^{i\delta_{13}} & c_{12}c_{23} - s_{12}s_{23}s_{13}e^{i\delta_{13}} & s_{23}c_{13} \\ s_{12}s_{23} - c_{12}c_{23}s_{13}e^{i\delta_{13}} & -c_{12}s_{23} - s_{12}c_{23}s_{13}e^{i\delta_{13}} & c_{23}c_{13} \end{pmatrix}$$

where $c_{ij} = \cos\theta_{ij}$ and $s_{ij} = \sin\theta_{ij}$ control the mixing between the three generations (i, j = 1,2,3) while δ_{13} is the CP violation phase. The advantage of this parametrization is that each of the rotation angles θ_{ij} relates to the mixing of two specific generations.
In order to use the CKM matrix in a more quantitative way, Wolfenstein [17] proposed in 1983 an other parametrization based on experimental results. Using the established hierarchy $|V_{ub}|^2 \ll |V_{cb}|^2 \ll |V_{us}|^2 \ll 1$ (Fig 1.1), Wolfenstein expressed the CKM matrix as an expansion in power of $\lambda \equiv \sin\theta_C \approx 0.22$:

$$V_{CKM} = \begin{pmatrix} 1-\frac{1}{2}\lambda^2 & \lambda & A\lambda^3(\rho - i\eta) \\ -\lambda & 1-\frac{1}{2}\lambda^2 & A\lambda^2 \\ A\lambda^3(1-\rho-i\eta) & -A\lambda^2 & 1 \end{pmatrix} + \mathcal{O}(\lambda^4)$$

For most of nowadays studies, the Wolfenstein expansion is used at the order $\mathcal{O}(\lambda^5)$:

$$V_{CKM} = \begin{pmatrix} 1-\frac{1}{2}\lambda^2-\frac{1}{8}\lambda^4 & \lambda & A\lambda^3(\rho - i\eta) \\ -\lambda+\frac{1}{2}A^2\lambda^5\left[1-2(\rho+i\eta)\right] & 1-\frac{1}{2}\lambda^2-\frac{1}{8}\lambda^4(1+4A^2) & A\lambda^2 \\ A\lambda^3\left[1-(1-\frac{1}{2}\lambda^2)(\rho+i\eta)\right] & -A\lambda^2+\frac{1}{2}A\lambda^4\left[1-2(\rho+i\eta)\right] & 1-\frac{1}{2}A^2\lambda^4 \end{pmatrix} + \mathcal{O}(\lambda^6) \tag{1.5}$$

1.1.3 Unitarity triangles

The unitary of the CKM matrix implies nine orthogonality conditions (equation 1.3) :

- three on the diagonal elements $\sum_{i=1}^{3}|V_{ij}|^2 = 1$ $(j = 1, 2, 3)$: the consequence of this is that the overall charged current coupling of each up-type quark to all the down-type quarks is of universal strength,

- six for the crossed equation, which requires the sum of three complex numbers to vanish. They can be represented in the complex plane as six triangles : the six "unitarity triangles".

The shape of these six triangles is different but their area are the same ($|J_{CP}|/2 = A^2\lambda^6|\eta|$) and given by the Jarlskog parameter J_{CP}:

$$J_{CP} = \pm\mathcal{I}m\left(V_{ik}V_{jl}V_{il}^{*}V_{jk}^{*}\right) \ (i \neq j, l \neq k) \tag{1.6}$$

B-meson	quarks	Mass [MeV/c^2]	Lifetime [ps]
B_u^+	$(u\bar{b})$	5279.13 ± 0.31	1.638 ± 0.011
B_d^0	$(d\bar{b})$	5279.50 ± 0.33	1.530 ± 0.009
B_s^0	$(s\bar{b})$	5366.1 ± 0.6	$1.437^{+0.031}_{-0.030}$
B_c^+	$(c\bar{b})$	6286 ± 5	0.46 ± 0.07

Table 1.1: Mass and lifetime of different B-mesons [15].

The Jarlskog parameter J_{CP} represents a measurement of the "strength" of CP violation in the Standard Model and $J_{CP} \simeq 10^{-5}$ shows that CP violation is a small effect in the Standard Model. The six triangles correspond to the following unitarity conditions:

$$V_{us}V_{ud}^* + V_{cs}V_{cd}^* + V_{ts}V_{td}^* = 0, \quad \textbf{(sd)} \tag{1.7}$$

$$V_{us}V_{ub}^* + V_{cs}V_{cb}^* + V_{ts}V_{tb}^* = 0, \quad \textbf{(sb)} \tag{1.8}$$

$$V_{ud}V_{ub}^* + V_{cd}V_{cb}^* + V_{td}V_{tb}^* = 0, \quad \textbf{(db)} \tag{1.9}$$

$$V_{ud}V_{cd}^* + V_{us}V_{cs}^* + V_{ub}V_{cb}^* = 0, \quad \textbf{(uc)} \tag{1.10}$$

$$V_{cd}V_{td}^* + V_{cs}V_{ts}^* + V_{cb}V_{tb}^* = 0, \quad \textbf{(ct)} \tag{1.11}$$

$$V_{td}V_{ud}^* + V_{ts}V_{us}^* + V_{tb}V_{ub}^* = 0, \quad \textbf{(tu)} \tag{1.12}$$

Among the six triangles, only two have sides of the same order ($\mathcal{O}(\lambda^4)$), **(db)** and **(ut)**. The other four triangles have one side significantly smaller than the others (see Fig 1.2). In B-meson decays, the unitary triangle **(db)** is used for B_d channels and the **(sb)** for B_s decays (Fig 1.2). With the equation 1.9, three angles can be defined:

$$\alpha \equiv \arg\left(-\frac{\mathrm{V_{td}V_{tb}^*}}{\mathrm{V_{ud}V_{ub}^*}}\right), \ \beta \equiv \arg\left(-\frac{\mathrm{V_{cd}V_{cb}^*}}{\mathrm{V_{td}V_{tb}^*}}\right), \ \gamma \equiv \arg\left(-\frac{\mathrm{V_{ud}V_{ub}^*}}{\mathrm{V_{cd}V_{cb}^*}}\right)$$

At the order $\mathcal{O}(\lambda^5)$ an other angle appears which is introduced by V_{ts}. We can defined an interesting angle for the B_s studies with the **(sb)** triangle, that is χ:

$$\chi \equiv \phi_s \equiv \arg\left(-\frac{\mathrm{V_{cb}V_{cs}^*}}{\mathrm{V_{tb}V_{ts}^*}}\right) \simeq \lambda^2\eta \simeq \arg\left(\mathrm{V_{ts}} - \pi\right)$$

1.2 Neutral B-Meson Mixing

The B mesons are quark−anti-quark bound states which contain a b quark or a $\bar{b}$ anti-quark. They have been discovered in 1981 by the CLEO and the Columbia University-Stony Brook experiments [19, 20]. The general charasteristics of these particles are summarized in Table 1.1.

Without weak interactions, the B mesons would be stable and form a particle−anti-particle pairs with the same mass. However, due to the existence of this interaction, the B mesons decay with a relatively long lifetime.

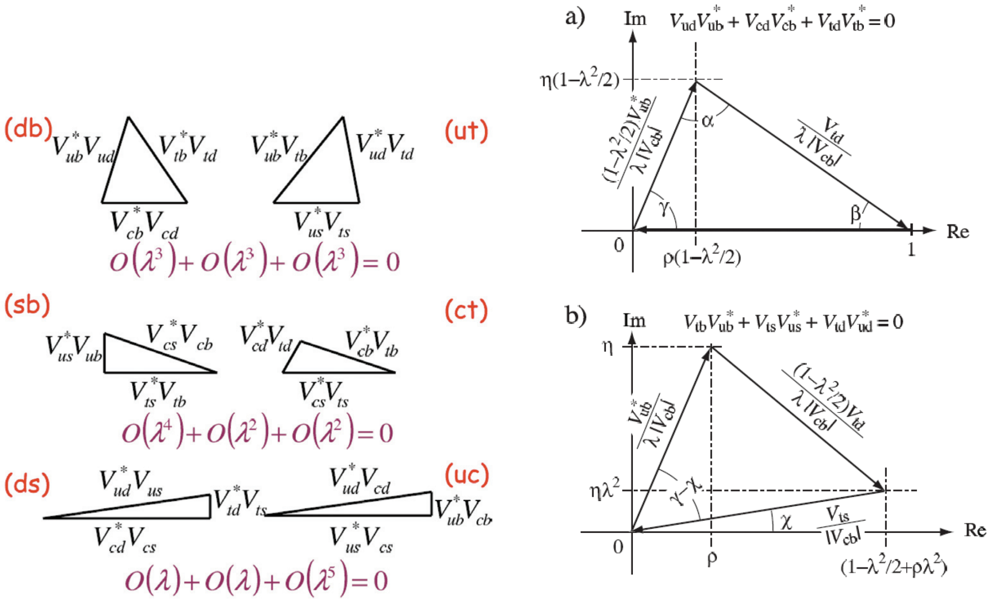

Figure 1.2: Left: the six CKM "unitarity triangles". Right: the two unsquashed unitarity triangles. These triangles have been normalised relative to the baseline of the **(db)** triangle so that $V_{cd}V_{cb}^* = -1$.

Consider the $|B_q^0\rangle$ and $|\overline{B}_q^0\rangle$ system ($q \in d, s$), $|B_q^0\rangle$ and $|\overline{B}_q^0\rangle$ being eigenstates of the strong interaction. As the weak interaction does not conserve the beauty, transitions from $|B_q^0\rangle$ to $|\overline{B}_q^0\rangle$, and vice versa, can occur leading to transitions in which $|\Delta B| = 2$. The consequence of this is that $|B_q^0\rangle$ and $|\overline{B}_q^0\rangle$ are not stationnary states or simply decaying states and they do not have the simple $\exp[-iEt/\hbar]$ time dependence.

Consider now a state vector $|\Psi(t)\rangle$ which has evolved from a $|B_q^0\rangle$ or $|\overline{B}_q^0\rangle$ state at time $t = 0$. We are interested in the projection of $|\Psi(t)\rangle$ onto the subspace spanned by $|B_q^0\rangle$ and $|\overline{B}_q^0\rangle$. We call this projection $|\psi(t)\rangle = a(t)|B_q^0\rangle + b(t)|\overline{B}_q^0\rangle$.
The time dependence of the "wave functions" $a(t)$ and $b(t)$ is controlled by a coupled Schrödinger equation:

$$i\frac{d}{dt}\begin{pmatrix} a(t) \\ b(t) \end{pmatrix} = \begin{pmatrix} H_{11} & H_{12} \\ H_{21} & H_{22} \end{pmatrix}\begin{pmatrix} a(t) \\ b(t) \end{pmatrix} = \mathbf{H_{eff}}\begin{pmatrix} a(t) \\ b(t) \end{pmatrix} \tag{1.13}$$

$\mathbf{H_{eff}}$ is the "effective Hamiltonian", which is, in general, not hermitian. We can write $\mathbf{H_{eff}}$ as:

$$\mathbf{H_{eff}} = (\mathbf{M} - \frac{i}{2}\mathbf{\Gamma}) \tag{1.14}$$

where $\mathbf{M}$, the mass matrix, and $\mathbf{\Gamma}$, the decay matrix, are both hermitians.

As CPT is conserved, one has $H_{11} = H_{22}$ and :

$$\mathbf{H_{eff}} = \begin{pmatrix} M - i\Gamma/2 & M_{12} - i\Gamma_{12}/2 \\ M_{12}^* - i\Gamma_{12}^*/2 & M - i\Gamma/2 \end{pmatrix} \tag{1.15}$$

The equation 1.14 can be diagonalized using a linear combination of the $|B_q^0\rangle$ and $|\overline{B}_q^0\rangle$:

$$|B_\pm^0\rangle = p|B_q^0\rangle \pm q|\overline{B}_q^0\rangle \tag{1.16}$$

with the normalization condition $|p|^2 + |q|^2 = 1$. The $|B_\pm^0\rangle$, being eigenstates of the coupled Schrödinger equation, have definite mass and can be labelled as $|B_H\rangle$ for the heavier state (originally $|B_-^0\rangle$) and $|B_L\rangle$ for the lighter one (originally $|B_+^0\rangle$). The eigenvalues obtained in the diagonalization are:

$$\begin{aligned} \lambda_\pm &= (M - \frac{i}{2}\Gamma) \pm \frac{q}{p}(M_{12} - \frac{i}{2}\Gamma_{12}) \\ &= H_{11} \pm H_{12}\frac{q}{p} \end{aligned} \tag{1.17}$$

with:

$$M = \frac{M_H + M_L}{2} \qquad \Gamma = \frac{\Gamma_H + \Gamma_L}{2}$$

Substituting into 1.13, one gets the time evolution of the so-called wave functions $a(t)$ and $b(t)$ which we note from now as $|B_j(t)\rangle$ with $j = H, L$:

$$|B_j(t)\rangle = e^{-iM_j t} e^{-\Gamma_j t/2} |B_j\rangle \tag{1.18}$$

We can now consider the time evolution of the states $|B_q^0\rangle$ and $|\overline{B}_q^0\rangle$ produced in a strong interaction at $t = 0$, using 1.16 and the above expression:

$$|B_q^0(t)\rangle = g_+(t)|B_q^0\rangle + \frac{q}{p} g_-(t)|\overline{B}_q^0\rangle \tag{1.19}$$

$$|\overline{B}_q^0(t)\rangle = g_+(t)|\overline{B}_q^0\rangle + \frac{p}{q} g_-(t)|B_q^0\rangle \tag{1.20}$$

where the time varying parts of these equations has been separated out from the rest [2]:

$$g_\pm(t) \equiv \frac{1}{2}\left[e^{-i\left(M_L - \frac{i}{2}\Gamma_L\right)t} \pm e^{-i\left(M_H - \frac{i}{2}\Gamma_H\right)t}\right] \tag{1.21}$$

The ratio between the coefficients q and p is:

$$\frac{q}{p} = -\sqrt{\frac{M_{12}^* - \frac{i}{2}\Gamma_{12}^*}{M_{12} - \frac{i}{2}\Gamma_{12}}} \tag{1.22}$$

---

[2] Here, $g_\pm(t) = \frac{1}{2}\left[e^{-i\lambda_+ t} \pm e^{-i\lambda_- t}\right]$ with $\lambda_+ = M_L - \frac{i}{2}\Gamma_L$ and $\lambda_- = M_H - \frac{i}{2}\Gamma_H$

Mass and width differences are defined as: $\Delta M \equiv M_H - M_L > 0$ and $\Delta\Gamma \equiv \Gamma_L - \Gamma_H$. The mixing parameter x is : $x = \dfrac{\Delta M}{\Gamma}$.
A peculiar situation occurs for B_d^0 where $\Delta\Gamma_d \simeq 0$. The mixing parameter is $x_d = 0.776 \pm 0.008$ [15] where as for the B_s^0 the figures are:

$$\begin{aligned} \Delta M_s &= 17.77 \pm 0.10(stat) \pm 0.07(syst)\,\mathrm{ps}^{-1} \quad [21] \\ \Delta\Gamma_s &= 0.19 \pm 0.07(stat) \pm^{0.02}_{0.01} (syst)\,\mathrm{ps}^{-1} \quad [22] \end{aligned}$$

We will now express the decay rates before to introduce the CP violation phenomenology.

1.3 Decay rates

Let us define the two decay amplitudes to a common final state f:

$$A_f = \langle f|T|B_q^0\rangle \quad , \quad \overline{A}_f = \langle f|T|\overline{B}_q^0\rangle$$

The time dependent decay rate of a $|B_q^0\rangle$ born at time $t = 0$ as a B_q^0 will then be, using 1.19 :

$$A\left[B_q^0(t) \to f\right] = \langle f|T|B_q^0(t)\rangle = g_+(t)A_f + \frac{q}{p}g_-(t)\overline{A}_f \tag{1.23}$$

and similary for a state created as $\overline{B}_q^0$ at $t = 0$:

$$A\left[\overline{B}_q^0(t) \to f\right] = \langle f|T|\overline{B}_q^0(t)\rangle = g_+(t)\overline{A}_f + \frac{p}{q}g_-(t)A_f \tag{1.24}$$

The associated decay rates are:

$$\begin{aligned} \Gamma_f(t) &\equiv \Gamma\left(B_q^0(t) \to f\right) \\ &= |A_f|^2 \left\{|g_+(t)|^2 + |\lambda_f|^2 |g_-(t)|^2 + 2\mathcal{R}e\left[\lambda_f g_+^*(t) g_-(t)\right]\right\} \\ \overline{\Gamma}_f(t) &\equiv \Gamma\left(\overline{B}_q^0(t) \to f\right) \\ &= |A_f|^2 \left|\frac{p}{q}\right|^2 \left\{|g_-(t)|^2 + |\lambda_f|^2 |g_+(t)|^2 + 2\mathcal{R}e\left[\lambda_f g_+(t) g_-^*(t)\right]\right\} \end{aligned} \tag{1.25}$$

where λ_f is defined as:

$$\lambda_f \equiv \frac{q}{p}\frac{\overline{A}_f}{A_f} \tag{1.26}$$

Similary, we can write the decay rates to the CP conjugated final state $\overline{f}$ as:

$$\begin{aligned}
\Gamma_{\overline{f}}(t) &\equiv \Gamma\left(B_q^0(t) \to \overline{f}\right) \\
&= \left|\overline{A}_{\overline{f}}\right|^2 \left|\frac{q}{p}\right|^2 \left\{ |g_-(t)|^2 + \left|\overline{\lambda}_{\overline{f}}\right|^2 |g_+(t)|^2 + 2\mathcal{R}e\left[\overline{\lambda}_{\overline{f}} g_+(t) g_-^*(t)\right] \right\} \\
\overline{\Gamma}_{\overline{f}}(t) &\equiv \Gamma\left(\overline{B}_q^0(t) \to \overline{f}\right) \\
&= \left|\overline{A}_{\overline{f}}\right|^2 \left\{ |g_+(t)|^2 + \left|\overline{\lambda}_{\overline{f}}\right|^2 |g_-(t)|^2 + 2\mathcal{R}e\left[\overline{\lambda}_{\overline{f}} g_+^*(t) g_-(t)\right] \right\}
\end{aligned} \tag{1.27}$$

where $\overline{\lambda}_{\overline{f}}$ is defined as:

$$\lambda_{\overline{f}} \equiv \frac{q}{p}\frac{\overline{A}_{\overline{f}}}{A_{\overline{f}}} \quad \text{and} \quad \overline{\lambda}_{\overline{f}} = \frac{1}{\lambda_{\overline{f}}} \tag{1.28}$$

The functions governing the time evolution in equations 1.25 and 1.27 are:

$$\begin{aligned}
|g_\pm(t)|^2 &= \frac{1}{4}\left[e^{-\Gamma_L t} + e^{-\Gamma_H t} \pm 2e^{-\Gamma t}\cos(\Delta M_q t)\right] \\
&= \frac{e^{-\Gamma t}}{2}\left[\cosh\left(\frac{\Delta\Gamma_q t}{2}\right) \pm \cos(\Delta M_q t)\right] \\
g_+^*(t) g_-(t) &= \frac{1}{4}\left[-e^{-\Gamma_H t} + e^{-\Gamma_L t} + 2ie^{-\Gamma t}\sin(\Delta M_q t)\right] \\
&= \frac{e^{-\Gamma t}}{2}\left[-\sinh\left(\frac{\Delta\Gamma_q t}{2}\right) + i\sin(\Delta M_q t)\right]
\end{aligned}$$

1.4 Phenomenology of CP violation

The CP symmetry violation can be classified in three different categories in a model independent way:

- **CP violation in mixing**. Mixing is one of the most interesting properties of the B^0 and was discovered in 1987 in the B_d^0 system by the ARGUS experiment[24]. In SM, mixing is a second order weak interaction dominated by box diagrams (see Fig. 1.4). CP violation occurs in mixing, when the $B^0 \to \overline{B}^0$ transition is not the same as the $\overline{B}^0 \to B^0$ one. This happens if $|q/p| \neq 1$.

- **CP violation in decay** occurs when a charged or neutral B meson has not the same decay amplitude as its CP conjugate partner, i.e. :

$$\left|\frac{\overline{A}_{\overline{f}}}{A_f}\right| \neq 1$$

- **CP violation in the interference of mixing and decay**: when a meson decay directly to a CP final eigenstate f ($B_q^0 \rightarrow f$) or after having oscillated before decaying ($B_q^0 \rightarrow \overline{B}_q^0 \rightarrow f$) and when an asymmetry exists, one then speaks of CP violation in the interference of mixing and decay. The condition for this CP violation type to occur is:

$$|\lambda_f| = 1\,,\, \mathcal{I}m\,(\lambda_f) \neq 0$$

We now review in more details these three CP violations.

1.4.1 CP violation in mixing

The CP violation in mixing comes from a difference in the rates of B_q^0 that becomes a $\overline{B}_q^0$ and of $\overline{B}_q^0$ that becomes a B_q^0. In the Schrödinger equation (1.13), CP violation in mixing appears when the magnitudes of the off-diagonal elements of the effective Hamiltonian are differents, i.e.:

$$\left|M_{12} - \frac{i}{2}\Gamma_{12}\right| \neq \left|M_{12}^* - \frac{i}{2}\Gamma_{12}^*\right| \tag{1.29}$$

Taking CP $|B_q^0\rangle = -|\overline{B}_q^0\rangle$ and CP$|\overline{B}_q^0\rangle = -|B_q^0\rangle$ the transition amplitude $|B_q^0\rangle \rightarrow |\overline{B}_q^0\rangle$ and $|\overline{B}_q^0\rangle \rightarrow |B_q^0\rangle$ are:

$$\begin{aligned}
\langle\overline{B}_q^0|T|B_q^0\rangle &= H_{21} &&= M_{12}^* - i\Gamma_{12}^*/2 \\
\langle B_q^0|T|\overline{B}_q^0\rangle &= H_{12} &&= M_{12} - i\Gamma_{12}/2
\end{aligned}$$

If CP was to be conserved, we would have, by summing over a complete set of physical states: $H_{12} = H_{21}$ or $M_{12} = M_{12}^*$, $\Gamma_{12} = \Gamma_{12}^*$ implying M_{12} and Γ_{12} are real and:

$$\left|\frac{q}{p}\right| = 1 \tag{1.30}$$

For the time being, no CP violation in the mixing of the B_q^0-$\overline{B}_q^0$ system has been discovered.

1.4.2 Direct CP violation

The CP violation in decay (or direct CP violation) occurs when the decay rates of $B_q^0 \rightarrow f$ and $\overline{B}_q^0 \rightarrow \overline{f}$ are different. At least, two kinds of phases must appear in the amplitudes for this CP violation to occur:

- **The weak phases**, ϕ_i coming from the V_{CKM} matrix changes sign for $B^0 \rightarrow f$ and $\overline{B}^0 \rightarrow \overline{f}$.

- **The strong phases**, δ_i, which are related to the final state strong interactions and do not change sign.

The amplitudes can then be writen as [3]:

$$A_f = \sum_j A_j e^{-i\phi_j} e^{i\delta_j}, \qquad \overline{A}_{\overline{f}} = \sum_j A_j e^{+i\phi_j} e^{j\delta_j}.$$

The convention independent ratio of amplitudes is:

$$\left|\frac{\overline{A}_{\overline{f}}}{A_f}\right| = \left|\frac{\sum_j A_j e^{i(\delta_j+\phi_j)}}{\sum_i A_i e^{i(\delta_i-\phi_i)}}\right|$$

CP violation in decay appears when:

$$\left|\frac{\overline{A}_{\overline{f}}}{A_f}\right| \neq 1$$

CP violation in decays is now firmly etablished in $B_d^0 \to K^+\pi^-$ decays. The asymmetry is [25]:

$$A_{K\pi} = \frac{\Gamma(\overline{B}_d^0 \to K^+\pi^-) - \Gamma(B_d^0 \to K^+\pi^-)}{\Gamma(\overline{B}_d^0 \to K^+\pi^-) + \Gamma(B_d^0 \to K^+\pi^-)} = -0.095 \pm 0.012$$

In this case, direct CP violation is due to the interference between tree and penguin diagrams.

We will come back with some details to the direct CP violation in $B_d^0 \to J/\psi K_s^0$ decay in section 1.5.

1.4.3 CP violation in the interference of mixing and decay

If the B_q^0 meson and its anti-meson $\overline{B}_q^0$ can both decay to the same final state f, CP violation can appear in the interplay between the mixing and the decay amplitudes (Fig. 1.3); the B meson has two possibilities to decay into the final state f: it can decay directly or it can oscillate before decaying. This process is controlled by:

$$\lambda_f = \left(\frac{q}{p}\right)\left(\frac{\overline{A}_f}{A_f}\right) \tag{1.31}$$

where $\left(\frac{q}{p}\right)$ accounts for the mixing (1.22) and $\left(\frac{\overline{A}_f}{A_f}\right)$ for the decay.
All these quantities are phase convention independent. The CP violation appears when $\lambda_f \neq 1$. Indeed, even if $\left|\frac{q}{p}\right| = 1$ and $\left|\frac{\overline{A}_f}{A_f}\right| = 1$, one can still observe CP violation when:

---

[3] We adopt the phase convention of R.Fleischer [8, 12].

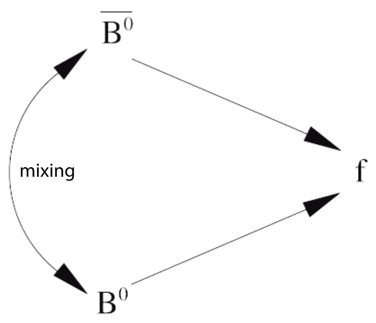

Figure 1.3: Schematic of the mixing between B_q^0 and $\overline{B}_q^0$ decaying in the same f final state.

$$|\lambda_f| = 1 \quad \text{but} \quad \mathcal{I}m\lambda_f \neq 0 \tag{1.32}$$

This type of CP violation is called CP violation in the interference between decay and mixing.

Let us now examine in more details the situation in the B_q^0 system.

1.4.4 CP violation in the B_q^0 system

In the following we restrict ourselves to the decay of the B_q^0 and $\overline{B}_q^0$ to a common final state f, which is also CP eigenstate with eigenvalue η_{CP}.

The mixing in the neutral B-system, $B_q^0 \leftrightarrow \overline{B}_q^0$ ($q \in d, s$), is described by the two box diagrams of Fig. 1.4. Due to the CKM matrix element values ($V_{tb} \simeq 1$) and because the amplitude in the loop is proportional to the mass, the quark t (top) contribution dominates the box diagram. Therefore, for the transition $B_q^0 \to \overline{B}_q^0$, one has $(V_{tb}^* V_{tq})^2 \approx V_{tq}^2$ and for the transition $\overline{B}_q^0 \to B_q^0$, $(V_{tb} V_{tq}^*)^2 \approx V_{tq}^{*2}$ with the same kinematic factors.
Moreover, in both B_d^0 and B_s^0 cases, one has $|\Gamma_{12}| \ll |M_{12}| \approx 5 \times 10^{-3}$ and q/p becomes (see equation 1.22):

$$\left(\frac{q}{p}\right)_{B_q^0} = -\left(\frac{H_{21}}{H_{12}}\right)^{1/2} \approx -\left(\frac{M_{21}}{M_{12}}\right)^{1/2} = -\left(\frac{M_{12}^*}{M_{12}}\right)^{1/2} = -\frac{M_{12}^*}{|M_{12}|}$$

The matrix element M_{12} can be written as [8, 12] $M_{12} = |M_{12}|e^{i\theta_M}$ where $\theta_M = 2\mathrm{arg}(\mathrm{V}_{\mathrm{tq}}^*\mathrm{V}_{\mathrm{tb}} + \pi - \varphi_{\mathrm{CP}})$ and φ_{CP} defined through $CP|B_q^0\rangle = e^{i\varphi_{CP}}|\overline{B}_q^0\rangle$.
In the SM : $2\mathrm{arg}(\mathrm{V}_{\mathrm{tq}}^*\mathrm{V}_{\mathrm{tb}}) = \varphi_{\mathrm{M}}$ with $\varphi_M = 2\beta$ if $q = d$ and $\varphi_M = -2\eta\lambda = -2\delta\gamma$ if $q = s$. Then:

$$\left(\frac{q}{p}\right)_{B_q^0} \simeq -e^{-i\theta_M} = e^{-i(\varphi_M - \varphi_{CP})} \tag{1.33}$$

Hence, $\left|\frac{q}{p}\right| = 1$.

Decay rates

With $\left|\frac{q}{p}\right| = 1$ and $|\lambda_f| = \left|\frac{\overline{A}_f}{A_f}\right|$, the decay rates (1.25) can be written as:

$$\begin{aligned}
\Gamma[B_q^0(t) \to f] &= \frac{|A_f|^2 + |\overline{A}_f|^2}{2}\, e^{-\Gamma_q t} \Bigg\{ \cosh\left(\frac{\Delta\Gamma_q\, t}{2}\right) + D_f \sinh\left(\frac{\Delta\Gamma_q\, t}{2}\right) \\
&\qquad + C_f \cos\left(\Delta M_q\, t\right) + S_f \sin\left(\Delta M_q\, t\right) \Bigg\} \\
\Gamma[\overline{B}_q^0(t) \to f] &= \frac{|A_f|^2 + |\overline{A}_f|^2}{2}\, e^{-\Gamma_q t} \Bigg\{ \cosh\left(\frac{\Delta\Gamma_q\, t}{2}\right) + D_f \sinh\left(\frac{\Delta\Gamma_q\, t}{2}\right) \\
&\qquad - C_f \cos\left(\Delta M_q\, t\right) - S_f \sin\left(\Delta M_q\, t\right) \Bigg\}
\end{aligned} \tag{1.34}$$

where:

$$D_f \equiv -\frac{2\mathcal{R}e(\lambda_f)}{1 + |\lambda_f|^2} \equiv \mathcal{A}_{\Delta\Gamma} \tag{1.35}$$

$$C_f \equiv \frac{1 - |\lambda_f|^2}{1 + |\lambda_f|^2} \equiv \mathcal{A}_{CP}^{dir} \tag{1.36}$$

$$S_f \equiv -\frac{2\mathcal{I}m(\lambda_f)}{1 + |\lambda_f|^2} \equiv \mathcal{A}_{CP}^{mix-ind} \tag{1.37}$$

These three observables satisfy the normalisation equation:

$$\left(\mathcal{A}_{CP}^{dir}\right)^2 + \left(\mathcal{A}_{CP}^{mix-ind}\right)^2 + \left(\mathcal{A}_{\Delta\Gamma}\right)^2 = 1 \tag{1.38}$$

We now consider the case of the interference of mixing and decay in the neutral B system; as there is no CP violation in mixing,

$$\left|\frac{q}{p}\right| = 1 \quad \Rightarrow \quad |\lambda_f| = \left|\frac{\overline{A}_f}{A_f}\right|$$

Moreover, if the decay is dominated by a single process and the ratio of the amplitudes described by one weak phase φ_D as for the decays $B_d^0 \to J/\psi K_s^0$ and $B_s^0 \to J/\psi\phi$, we have (with phase convention [8, 12]):

$$\frac{\overline{A}_f}{A_f} = \eta_{CP} e^{i(2\varphi_D - \varphi_{CP})}$$

Therefore, using 1.33:

$$\lambda_f \equiv \left(\frac{q}{p}\right)_{B_q^0} \cdot \frac{\overline{A}_f}{A_f} = \eta_{CP} e^{-i(\varphi_M - 2\varphi_D)}$$

The phase $\varphi = \varphi_M - 2\varphi_D$ is the difference between the mixing phase φ_M and twice the decay phase φ_D. The decay phase φ_D is equal to 0 for the dominant amplitude $\overline{b} \to \overline{c}c\overline{q}$ $(q = d, s)$, i.e. for $B_d^0 \to J/\psi K_s^0$ and $B_s^0 \to J/\psi\phi$, and $\varphi = \varphi_M$. Hence, in the case of no violation in mixing and a sole amplitude in the decay we have:

$$|\lambda_f| = 1 \quad \Rightarrow \quad C_f \equiv 0 \quad S_f \equiv \eta_{CP}\sin(\varphi) \quad D_f \equiv -\eta_{CP}\cos(\varphi)$$

and the time dependent decay rates write:

$$\begin{aligned}\Gamma(B_d^0(t) \to f_{CP}) &= |A_{f_{CP}}|^2 e^{-\Gamma_q t}\Bigg[\cosh\left(\frac{\Delta\Gamma_q t}{2}\right) - \eta_{CP}\cos(\varphi)\sinh\left(\frac{\Delta\Gamma_q t}{2}\right) \\ &\qquad + \eta_{CP}\sin(\varphi)\sin(\Delta M_q t)\Bigg] \\ \Gamma(\overline{B}_d^0(t) \to f_{CP}) &= |A_{f_{CP}}|^2 e^{-\Gamma_q t}\Bigg[\cosh\left(\frac{\Delta\Gamma_q t}{2}\right) - \eta_{CP}\cos(\varphi)\sinh\left(\frac{\Delta\Gamma_q t}{2}\right) \\ &\qquad - \eta_{CP}\sin(\varphi)\sin(\Delta M_q t)\Bigg]\end{aligned}$$

The time dependent asymmetry reduces to:

$$\mathcal{A}_{CP}(t) = \frac{\Gamma\left[\overline{B}_q^0(t) \to f_{CP}\right] - \Gamma\left[B_q^0(t) \to f_{CP}\right]}{\Gamma\left[\overline{B}_q^0(t) \to f_{CP}\right] + \Gamma\left[B_q^0(t) \to f_{CP}\right]} = \frac{-\eta_{CP}\sin(\varphi)\sin(\Delta M_q t)}{\cosh\left(\frac{\Delta\Gamma_q t}{2}\right) - \eta_{CP}\cos(\varphi)\sinh\left(\frac{\Delta\Gamma_q t}{2}\right)} \tag{1.39}$$

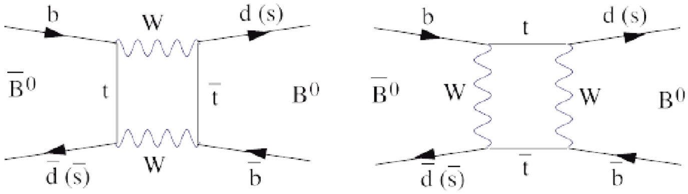

Figure 1.4: Box diagrams of neutral B-meson oscillation. The quark t can be replaced by a u quark or a c quark.

1.5 Direct CP violation in $B_d^0 \to J/\psi K_s^0$ decay

1.5.1 The $B_d^0 \to J/\psi K_s^0$ asymmetry

In the measurement of $\sin 2\beta$, where $2\beta = \varphi_M$ using the time dependent asymmetry of the decay rate of $B_d^0 \to J/\psi K_s^0$, the general assumption is that the decay is dominated by the tree diagram. In this case, as described in the previous section, the direct asymmetry vanishes and we have only the mixing induced asymmetry $\mathcal{A}_{CP}^{mix-ind}$, which allows to access to $\varphi_M = \phi_d$, the mixing angle for the B_d^0 system.

Allowing direct CP violation to occur by the presence of more than one diagram, the time dependent asymmetry transforms to:

$$\begin{aligned}\mathcal{A}_{CP}(t) &= -\frac{\mathcal{A}_{CP}^{dir}\cos(\Delta M t) + \mathcal{A}_{CP}^{mix-ind}\sin(\Delta M t)}{\cosh(\Delta\Gamma t/2) + \mathcal{A}_{\Delta\Gamma}\sinh(\Delta\Gamma t/2)} \\ &\underbrace{=}_{\Delta\Gamma=0} -\left(\mathcal{A}_{CP}^{dir}\cos(\Delta M t) + \mathcal{A}_{CP}^{mix-ind}\sin(\Delta M t)\right)\end{aligned} \tag{1.40}$$

1.5.2 The current state of the art in the measurement of $\sin 2\beta$

The last results from the CKMfitter Group [23] are:

$$\sin 2\beta = 0.688\,[+0.0257, -0.024]$$

This is the result of a global adjustment in which $\sin 2\beta$ also enters, and which is dominated by the experimental measurements of $\sin 2\beta$. The world average of $\sin 2\beta$, as presented at the Lepton-Photon 2008 conference (Daegu, Korea) [25], is $\sin 2\beta = 0.678 \pm 0.026$.

The measurements of $\sin 2\beta$ at Belle [26] and Babar [27] have also provided $\mathcal{A}_{CP}^{dir} \equiv C$ (equation 1.36) values which are compatible with zero:

$$\begin{array}{lll} S = 0.714 \pm 0.032 \pm 0.018 & C = 0.049 \pm 0.022 \pm 0.017 & \text{(Babar)} \\ S = 0.642 \pm 0.031 \pm 0.017 & C = 0.018 \pm 0.021 \pm 0.014 & \text{(Belle)} \end{array}$$

where, $S = \eta_{CP}\sin 2\beta = \mathcal{A}_{CP}^{mix-ind}$ and $C = \mathcal{A}_{CP}^{dir}$.

1.5.3 Decay amplitudes

Let us have a closer look to the B^0 decay amplitudes.

We can write the amplitude (Fig. 1.5) as:

$$\text{Amp}(B_d^0 \to J/\psi K_s^0) = V_{cs}V_{cb}^*\,(A_T + P_c) + V_{us}V_{ub}^* P_u + V_{ts}V_{tb}^* P_t \tag{1.41}$$

where A_T is the tree amplitude, P_u, P_c and P_t the penguin amplitudes mediated by the u, c and t quarks. One often finds using the unitary condition $V_{us}V_{ub}^* + V_{cs}V_{cb}^* + V_{ts}V_{tb}^* = 0$:

$$\text{Amp}(B_d^0 \to J/\psi K_s^0) = \underbrace{V_{cs}V_{cb}^*}_{\propto\lambda^2}\,(A_T + P_c - P_t) + \underbrace{V_{us}V_{ub}^*}_{\propto\lambda^4}\,(P_u - P_t)$$

The decay has therefore both tree and penguin diagrams, the latter being higher order in perturbation theory, and as such, must have a smaller amplitude.

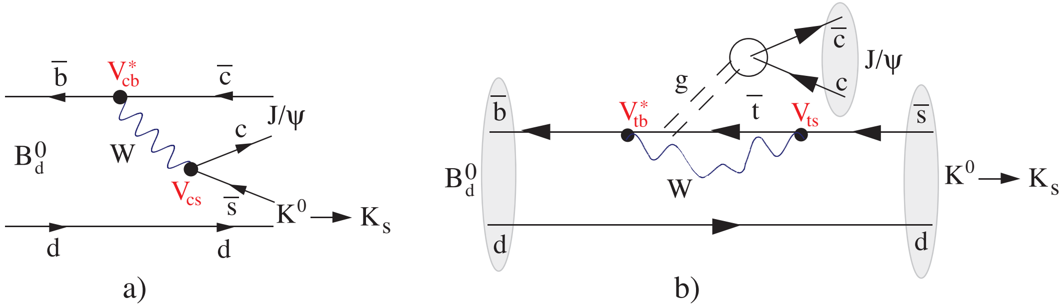

Figure 1.5: Feynman diagrams contributing to $B_{d,s}^0 \to J/\psi K_s^0$. a) the tree (current-current) diagram and b) the penguin one. The dashed lines in the penguin topology represent a colour-singlet exchange.

Furthermore, if two amplitudes are present in the decay with distinct weak phases φ_1 and φ_2 and a steep hierarchy such that the decay amplitudes ratio r is small ($r < 1$), the direct asymmetry becomes [8, 12, 13]:

$$C \simeq 2r \sin(\varphi_1 - \varphi_2) \sin\theta$$

θ is the phase difference of the strong final state interaction. Hence, for direct CP violation to occur, one must have:

- at least two diagrams mediating the decay
- these two diagrams must have different weak phases
- they must have different strong phases.

Let us consider the main penguin term in which a top quark is exchanged. We have:

- the current-current tree diagram, which is proportional to $V_{cs}V_{cb}^* \sim (1)(A\lambda^2)$
- the penguin "top" diagram, which is proportional to $V_{tb}^* V_{ts} \sim (-A\lambda^2)\exp(i\,\mathrm{arg}V_{ts})(1)$.

The weak phase of the penguin term is $\arg(V_{ts}) = \delta\gamma = -\phi_s$, i.e. the mixing phase that we are searching for in the measurement of the asymmetry in $B_s^0 \to J/\psi\phi$ or $B_s^0 \to J/\psi\eta$. In SM, this phase is proportional to λ^2 (a few percents). Therefore, the difference between the tree and penguin diagram phases expected to be $\varphi_{tree} - \varphi_{pen} \sim \lambda^2$. The direct asymmetry is therefore strongly suppressed as:

$$r \sin(\varphi_{tree} - \varphi_{pen}) \sim \lambda^2 r$$

If there is no CP violation in the decay, the strong phase can also be small. The mixing induced asymmetry also contains additive term proportionnal to $r \sin(\varphi_{tree} - \varphi_{pen})$ and can be slightly affected by penguin pollution.

The question is to know if we can experimentaly determine the importance of these penguin diagrams.

Conclusion

1. We can consider, to a very good approximation, that the decay $B_d^0 \rightarrow J/\psi K_s^0$ is dominated only by the tree amplitude and therefore, that the measurement of the time dependent asymmetry gives the mixing angle ϕ_d.
2. However, to what extent can we neglect the penguin amplitudes whereas experimental accuracy is improving year after year?

1.5.4 Expected and requested accuracies at LHCb

Currently, LHCb foresees a precision on the $\sin 2\beta$ of :

$$\sigma_{stat}\left(\sin 2\beta\right) = 0.020 \quad \Rightarrow \quad \sigma_{stat}\left(\beta\right) = 0.78^\circ \quad \text{for} \quad 2\,\text{fb}^{-1}$$

This means that in one year, the achieved precision will be higher than the present one on the combined results of the B-factories. In five years of running, we expect:

$$\sigma_{stat}\left(\sin 2\beta\right) = 0.010 \quad \Rightarrow \quad \sigma_{stat}\left(\beta\right) = 0.39^\circ \quad \text{for} \quad 10\,\text{fb}^{-1}$$

Moreover, if the error on the angle β is to match one of the opposite side to β, we must examine the error on V_{ub}. From CKMfitter Group [23]:

$$|V_{ub}| = 0.00357 \pm 0.00017$$

This relative error of 4.76% reflectes in an error on β of 1°. Thus, direct errors on β and indirect errors from V_{ub} are equivalent at the moment. A decrease to 2% of the error on V_{ub} would lead to an "indirect error" on β of 0.42°, i.e. a precision that we would reach after five year of running. However, to achieve such a precision, we must on one hand reduce systematics errors and on the other hand master the theoretical errors.

Theoretical errors

Mastering the theoretical errors implies the determination of pollution from penguin diagrams which result not only in the existence of an asymmetry from direct CP violation, but also affects $\mathcal{A}_{CP}^{mix-ind}$ term (because of $\sin\left(\varphi_{tree} - \varphi_{pen}\right)$ seen previously).

A method has been proposed by Robert Fleischer [29] in 1999, which consists in the measurement of the time dependent asymmetries of the $B_s^0 \rightarrow J/\psi K_s^0$ decay. These measurements allow to determine the amplitude and the phase of the penguin diagram(s) of $B_d^0 \rightarrow J/\psi K_s^0$, under the assumption of U-spin symmetry.

1.5.5 The method proposed by R.Fleischer, based on the U-spin symmetry.

In the following, we refer to the articles of R. Fleischer [29] and [30]. In these papers, R. Fleischer proposed to use the U-spin symmetry to connect the amplitudes and the

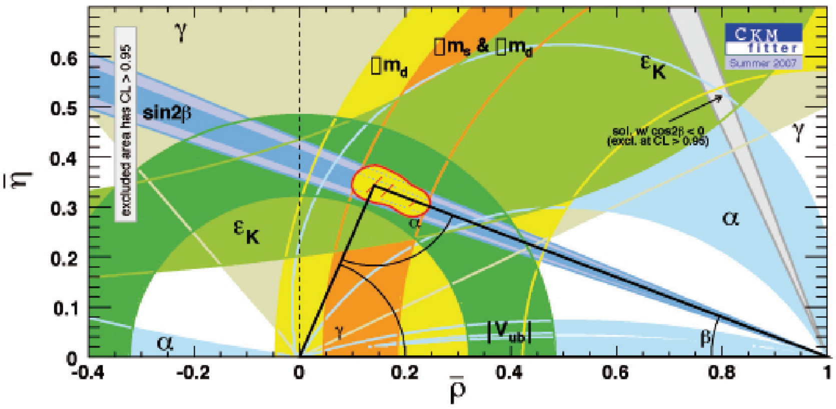

Figure 1.6: The unitarity triangle from CKMfitter Group [23] as of summer 2007. The incertainty on $|V_{ub}|$ is given by the green half-ring centered on zero.

phases of the two decays $B_{d(s)}^0 \to J/\psi K_s^0$.

Let us rewrite the amplitude $\mathrm{Amp}(B_{d,s}^0 \to J/\psi K_s^0)$. As Fleischer, we will put a prime ' to the amplitudes corresponding to $B_d^0 \to J/\psi K_s^0$. Equation 1.41 then writes:

$$\mathrm{Amp}(B_d^0 \to J/\psi K_s^0) = V_{cs}V_{cb}^*\left(A_T^{'} + P_c^{'}\right) + V_{us}V_{ub}^*P_u^{'} + V_{ts}V_{tb}^*P_t^{'} \tag{1.42}$$

with 1.5:

$$\begin{array}{ll}
V_{cs} = 1 - \dfrac{\lambda^2}{2} + \mathcal{O}(\lambda^4) & V_{cb} = A\lambda^2 + \mathcal{O}(\lambda^8) \\
V_{us} = \lambda + \mathcal{O}(\lambda^7) & V_{ub} = A\lambda^3(\rho - i\eta) + \mathcal{O}(\lambda^6) \\
V_{ts} = -A\lambda^2 + \dfrac{1}{2}A\lambda^4\left[1 - 2(\rho + i\eta)\right] + \mathcal{O}(\lambda^6) & V_{tb} = 1 + \mathcal{O}(\lambda^4)
\end{array}$$

The amplitude becomes:

$$\begin{aligned}
\mathrm{Amp}(B_d^0 \to J/\psi K_s^0) &= \left(1 - \frac{\lambda^2}{2}\right) A\lambda^2 \left(A_T^{'} + P_c^{'}\right) + \lambda A\lambda^3 \left(\rho + i\eta\right) P_u^{'} \\
&\quad - A\lambda^2 \left[\left(1 - \frac{\lambda^2}{2}\right) + \lambda^2 \left(\rho + i\eta\right)\right] P_t^{'} \\
&= \left(1 - \frac{\lambda^2}{2}\right) A\lambda^2 \left(A_T^{'} + P_c^{'} - P_t^{'}\right) + A\lambda^4 \left(\rho + i\eta\right) \left(P_u^{'} - P_t^{'}\right)
\end{aligned}$$

With $(\rho + i\eta) = R_B e^{i\gamma}$ and $P_{ct}^{'} = P_c^{'} - P_t^{'}$ and $P_{ut}^{'} = P_u^{'} - P_t^{'}$:

$$\begin{aligned}
\mathrm{Amp}(B_d^0 \to J/\psi K_s^0) &= \left(1-\frac{\lambda^2}{2}\right) A\lambda^2 \left(A_T^{'}+P_{ct}^{'}\right) + A\lambda^4 R_B e^{i\gamma} P_{ut}^{'} \\
&= \left(1-\frac{\lambda^2}{2}\right) A\lambda^2 \left(A_T^{'}+P_{ct}^{'}\right) \left[1+\frac{A\lambda^4 R_B e^{i\gamma} P_{ut}^{'}}{\left(1-\frac{\lambda^2}{2}\right) A\lambda^2 \left(A_T^{'}+P_{ct}^{'}\right)}\right] \\
&= \left(1-\frac{\lambda^2}{2}\right) A\lambda^2 \left(A_T^{'}+P_{ct}^{'}\right) \left[1+\frac{A\lambda^4 \left(1-\frac{\lambda^2}{2}\right) R_B e^{i\gamma}}{\left(1-\frac{\lambda^2}{2}\right)^2 A\lambda^2} \cdot \left(\frac{P_{ut}^{'}}{A_T^{'}+P_{ct}^{'}}\right)\right]
\end{aligned}$$

As $\left(1-\frac{\lambda^2}{2}\right)^2 \simeq 1-\lambda^2$, we have:

$$\mathrm{Amp}(B_d^0 \to J/\psi K_s^0) = \left(1-\frac{\lambda^2}{2}\right) A\lambda^2 \left(A_T^{'}+P_{ct}^{'}\right) \left[1+\frac{\lambda^2}{1-\lambda^2} R_B \left(1-\frac{\lambda^2}{2}\right) e^{i\gamma} \cdot \left(\frac{P_{ut}^{'}}{A_T^{'}+P_{ct}^{'}}\right)\right]$$

By defining $\mathcal{A}mp^{'} \equiv A\lambda^2 \left(A_T^{'}+P_{ct}^{'}\right)$ and $a^{'} e^{i\theta^{'}} \equiv R_B \left(1-\frac{\lambda^2}{2}\right) \cdot \left(\frac{P_{ut}^{'}}{A_T^{'}+P_{ct}^{'}}\right)$, we obtain:

$$\mathrm{Amp}(B_d^0 \to J/\psi K_s^0) = \left(1-\frac{\lambda^2}{2}\right) \mathcal{A}mp^{'} \cdot \left[1+\frac{\lambda^2}{1-\lambda^2} a^{'} e^{i\theta^{'}} e^{i\gamma}\right] \tag{1.43}$$

Similarly, for $B_s^0 \to J/\psi K_s^0$:

$$\mathrm{Amp}(B_s^0 \to J/\psi K_s^0) = V_{cd}V_{cb}^* \left(A_T+P_c\right) + V_{ud}V_{ub}^* P_u + V_{td}V_{tb}^* P_t \tag{1.44}$$

with :

$$V_{cd} = -\lambda \quad V_{ud} = 1-\frac{1}{2}\lambda^2 \quad V_{td} = A\lambda^3 \left[1-(\rho+i\eta)\left(1-\frac{1}{2}\lambda^2\right)\right]$$

We get easily:

$$\mathrm{Amp}(B_s^0 \to J/\psi K_s^0) = -\lambda \mathcal{A}mp \cdot \left[1-ae^{i\theta}e^{i\gamma}\right] \tag{1.45}$$

with : $\mathcal{A}mp \equiv A\lambda^2 \left(A_T+P_{ct}\right)$ and $ae^{i\theta} \equiv R_B \left(1-\frac{\lambda^2}{2}\right) \cdot \left(\frac{P_{ut}}{A_T+P_{ct}}\right)$.
In the above expressions, $R_B = \sqrt{\rho^2+\eta^2}$, γ is the third angle of the unitary triangle, θ and $\theta^{'}$ are the strong phase differences among the amplitudes. a and $a^{'}$ are proportionnal to the ratio of the amplitudes defined above that we are looking for.

Remarks on the amplitudes

A priori, $a^{'}$ could be important (20% as predicted Fleischer). Fortunately, this amplitude is multiplied by λ^2 in $B_d^0 \to J/\psi K_s^0$, which strongly diminishes its importance, whereas a enters in Amp $\left(B_s^0 \to J/\psi K_s^0\right)$ in a Cabibbo allowed way.
Another consequence, if a is non zero, there will be more than a single diagram: direct asymmetry will be present in $B_s^0 \to J/\psi K_s^0$.

The time dependent asymmetries

With the presence of several diagrams allowing direct, mixing-induced asymmetries as well as the asymmetry arising from the presence of $\Delta\Gamma$, the time depedent asymmetry writes:

$$\mathcal{A}_{CP}(t) = -\frac{\mathcal{A}_{CP}^{dir}\cos(\Delta M t) + \mathcal{A}_{CP}^{mix-ind}\sin(\Delta M t)}{\cosh\left(\Delta\Gamma t/2\right) + \mathcal{A}_{\Delta\Gamma}\sinh(\Delta\Gamma t/2)}$$

with:

$$\begin{aligned}
\mathcal{A}_{CP}^{dir} &= \frac{2b\sin\rho\sin\gamma}{1-2b\cos\rho\cos\gamma+b^2} \\
\mathcal{A}_{CP}^{mix-ind} &= \eta_{CP}\left[\frac{\sin\phi - 2b\cos\rho\sin\left(\phi+\gamma\right) + b^2\sin\left(\phi+2\gamma\right)}{1-2b\cos\rho\cos\gamma+b^2}\right] \\
\mathcal{A}_{\Delta\Gamma} &= -\eta_{CP}\left[\frac{\cos\phi - 2b\cos\rho\cos\left(\phi+\gamma\right) + b^2\cos\left(\phi+2\gamma\right)}{1-2b\cos\rho\cos\gamma+b^2}\right]
\end{aligned}$$

where we are used the parametrizations of [29]. In these expressions, ϕ is the weak mixing angle [4]: $\phi = 2\beta$ for B_d^0 and $\phi = \phi_s = -2\delta\gamma$ for B_s^0.

For $B_d^0 \to J/\psi K_s^0$: $\quad b = \epsilon a^{'} \quad \rho = \theta^{'} + 180^\circ \quad$ with $\quad \epsilon \equiv \frac{\lambda^2}{1-\lambda^2}$.

For $B_s^0 \to J/\psi K_s^0$: $\quad b = a \quad$ and $\quad \rho = \theta$.

The strategy proposed by R. Fleischer is:

- to use the U-spin symmetry that interchanges d and s quarks. This implies that $a = a^{'}$ and $\theta = \theta^{'}$,
- to measure the ratio of the $B_s^0 \to J/\psi K_s^0$ over $B_d^0 \to J/\psi K_s^0$ production rates, H. Its parametrization gives : $H = \dfrac{1-2a\cos\theta\cos\gamma+a^2}{1+2\epsilon a^{'}\cos\theta^{'}\cos\gamma+\epsilon^2 a^{'2}}$
- to measure the asymmetries in $B_s^0 \to J/\psi K_s^0$ decay,

---

[4] This mixing phase was written φ_M in the relation 1.33

- and to plot the ($\mathcal{A}_{CP}^{dir}$ vs $\mathcal{A}_{CP}^{mix-ind}$) and ($\mathcal{A}_{CP}^{mix-ind}$ vs H) curves in the $a-\gamma$ plane. Their intersection will give γ and a. A third contour can be defined as ($\mathcal{A}_{\Delta\Gamma}$ vs H), which is almost equivalent to ($\mathcal{A}_{CP}^{dir}$ vs $\mathcal{A}_{CP}^{mix-ind}$).

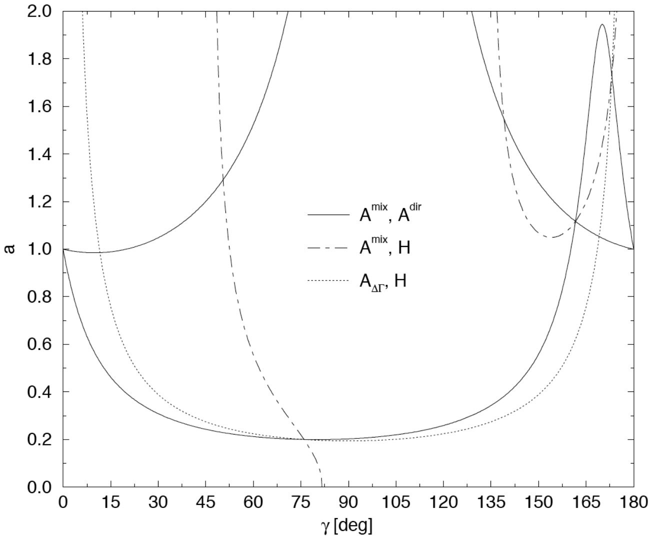

Figure 1.7: The contours in a $\gamma - a$ plane for the specific example developped in [29]. The solid lines represent the contours made by combining the two CP asymmetries $\mathcal{A}_{CP}^{dir}$ and $\mathcal{A}_{CP}^{mix-ind}$. The dotted line is obtained by combining of H and $\mathcal{A}_{CP}^{mix-ind}$ and the dotted-dashed line is obtained combining H and $\mathcal{A}_{\Delta\Gamma}$.

Using the asymmetries

The accuracy of the measurements of the γ angle is currently (CKMfitter summer 2007 [23]):

$$\begin{aligned}\gamma &= \left[67.6\ {}^{-2.8}_{+4.5}\right]^{\circ} \quad \text{(fits)}\\ \gamma &= \left[76.8\ {}^{-31.5}_{+30.4}\right]^{\circ} \quad \text{(direct measurements)}\end{aligned}$$

The expected precision on a measurement of $(\gamma + \phi_s)$ from the proper time distributions of $B_s^0 \to D_s^- \pi^+$ and $B_s^0 \to D_s^{\mp} K^{\pm}$ is $\sim 10^{\circ}$ for one year of data taking, which represents a reduction by a factor of 3 of the error on the current direct measurements [32].

Looking at the ($\mathcal{A}_{CP}^{dir}$ vs $\mathcal{A}_{CP}^{mix-ind}$) and ($\mathcal{A}_{CP}^{mix-ind}$ vs H) contours, we can conclude that:

- The sensitivity to γ depends upon the shape of the contour ($\mathcal{A}_{CP}^{dir}$ vs $\mathcal{A}_{CP}^{mix-ind}$), which presents a kind of plateau in the zone $[45^{\circ} - 105^{\circ}]$. A priori, the sensitivity to γ does not seem very large when compared to the precisions that could be reached at LHCb in five years.

- The sensitivity to the parameter a could be significant and we should use the fact that ($\mathcal{A}_{CP}^{dir}$ vs $\mathcal{A}_{CP}^{mix-ind}$) has a “ flat-bottom” in the domain where the value of γ is expected to be: the uncertainty in the determination of a will not be dependent on the uncertainty on γ.

1.6 Conclusions

1.6.1 Our strategy

We propose the following strategy:

- Measure the time dependent asymmetries of $B_s^0 \to J/\psi K_s^0$,
- Use the γ value obtained either from the global adjustments or from the direct measurements; in any case, for the direct measurements, we already expect an improvement of the measurement precision after one year of running.
- Using the asymmetries $\mathcal{A}_{CP}^{dir}$ and $\mathcal{A}_{CP}^{mix-ind}$ and γ, we have access to a and θ. This method is totally independent of theoretical calculations, except the U-spin symmetry assumption.
- Knowing a and θ, i.e. $a^{'}$ and $\theta^{'}$ via U-spin, we can determine the penguin diagram contribution in the measurement of $\sin 2\beta$.

The purpose of this work is then:

1. Study of the possibility of extracting the $B_s^0 \to J/\psi K_s^0$ signal from the background at LHCb and calculate its rate with the cuts which enables the extraction of the signal.
2. Estimate the sensitivity of the LHCb experiment to the determination of a and θ.

1.6.2 The current status of the study of $B_s^0 \to J/\psi K_s^0$

Preliminary studies about a measurement of the time-dependent CP asymmetry in the $B_s^0 \to J/\psi K_S^0$ decay have been reported [31]. These studies were made in the year 2000 by the CMS group and by LHCb and were not very conclusive: using standard cuts tuned for $B_d^0 \to J/\psi K_s^0$, the selection results in a combinatoric background which is an order of magnitude above the $B_s^0 \to J/\psi K_s^0$ signal (Fig. 1.8).

Indeed, using the fact that hadronization fractions of b-quarks into B_d^0 and B_s^0 are 0.398 ± 0.012 and 0.103 ± 0.014 respectively, and that their visible branching ratios to $J/\psi(\mu^+\mu^-)K_s^0(\pi^+\pi^-)$ are $17.9 \cdot 10^{-6}$ and $8.21 \cdot 10^{-7}$, the B_s^0 event yield will be 1/81 that of the B_d^0 when the same selection criteria are applied.

Hence, the big challenge of this analysis is to extract the B_s^0 signal from the large background. The mass resolution of the B_d^0 must also be less than $10\,\mathrm{MeV/c^2}$ to allow a clean separation of the B_d^0 and B_s^0 peaks.

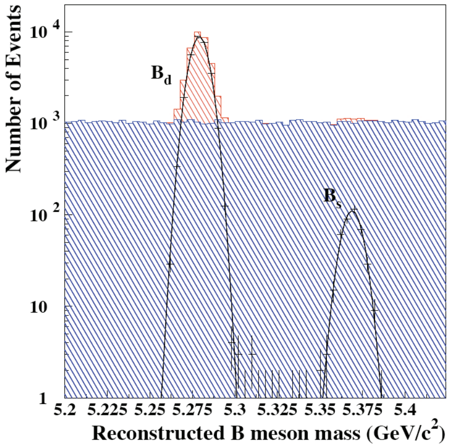

Figure 1.8: $B_d^0 \to J/\psi(\mu^+\mu^-)K_s^0$ and $B_s^0 \to J/\psi(\mu^+\mu^-)K_s^0$ mass peaks at LHCb. Histogram taken from [31].

A simple simulation, generating single gaussians with a resolution $\sigma = 12.82\,\mathrm{MeV/c^2}$, conservative values of the B_d^0/B_s^0 production ratio of 4 and a ratio of branching ratios of 22 (Fig. 1.9), shows that to see B_s^0 mass peak, the B/S ratio for the $B_d^0 \to J/\psi K_s^0$ decay must be around 0.01. In that case, the B/S for $B_s^0 \to J/\psi K_s^0$ will be around 1.
From an experimental point of view, the search for the K_s^0, decaying in $K_s^0 \to \pi^+\pi^-$ will represent the most difficult challenge as pions are copiously produced, thus contributing to the combinatoric background.
The decay $B_d^0 \to J/\psi(\mu^+\mu^-)K_s^0(\pi^+\pi^-)$ is illustrated on Fig. 1.10. The J/ψ particle has a very short lifetime, its decay vertex and the one of the B_d^0 will coincide.
The K_s^0 will have a flight path of several tens of milimeters. We chose to consider only those K_s^0 decays occuring in the Vertex Locator region and giving ”long tracks” for the sake of a good mass resolution. We will come back to this point in Chapter 5.

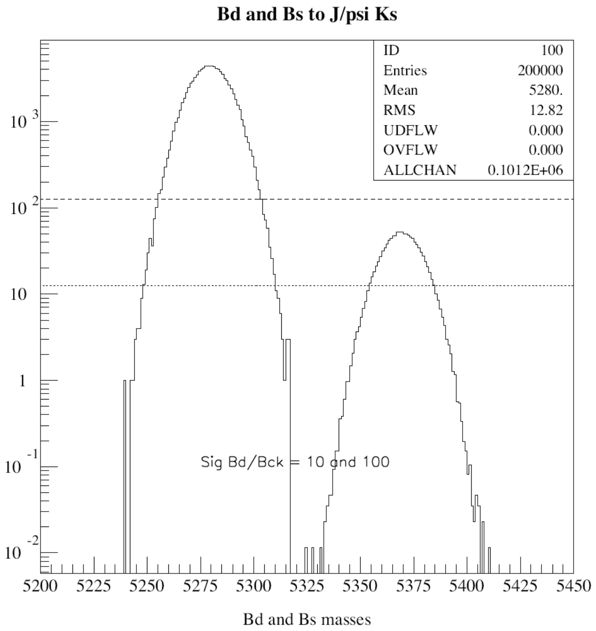

Figure 1.9: $B_d^0 \to J/\psi(\mu^+\mu^-)K_s^0$ and $B_s^0 \to J/\psi(\mu^+\mu^-)K_s^0$ signals and background with S(B_d^0)/B = 10 and 100.

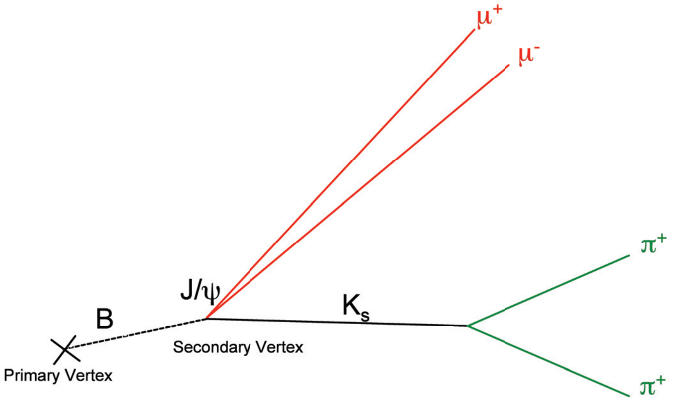

Figure 1.10: Topology of the decay channel $B_d^0 \to J/\psi(\mu^+\mu^-)K_s^0(\pi^+\pi^-)$.

Chapter 2

The LHCb experiment

2.1 Large Hadronic Collider (LHC)

CERN (Conseil Européen pour la Recherche Nucléaire) [33], founded in 1954, is the world's largest particle physics center and includes 20 member states. This laboratory provides scientists the necessary tools to study the building blocks of matter and the forces that hold them together. The Large Hadronic Collider (LHC) [34] (Fig 2.1) is the successor of the Large Electron Positron (LEP) collider, which has tested the Standard Model with an extreme precision. Instead of electron-positron, the LHC collides protons or heavy ions. With minor civil engineering modifications, the LHC is placed in the same tunnel, which was used by the LEP accelerator. This ring, located 100 m underground across the Swiss and French border, is 27 km in circonference. The two opposite beams of protons collide with a center-of-mass (CM) energy of $\sqrt{s} = 14\,\mathrm{TeV}$, an energy which is difficult to reach with conventional electron-positron colliders due to synchrotron radiation. The main experimental challenge of the LHC is to search for the Higgs Boson that could provide an explanation for the mass of elementary particles, and the SUSY particles to explore the physics beyond the Standard Model (SM). The main disadvantage of the proton-proton collisions is the high background due to hadronic interactions.

2.1.1 The accelerator chain and the LHC experiments

To get an energy of 7 TeV, protons are accelerated through the complex accelerator chain at CERN (Fig 2.2). Protons are produced by hydrogen atoms and injected into a linear accelerator (LINAC) to be accelerated at an energy of 50 MeV. They reach an energy of 1.4 GeV in the PS Booster (PSB) and pass into the Proton Synchrotron (PS) where they are accelerated up to 25 GeV. Before being injected in the LHC, protons are sent in the Super Proton Synchrotron (SPS) where they are accelerated to 450 GeV.

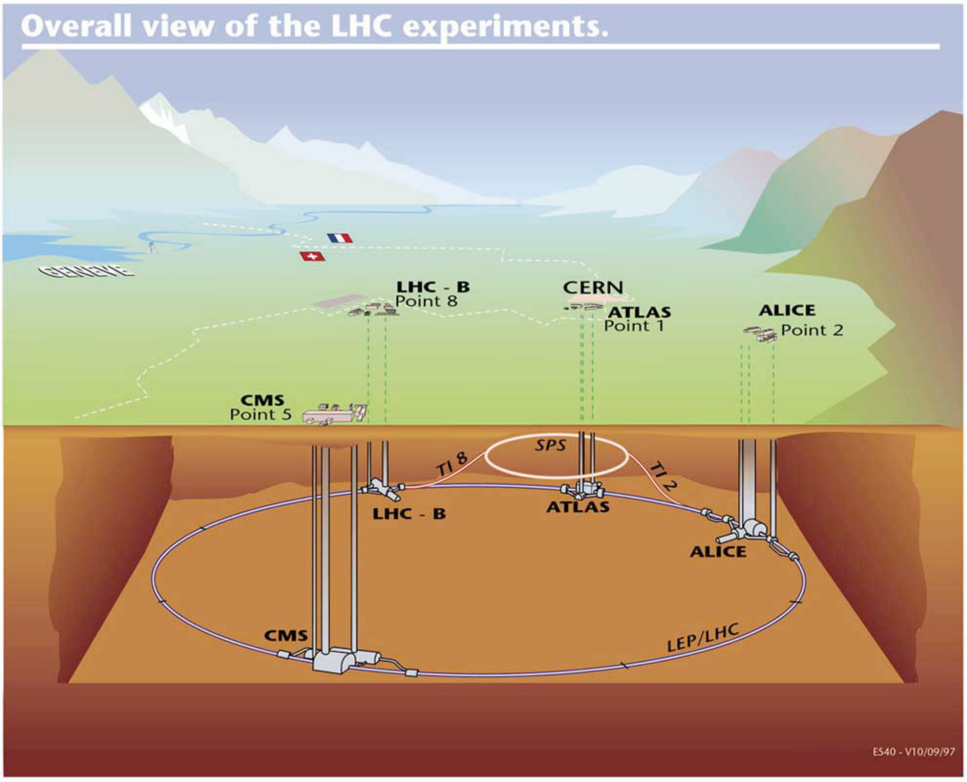

Figure 2.1: Schematic diagram of the LHC accelerator ring at the surface and underground. The general purpose experiments ATLAS and CMS are located at points 1 and 5, the heavy ion experiment ALICE is situated at interaction point 2 and the LHCb experiment is located at interaction point 8. Picture taken from [33].

Protons arrive in the LHC rings in 2’808 ”bunches”, which consists of $1.15{\cdot}10^{11}$ protons each. The time interval between two consecutive bunches is 25 ns and the bunch crossing frequency is 40 MHz. The bunches of protons circulate via two opposite tunnels to reach an energy of 7 TeV. This energy is limited by the strength of the dipole field for a specific circumference. At the LHC, the superconducting dipole magnets provide a 8.3 T field and operate at 1.9 K.

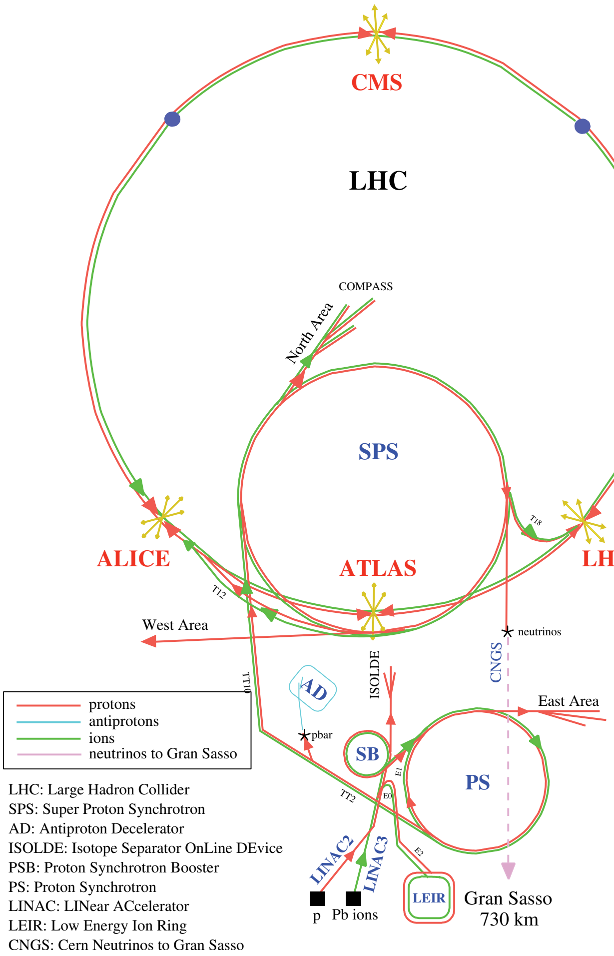

Figure 2.2: The CERN accelerator complex chain. Picture from [33]

Proton-proton collisions take place at a rate of 40 MHz in four interaction points along the LHC (Fig 2.1), where four experiments are located. Two general purpose detectors, ATLAS and Compact Muon Solenoid (CMS), are primarily dedicated to the search of the Higgs boson, supersymmetry particles (SUSY) and extra dimensions. A Large Ion Collider Experiment (ALICE) is a detector specialized in analysing heavy-ion (Pb-Pb) collisions to study the quark-gluon plasma. Finally, the Large Hadronic Collider beauty (LHCb) experiment is interested in *b*-physics (see chapter 1).

Cross-section		
Total	σ_{tot}	100 mb
Inelastic	σ_{inel}	55 mb
$\mathrm{c\bar{c}}$	$\sigma_{\mathrm{c\bar{c}}}$	3.5 mb
$\mathrm{b\bar{b}}$	$\sigma_{\mathrm{b\bar{b}}}$	500 μb

Table 2.1: Value of the differents cross sections assumed throughout the document [35].

2.1.2 Luminosity

A very high luminosity is necessary for a Higgs with a mass between 114 and 219 $\mathrm{GeV/c^2}$ to be observed and to study New Physics phenomena. At the LHC, the design luminosity is $\mathcal{L} = 10^{34}\mathrm{cm^{-2}s^{-1}}$ and will be reached after 1 to 4 years of operation. The luminosity for a collider is given by:

$$\mathcal{L} = \frac{N_1 N_2 k_b f \gamma F}{4\pi\beta^*\epsilon}$$

where $N_i \sim 10^{11}$ are the number of protons per bunch, k_b the number of bunch crossings at the considered interaction point, $f = 11.25\,\mathrm{kHz}$ the revolution frequency and $\gamma = E_{\mathrm{p}}/m_{\mathrm{p}}$. $F \sim 0.9$ is a factor which takes into account the crossing angle of the two beams and $\beta^* = 0.5$ m measures the ability of the magnets to focus the beam at the interaction point. Finally the normal transverse emittance $\epsilon = 3.75\ \mu\mathrm{m}\cdot\mathrm{rad}$ measures the compactness of the beam.

The two experiments ATLAS and CMS need the full LHC luminosity. At LHCb, the luminosity is locally reduced to $\mathcal{L}_{LHCb} = 2\cdot 10^{32}\mathrm{cm^{-2}s^{-1}}$ in order to reduce the number of multiple interactions per bunch crossing.

2.1.3 Cross sections at the LHC

The relevant cross sections at LHC are given in Tab. 2.1. The values are extrapolated from SPS and Tevatron data, and the errors on these estimations are quite large: for example the expected $b\bar{b}$ cross section is between 175 and 950 μb. In this document we assume it to be 500 μb, which is the value currently adopted as a reference by LHC collaborations. These numbers need of course reconfirmation as soon as the LHC starts taking data.
The average number of interactions per bunch crossing is proportionnal to the inelastic cross section through the formula:

$$< N_{pp} >= \frac{\mathcal{L}\sigma_{\mathrm{inel}}}{k_b f} \tag{2.1}$$

where k_b, $\mathcal{L}$, and f are defined above. The table below shows the different values of luminosity and the average number of interactions per bunch crossing for ATLAS, CMS and LHCb.

	$\mathcal{L}$ (cm^{-2}s^{-1})	k_b	$< N_{pp} >$
ATLAS, CMS	$1 \cdot 10^{34}$	2808	17.4
LHCb	$2 \cdot 10^{32}$	2652	0.37

The heavy quarks, especially the b (and $\bar{b}$) quarks, are mainly produced by gluon fusion. The B hadrons pairs are produced with a fairly flat rapidity distribution which, because of the large rapidity interval of the LHC, translates to the conspicuous forward (backward) peaking shown fig 2.3. This motivates the design of LHCb as a single arm forward spectrometer.

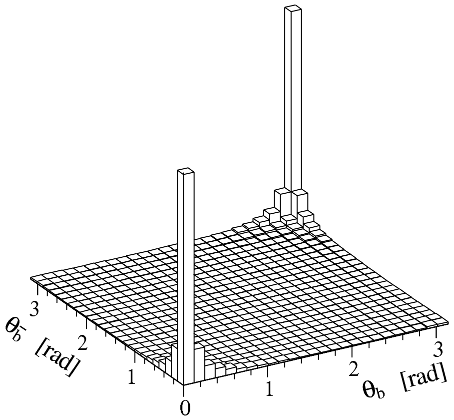

Figure 2.3: The polar angle distribution of b hadrons at LHC. Picture taken from [36].

2.2 The LHCb Spectrometer

The Large Hadronic Collider beauty experiment (LHCb) is dedicated to precision measurements of CP violation and the search for rare decays. The forward single arm detector design was adopted to cover an angular range from 10 mrad to 300 (250) mrad in the bending (non-bending) plane. The layout of the experiment is shown in Fig. 2.4. LHCb is installed in the IP8 cavern, which was occupied by DELPHI during the LEP era. Given the limited space available, the choice was taken to build a one-arm detector. LHCb is 20 m long and 10 m wide. The original Technical Design Report TDR ([36]) was modified to improve the trigger performances and reduce the material budget. The changes are described in the Reoptimized Detector TDR [37]. The main requirements that the LHCb detector has to meet to study rare B decays are:

- **a high resolution vertex detector** in order to well define the primary and secondary vertices which characterize B-decay channels. A high vertexing precision is required to ensure an excellent time resolution needed to resolve the fast B_s oscillations.

- **a precise particle identification** to clearly distinguish pions from kaons and assign leptons ID. The π/K separation is needed to study rare decays, e. g. $B_d^0 \to \pi^+\pi^-$ whereas lepton ID is mandatory for trigger and tagging purposes.
- **a precise mass reconstruction**: this requirement implies an excellent momentum reconstruction and is needed to reduce the combinatorial background level.
- **a versatile and efficient trigger scheme** is required to differentiate events with B-mesons from minimum-bias events.

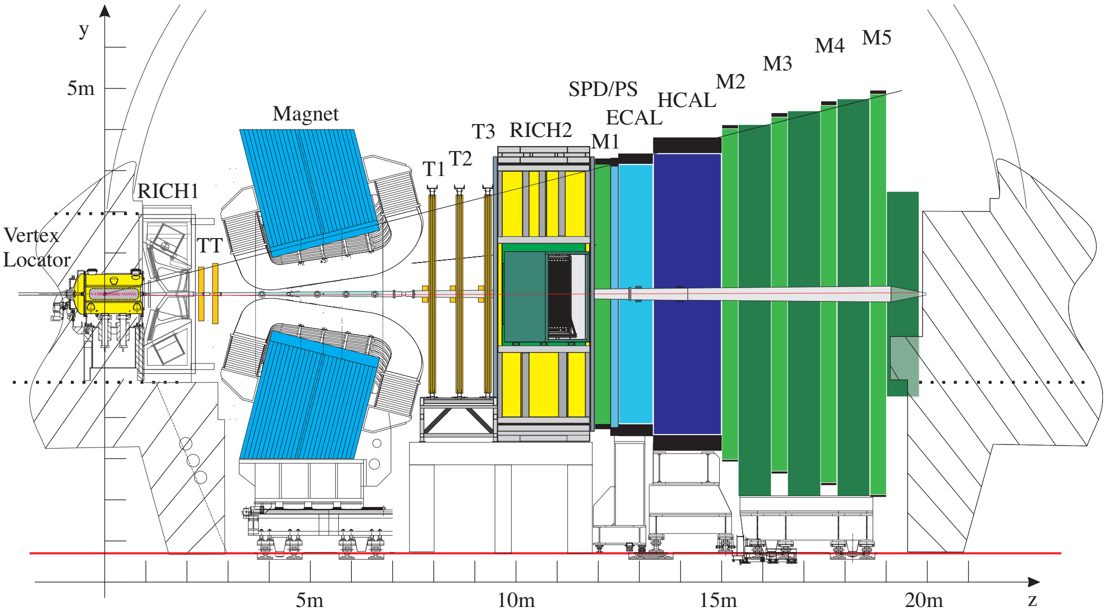

Figure 2.4: Side view of the LHCb spectrometer (non-bending plane): the z axis is along the beam pipe, with the origin close to the interaction point and pointing toward the detector. The y axis is in the vertical direction, which also coincides with LHCb magnetic field direction. The x axis is horizontal and is chosen to have a right handed coordinate system. Picture taken from [37].

LHCb can be divided in five subdetector systems (see Fig. 2.4) :

- Vertex detector system (VELO, VErtex LOcator);
- Tracking system, composed of the Trigger Tracker (TT), a bending magnet, and three Tracking stations (T1, T2 and T3) each composed of the Outer Tracker (OT) and the Inner Tracker (IT);
- Ring Imaging Cherenkov detectors system, RICH1 and RICH2 placed respectively in front of and behind the bending magnet;

- The calorimeters consisting of the Scintillating Pad Detector (SPD), the PreShower (PS), the Electromagnetic CALorimeter (ECAL) and the Hadronic CALorimeter (HCAL);
- Muon chambers (M1-M5).

The prompt tracks are reconstructed to find the primary vertex, and a b hadron which its secondary vertex in the VELO is searched for. The four tracking stations (TT, T1, T2 and T3) and the magnet allow measurement of the particle momentum. The calorimeters are intended for energy measurements and muons are detected in muon chambers. In addition to the detectors a multi-level trigger is designed and will be described in detail in chapter 2.6.

2.3 Vertex detector system

The Vertex locator [38] subdetector allows a precise reconstruction of the vertices to 40μm and thus, is fundamental for the B-meson analysis in LHCb. The angular coverage of the VELO is achieved with a serie of stations, each providing an R and a ϕ measurement. The number of stations is kept to a minimum: 21 silicon disk stations placed transversaly to the beam direction (Fig. 2.5). Two stations at low z are dedicated to the pile-up rejection. Each sensor covers an angle of about 182 degrees thus allowing a full coverage of the azimuthal angle and a small overlap between he left and right halves for relative alignment purposes. The half stations are displaced by 2 cm along the beam axis.

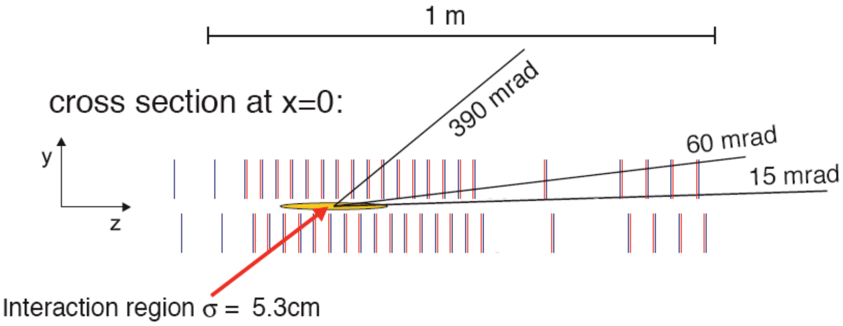

Figure 2.5: Pile-up veto counter and VELO station setup shown in the yz plane. The pile-up veto consists of the two single R-measuring stations situated at the lowest z positions. The VELO is made of 21 stations, each consisting of two silicon planes. Figure is taken from [37].

The sensors have a circular shape (Fig. 2.6) and are patterned with azimuthal or quasi-radial strips for R and ϕ measuring. The innermost radius of the sensitive area is 8 mm and the outermost radius is approximately 42 mm. The strips of the ϕ-sensor are split into an inner and an outer region to equalize the occupancy in the two regions. The detectors are flipped from station to station, thus allowing a stereo recording. The R-sensors have circular strips with pitches varying from 40 to 92 μm. The strips are further segmented in four (two) azimuthal regions in the inner (outer) regions.

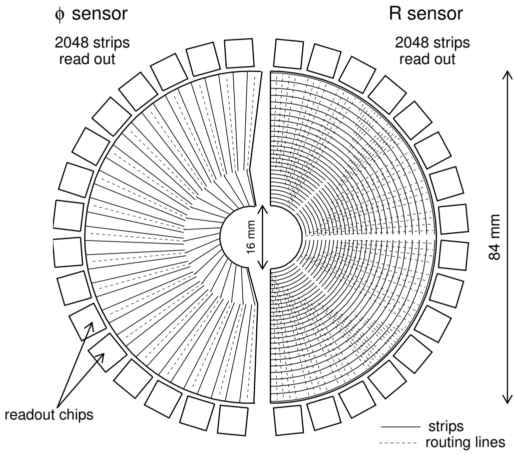

Figure 2.6: Schematic view of the R and ϕ silicon sensors. The figure is from [38].

The VELO will be subject to a very harsh radiation environment. Extensive prototyping has led to the choice of n-on-n technology for the sensor, a kind of technology which will allow an efficient operation up to three years in the LHCb environment.

The VELO has to provide a very precise measurements of track coordinates close to the interaction point and associate them with a good accuracy to their vertex. This subdetector is also the first element of the tracking system of LHCb and gives information about the possible B-meson signature to the High Level Trigger. The error on the primary vertex depends on the number of tracks produced in the pp-collision. For a B-event, the resolution is 42 μm in the beam direction and 10 μm perpendicular to it for the primary vertex. The precision on the decay length ranges from 220 μm to 375 μm according to the decay channel. The B proper time is deduced from the decay length. For the channel $B_s^0 \to D_s^- \pi^+$ from which ΔM_s will be measured, the proper time resolution is found to be $\sigma_\tau = 40\,\mathrm{fs}$. This resolution is largely sufficient to determine ΔM_s down to $\Delta M_s < 50\,\mathrm{ps}^{-1}$.

The sensors have to be placed as close as possible to the beam. This requirement dictates the choice of silicon detector technology, which can cope with the hard radiation. It also dictates the fact that the sensors and the front-end electronics have to be put in a retractable ”Roman pot” as the sensor radial distances is smaller than the aperture required during the proton injection in the LHC.

All the detectors and the readout electronics are located inside a special vacuum vessel consisting of a thin aluminum box with a primary vacuum of less than 10^{-4} mbar. The sensors can be placed at 8 mm from the beam during normal operation of data taking. The Roman pot system is added to move the detector away to avoid damaging of the VELO during instable beam conditions (Fig. 2.7). The main vacuum tank is bonded directly to the LHC beampipe at the same pressure.

The readout electronics consists of 16 Beetle chips [40] per sensor. The DAQ electronics are placed as far as possible from the wafers in order to avoid radiation damage of the Beetle chips. The sensors are protected from the RF currents induced by the beam bunches by a 0.3 mm aluminum foil. The heat produced by the detector modules are removed by using a mixed-phase CO_2 cooling system. The CO_2 is particularly adequate in high radiations environment as it does not produce free radicals or toxic components and has excellent cooling properties. CO_2 is supplied as liquid and is expanded into stainless steel capilaries (one for each module). The working temperature ranges between −25°C and +10°C. The required cooling capacity is 2.5 kW.

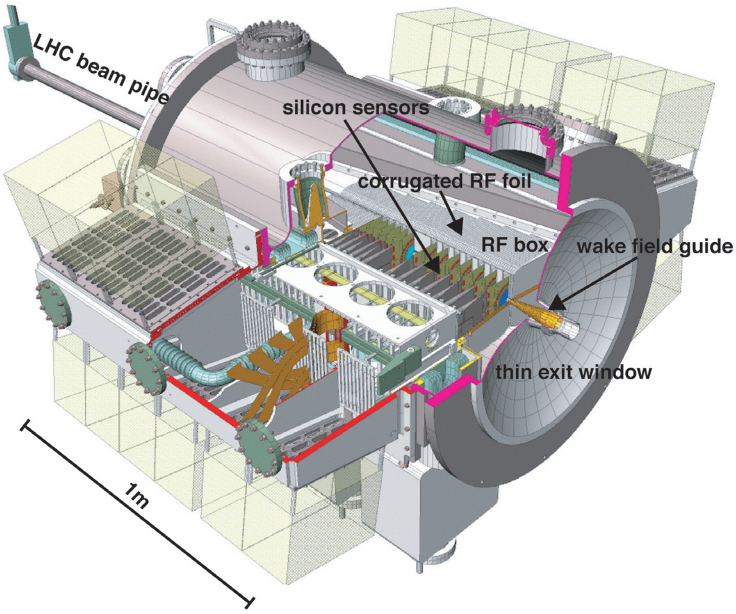

Figure 2.7: The LHCb Vertex locator: 3D view of the vacuum vessel with the silicon sensors (TDR layout with 25 stations) and the corrugated RF-foils. Picture is taken from [37].

2.4 Tracking System

The tracking system of LHCb allows the measurement of the momentum of charged particles given the track curvature in the magnetic field. The particle momentum resolution is expected to be of $\delta p/p \approx 0.4\%$ or better for charged particles from a B-decay.
The tracking system consists of the VELO detector and of four stations (eleven in the original design in Technical Proposal [36]): the Trigger Tracker TT positioned between the RICH1 and the bending magnet, and three other stations (T1, T2 and T3) between the magnet and RICH2 (see Fig. 2.4). Each T station is composed of two different detectors:

- the Inner Tracker (IT), which covers the central part of the station. It represents only 2% of the area of the station but receives about 20% of the tracks.
- the Outer Tracker (OT), composed of drift straw tubes to cover the external area.

The TT and IT are microstrip Si detectors and form the Silicon Tracker.

2.4.1 Magnet

The bending magnet [42] of LHCb is a warm dipole magnet with its field oriented vertically. Its geometry is completely determined by the LHCb acceptance, which requires a bending power of 4 Tm to give a resolution of 0.4% for momenta up to 200 GeV/c. The magnet is located immediately downstream of the first RICH detector and just upstream of the first tracking station T1. Due to the high cost and mechanical risk, the superconducting magnet proposed initially was rejected. The magnet's aperture is ±250 mrad vertically and ±300 mrad horizontally. A non uniformity of the bending power of less than ±5% is expected in the acceptance.

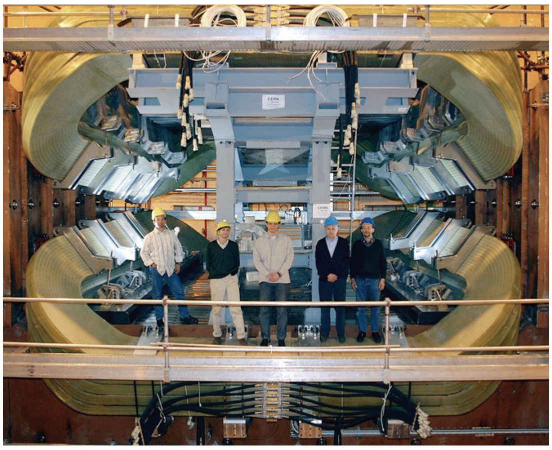

Figure 2.8: The LHCb magnet during its assembly phase. This picture is taken from the CERN public web.

2.4.2 Beampipe

The beampipe has to be mechanically strong to support the difference of pressure between the Ultra High Vacuum inside and the ambient outside it. It consists of a conical tube which passes through the center of all LHCb detectors. Two considerations dictate the design of the beampipe:

1. The beampipe is located in a region of high rapidity of the experiment: for this reason, a special cone has to be brought in order to avoid as much as possible the creation of secondaries in the pipe which can reach the active elements of the detector and increase the occupancy of the sub-detectors, particularly the tracking detectors and the RICH's, thus rendering the reconstruction of the tracks and the particle identification impossible. Moreover, the secondaries can create a high fluence of particles around the beampipe which can damage the electronics located near the beam.

2. Moreover, a "heavy" beampipe, constructed in, for instance in strainless steel, will present a too "high" thickness in term of radiation length. One has to choose a material and a shape for the beampipe which reduce the thickness seen by the particles produced at this interaction point.

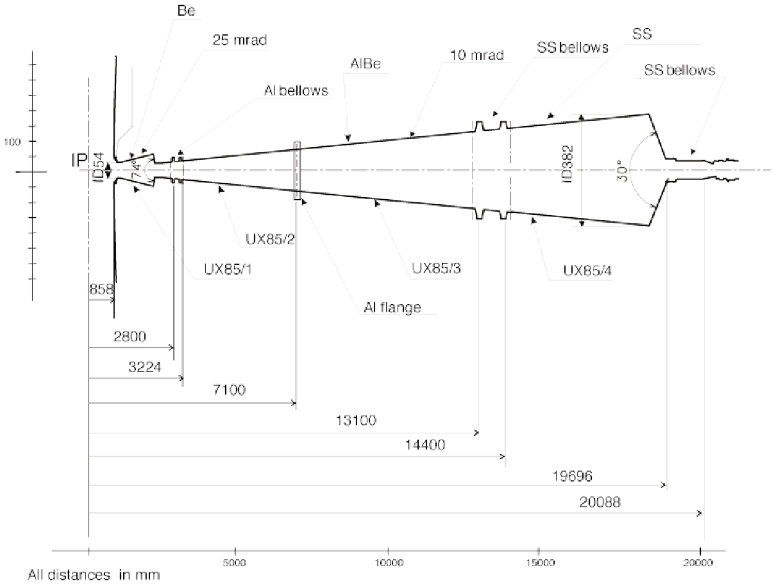

Figure 2.9: Drawing of beampipe. The second section is now completely made of Beryllium. The scale in the vertical axis is enlarged with respect to Fig. 2.4. Picture is taken from [33].

The material chosen for the pipe is Beryllium which is the most transparent one. It is composed of two cones:

- the first one is made of 1 mm thick Beryllium and has a conic section with a length of 1.5 m and 25 mrad of angular aperture.
- the second one has a conic section, an aperture of 15 mrad, a thickness of 1 to 2.4 mm of Beryllium and is 16 m long.

2.4.3 Trigger Tracker (TT)

The TT design can be found in [39]. To cope with the high density of tracks and the radiation in this specific region, the silicon microstrip technology was chosen for the TT (and IT) detector. The other advantage of this type of detector is its hit resolution and fast response time. The Trigger Tracker [37, 41] consists of four layers of Si sensors distributed along the beam axis. It covers an area of $130 \times 160\,\text{cm}^2$ and is split in two pairs separated by 27 cm: TTa and TTb. The Si wafer is $500\,\mu$m thick with a strip pitch of $183\,\mu$m. To ensure the heat removal, the sensors are mounted on carbon support rails. As for the Inner and Outer tracker, the first and fourth plane of the readout strips are disposed vertically (x-layer Fig. 2.10) and the second and third are tilted with a stereo angle of -5° (u-layer Fig. 2.10) and $+5^\circ$ (v-layer).

The vertical dimensions of the detector being up to 120 cm, the sensors have been ganged in ladders of 4-2-1 sensors and 4-3 sensors, the 4-2-1 arrangement corresponding to the ladders which are the clostest to the beampipe and the 4-3 arrangement for the remaining of the TT. The sensors are bounded together and, for those which are at low $|y|$, the signals are brought to the front-end chips by one (two) flexible interconnect cables.

The detector is placed in two movable half stations. Each half consists of the cooling plate, insulation walls, honeycomb structure and C-shaped support beam. The heavy parts of the station (cooling plates, support beam) are outside LHCb acceptance.
The station insulation is ensured by a common thick Airex R82.60 foam inside honeycomb walls with a 1 mm Al cladding. The detector is kept at 5°C by four cooling plates in which a cooling fluid (C_6F_{14}) is circulating.
The front-end readout consists of Beetle chips [40] that has been developed by the ASIC-laboratory of the University of Heidelberg for the LHCb experiment and is used to read out the silicon microstrip detectors in the VELO, Trigger Tracker and IT. The Beetle chip integrates 128 channels, each consisting of a low-noise, charge-sensitive preamplifier, a CR-RC pulse shaper and a pipelined buffer. The shaper output is sampled with the LHC bunch crossing frequency of 40MHz into the analogue pipeline memory of the Beetle, where the charge information for each channel of the last 160 bunch crossings is stored. The electronics allow for a fast shaping time which avoid the pile-up of events to be reconstructed. The analogue output data of the Beetle is transmitted to a service box that is located close to the detector put outside of the LHCb acceptance. In the service box, the analogue data are amplified, digitised and multiplexed before being transmitted to the TELL1 readout board via optical fibres. The TELL1 is the data acquisition board of the LHCb experiment, which provides data formating, event synchronisation, a large

network interface buffer and other features.

The sub-detector will be used in the Level-1 trigger to give the transverse momentum information to the large impact parameter tracks found in the VELO. For this purpose, it is located in the fringe field of the magnet.

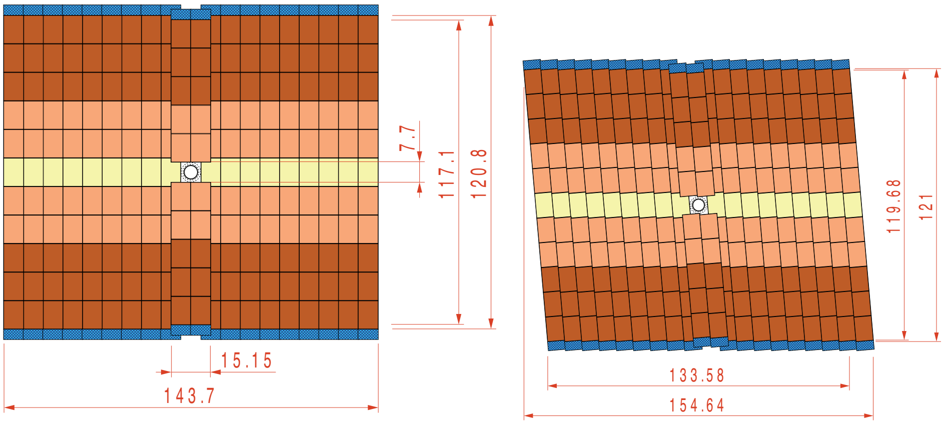

Figure 2.10: Front view of a x-layer and u-layer in TTa. Dimensions are in cm. Picture taken from [37].

2.4.4 Inner Tracker

In the inner region of the three Tracking Stations, the expected charged particle flux is around $5 \cdot 10^5\,\mathrm{cm}^{-2}\mathrm{s}^{-1}$. Clearly, the straw drift tubes of the Outer tracker cannot cope with this high fluxes. Decision was therefore made to add an "Inner Tracker" using Si strip detectors for which an occupancy of the order of a few percent can be easily reached with the above mentioned fluxes. The design choice was to have three stations each consisting of four individual detector boxes arranged around the beampipe. The side boxes house Si-ladders of 22 cm long and 7.8 cm wide built out of two single side p^+-on-n silicon strip sensors. The Si thickness is here 400 μm and the strip pitchs is 198 μm. The top-bottom boxes have single sensor ladders, the thickness of which is 320 μm and the pitch 198 μm. The sensor length is 11 cm. Each station consists of four detection planes having their strip orientation at 0°, -5°, +5°, 0° with respect to the vertical axis. The front end electronics is the Beetle chips (see above).
A more detailed description will be given in the section dedicated to the cooling of the Inner Tracker (Chapter 4).

2.4.5 Outer Tracker

The Outer Tracker [43] (OT) covers the LHCb acceptance at T1, T2 and T3. The track occupancy in the OT region is much lower and the straw drift tubes technology can be

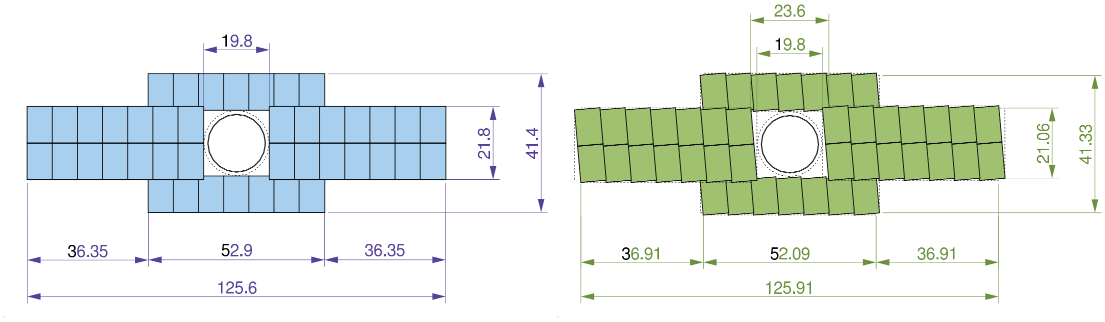

Figure 2.11: Layout of x-layer and u-layer of the Inner Tracker in T2. Dimensions are given in cm. Picture is taken from [41].

used. The OT is built of four layers of modules disposed with the ($xuvx$) geometry as in TT and IT.

Each module is composed of two layers of 5 mm radius straw tubes. Each straw tube is filled with a gas mixture composed of 75% of Argon, 10% of CO_2 and 15% of CF_4 chosen to optimize drift speed. The signal of the anode is read out by electronic cards located out of the acceptance.

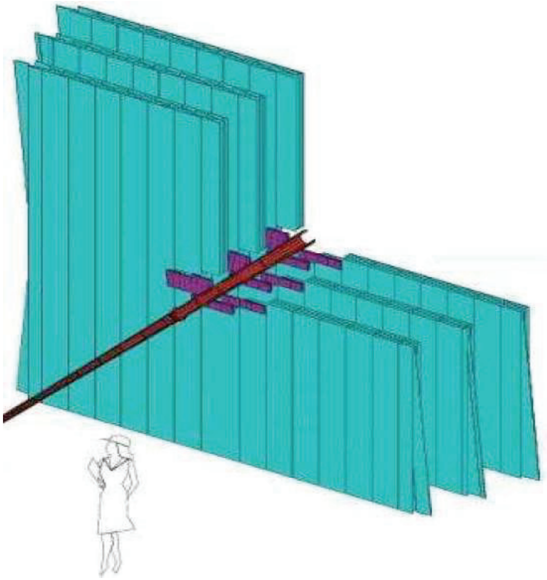

Figure 2.12: 3D view of the tracking stations. Picture is taken from [37].

2.5 Particle identification

Particle identification is mandatory in B physics. The LHCb electrons and hadrons are distinguished using the electromagnetic calorimeters, muons are identified in the muon chambers, and hadrons (Kaons and pions) are identified over a large momentum range by the RICH system.

2.5.1 The RICH system

High momentum particles (up to $\sim$ 100 GeV/c) are identified by the RICH2 detector placed downstream of the tracking stations. The RICH1 will cover a momentum range extending to about 60 GeV/c and is located upstream of the magnet.
These two detectors are based on the Cherenkov effect discovered by P.A. Cherenkov in 1934. When a high energy charged particle passes through a medium of refractive index $n > 1$ with a velocity β greater than the speed of light in this medium, an electromagnetic wave is emitted. Its propagation direction forms an angle θ_c with respect to the direction of the particle:

$$cos\theta_c = \frac{c/n}{\beta c} = \frac{1}{n\beta} \tag{2.2}$$

Knowing the velocity of the particle (related to the angle θ_c) and the specific refractive index in the medium, the mass and the momentum of the particle can be determined. Conversely, given the momentum of the particle, one can separate the different particles by measuring the radius of the produced ring. Both RICH detectors in LHCb use a combination of spherical and flat mirrors that guide the Cherenkov light out of the acceptance to the Hybrid Photon Detectors (HPD).
The upstream Cherenkov detector RICH1 is located between Velo and the magnet (see Fig 2.4). It is placed close to the interaction point to cover the angular acceptance of low and medium momentum tracks, i.e. with polar angles ranging from 25 mrad to 330 mrad for momenta between 1 and 65 GeV/c. It uses an aerogel as radiator with a refraction index of $n = 1.03$ for K identification above 2 GeV/c and $\pi - K$ separation up to 10 GeV/c and a gas, C_4F_{10}, with $n = 1.0014$ for $\pi - K$ separation up to 60 GeV/c (see Fig 2.13). It has a vertical optical layout symmetry. Photodetectors (Hammamatsu photomultipliers) are placed outside the acceptance. Spherical and plane mirors bring the Cherenkov light to the PMT's.
The downstream RICH2 detector is placed after the magnet and behind the T stations. It uses CF_4 gas with a refractive index of $n = 1.0005$ as radiator and allows identification of high momentum charged particles between 15 GeV/c and 100 Gev/c.

2.5.2 Calorimeters

The main purpose of the calorimeter system [46] is the measurement of the particles energy and position and a contribution to their identification. In LHCb, the calorimeter

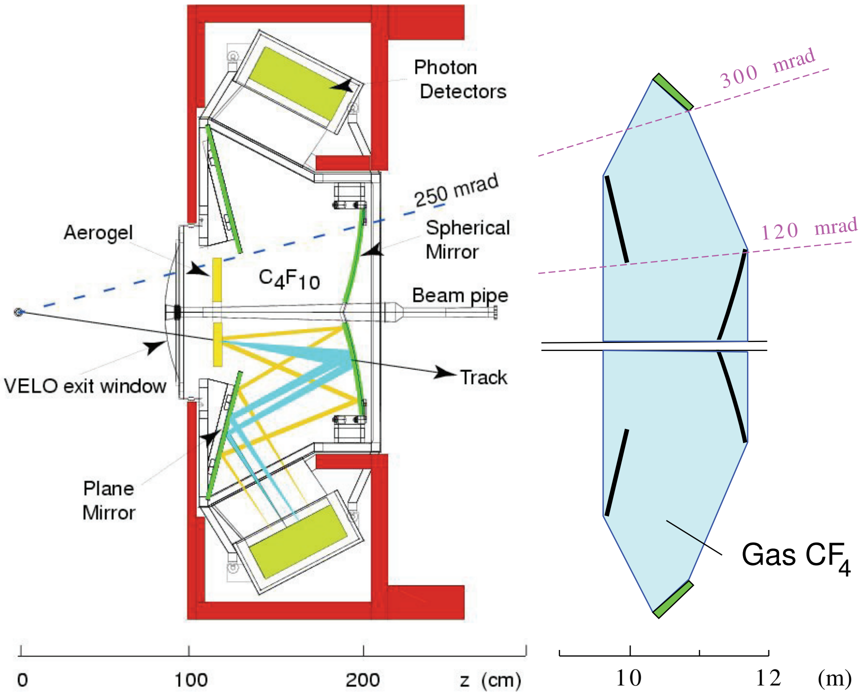

Figure 2.13: Vertical cross section of the RICH1 detector (left). Horizontal cross section of the RICH2 detector (right). Picture is taken from [44].

system is located between the first and the second muon station (see section 2.5.3). It consists of four detectors:

- the Scintillating Pad Detector (SPD)
- the Preshower detector (PS)
- the Electromagnetic Calorimeter (ECAL)
- the Hadronic Calorimeter (HCAL)

The calorimeter system will be used at several stages. It provides the p_T information for the first level trigger, the identification of electrons for flavour tagging through semi leptonic decays of B mesons and the reconstruction of π^0 and γ for B decay channels. For these channels, a good resolution and a good shower separation are required. The detectors measure the energy and the position by absorbing the particles. A shower of secondary particles is produced in the absorbing material of the calorimeter by the incident particles and the resulting shower will leave part of their energy in the sampling part of the calorimeter. This sampling is made of scintillators in LHCb and the light will be bought out with wave length shifter and clear fibres. The total amount of light produced is proportional to the energy of the particle in the total absorbing part of the calorimeter.

The detectors which make up the LHCb calorimeters are grouped in "areas" corresponding to "inner", "middle" and "outer" regions, according to the multiplicities of particles in the regions (Fig. 2.14). The device of the regions is the result of a compromise between a small number of channels and the low occupancies, which still ensures a good position and energy resolution.

Scintillating Pad (SPD) and Preshower (PS) detectors

The SPD and the PS are located in front and behind a 12 mm lead plate. They consist of 15 mm thick of scintillator tiles and have the same transverse size as the ECAL detector. The total sensitive area of these two detectors is 6.2 m high and 7.6 m wide. The SPD is dedicated to distinguishing electrons from photons. The lead plate sandwiched between the two detectors initiates the electromagnetic shower. The purpose of the PS detector is to detect this shower. Both detectors are composed of different cell sizes grouped in the three regions defined above (see Fig. 2.14). The scintillation light is collected by a wavelength shifting (WLS) fibre embedded in the scintillation tiles and sent to multianode (8×8) photomultipliers placed outside the acceptance with clear fibres.

The Electromagnetic Calorimeter

The ECAL is located behind the SPD/PS system. It uses the "Shashlik" technology and it is composed of 4 mm thick scintillator plates as active material inter-spaced with 66 lead absorber sheets with a thickness of 2 mm. The readout is done with WLS fibres passing through the lead-scintillator stacks and readout at the back of the detector by photomultipliers. The ECAL structure is segmented into three regions with different modules definition like the SPD/PS detectors (see Fig. 2.14). The modules have the same external dimensions but the number of readout cells is different for each region. In the inner part there are 167 modules of 9 readout cells each, the middle part consists of 448 modules with 4 readout cells each and 2688 modules containing only one readout cell constitute the outer part. The electromagnetic shower energies have a resolution of $\sigma(E)/E = 10\%/\sqrt{E} \oplus 1.5\%$ when energies are expressed in GeV and the symbol $\oplus$ means that the two terms have to be added in quadrature.

The Hadronic calorimeter

The HCAL is located behind the ECAL detector and it is based on an iron/scintillating tile technology. It consists of a sampling structure parallel to the beam and composed of 4 mm thick scintillator plates inter-spaced with 16 mm of iron tiles. The overall material thickness is 1.2 m. The readout is provided by WLS fibres. In the case of the HCAL, the structure is divided into two regions, the inner and the outer part (see Fig. 2.14). With a total thickness of 1.20 meters, 5.6 interaction lengths, the energy resolution is $80\%\sqrt{E} \oplus 10\%$.

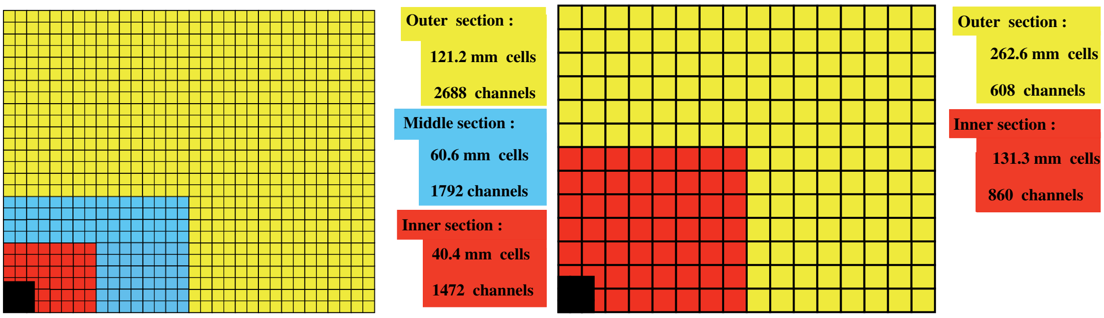

Figure 2.14: Transverse segmentation of the SPD, PS and ECAL cells (left). A square represents a module. One quarter of the detector front face is shown. Transverse segmentation of the HCAL cells (right). A square represents a module. One quarter of the detector front face is shown. Figures are taken from [46].

2.5.3 Muon Chambers

The LHCb Muon System [47] provides fast triggering and off line muon identification. Muons are present in several final states of B-decays, such as channels containing a J/ψ that decays to two muons. Muons also enters the flavour tagging through semi leptonic decays of B-mesons. The muon system is made of five Stations (M1-M5) of rectangular shape. The first station is located in front of the SPD/PS detector and the four other stations are placed behind the HCAL and are separated by 800 mm thick iron filters (see Fig 2.15). The five stations cover an acceptance of ±300 mrad horizontally and ±200 mrad vertically, and a total area of 435 m^2. Each station is divided into four regions, R1 to R4. The regions have the same acceptance but differ in granularity of the readout, in order to keep the occupancy constant over the detector. The active areas consists of Multi Wire Proportional Chambers (MWPC) with 2 mm wire spacing and a 5 mm gas gap. There are 1380 chambers in the Muon System, of 20 different sizes.

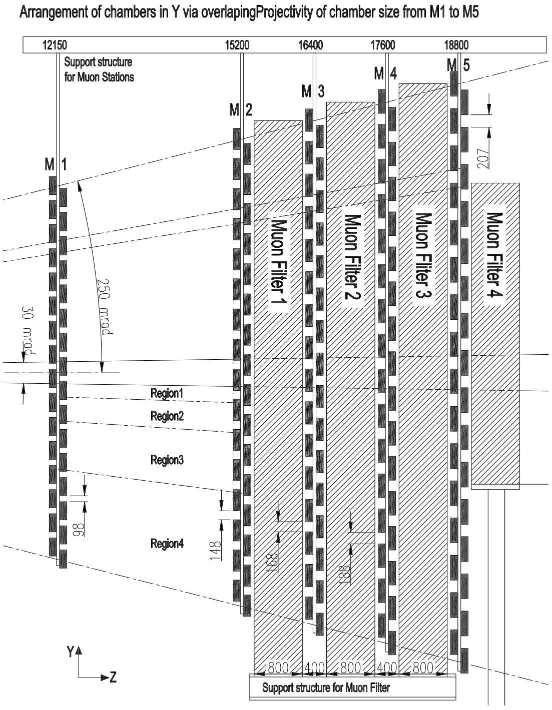

Figure 2.15: Sideview of the Muon System in the (yz) plane. Picture is taken from [47].

The granularity of the readout is higher in the horizontal plane in order to give an accurate measurement of the track momentum. The information must be gathered within 20 ns, so the detectors are optimized for speed. For this reason, the choice went to MWPC. Triple-GEM detectors are used in the innermost region (Region 1) of Station M1. This choice was dictated by the better aging properties of this type of detector.

2.6 Triggers

With a luminosity of $2 \cdot 10^{32} \mathrm{cm}^{-1}\mathrm{s}^{-1}$ and an inelastic cross section of 80μb, it is not possible to record all the events. The $b\bar{b}$ pair cross section is some 10^{-2} times lower than the pp inelastic cross section, and the fraction of bunch crossings which will give an interesting event in LHCb will be still lower. To select only those events that produced an interesting $b\bar{b}$ pair, a trigger system [48, 49] has been developed. It consists of three levels:

- Level-0 (L0) is a hardware trigger and provides fast decisions which reduce the rate to 1 MHz.
- Level-1 (L1) trigger, implemented in a software algorithm.
- High Level Trigger (HLT) [50], also implemented in a software algorithm.

2.6.1 Level-0 Trigger

This trigger uses four sub-systems: the pile-up rejection system, the calorimeter trigger system and the muon trigger system. A Decision unit gathers the above informations to form the L0 Trigger Decision. The purpose of Level-0 is to reduce the beam crossing rate of 40 MHz, of which $\sim$ 10 MHz have a visible pp interaction, down to a rate of $\sim$ 1 MHz at which all the sub-detectors can be used for triggering. As we deal with massive B decays, which give large E_T leptons, hadrons or photons, the Level-0 trigger will reconstruct the above particle with the highest E_T and the two highest p_T muons in the muon chambers. This information is then sent to the Decision unit to select the events. Pile up rejection aims at distinguishing crossings with a single or multiple interactions and uses the backward R-sensors of the VELO.

Calorimeter trigger

An event is accepted when it contains a calorimeter cluster with: $E_T > 2.6\,\mathrm{GeV}$ for electrons, $E_T > 2.3\,\mathrm{GeV}$ for photons, $E_T > 3.5\,\mathrm{GeV}$ for hadrons or $E_T > 4.0\,\mathrm{GeV}$ for π^0's. The event is discarded if the total energy in the calorimeters is below 5.0 GeV and if the SPD has a multiplicity exeeding 280.

Muon trigger

An event is accepted if there is a muon with transverse momentum $p_T > 1.3\,\mathrm{GeV/c}$ or if the sum of the p_T of the two largest p_T muons is higher than 1.5 GeV/c. No veto is applied for this last case.

Pile up system

The pile up system relies on the two R-sensors placed upstream of the VELO and perpendicular to the beam line. Recording the radii of the track hits in the two R-sensors allows to deduce the track's origin and reject multiple vertices events.

Level-0 Decision unit

It collects this informations from the Level-0 components and form the Level-0 Trigger.

2.6.2 Level-1 and High Level Trigger

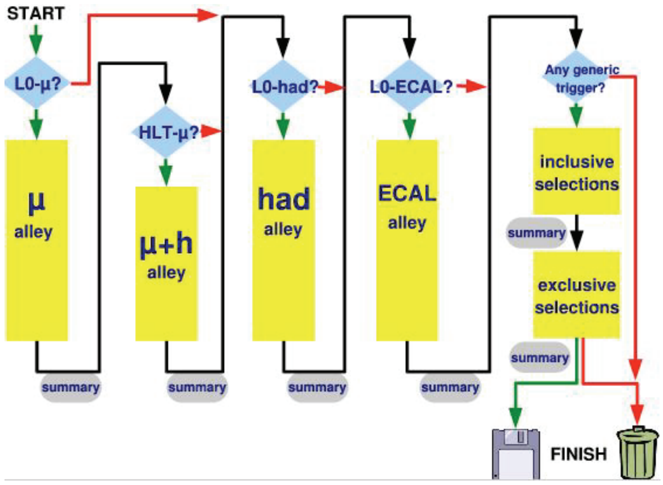

Figure 2.16: Flow-diagram of the different trigger sequences in the HLT. Diamonds indicate where the trigger decisions are taken, while squares represent the reconstruction algorithms. Picture is taken from [49].

The Level-1 trigger will reduce the 1 MHz rate at the output of L0 to about 40 kHz. It is a "software trigger" which shares the out live form with the High Level Trigger. Its decision is based on the data of VELO, the TT and the decisions of the L0 Decision unit. The algorithm reconstructs the tracks in the VELO and matches them to L0 muons or calorimeters clusters to identify them and determine their momenta. The fringing field in the region between the VELO and the TT allows to determine the momenta of the particle to a precision of about 30%. These informations allow to select tracks with a large p_T and a significant impact parameter to the primary vertex. The events passing the L1 trigger are selected by different parallel trigger lines:

- The **generic line**, i.e. generic high p_T, requires the logarithmic sum of the transverse momenta of the two highest p_T tracks to be greater than 14.
- The **single muon line**, in which a muon of $p_T > 2.3\,\mathrm{GeV/c}$ is selected.
- The **di-muon line** where the invariant mass of the pair should be greater than 500 MeV/c and its impact parameter greater than 0.075 mm.
- The **J/ψline** demands that the μ pair be 500 MeV/c around the tabulated J/ψ mass.

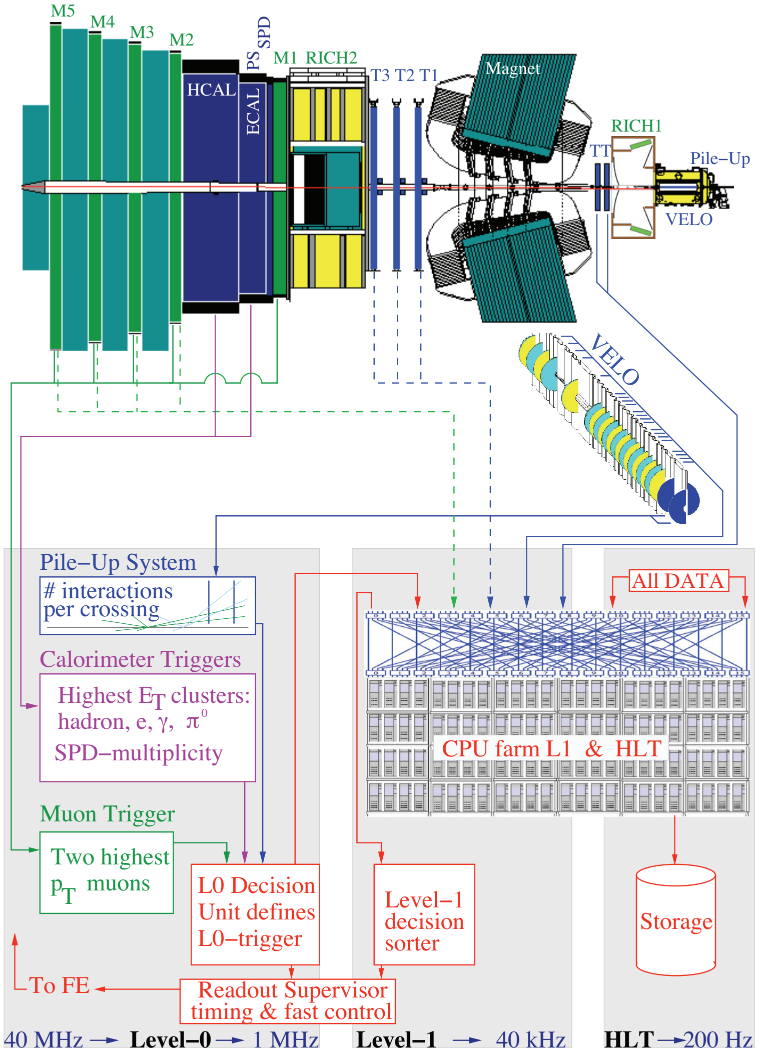

Figure 2.17: Shematic of the Trigger system of LHCb. Picture is taken from [48].

- The **electron and photon line** trigger on high E_T electrons and γ ($E_T > 3.04\,\mathrm{GeV}$ and $\sum \ln E_T < 13.2$).

The **High Level Trigger** shares the same network with the L1. It reconstructs the VELO tracks and the primary vertex. The final selection of interesting events confirms L1 decision with a better resolution and selects the events according to specific final states with particular selection cuts. The storage rate will be around 200 Hz.

Chapter 3

The LHCb software

3.1 LHCb computing framework

LHCb uses a common software framework which is specifically built for all the required applications [51]. Implementations of the software have to be readaptable during all the conception period of the detector and over the expected lifetime of the experiment. The applications of LHCb are managed by GAUDI [52, 53], an Object Oriented framework using C++ language. It is designed to provide a common infrastructure and environment for the different software applications.

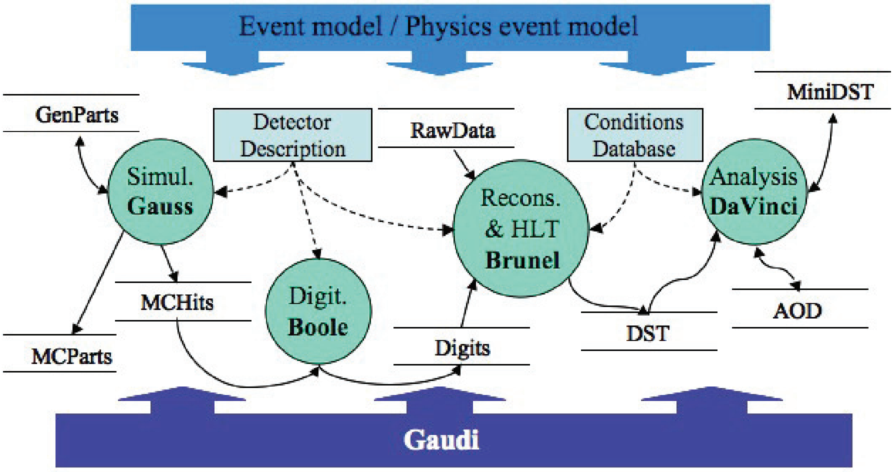

Figure 3.1: Schematic of the software organisation of LHCb. Picture is taken from [51].

The structure of the software is organized in four blocks (Fig 3.1). First, the generator simulates the proton-proton collisions and generates the particles that will be propagated through the dectectors. Second, the simulator emulates the response of the real detector. All the digitalized data, coming from the simulation step or the real measurements, are then sent to the reconstruction step to build an event. In the last part, the analysis step, the physics parameters are extracted from the events. For the simulation part, Monte Carlo (MC) techniques are used to generate data. Different programs are used for the generation, simulation and analysis:

- **GAUSS** [54] simulates the behavior of the detector to allow the understanding of its experimental conditions and its performances. It integrates two independent phases: the "Generator Phase" consisting of the generation of the pp collisions by the PYTHIA package and the decay of the b-particles produced via EvtGen [55] and the "Simulation Phase". It consists in the tracking of the particles in the detector and the simulation of the physics processes occuring in the experimental setup and those leading to the detection. The GEANT4 [56] package is used in this phase.

- **BOOLE** [57] digitalizes the data produced in the simulation phase. It applies the detector response to the hits previously generated in the sensitive detectors by GEANT4. Other hits are added from "Spill-over" [1] events and from LHC background. In this phase, the simulation of the detectors, including their efficiencies and responses, and of the readout electronics, as well as of the L0 trigger hardware are digitalized and the output data mimic the real data coming from the real detector.

- **BRUNEL** [58] is the reconstruction program. It can process either the output of the detector digitization with BOOLE, or real data from the LHCb DAQ system. It associates hits from the different sub-detectors to reconstruct tracks and defines the particle identity (PID) with the help of the RICH's, ECAL, HCAL and muon chambers.

- **DaVinci** [59] is the physics analysis software for the LHCb experiment. The final stage of the data processing, which is the selection of the decay of interest, is purposed within the DaVinci application. Selection criteria are applied to the particle object, e.g. criteria on their PID, their p_T or their impact parameter etc... These particles are then combined to form vertices, resonances, etc... Other criteria, such as vertex quality, resonnance masses, flight distance for long lived candidates, can be applied. The result is the selection of the "good events".

- Other programs are developped in LHCb to perform the analysis of the data, like PANORAMIX [60] for the data visualization, Moore [61] for the trigger studies, or Bender [62], a Python-based physics analysis environment. An alignment program at the reconstruction stage and an online monitoring project, Orwell [63], are developped in parallel.

---

[1] The "spill-over" events are the amount of signal remaining after 25 ns.

3.2 Track reconstruction

The track reconstruction in the LHCb experiment is organized in three steps : first define the type of the track, second find this track and third fit the track.

3.2.1 The different types of tracks

According to their production vertices, trajectories and momenta, the charged particles leave hits in the tracking system. Different types of tracks are defined in LHCb (see Fig 3.2):

- the "Long" tracks are generated by charged particles which traverse the whole tracking system. Those tracks have enough momentum and a correct initial direction to leave hits from the VELO down to the T-stations. They are the most used tracks for the physic analysis.
- the "Upstream" tracks are low momentum particles that are swept out of the acceptance by the magnet field and leave hits in the VELO and TT-stations only. Some often are used to study soft pions coming, e.g., from a D^* decay.
- the "Downstream" tracks traverse only the TT and T-stations. They are usefull to measure the long-lived particles like K_s^0 or Λ which decay outside the VELO acceptance.
- the "Velo" tracks are seen only in the VELO detector. These tracks are producted by particles that decay with large polar angles. They are useful for a precise reconstruction of primary vertices.
- finally, the "T" tracks leave hits only on the T stations. They originate from some secondary interactions and will be useful for the RICH2 pattern recognition.

3.2.2 Find and fit a track

Find a track

To reconstruct a track, the different tracking sub-detector measurements have to be associated to possible track candidates. The tracking strategy is to form small track-segments called seeds:

1. the **VELO seeds**: as the magnetic field in the VELO region can be neglected, the tracks in the VELO are considered to be straight lines.
2. the **T seeds**: at first only the bending plane measurements are considered and the hits in the T-stations are combined as straight lines. Then, the tracks are refitted as parabola to take the magnetic field curvature into account. To confirm the track fit, the hit stereo coordinates are added.

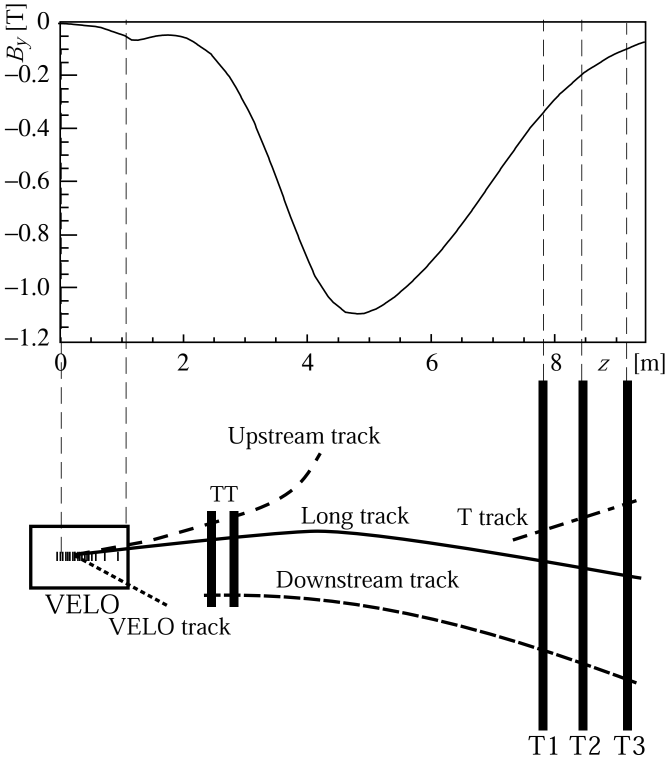

Figure 3.2: The above graph gives the intensity of the y component of the B field. Picture is taken from [37]

Several algorithms run in a specific order to reconstruct a track:

- the **Long tracks forward tracking**: this method creates long tracks from VELO seeds and T stations hits. First, VELO seeds are combined with each hit of the T station successively. An initial track candidate is found if the hits can match the VELO seed. In a following step, the algorithm searches for any other hits in other detectors including TT that confirm the track along the trajectory defined above. The track is reconstructed when a sufficient number of hits has been associated. A likelihood function is applied to confirm the track or consider it like a ghost track. The majority of long tracks ($\sim$ 90%) are reconstructed this way. Once a track is reconstructed, the momentum is determined. Once the method has been applied to all the seeds, the used hits in the T-Station are removed.

- the **Long track matching**: when a long track is not reconstructed by the forward tracking method, the Runge-Kutta method is user to combine T and VELO seeds.

- the **Upstream tracking**: an algorithm [64] matches the VELO seeds and TT tracks requiring both TTa and TTb hits.

- the **Downstream tracking**: there are two methods to obtain downstream tracks [65]. The first method uses an algorithm that extrapolates the T seeds back to the TT stations with a similar technique to the forward tracking [66]. The second algotithm makes an estimation of the momentum of the T seeds assuming that they originate from the interaction point and taking the momentum kick into account. To match the T seeds and hits on the TT stations, the χ^2 of a Kalman fit is used in this second method.

- the **VELO and T tracking**: at the final stage of the tracking, any other VELO or T seeds that have not been used are stored as VELO and T tracks respectively.

Fit a track

In this step of the track reconstruction (Fig. 3.3), tracks have been identified and need to be refitted to find the track parameters that correspond to the covariance matrice with the best possible accuracy. The Kalman Filter [67] technique is used at this step to fit the reconstructed trajectory. The tracks are defined as states vectors (x, y, dx/dz, dy/dz, q/p [68]) given a z-position in the LHCb experiment. The purpose of the Kalman filter is to update every state vector at each measurement plane starting from the most downstream state and taking into account detector material effects and the loss of energy. At the most upstream measurement, the fit reverses direction to update all the states with the full information.

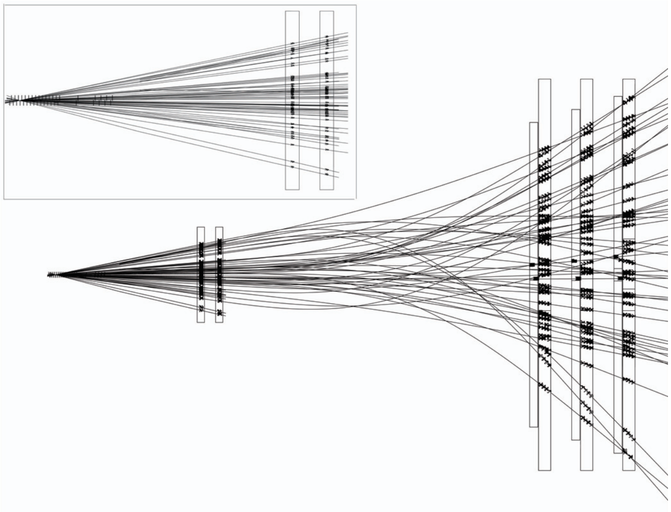

Figure 3.3: Display of the reconstructed tracks and corresponding assigned clusters in a busy event. This event contains 50% more hits than an average $b\bar{b}$ event. This picture is taken from [37].

3.2.3 Reconstruction performance

To evaluate the performance of the track reconstruction algorithms, the reconstruction efficiencies for each type of tracks, including ghosts, have to be defined. Momentum and space residuals are calculated. The reconstructed tracks are compared to the MC truth information.

The quality of the reconstructed tracks is determined by the χ^2 of the fit and the pull distribution of a set of parameters, like momentum or impact parameter (See: Fig 3.4). For long tracks with momentum over 10 GeV/c, the average reconstruction efficiency is 94% whereas for final states of specific B decays, the observed efficiencies reach ~95%. The average ghost rate reaches 9%, however most of the ghosts have a low transverse momentum and can easily be suppressed in the analysis.

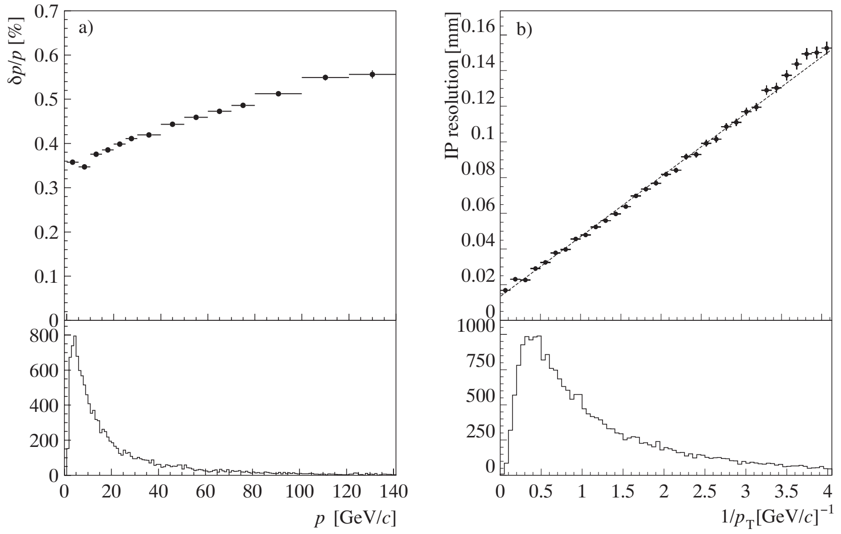

Figure 3.4: Momentum resolution (left) and impact parameter resolution (right) of long tracks at the production vertex as a function of momentum and $1/p_T$ respectively. Spectra of B-decay particles are shown in the lower parts. This figure is taken from [37].

3.3 Flavour tagging

In order to measure the CP violation in B-mesons decays, it is essential to know their initial flavour state. The flavour tagging identifies the B-meson. Different algorithms [69] have been envisaged to perform this task.

The "tagging algorithm" includes two main parts: the definition of the best tagging variables and the way to combine them. Two strategies have been developpped:

- The **opposite-side tagging** consists in the identification of the other b hadron produced in a $b\bar{b}$ event. This can be determined in the semi-leptonic decays of the

B meson by the detection of leptons (muons or electrons) or during a $b \to c \to s$ transition by observing the sign of kaons. To find such particles, high transverse momentum and large impact parameter leptons and kaons are selected. In case of neutral meson production, the B oscillates before decaying, therefore an intrinsic dilution cannot be avoided.

- In the **same-side tagging**, the meson flavour can be determined directly. For example, in the case of the B_s^0 meson (composed of a $\overline{b}s$ quarks), there is an extra $\overline{s}$ quark produced in the pp collision (a s quark is produced with $\overline{B}_s^0$). The s and $\overline{s}$ quarks hadronize essentially into charged kaons. The B_s^0 tagging can be determined with the identification of the charged kaons coming from the primary vertex in the same phase space region as the B_s^0. In the B_d^0 case, the pion multiplicity is too high to use this method.

The two methods are combined to determine the probability that the tagging procedure gives an answer, the so called "tagging efficiency" ε_{tag} and the mistag fraction ω_{tag} which corresponds to the probability to have a incorrect answer when a tag is present. The definition of these two parameters is:

$$\varepsilon_{tag} = \frac{N_R + N_W}{N_R + N_W + N_U} \tag{3.1}$$

$$\omega_{tag} = \frac{N_W}{N_R + N_W} \tag{3.2}$$

where N_R, N_W, and N_U are the number of correctly tagged, wrongly tagged and untagged events respectively. The mistag fraction has a diluting effect on the amplitude of $B_q^0 - \overline{B}_q^0$ oscillation by the "dilution factor" $D = 1 - 2\omega_{tag}$. Therefore, the observed time-dependent asymmetry defined for a final CP-eigenstate, $\mathcal{A}_{obs}$, is related to the true asymmetry as:

$$\mathcal{A}_{obs}(t) = \frac{R[\overline{B}_s(t) \to f_{CP}] - R[B_s(t) \to f_{CP}]}{R[\overline{B}_s(t) \to f_{CP}] + R[B_s(t) \to f_{CP}]} = D \times \mathcal{A}_{true}(t) \tag{3.3}$$

where $R[B_s(t) \to f_{CP}]$ and $R[\overline{B}_s(t) \to f_{CP}]$ are the time decay rates of B_s ($\overline{B}_s$) decaying into a final CP-eigenstate f_{CP}.

The statistical uncertainty on the observed asymmetry, $\sigma_{A_{obs}}$, is proportionnal to:

$$\sigma_{A_{obs}} \propto \frac{1}{\sqrt{\varepsilon_{tag}^{eff} N}} \tag{3.4}$$

where N is the number of selected and triggered events. The effective tagging efficiency, ε_{tag}^{eff}, is defined as:

$$\varepsilon_{tag}^{eff} = \varepsilon_{tag} D^2 = \varepsilon_{tag}(1 - 2\omega_{tag})^2 \tag{3.5}$$

The effective tagging efficiency is the quantity to be maximized in order to diminish the error on the asymmetry. It combines the knowledge of ε_{tag} and ω_{tag} in one parameter to be optimized in the tagging procedure.

3.4 Data Samples DC06

The analysis presented in the next chapter was achieved using Monte Carlo of different sizes as part of the so-called Data Challenge 06 (DC06)(see [70]). In each of signal and background samples, a cut is imposed at the generator level in such a way that the particles have a true polar angle of less than 400 mrad to avoid the tracking and the reconstruction of events for which the decay products are in any case not in the acceptance. This implies that each sample has an efficiency of generation ε_{gen}. The samples of Monte Carlo data used in our selection, which were generated with BRUNEL v31r11 and stripped with DaVinci v19r7 (DC06-Stripping-v31-lumi2), are listed here after:

- the **signal** samples: "Bd_ JpsiKS,mm=CPV,DecProdCut" consists of 1'225'056 events for the loose pre-selection (described in section 5)and 1'151'051 events for the selection and the efficiency of generation is $\varepsilon_{gen}^{signal} = 20.6 \pm 1.3\%$,
- the **inclusive $b\bar{b}$** sample: "incl_b" consists of 35'120'198 events for the pre-selection loose and 35'586'759 events for the selection and the efficiency of generation is $\varepsilon_{gen}^{b\bar{b}} = 43.4 \pm 0.3\%$,
- the **inclusive J/ψ** sample: "incl_Jpsi,mm=DecProdCut" consists of 1'935'235 events in total and the efficiency of generation is $\varepsilon_{gen}^{\mathrm{incl\_}J/\psi} = 19.70 \pm 0.04\%$,
- the **background $B_u^+ \longrightarrow J/\psi K^+$** sample: "Bu_JpsiK,mm=DecProdCut" consists of 1'753'742 events in total and the efficiency of generation is $\varepsilon_{gen}^{B_u^+ \to J/\psi K^+} = 17.89 \pm 0.03\%$,
- the **background $\Lambda_b \longrightarrow J/\psi\Lambda$** sample: "Lb_JpsiLambda,mm=DecProdCut" consists of 138'723 events in total and the efficiency of generation is $\varepsilon_{gen}^{\Lambda_b \to J/\psi\Lambda} = 20.76 \pm 0.05\%$.

Part II

Contribution of the construction of the Inner Tracker

Chapter 4

The Inner Tracker contribution

This chapter describes the technical part of this thesis work. The IT design is described in a first part, the description of the participation of the Inner Tracker detector design and production is exposed. The cooling experiment is completely developped after a brief description of the material budget studies.

4.1 IT description

The Inner Tracker [41] is a part of three tracking stations located behind the bending magnet that consist of Inner and Outer Trackers. The Inner Tracker covers the parts close to the beampipe where particle densities are high and uses silicon micro-strip detectors, while the Outer Tracker is a straw drift tube tracker.

Each station of the Inner Tracker consists of four individual detector boxes, which are arranged around the beampipe as shown in Fig. 4.1. The boxes placed at the sides of the beampipe host modules built out of two silicon sensors bonded together to form 22 cm long detector modules, while the modules above and below the beampipe consist of one single sensor only. Each box houses 28 modules which are arranged in four layers allowing x,u,v,x coordinate measurements. The u and v layers make an angle of -5° and +5° respectively with the y axis.

To insure a signal over noise larger than 12, the silicon thickness is 410 μm for the side boxes and 320 μm for the top and bottom boxes. The sensors have a pitch of 198 μm and an implant width of 50 μm.

The silicon sensors are glued on a support structure (named ladder), which is a sandwich made up by four layers to ensure its mechanical stiffness (see Fig. 4.2):

- 25μm of kapton [75] (polyimide) used for electrical insulation,
- 200μm of heat conducting carbon fibre (Mitsubishi K13D2U [76]), which has a thermal conductivity of 800 W/m·K. When the fibre are immerged in the resin and formed to make the ladder, the conductivity drops to ∼200 W/m·K as measurements have shown [77]. It should be noted that due to the high bi-directionality

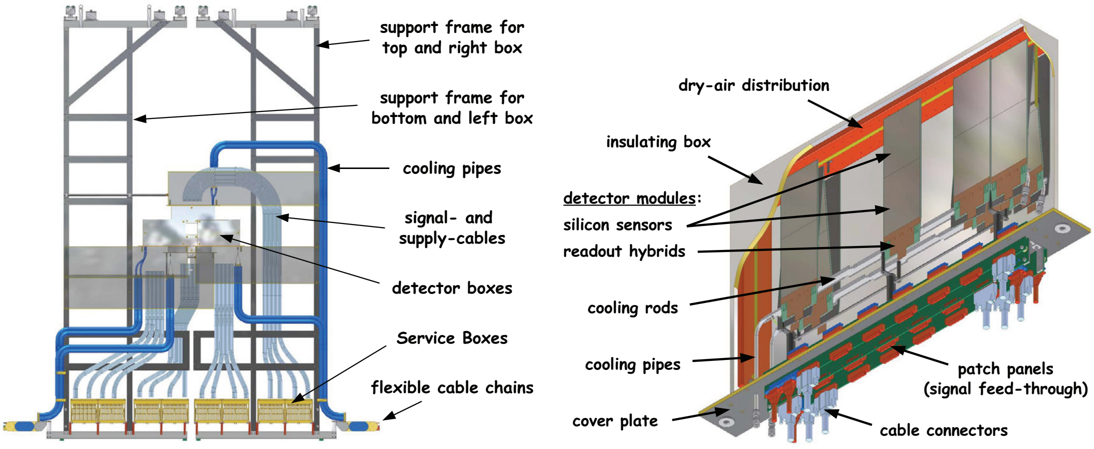

Figure 4.1: The Inner Tracker design : station T1 (left) and a side detector box (right).

of the fibre conductivity, the fibres are laid at 10° with respect to the longitudinal direction of the ladders to ensure the heat transfert from the tip of the ladders to its top when the cooling is made [1],

- 1 mm of foam (Airex R82 [78]),
- another layer of 200μm carbon fiber.

The use of foam in between the two C fibre layers increases the ladder's inertia and flatness. The front-end electronics, i.e. three Beetle chips [40], resistors and capacitors, are mounted on a hybrid circuit which is glued on an aluminium piece called "balcony". This balcony has been inserted in the sandwich support (Fig. 4.2) and glued to the carbon layers using heat-conducting silver glue [79]. It ensures thermal contact between the ladder and the "cooling rod" which is described hereafter.

The mechanical structure used to hold the ladders also serves to cool it. It is made of two 55 cm long aluminium pieces, named cooling rods (see Fig. 4.3). A 6 mm outer diameter aluminium pipe is glued on each cooling rod using thermally conductive glue (Epo-Tek H20E [80]). Its wall thickness is 0.4 mm. The coolant, C_6F_{14} [82], circulates through this pipe at a temperature of -15°C and a flow of 250 l/hour. Two layers of seven detector modules each are mounted on the two sides of a cooling rod. The thermal contact between the module and the cooling rod is made through the balcony which is in contact with the cooling rod through a thin layer of conductive paste (Artic Silver [83]). The modules are aligned by precision pins inserted in the cooling rod. Each detector box contains two cooling rods. They are connected in series using two Legris connectors [84] and a stainless steel U-shape pipe, which has a 5 mm inner diameter (see Fig. 4.3).

The 28 detector modules are put in an insulating box whose walls are made of a sandwich of 50 μm thick glass-fibre sheets on each side of a 8 mm (3 mm on the beam side) thick

---

[1] The Si sensors are not in direct contact with the fibres, see Fig. 4.2.

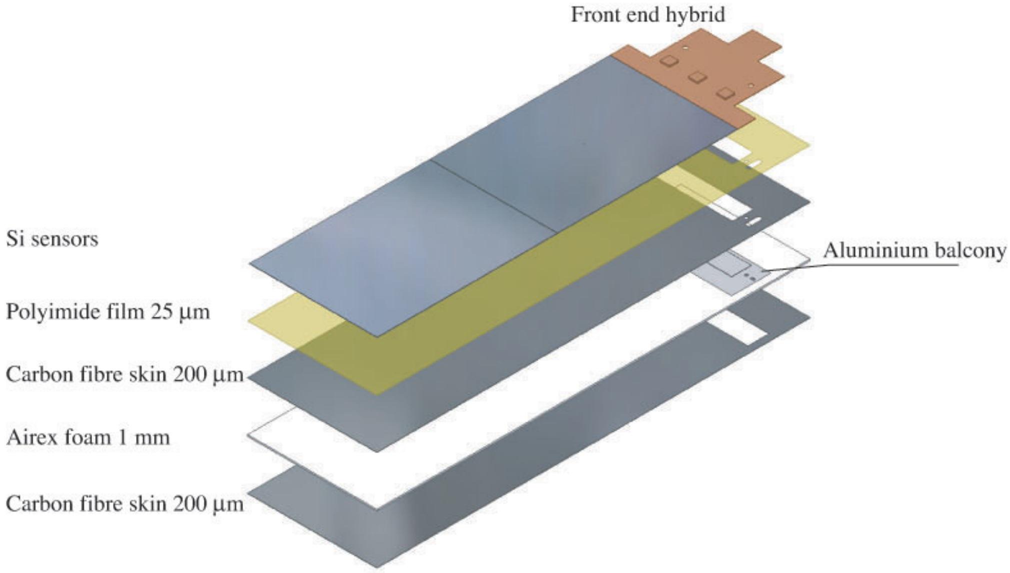

Figure 4.2: Components of the detector ladder.

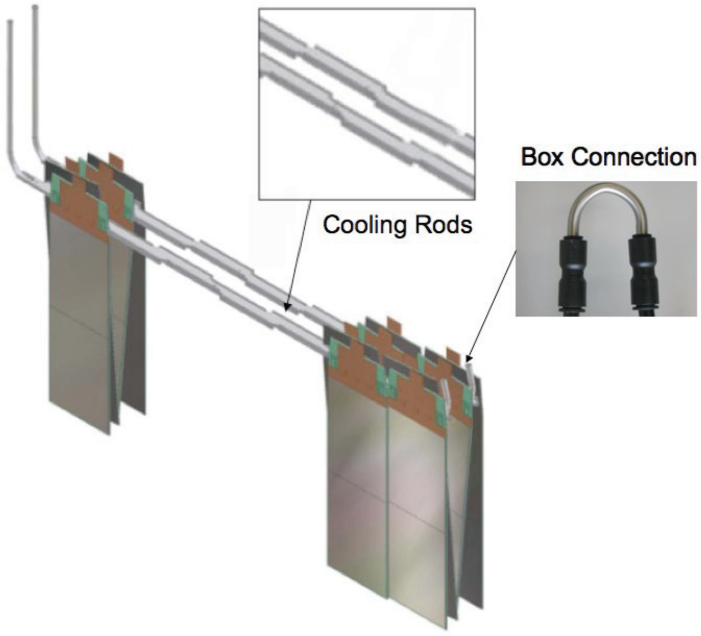

Figure 4.3: Design of the cooling rods and rod connection.

polyisocyanurate (PIR [85]) foam, which has a thermal conductivity of 0.025 W/m·K. The electromagnetic noise shielding is ensured by two 25 μm thick foils of aluminium (see Fig. 4.4). A 0.5 l/hour flux [2] of dry nitrogen circulates in the box to avoid condensation.

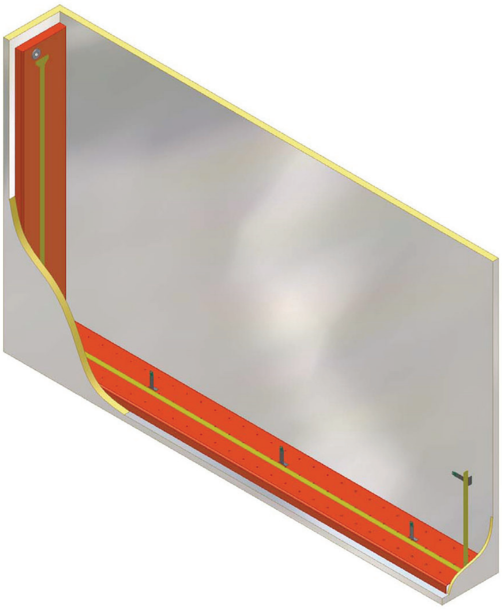

Figure 4.4: Design of a detector box. The channels for distributing the dry nitrogen are visible on the side and at the bottom of the box.

The two cooling rods are attached by carbon columns to the cover of the box. This cover is a sandwich of two 200 μm thick layers of carbon fiber glued on each side of a 12 mm slice of Airex R82 foam [78]. Stesalite inserts are glued in this cover plate to allow its mounting onto the detector box. Four Printed Circuit Boards (PCB) and two cooling pipes traverse the cover plate and provide the necessary feed throughs from the inside of the box to the outside and vice-versa. This cover is screwed onto the insulating box. Coolant transfer lines, coming from the manifolds in the bunker, split into individual cooling lines for each detector box with a flow of 250 l/hour at a maximum pressure of 2.5 bar [3]. From there, the cooling lines are nitril rubber tubes [86] insulated with Armaflex [87]. The inner diameter of the tubes 9 mm for the inlet and 14 mm for the outlet. The tubes are fixed to the Inner Tracker support and connected to the detector boxes via a custom made connection (see Fig. 4.14 in Section 4.4.1) using Legris connectors [88]. Two polyurethane tubes [89], insulated with Armaflex, are connected to those connectors at one side and to the aluminium cooling pipes via others rapid Legris connectors [90] at the other side.

---

[2] The nitrogen flux has been increased to 25 l/hour to avoid condensation in the real boxes.

[3] The pressure of the cooling fluid in the experiment will be increased to 4 bar in the chiller to obtain a flow of 250 l/hour.

4.2 IT production

The Inner Tracker dectectors and structure have been assembled mostly in CERN and Lausanne in our labs. In this section, the different steps of the production are described.

4.2.1 Test on the ladder before gluing procedure

The carbon fibre supports (Fig 4.2) are provided by an external company [71] before being tested in our lab:

- The external dimensions and the precision drilling of holes in the balcony are controlled. The requirement for the cutting precision of the CF-support is of $\pm 100\,\mu$m.
- The flatness of the ladders is measured with a laser system (see Fig 4.5) and data stored in a data base. A precision of $\pm 200\,\mu$m has been agreed on with the company.
- The electrical insulation of the ladder is checked by applying directly on the kapton skin of the ladder a high voltage (0-1000 V) (Fig 4.6).

The ladders have been returned to the company in a case of failure in one of the above points. I have participated in the design of these tests and have made them as a part of the ladder production.

4.2.2 Gluing procedure of the modules

The precision of the Si-sensor positioning and its reproducibility is of primordial importance for the detector. This precision and reproducibility are insured by two alignment pins (diameter of 1.5 mm) inserted in the balcony. These two alignment pins will also serve as position reference points for the ladder to a precision of much better than $10\,\mu$m. The two reference points are transposed to the sandwich support via two precision holes drilling with a precision of $10\,\mu$m.

After the "preparation" tests of the ladders, the hybrid is glued on the ladder support. The hybrid is checked electrically before and after gluing. The ladder is placed on the hybrid gluing jig (Fig 4.7) using the precision pins of the jig and the glue is applied by a glue [4] dispenser robot [72]. Once the glue is applied on the ladder surface. The hybrid is placed on the jig adjusting the position of the pitch adaptor, which is a cut of a ceramic piece with a precision of $\pm 25\,\mu$m, with a precise end stop. Some weight are added on the Beetles and the pitch adaptor during the drying of the glue. The precision of the position of the hybrid is around $\pm 25\,\mu$m at the end.

---

[4] There are two types of glue to be used: Araldit mixed with 1% of micro-balloons to be applied underneath the pitch adapter and the hybrid using the robot. The three rectangular areas underneath the Beetle chips are manually coated with the silver-loaded epoxy glue.

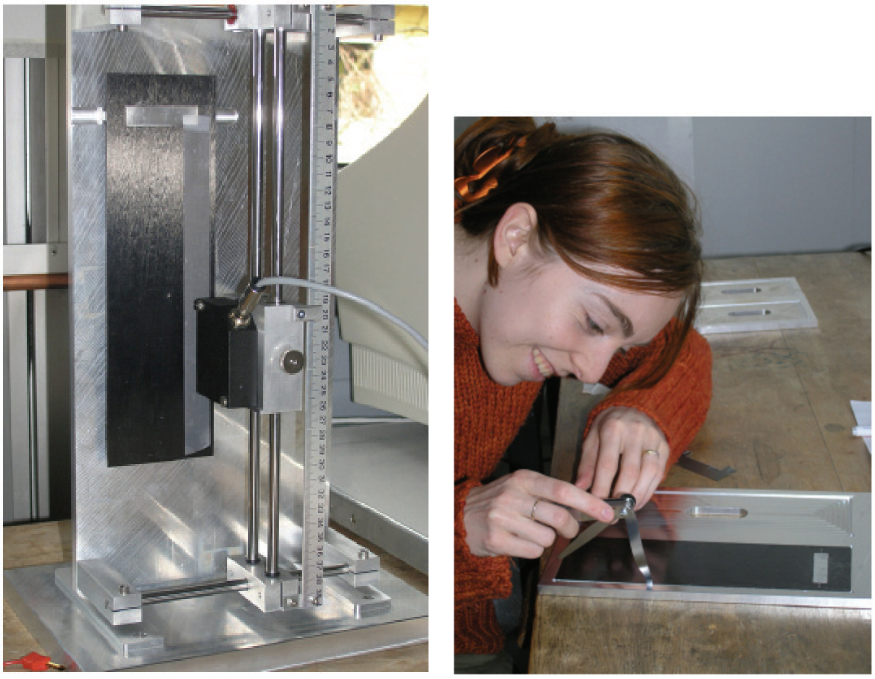

Figure 4.5: Pictures of test setup of the flatness of the ladders (left) and control of the dimensions of the ladder (right).

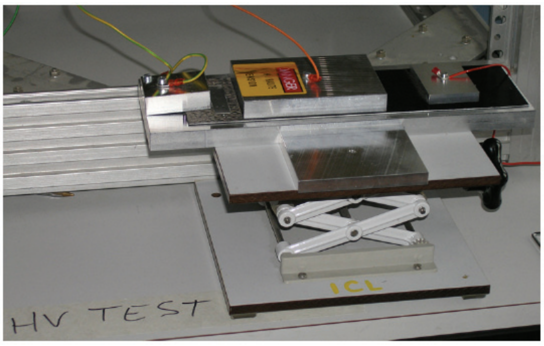

Figure 4.6: Pictures of HV test setup.

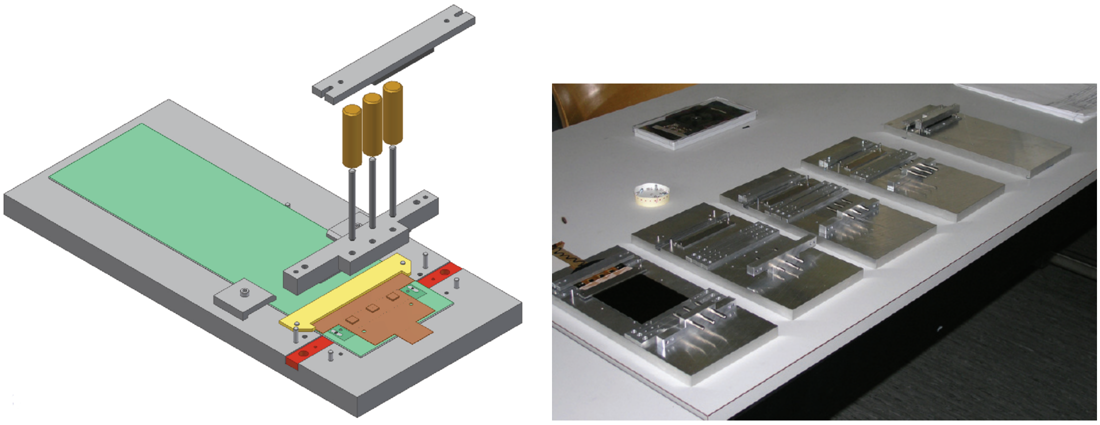

Figure 4.7: Pictures of the hybrid gluing jig.

Next, the sensor are glued on the ladder using the transfert and the gluing wafer jigs (Fig 4.8). Sensor's dimensions have a precision of less than ±20 μm. The sensor is placed with an extreme accuracy on the transfert jig. In parallel, the ladder is placed on the gluing jig via the precision pins. The glue is applied with the glue dispenser robot and the sensor is transfered on the prepared ladder (see [72] for more details). The precision of the position of the sensors is around ±25 μm at the end.

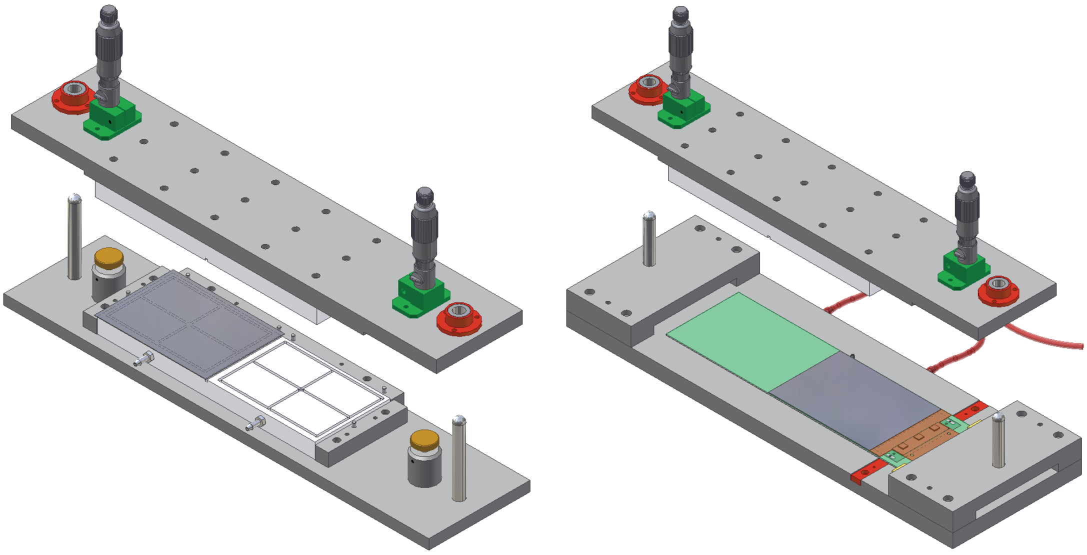

Figure 4.8: Pictures of the transfert jig (left) and the gluing jig (right).

All the pieces of the modules are now assemblied. The module is transported to the CERN lab.

4.2.3 Bonding and tests at CERN

Hybrids, pitch adaptors and sensors have been bonded in the cleanroom at CERN (ref. [73]). The following tests are performed on the modules:

- burn-in and temperature cycling of all modules in a thermally isolated box with temperature control built by the University of Santiago (see Fig 4.9).
- HV tests on the sensors.
- Geometry measurements with an X-Y table.
- A final readout test with a real TELL1 setup.

Figure 4.9: Burn-in and temperature cycling box at CERN. All modules have been tested in a thermally isolated box with temperature control built by the University of Santiago. The measurements include IV-curves reading and the leakage current monitoring during the temperature cycling. Readout of the modules using the internally provided test pulses has also been performed during this temperature cycling in order to spot broken (open/shorted) channels.

4.2.4 The detector boxes

The detector boxes (machined in Santiago) are assembled with the cooling rod and the box cover that have been machined in Lausanne. The cooling rods have been tested (see pressure tests section 4.4.1) and mounted on the equipped cover. Next, the modules are mounted on the cooling rods and the detector is inserted in the box (Fig. 4.10) at CERN. I participated to the conception of the jigs to mounted the box detectors (Fig. 4.11).

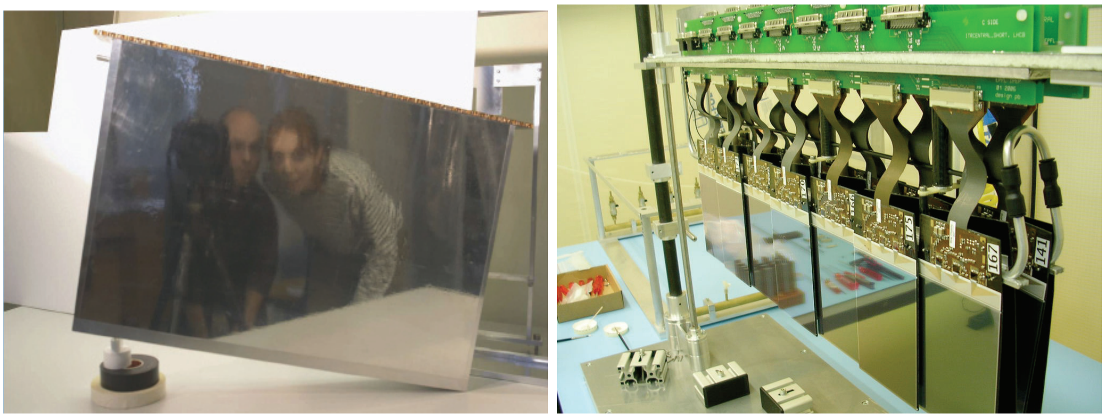

Figure 4.10: Picture of the detector box at left and of a cover eqquiped with PCBs and modules at right.

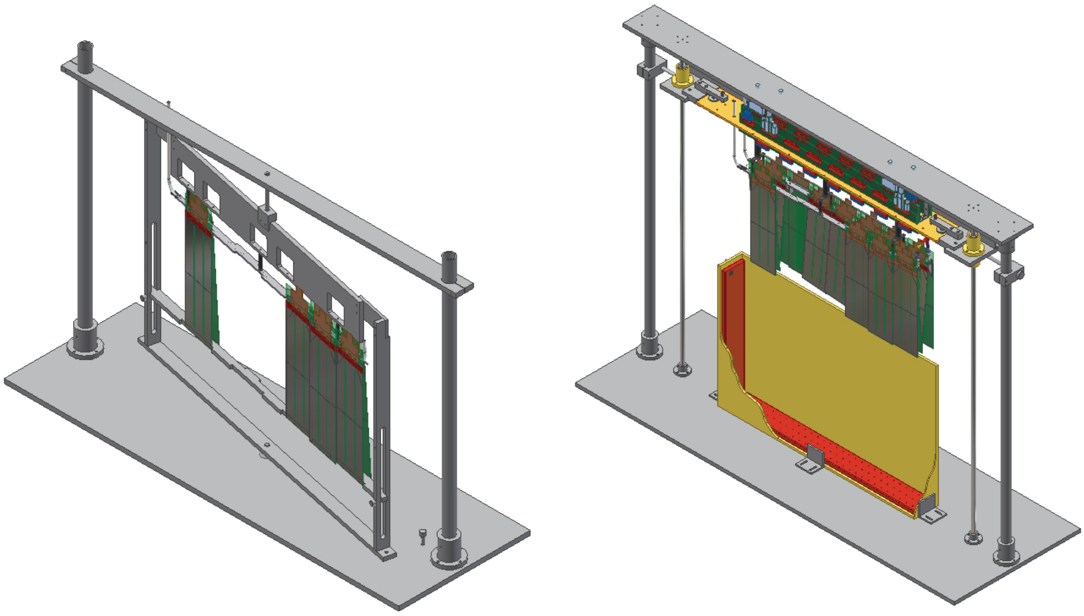

Figure 4.11: At left: picture of the jig use to mount the modules on the cooling rods and at right the jig to put the modules in the box.

4.3 IT material budget

Charged particles traversing a material loose a part of their energy and undergo multiple scattering. They can also interact in the material and produce secondary particles. Therefore, a precise description of the detector geometry is mandatory. A precise placement of the sensors in this description is also of great importance as it will be used in the track reconstruction.

The material implementation of the detector description is done in different steps. First a detailed list of all the different materials of the whole detector [5], including the supports, the cables, the cooling pipes etc..., is made. Then the detector is divided into "logical volumes" to which a single type of material is assigned. Because of the large number of volumes and the requirement that each volume has a fast access, a tree structure is implemented with as few branches per node as possible. This is done using the XML (eXtensible Markup Language) language.

All the description and the results are detailed in a note written by my colleague Kim Vervink and me about this material budget [92] (see Appendix A).

4.4 IT cooling

The cooling of the Inner Tracker has to remove the power dissipated by the front-end electronics, which corresponds to 0.86 W per front-end readout chip, i.e. about 72 W per box, the power generated by the sensors themselves, and the heat sinking into the detector box, which has been estimated to about 30 to 40 W assuming a temperature of 0° C inside the box and an ambient temperature of 22° C [91]. These figures have to be met in order to keep the sensors below 10°C and avoid thermal run-away. A final requirement is that the amont of material used in the cooling must be small as the Inner Tracker is located in the acceptance of the experiment [92].

The detector boxes are placed as close as possible to the beampipe and the innermost detectors are subject to a substantial radiation dose. Irradiation induces damages in the bulk of the detector which lead to an increase of leakage currents. These leakage currents cause shot noise and dissipate power in the sensors which needs to be removed. The leakage currents can be decreased by cooling the detector. The exponential dependence of the leakage currents on the silicon bulk temperature is given by:

$$\frac{I_{leak}(T_1)}{I_{leak}(T_2)} = \left(\frac{T_1}{T_2}\right)^2 \cdot exp\frac{E_g(T_1 - T_2)}{2k_B T_1 T_2} \tag{4.1}$$

where $E_g = 1.2\,\text{eV}$ is the band gap for silicon and $k_B = 8.617 \cdot 10^{-5}\,\text{eV/K}$ is the Boltzmann constant [74].

If this leakage current generated heat is not removed, so-called "thermal run-away" can occur. Heating of the silicon increases the leakage currents, which increase the power dissipation and so on...

---

[5] The detector box with all its components was described with a total error of 20 g over ∼ 2 kg!

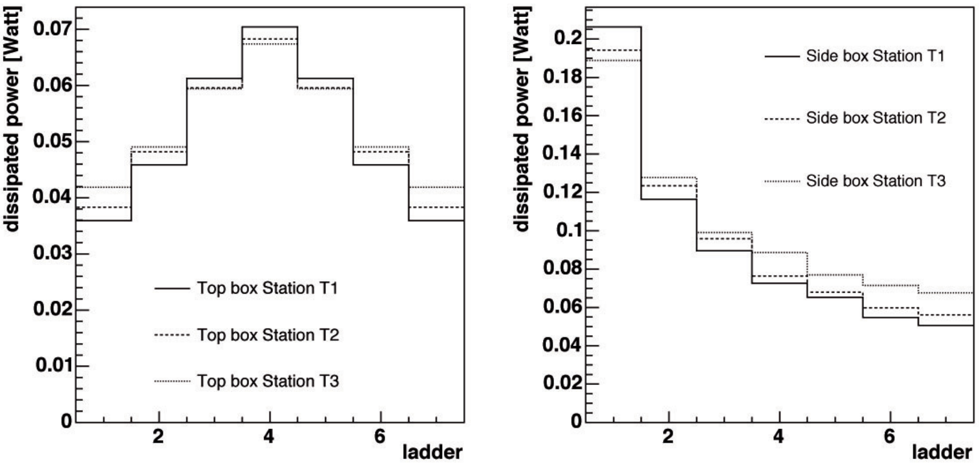

Figure 4.12: The power dissipation in the various ladders at 10°C after 10 years of operation for a bias voltage of 300V.

Stable operation is guaranteed when the cooling power is large enough to cool the sensor below the temperature at which the power dissipated by leakage currents would exceed the power that can be removed by cooling. In [74] it has been estimated that after 10 years of LHCb operation ($1.6 \cdot 10^{15}$ pp-collisions) the resulting power dissipation due to leakage currents is ~ 0.2 W/module at ~ 10°C on the silicon sensors closest to the beampipe (see Fig. 4.12).
The tests described in this chapter aim to demonstrate that, provided the outside temperature does not exceed 22°C, our cooling system is able to keep the sensor temperature below 10°C for a power dissipation of 0.2 W per module, which would result in a stable running condition.
We first describe the pressure and vibration tests done on the cooling design, and in a second part, the cooling tests will be described and analysed.

4.4.1 Pressure and vibration tests

The cooling circuit has to be tested against leakage to ensure proper operation at 2.5 bar of C_6F_{14}. In addition we have checked for possible vibrations induced by the turbulent flow of the cooling liquid. In this section we will present the different pressure tests applied on each part of the cooling circuit and describe the vibration tests which have been made.

Pressure tests

We have performed pressure tests on the nitril rubber circuit and on the cooling rod connection using water at room temperature at a pressure of 2.5 bar for one hour and at 4 bar for 5 min. The test setup is shown in Fig. 4.13. The tests have been repeated it about 20 times (see Fig. 4.13). The initially tested nitril tubes did not withstand the pressure without deformation and were subsequently exchanged by reinforced nitril rubber tubes [86], which can withstand a pressure of 4 bar without visible deformation.

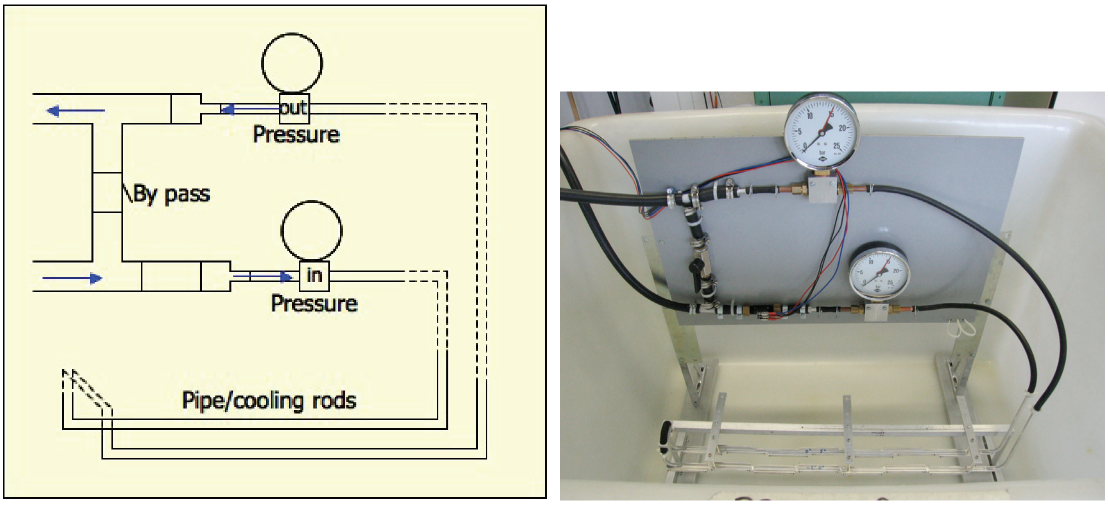

Figure 4.13: Schematic and picture of the pressure tests set-up.

The connection between the two cooling rods (Fig. 4.3) was tested with water in the same way as the nitril rubber tubes. In addition, we have looked for possible leaks using Helium at 4 bar [6]. Here, the setup was placed under water in order to see any appearance of bubbles.

During the production of the cooling rods, each aluminium pipe was tested in water with Helium at 4 bar before and after being glued onto the cooling rod.

The cooling connection between the detector box and the nitril rubber pipes outside the box (see Fig. 4.14) was also tested with Helium at 4 bar.

Vibration test

The turbulent flow of C_6F_{14} could cause unwanted vibrations in the detector box. We have tested a system of two cooling rods equipped with four ladders (see Fig. 4.15). Water at 10°C and 360 l/hour was circulating through the cooling tubes. A mirror was glued on one of the ladders and a measurement of its vibrations was taken with a laser beam reflected off the mirror and projected on a screen at 3 m distance (see Fig. 4.15). Water at 10°C and 360 l/hour has a Reynolds number of $\mathcal{R}e(water) = 18715$ whereas C_6F_{14} at -15°C and 250 l/hour (real conditions) has $\mathcal{R}e(C_6F_{14}) = 24338$. Both are far in the turbulent regime. We can therefore assume that our experimental conditions are similar to the real conditions.

We did not see any deviation of the laser beam on the screen with an estimated accuracy of ± 0.5 mm. This translates to an upper limit of $\pm 40\mu$m on the amplitude of possible

---

[6] The real setup has been tested at 5 bar.

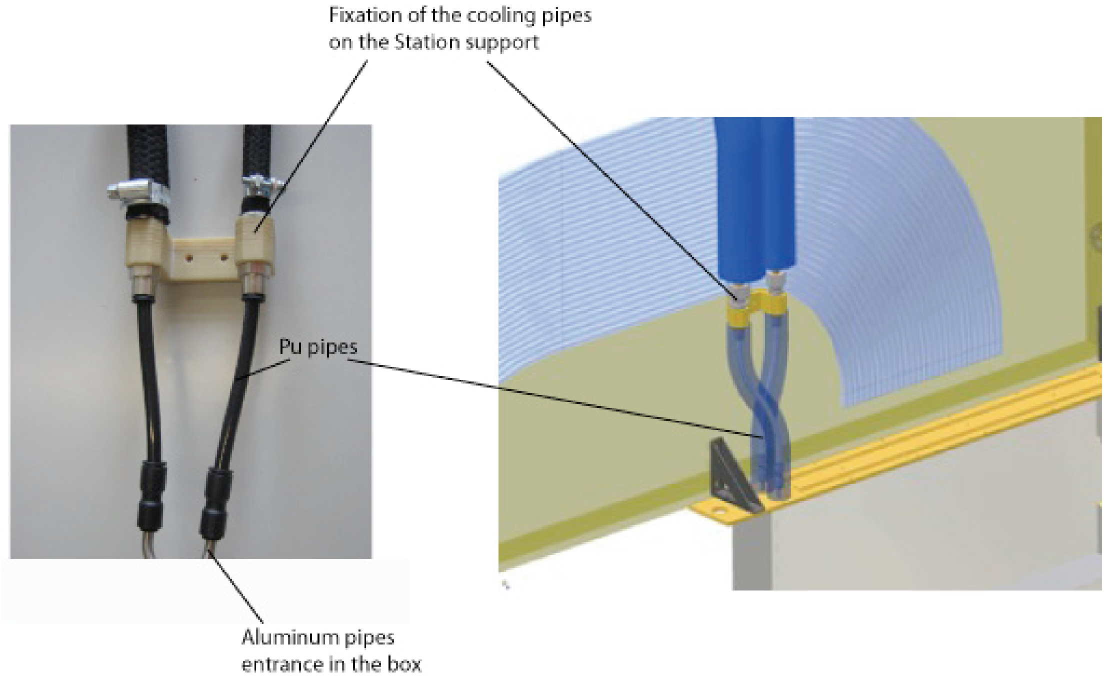

Figure 4.14: Photo and drawing of the cooling connection between the detector box and the nitril rubber pipes.

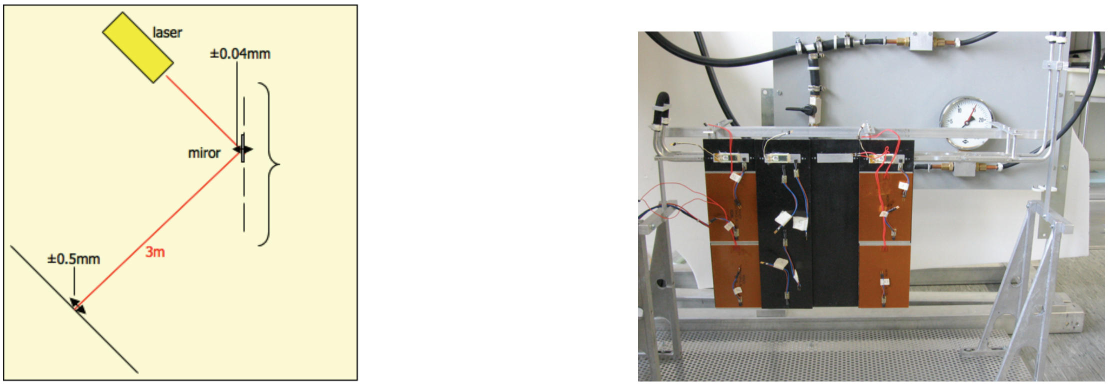

Figure 4.15: Schematic and picture of the vibration test set-up.

vibrations at the end of the ladder furthest from the cooling rod. We conclude that the vibrations, if any, are very small and can be accepted.

4.4.2 Cooling test: the setup

The tests were performed with a side detector box under conditions which were as close as possible to the ones in the final setup. Two cooling rods were equipped with 24 real sandwich supports and four ladders made out of high conductive carbon fiber only (see Fig. 4.16). Each ladder was equipped with a resistor positioned on the balcony with conductive glue to simulate the heat generated by the front-end electronics. On the eight ladders furthest from the cooling inlet/outlet (i.e. near the beampipe), a resistive coil was glued on each of the two silicon sensors to simulate the expected power dissipation of the sensors (see Fig. 4.16 and Fig. 4.17). These sensors are expected to suffer most from irradiation damage and are expected to dissipate about 0.2 Watt after 10 years in the experiment (see Fig. 4.12). To simulate the silicon sensors on these eight ladders, we used eight real pieces of silicon, four glass pieces of 300 μm in thickness and four aluminium pieces. Each one of these was glued onto its sandwich support using the same silicone glue that will be used for the real detector module.

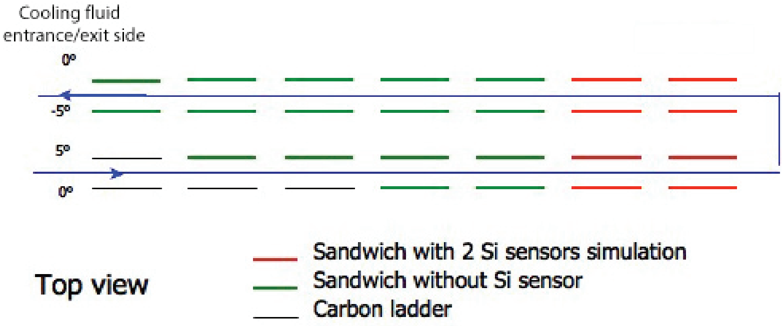

Figure 4.16: Disposition of the ladders in the box.

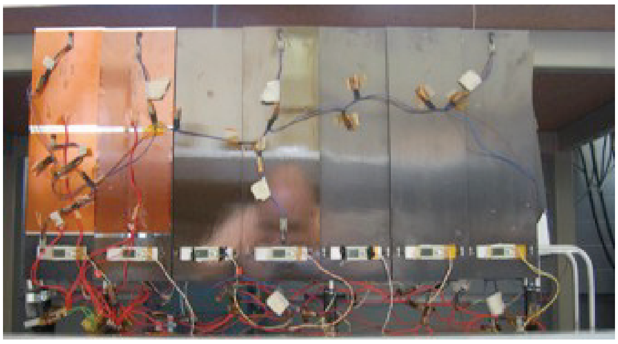

Figure 4.17: Picture of the ladders in the box.

The two cooling rods had their aluminium pipe glued with silver glue [80] and a few points of Araldite [7]. We added a brim of plastic metal (essentially aluminum [81]) to increase the contact surface and hence the thermal contact between the pipe and the cooling rod. The two cooling rods were mounted on a box-cover using carbon and Stesalite columns. Four pieces of PCB material (copper and glass fiber) were inserted inside the cover to simulate the interface-PCBs (see Fig. 4.18). All this equipment was inserted in a final detector box and was turned upside down, i.e. with the cooling rods and the cover plate at the bottom. This is the same orientation in which the detector boxes will be operated in LHCb (see Fig. 4.1).

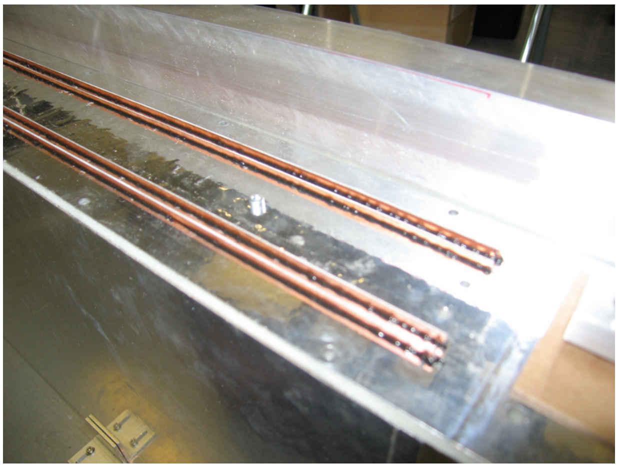

Figure 4.18: Picture of the cover equipped with the PCB.

Two humidity sensors were fixed in the box, one near the PCB's and a second one between the two cooling rods near the end furthest from the cooling inlet. Nitrogen at a flux of 0.5 l/hour circulated through the box during all tests. Fortyfive temperature probes [93] were glued with cyanolite glue to monitor the temperature at different points in the box. They were distributed as follows:

- three on each cooling rod
- four in the box and one on the cover plate to measure the ambiant temperature in the box
- one on each resistor coil which simulates the sensor dissipation
- eleven on the tips of the ladders (eight directly glued on the sensor and the other three on the carbon fiber support)
- four on balconies

---

[7] Recent tests indicated that the thermal contact can probably be improved without compromising the mechanical stesility if one omits these Araldite points.

- the rest distributed among different ladders

The measurement error of this type of probe is quoted as ±0.5°C. They are directly readout via the serial port of a PC.
C_6F_{14} circulated at its design flow and at temperatures ranging from -5 to -15°C. Two PT100 temperature sensors were placed inside the coolant circuit to measure the coolant temperature at inlet and oulet, another one was fixed near the detector box to measure the temperature in the lab. A flowmeter was inserted in the cooling circuit to monitor the flow (see Fig. 4.19).

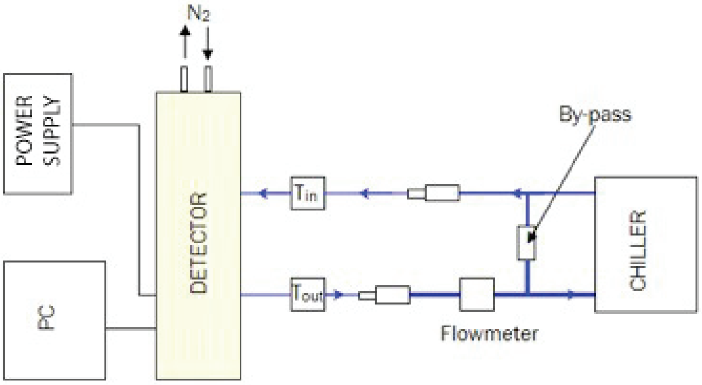

Figure 4.19: The cooling set-up. The flow of the coolant is regulated by a by-pass. The two PT100 to measure T_{in} and T_{out} and a flowmeter are inserted in the circuit. A dry nitrogen flux is connected to the detector box. The sensor and hybrid simulation resistors are connected to a power supply and a PC reads out the temperature probes.

4.4.3 Measurements and analysis

Temperature on the sensors

To avoid the risk of thermal run-away after several years of operation, the temperature on the sensors has to be kept below 10°C. The point where the temperature is expected to be the highest is the tip of the sensor located furthest from the cooling inlet/outlet in the side boxes (labeled 1 to 4 in Fig. 4.20.).
Under normal running conditions (1 MHz trigger rate and standard readout chip parameter settings [40]), the power dissipation of each readout hybrid is about 2.57 W. We performed measurements with a simulated front-end electronics dissipation of 0 W, 1.5 W, 2.57 W and 3 W per module. On the eight modules equipped with resistive coils, the sensor dissipation was simulated for 0 W, 0.125 W and 0.25 W per sensor. The expected average dissipation after 10 years of operation in LHCb is 0.125 W/sensor at 10°C.
In Fig. 4.21 we can see that the highest temperature that we measured on a sensor was around 7 ± 0.5°C. The trend of the measurements showing some ladders being

systematically warmer (colder) than others can be qualitatively explained by the shape of the cooling rod (see Fig. 4.22 and Section 4.4.3), and has been observed in several different measurement set-ups. In addition, the sensor in position 1 is especially poorly cooled, because only one half of the balcony is in contact with the cooling pipe (see Fig. 4.22). The two sensors facing the box wall are warmer than the two stereo sensors. The first group of four sensors near the beam (temperature probes 1, 2, 3, and 4) is hotter than the second group (temperature probes 5, 6, 7, and 8) probably due to weaker convection near the box side wall. However, the measurements show that the cooling capacity allows for cooling of the sensors to below 10°C, given an outside temperature of 22°C.

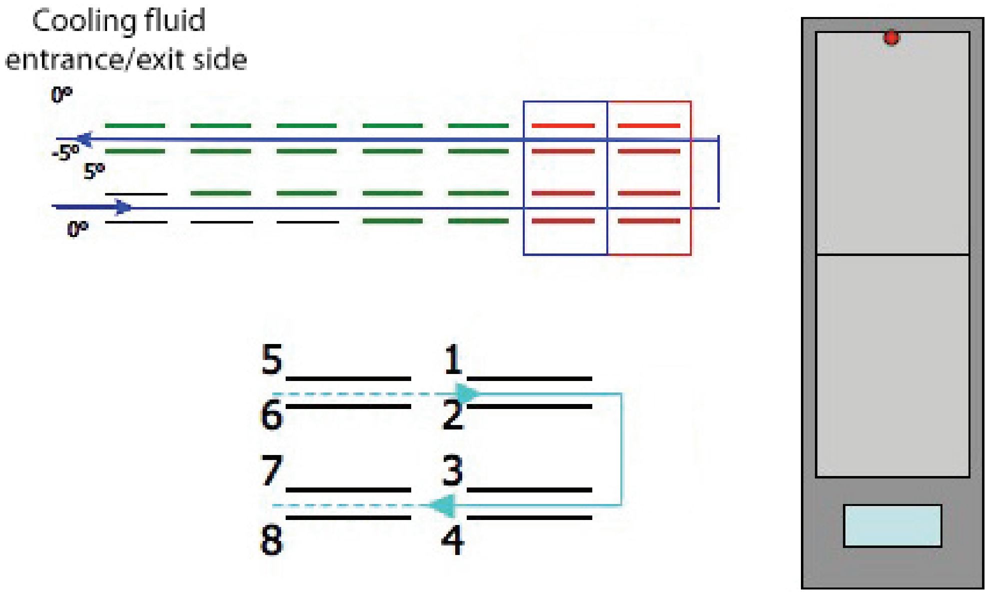

Figure 4.20: This schematic shows the position of the temperature probes as discussed in Fig. 4.21 and 4.23. At the top is a top view of the four layers of ladders in the box. The measurements are only made for the eight highlighted ladders, which are located furthest from the cooling inlet/outlet. The temperature probes are located at the tip of the sensor furthest from the cooling rod (right hand side of the figure). At the left bottom part, is a description of the numbers associated to the temperature probes of the sensors. The temperature probes are directly glued onto the sensors.

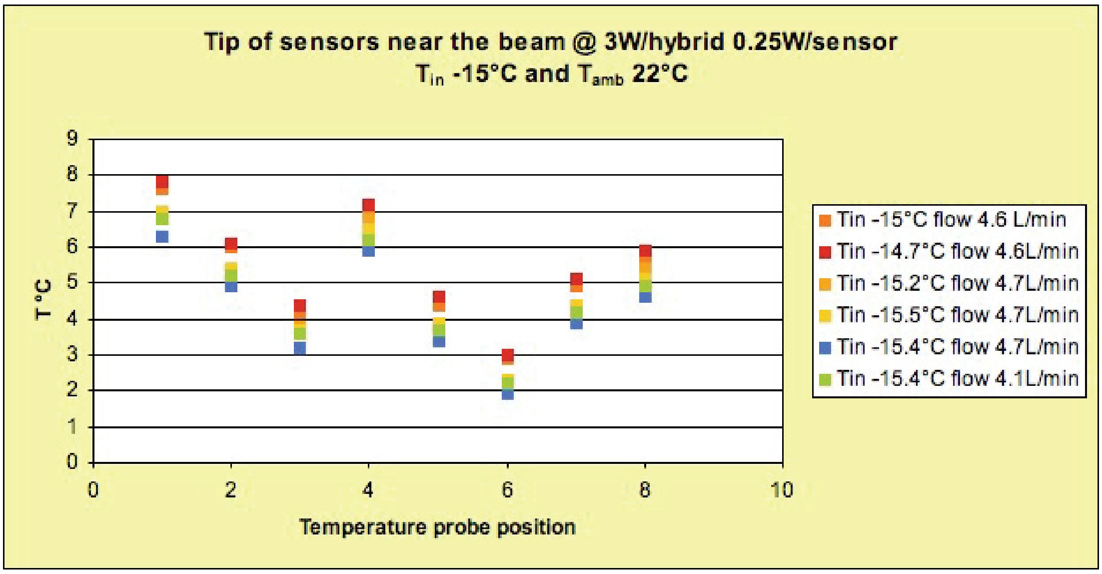

Figure 4.21: Measurements of the temperatures on the tip of the sensors on ladders 1 to 8, with a dissipation of 3 W per hybrid, 0.25 W per "sensor" and for an outside temperature of 22°C. The different colours correspond to different temperatures and flows of the coolant.

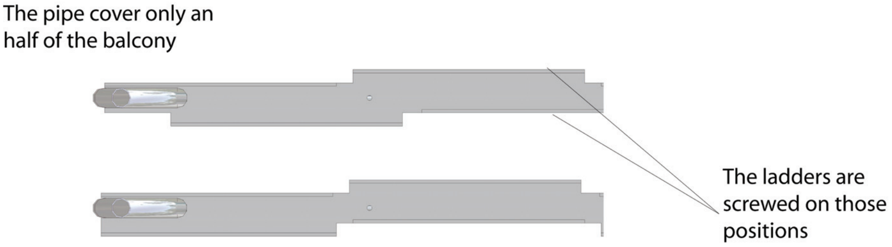

Figure 4.22: Top view of the part of the cooling rods near the beam.

At the beginning of the LHCb experiment, the sensors will hardly dissipate any power as the leakage currents are still very low. With 3 W dissipated per hybrid and no sensor heating, the maximum temperature at the tip of sensor 1 is around 4±0.5°C. If the eight ladders nearest the beampipe are allowed to dissipate 0.25 W per sensor, this temperature rises to 6.5±0.5°C. Fig. 4.23 shows the temperature at the top of ladders 1 to 4. All other sensors operate at less than 5°C when the detector is operated with an outside temperature of 22°C.

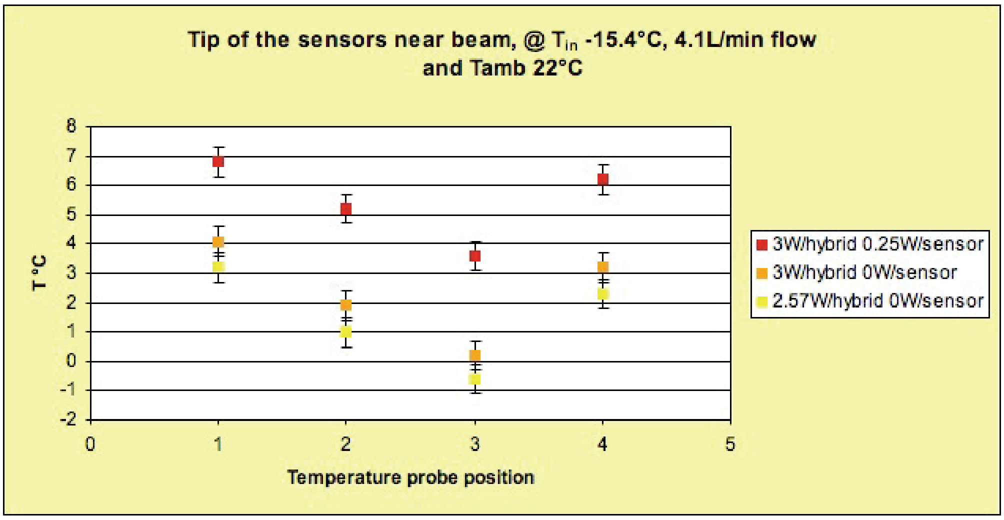

Figure 4.23: Measurements of the temperatures on the tips of the sensors near the beam with the coolant at $T_{in} = -15.4°C$ and 4.1 l/min flow. The temperature outside the box was 22°C. The colours correspond to various thermal power simulating the hybrids and sensors.

Horizontal temperature profile

The measurements of the temperatures on the tips of all ladders in one of the x-layers (see Fig. 4.24 and 4.25) show that all temperatures are less than 5°C except for the ladder which will be closest to the beam. We observe a jig-saw pattern which can be qualitatively explained by the shape of the cooling rod. Neighbouring ladders in a layer are staggered by ± 2 mm to allow for an overlap between the sensors. Hence, the cooling rod has a different thickness at various positions (see Fig. 4.22), and some ladders are 4 mm “closer” to the cooling pipe than others. The noticeable temperature increase for ladders 6 and 7 is due to the heating of the sensors (these two ladders correspond to ladders 1 and 5 in Fig. 4.20) implemented on these ladders.
To see how the shape of the cooling rod influences the measurements, we have calculated the expected temperature difference induced by the difference of the thickness of the cooling rod. Theoretically, we would expect a temperature difference between two adjacent positions on the cooling rod of:

$$\Delta T = \ell \cdot \frac{\Delta Q}{\lambda A} = 0.5°\mathrm{C} \tag{4.2}$$

with:
λ = thermal conductivity of aluminium: 160 W/m·K
A = surface of the balcony contact: $70 \times 3\mathrm{mm}^2$
ℓ = thickness of aluminium: 4mm
ΔQ = power absorbed from the balcony: 4W (3W from the Beetles and 1W from the heat inside the box)

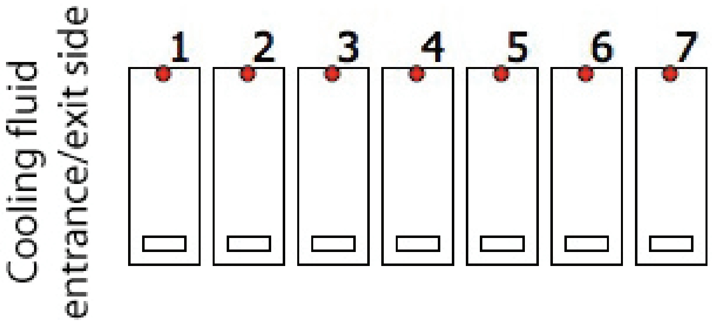

Figure 4.24: This figure shows the position of the temperature probes as discussed in Fig. 4.25. While temperature probes 1-5 are glued onto the CF-support directly, probes 6 and 7 are glued to a glass or silicon plate that is eqquiped with a resistive coil heater simulating the Si-sensor dissipation.

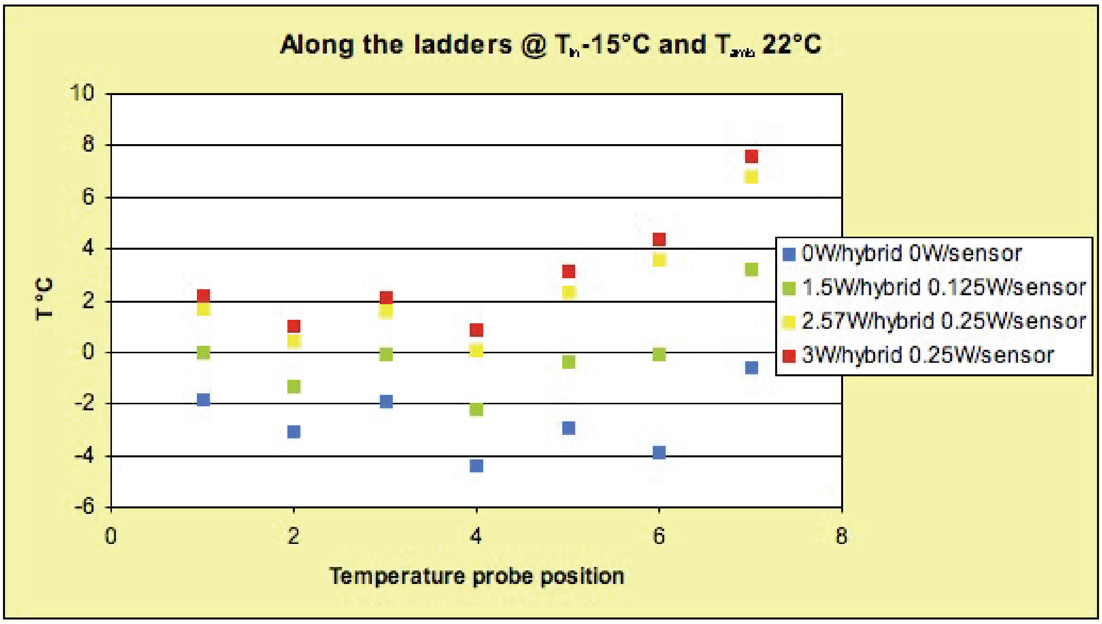

Figure 4.25: Measurements of the temperatures on the tips of all ladders in an x-layer of the box, with the coolant at -15°C and an outside temperature of 22°C.

We observe at the tip of the ladders a temperature difference of around 1-2°C.

Contact with cooling rod

The thermal contact between the balcony and the cooling rod is achieved by tightening it with two screws and improved by a thin layer of thermal conductive paste [83]. The measurements of the temperature on balconies and cooling rods (see Fig. 4.26 and 4.27) indicates that the contact between balconies and cooling rod is not established reliably. The temperature difference between the first balcony (1) and the cooling rod (2) is around 1.5°C for the maximum power applied, whereas for the second balcony (3), this difference is 5°C. This discrepancy indicates that here the contact is not established in a reliable way.

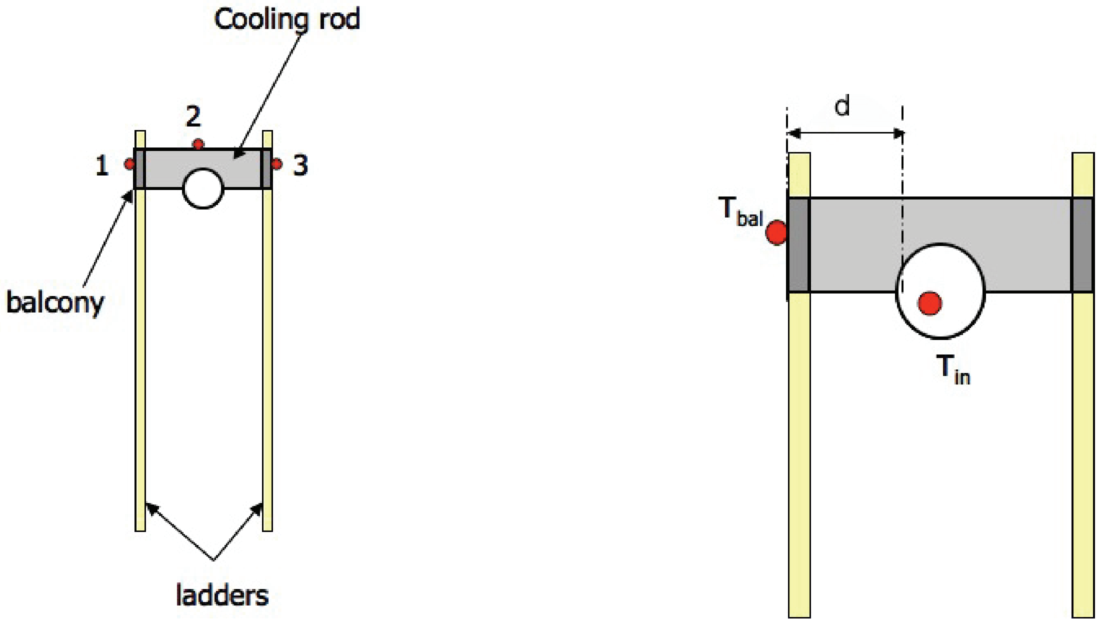

Figure 4.26: The left drawing explains the positions of the temperature probes as displayed in Fig. 4.27. There are two probes glued on two opposite balconies and a third one is fixed on the cooling rod just between the two balconies. The measurements are taken in the hottest position of the ladders in the box. The right figure shows the arrangement used in the determination of the average thermal conductivity between the coolant and at the balcony (equation 4.3). Here, one probe is glued on the balcony and the other one put inside the cooling fluid.

The calculation of the averaged thermal conductivity between the coolant and the balcony is done using:

$$\lambda = \frac{\Delta Q d}{\Delta T A} \tag{4.3}$$

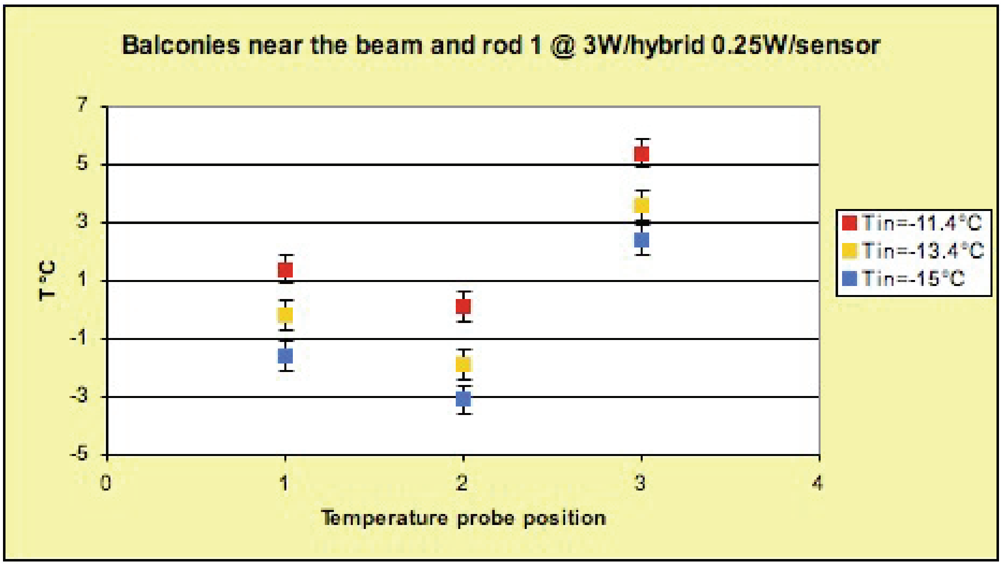

Figure 4.27: Measurements of the temperature of the balconies and comparison to the temperature of the cooling rod at the same place. The power dissipated by the resistors simulating the hybrids is 3 W and the ones for this sensors is 0.25 W.

with:
A = contact surface of the balcony: $70 \times 3\text{mm}^2$
d = thickness of aluminium [mm]
ΔQ = power applied on the balcony: 4W (3W for the Beetles and 1 for the heat inside the box)
ΔT = temperature difference between the balcony and the coolant: $T_{bal} - T_{in}$ [°K]

For $d = 3.9\,\text{mm}$, $\lambda = 7\,\text{W/m·K}$ and for $d = 7.9\,\text{mm}$[8] we obtain $\lambda = 10\,\text{W/m·K}$. These figures are to be compared to thermal conductivity of aluminium. The loss of thermal conductivity is essentially due to a bad thermal contact between the cooling pipe and the cooling rod. There are currently tests going on that aim to improve this contact.

Cooling rods

In measurements of the temperatures on the cooling rod directly (Fig. 4.28 and 4.29), we observe the following points:

- the cooling fluid heats up by only 1 degree from the inlet to the outlet
- on both cooling rods, the temperature increases towards the end furthest from the inlet/outlet

---

[8] The two d values correspond to the two different thicknesses of the cooling rod (See Fig A.3.)

- there is a temperature difference of 2 degrees up to 5 degrees between the inlet/oulet cooling fluid and the temperature probes on the cooling rod near by.

Between the first and the second cooling rod, the temperature decreases a little. The only explanation we can offer for the temperature profile observed on the second cooling rod is that it is due to a bad thermal contact between the cooling pipe and the cooling rod. Otherwise there is no reason why the temperature on the cooling rod should decrease towards the outlet. We are currently working to improve the gluing of the cooling pipe[9].

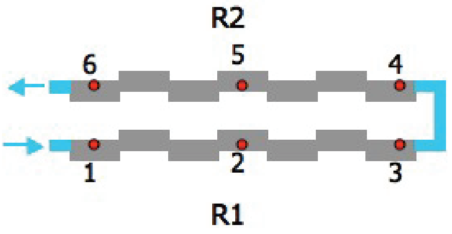

Figure 4.28: This figure shows the position of the temperature probes as used in Fig. 4.29. It shows a top view of the two cooling rods connected together. The direction of the flow of the coolant is indicated.

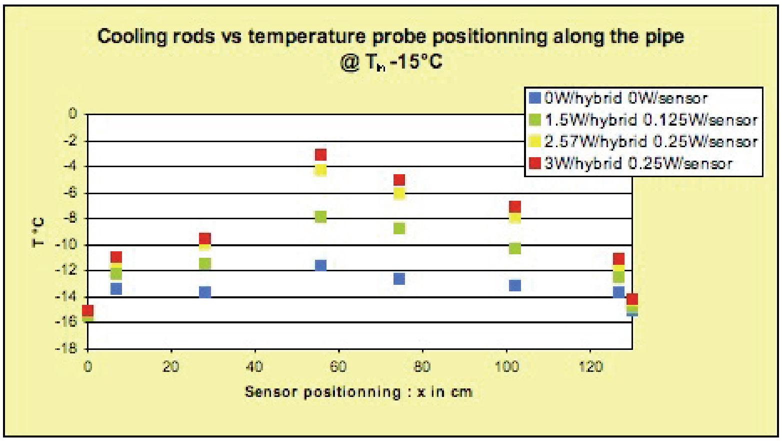

Figure 4.29: Measurements of the temperature on the cooling rods with the coolant at -15°C. On the x-axis are the position of the temperature probes in centimeters along the rod. At 0 cm is the inlet and at 130 cm the oulet. The six positions of the temperature probes on the cooling rod are indicated in Fig. 4.28.

---

[9] We have performed a quick test of the gluing and conclude that the points of Araldite added in between the silver glue, that aimed to improve the mechanical rigidity, seriously hampers the thermal contact.

Temperature inside the box

Another important parameter in our cooling measurements is the temperature of the air in the box. Shown in Fig. 4.31 is the air temperature at various locations in the box. The cover is colder than the rest of the box because it is at the bottom of the box. Temperature probes 3 and 4 are fixed near the heated silicon/glass pieces that simulate the silicon sensors. This explains the temperature difference of 3°C for these two temperature probes between the measurements with the Si-sensor heating "on" (0.25 W) and "off" (0 W). An interesting result is that the temperatures measured on probe 3 are significantly higher than those measured on the tips of the silicon sensors nearby (see Section 4.4.3 below). This observation could indicate that, contrary to our initial expectation, the silicon sensors themselves are actively cooled through the CF supports. For the fact that probe 2 shows a significantly lower temperature than probes 1 and 3, we have no other explanation than that it could be due to the flow of nitrogen or to differences in the air convection inside the box.

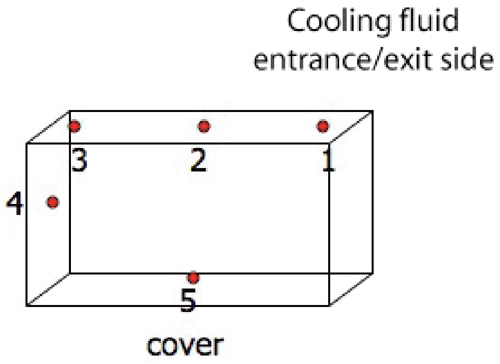

Figure 4.30: This figure shows the position of the temperature probes for Fig. 4.31. Three temperature probes, 1,2 and 3, are fixed on the gas channel in the box. Probe 4 is in the middle of the thin wall of the box and probe 5 is fixed on the cover.

Tip of the sensors and ambient temperature in the box

In Fig. 4.32 and 4.33, the temperature at the tip of the sensors is compared to the temperature of the air in the box. The fact that the temperature at position 3, i.e. at the end furthest from the coolant inlet/outlet and close to the thin wall of the insulating box, is higher than the sensor temperature at the tips of the modules can be qualitatively explained by the convection of hot air.

The measurements seem to indicate that the CF-fibre supports do play a role in cooling the sensors.

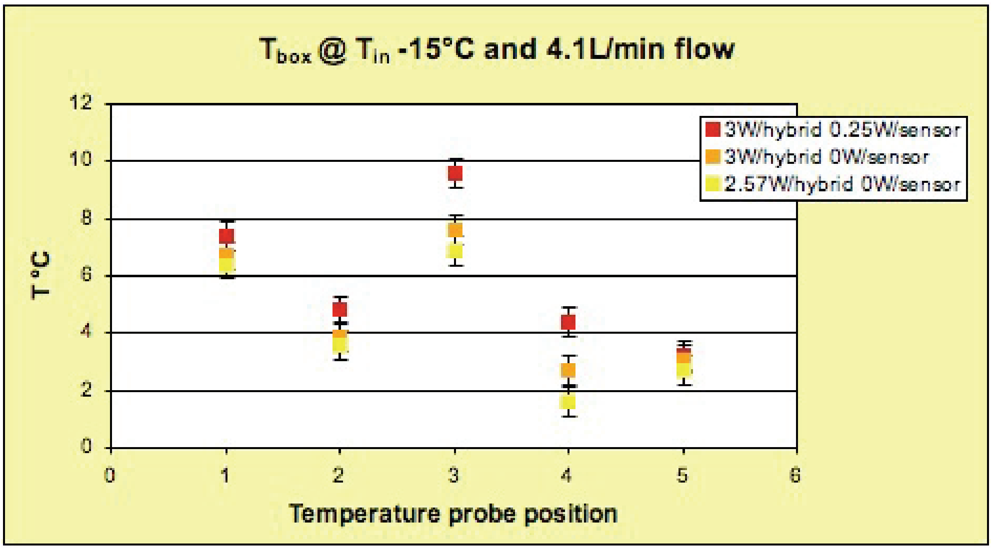

Figure 4.31: Measurements of the air temperature in the box. The coolant circulates at -15°C and 4.1 L/min.

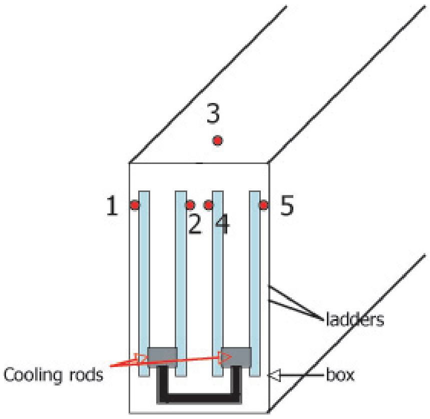

Figure 4.32: This drawing shows a side view of the box. Probe number 3 is fixed on the gas channel in the box (See Fig. 4.30, probe number 3). The temperature probes 1, 2, 4, and 5 are glued on the tips of the four sensors furthest from the coolant inlet/outlet and closest to the beampipe.

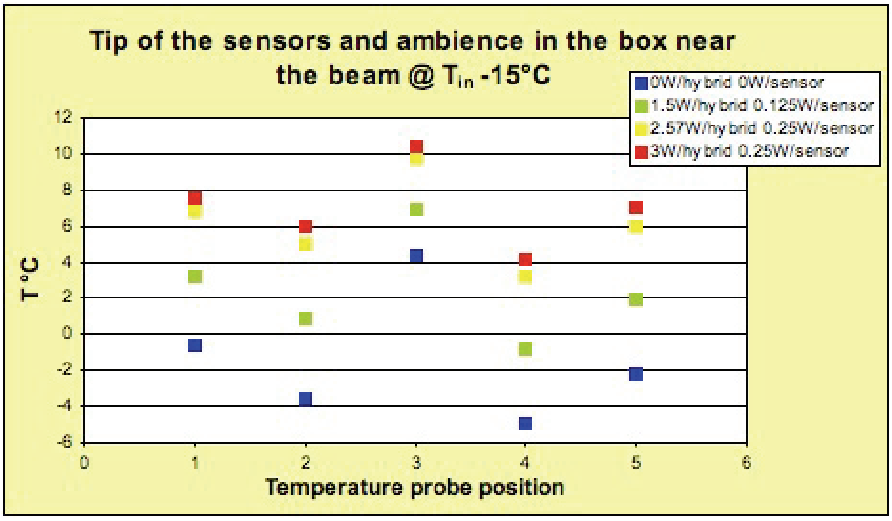

Figure 4.33: Measurements of the temperature at the tips of the sensors furthest from the coolant inlet/outlet and closest to the beampipe.

Calculation of the heat transfer coefficient

To compare our results to earlier studies of the cooling of the Inner Tracker [91], we used a calculation of the box temperature based on the thermal equilibrium of the heat transfer process. The power removed by the circulating coolant, Q_{tot}, is given by the temperatures at inlet and outlet and by the flow. This heat is equal to the power generated inside the box (hybrid and sensor simulations) plus the heat flow into the box.

$$Q_{tot} = C_p F \Delta T = \Delta Q + Q_R \tag{4.4}$$

with:
Q_{tot} = heat power absorbed by the coolant [W]
C_p = specific heat coefficient of $C_6F_{14} \sim 1000\,\mathrm{J/kg{\cdot}K}$
F = flow of the coolant [kg/s]
ΔT = difference of temperature between outlet and inlet of the coolant: $T_{out} - T_{in}$ [K]
ΔQ = heat power sinking into the box [W]
Q_R = heat power dissipated by the hybrids and the sensors in the box [W]

Averaging over all measurements, we obtain a heat flow into the box of $\Delta Q = 36.45 \pm 2.69\,\mathrm{W}$ [10].
We can calculate the average heat transfer k coefficient of the box using the above average value for ΔQ.

---

[10] This can be compared to the first estimations with an old version of Inner Tracker detector [91] where ΔQ was estimated to about 30 W.

$$\Delta Q = kA(T_{amb} - T_{box}) \tag{4.5}$$

with:
ΔQ = heat flow into the box [W]
k = average heat transfer coefficient of the box [W/m^2·K]
A = total surface of the box: 0.64 m^2
T_{amb} = temperature outside the box $\sim$ 295K
T_{box} = average of the 5 temperature probes in the box [K]

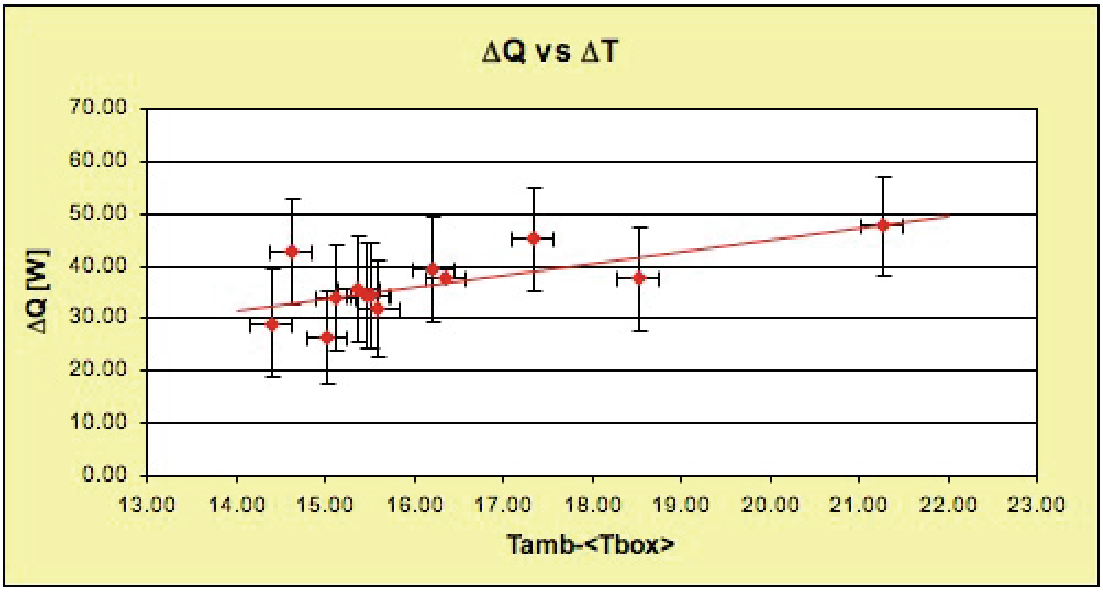

Figure 4.34: Fit of the ΔQ vs $T_{amb} - T_{box}$. The slope is proportionnal to the k factor of the box.

From Figure 4.34, we deduce a value of $k = 3.49 \pm 2.31$ W/m^2·K. The large uncertainty arises from the fact that the temperature range of the fluid temperature is too small to obtain a good determination of the slope (most of the measurements are with a coolant temperature between -15 and 0°C).

Cooling with 30°C ambience outside the box

Using the value of the heat transfer coefficient obtained above, we have estimated the increase of cooling power that we must face if the outside air temperature is increased from the nominal value of 22°C. For instance, if the outside temperature is 30°C, we will have to cope with $\Delta Q(30)$ sinking into the insulating box.

$$\Delta Q(30) = kA(30 - T_{box}) = 53.6\text{W} \tag{4.6}$$

with:
$\Delta Q(30)$ = heat power sinking into the box with an outside temperature of 30°C [W]
$k = 3.49\,\mathrm{W/m^2{\cdot}K}$
A = total surface of the box = $0.64\,\mathrm{m}^2$
$T_{box} = 6.16$°C average of the temperature probes in the box

At 30°C, we must remove 17.2 W more than in the case where $T = 22$°C. Our cooling system is designed for $Q_{tot} = \Delta Q(22) + Q_R = 124.4\,\mathrm{W}$ where $Q_R = 88\,\mathrm{W}$ is the total power of hybrids and sensors in the box. To dissipate 17.2 W more, we have to improve the cooling power by 14%.

T ambience	ΔQ flow into the box	cooling increase
28°C	49.1 W	11%
30°C	53.6 W	14%
33°C	60.4 W	19%
35°C	64.9 W	23%

If the ambient temperature outside the detector box is around 35°C, the cooling power must be increased by about 20%. To resolve this problem, an aluminium cooling plate (Fig. 4.35) is inserted between the Inner Tracker and the magnet. The ambient temperature outside the box when the magnet is on is around 20° C.

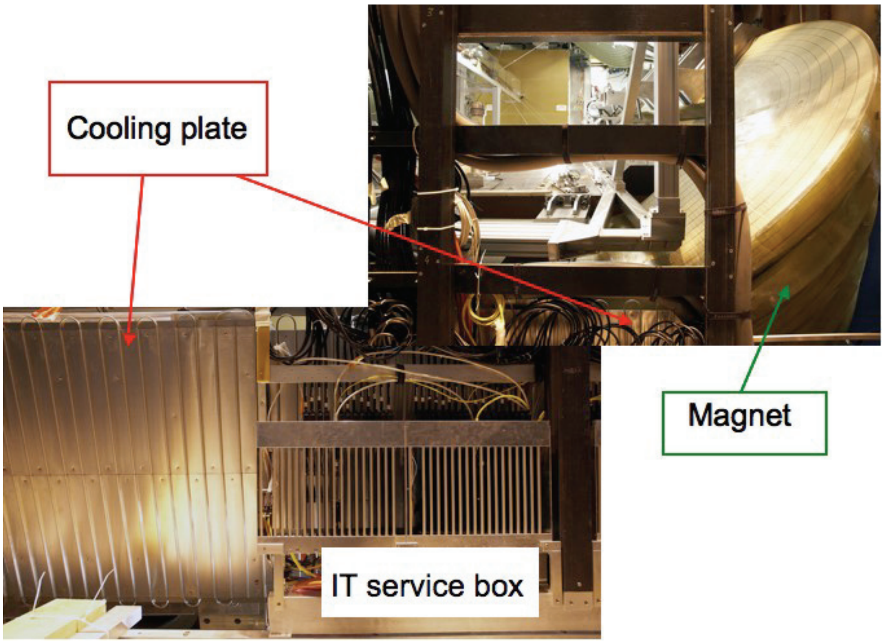

Figure 4.35: Picture of the cooling plate fixed on the magnet coil. It is an aluminium tube sandwiches in two aluminium plates.

4.5 Conclusion of the cooling tests

The cooling tests show that with an external air temperature of 22°C, the cooling ability of our detector is sufficient. The expected temperature on the hottest sensor after ten years of operation is 7°C, while the critical temperature above which thermal run-away might occur is estimated to be above 10°C. The cooling circuit has been leak tested at 2.5 bars. The turbulent flow of the coolant in the cooling rod does not create unacceptable vibration. The shape of the cooling rod seems to have an influence on the temperatures of the ladders and sensors. The temperature profile along the cooling rods indicates that the gluing of the cooling pipe is a delicate operation. New gluing procedures are being defined. The air temperature in the box is higher than on the surface of the Si sensors, indicating that conductive cooling through the high conductive CF-carbon fibre seems to contribute to the cooling of the silicon sensors. The calculations of the heat transfer coefficient of the box has large measurement uncertainties, but it allows to assert that the cooling capacitance of the Inner Tracker have to be improved if the outside temperature rises to 30°C. Fortunately, the solution of the active cooling of the magnet resolves this problem.

The detectors are now installed in the pit and is running in summer 2008. The first cooling tests indicate that the cooling is working well. The measurements have been taken when the Beetle chips[11] are running, with non-irradiated sensors and with a nitrogen flow at 25 l/hour. They show that the temperature in the side boxes is lower (-5° C to 0° C) than in our measurements.

---

[11] The Beetle chips were non triggered for this test.

Part III

Analysis

Chapter 5

$B_d^0 \rightarrow J/\psi K_s^0$ events selection

In this chapter, we present the analysis of the decay channel $B_d^0 \rightarrow J/\psi K_s^0$ using the full LHCb simulation and having in mind that a B/S ratio at the percent level has to be achieved on the B_d^0 selection. Indeed, analyses of $B_d^0 \rightarrow J/\psi K_s^0$ decays have been made in LHCb [98], [99]. In [99] the B/S ratio was estimated to be 0.63 ± 0.06 in a mass window of $\pm 60\,\mathrm{MeV/c^2}$ around the nominal B_d^0 mass. In this estimation, the authors took into account all types of pion tracks (Long, Downstream and Upstream together) and used DC04 samples. This result shows the great difficulty to reach the percent level for the B/S ratio. A mass resolution of the order or better than $10\,\mathrm{MeV/c^2}$ must also be obtained to allow the separation of the B_d^0 and the B_s^0. The mass resolution which has been achieved in [98] and [99] were $8.9\,\mathrm{MeV/c^2}$ and $8\,\mathrm{MeV/c^2}$ respectively.

In this chapter, we first describe the pre-selection, then we will present the tuning of the final selection. The different resolutions as well as the background level will be discussed. Finally, the expected rates will be calculated once the efficiencies and acceptances are determined.

5.1 Pre-selection studies of $B_d^0 \rightarrow J/\psi K_s^0$

After a year of running at nominal luminosity, the number of recorded p-p events will be around 20×10^{10}. Out of this number, only 17'340 $B_s^0 \rightarrow J/\psi(\mu^+\mu^-)K_s^0(\pi^+\pi^-)$ will be produced in LHCb prior to any selection. A very tight selection is therefore required to eliminate the unwanted events from the selected sample. For the optimization of the selection, we will use the full Monte Carlo simulation (DC06) and DaVinci v19r11. The pre-selection is done in two steps:

- In the first one, the aim is to reduce the huge amount of possible combinations giving a mass in a given window around the B_d^0 mass. A set of loose cuts is applied and the decay channel is reconstructed (section 5.1.1).

- In a second step, the pre-selection of the J/ψ and the K_s^0 is improved to reach a B/S ratio as small as possible (section 5.1.2).

5.1.1 Loose pre-selection

The reconstruction of $B_d^0 \to J/\psi K_s^0$ is performed in three steps:

1. Search for the muon candidates for the J/ψ reconstruction.
2. If a J/ψ is found, reconstruction of the K_s^0 from two pions.
3. Combination of the J/ψ and of the K_s^0 candidates to reconstruct a B_d^0.

Particle Identification

We start with the selection of a track in an event by assigning to it a particle identification (PID) depending upon the information delivered by the subdetectors traversed by this track. The PID is used in offline selection through the likelihood hypothesis which combines the information of the detectors:

$$\begin{aligned}
\mathcal{L}(e) &= \mathcal{L}^{\mathrm{RICH}}(e)\mathcal{L}^{\mathrm{CALO}}(e)\mathcal{L}^{\mathrm{MUON}}(\text{non } \mu) \\
\mathcal{L}(\mu) &= \mathcal{L}^{\mathrm{RICH}}(\mu)\mathcal{L}^{\mathrm{CALO}}(\text{non } e)\mathcal{L}^{\mathrm{MUON}}(\mu) \\
\mathcal{L}(h) &= \mathcal{L}^{\mathrm{RICH}}(h)\mathcal{L}^{\mathrm{CALO}}(\text{non } e)\mathcal{L}^{\mathrm{MUON}}(\text{non } \mu)
\end{aligned}$$

In this above expression, e represents an electron, μ a muon and h a charged pion or kaon. The RICH dectectors allow to distinguish between hadrons (π, K, or p). The ECAL and HCAL give the probability for a track to be an electron, a photon or a hadron. Finally, the muon PID is assigned by the muon system. The PID information for a charged particle of type "A" is expressed as a likelihood ratio between the given PID hypothesis and the π hypothesis:

$$\Delta \ln \mathcal{L}_{A\pi} = \ln \mathcal{L}(A) - \ln \mathcal{L}(\pi) = \ln \left[\frac{\mathcal{L}(A)}{\mathcal{L}(\pi)} \right], \tag{5.1}$$

where $\mathcal{L}(A)$ is the combined likelihood assuming the particle is of type "A". The Delta Log Likelihood (DLL), $\Delta \ln \mathcal{L}_{A\pi}$, tends to be positive for correctly identified "A" particles. As the DLL is defined with respect to the π hypothesis, we can obtain the DLL between two hypothesis A or B:

$$\Delta \ln \mathcal{L}_{AB} = \ln \mathcal{L}(A\pi) - \ln \mathcal{L}(B\pi). \tag{5.2}$$

The neutral particles, π^0 and γ, are treated differently. Photons are identified as neutral clusters in the ECAL. For photons which have converted in the material behind the magnet, one looks for a hit on the SPD cell in front of the initial cell of the ECAL cluster. π^0 are reconstructed from two photons. At low energy (less than 3 GeV/c), they are mostly from two "resolved" photons, whereas at high momentum, the granularity of the ECAL does not allow in general to separate the two γ: in this case, they are seen as a single cluster, called "merged" π^0. Electrons which have radiated before the magnet show a characteristic signature with a row of ECAL clusters ending at the electron impact.

Loose pre-selection cuts

J/ψ reconstruction

To reconstruct the $J/\psi \to \mu^+\mu^-$ decay, two long muon tracks (using "StdLooseMuons" standard particles) are chosen with a $\Delta \ln \mathcal{L}_{\mu\pi} > -1$ and $p_T(\mu^{\pm}) > 500\,\mathrm{MeV/c}$ [94]. This p_T cut is mainly intended to reduce the combinatorics at an early stage of the analysis. It will not introduce any bias in the J/ψ angular distribution and will enhance B events over prompt and non-B events particles. Pairs of muons with opposite charge are required to come from a common vertex for which the reconstruction gives a χ^2 per number of degree of freedom ($Ndof$) less than 15, which is a very loose cut. The $\mu^+\mu^-$ pair mass must be within $\pm 400\,\mathrm{MeV/c^2}$ of the nominal J/ψ mass.

K_s^0 reconstruction

For the first studies, only long tracks (using "StdLoosePions" standard particles) are used to reconstruct $K_s^0 \to \pi^+\pi^-$, as the downstream tracks have a worse momentum resolution than the long tracks. Pions are selected with a momentum greater than 2 GeV/c and the quality of the tracks is ensured by a χ^2 per degree of freedom less than 20. Pairs of pions with opposite charge are allowed to come from a common vertex with $\chi^2/Ndof < 20$. Having asked for long-long tracks, the vertex position of the K_s^0 is restricted to the VELO region. The mass of the pions pair must be within $\pm 200\,\mathrm{MeV/c^2}$ of the true K_s^0 mass to be accepted in the pre-selection.

B_d^0 reconstruction

The pre-selection ends with the combination of the reconstructed J/ψ and K_s^0 particles into a B_d^0 candidate. A common vertex between these two reconstructed particles is required with a $\chi^2/Ndof$ less than 50. The mass window is chosen to be very loose, $\delta m_{B_d^0} = \pm 500\,\mathrm{MeV/c^2}$ around the true B_d^0 mass, to allow the study of the background (section 5.6).

The loose pre-selection is summarized in table 5.1. The mass distribution of the J/ψ (Fig. 5.1) shows that the J/ψ signal is already quite clean at this stage of the pre-selection. The prompt J/ψ pollution background will be easily removed in the next step. The K_s^0 mass peak is visible (Fig. 5.1) but the background is very high. In order to obtain a good K_s^0 mass resolution, a tighter selection of the pions is required. Fig. 5.2

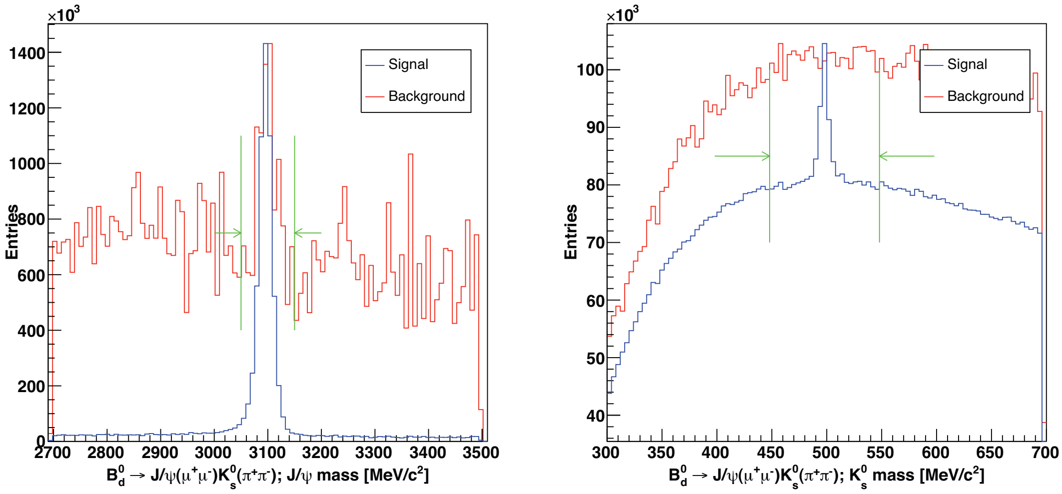

Figure 5.1: Mass distribution of the reconstructed J/ψ (left) and K_s^0 (right) after the pre-selection cuts. The associated signal is in blue and the $b\bar{b}$ inclusive background in red. The mass cuts are shown by the green line.

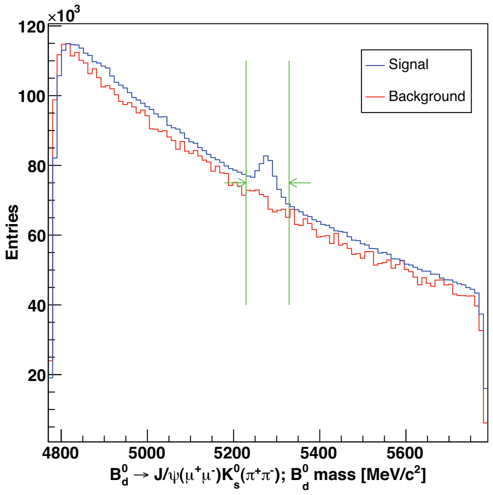

Figure 5.2: Mass distribution of the reconstructed of B_d^0 after the pre-selection cuts. The associated signal is in blue and the $b\bar{b}$ inclusive background in red. The mass cuts are shown by the green line.

shows the distribution of the reconstructed B_d^0 mass after the loose pre-selection. Here too, a deep investigation to find the appropriate cuts is necessary.

Loose pre-selection cuts	**LL-tracks**
muons	StdLooseMuons
J/ψ mass window	$\pm 400\,\mathrm{MeV/c^2}$
$\chi^2/Ndof$ vertex J/ψ	< 15
DLL(μ/π)	> -1
$\mathrm{p}_T(\mu^\pm)$	$> 500\,\mathrm{MeV/c}$
pions	StdLoosePions
track quality $\chi^2/Ndof$	< 20
$p_{\pi^\pm}$	$> 2\,\mathrm{GeV/c}$
K_s^0 mass window	$\pm 200\,\mathrm{MeV/c^2}$
$\chi^2/Ndof$ vertex K_s^0	< 20
B_d^0 mass window	$\pm 500\,\mathrm{MeV/c^2}$
$\chi^2/Ndof$ vertex B_d^0	< 50

Table 5.1: Loose pre-selection cuts used for $B_d^0 \to J/\psi(\mu^+\mu^-)K_s^0(\pi^+\pi^-)$ decay.

5.1.2 Pre-selection, second step

In this second stage of pre-selection, we refine our selection to obtain a cleaner sample of $B_d^0 \to J/\psi K_s^0$ events on which we can optimize the final cuts in order to reach the desired B/S ratio.

The aim of the selection is therefore:

1. reduce the fraction of prompt J/ψ,
2. search for an efficient set of cuts for K_s^0. We will start here with the "standard" DC06 cuts proposed by G. Lanfranchi [95].

At this stage, the B_d^0 vertex is reconstructed with a fit whose $\chi^2/Ndof$ is less than 20 and a mass window of $\pm 200\,\mathrm{MeV/c^2}$ around its nominal mass is considered.

Fine tuning the cuts for the J/ψ and K_s^0

A cut is applied on the χ^2 of the reconstructed vertex: $\chi^2/Ndof < 6$ (Fig. 5.3). This cut is intended to reduce random combination of muons. Finally, the J/ψ is accepted in a mass window of $\pm 50\,\mathrm{MeV/c^2}$ around its nominal value.

To eliminate the prompt J/ψ, the flight distance significance with respect to the primary vertex (FSPV) of the J/ψ is required to be greater than 2 as proposed in the DC06 standard selection of the $J/\psi \to \mu^+\mu^-$ [94]. The FSPV is defined as:

$$FSPV = \frac{\|\overrightarrow{FD}\|}{\sqrt{\sigma_{FD}^2}}$$

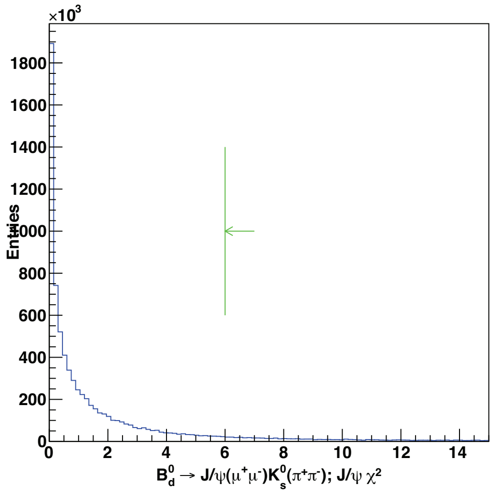

Figure 5.3: $\chi^2/Ndof$ of the vertex fit of the J/ψ after the loose pre-selection. The final cut is shown by the green line.

where $\overrightarrow{FD} = \left(\overrightarrow{Decay\quad Vertex} - \overrightarrow{Primary\quad Vertex}\right)$ is the vector from the primary vertex to the B^0_d decay vertex and σ_{FD} is the error computed for the measurement of FD; this error is mainly due to the spatial resolution of the apparatus, particularly the VELO.

To optimize the selection of the K^0_s, we started with the standard selection and finally ended-up with the "tight selection" proposed for $K^0_s \to \pi^+\pi^-$ in [95]:

- A selection on the quality of the two pion tracks which remains at $\chi^2/Ndof < 20$. An investigation on this cut has been done in [95] and has shown that a tighter cut deteriorates significantly the efficiency of the selection. Keeping the cut $\chi^2/Ndof < 20$ is the best compromise between efficiency and resolution.

  Pions coming from a B are energetic, and their momentum is on average higher than the one of prompt π from the primary vertex (PV). Therefore, a cut on the pion momentum $p(\pi^\pm) > 3\,\mathrm{GeV/c}$ (Fig. 5.4) can be effective. To reduce more drastically the number of K^0_s candidates formed from pions originating from the PV, the impact parameter significance[1] (IPS) with respect to the primary vertex is required to be greater than 10 (Fig. 5.4).

- The K^0_s vertex is reconstructed with a fit whose $\chi^2/Ndof$ is less than 5 (Fig. 5.5). The K^0_s is accepted in a mass window of $\pm 50\,\mathrm{MeV/c^2}$ around its nominal mass to reduce the random combinations of pions. To eliminate the prompt K^0_s, the z

---

[1] The Impact Parameter of a track with respect to a point is the significance of the shortest distance of the point to the track. The impact parameter significance is the ratio of the IP value to its error.

position of the vertex must be higher than 0 mm (Fig. 5.5) and the K_s^0 transverse momentum greater than 300 MeV/c. Indeed, the neutral kaons, coming from a heavy particle like the B_d^0 are expected to have a large p_T.

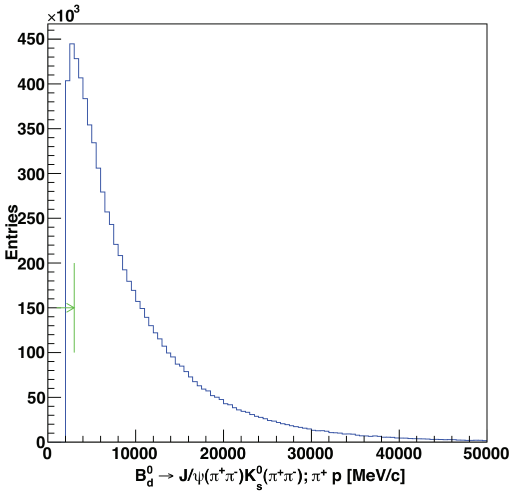

Figure 5.4: Left, momentum of the π^+ in [MeV/c] and right impact parameter significance of the π^+ with respect to the primary vertex after the loose pre-selection. The final cuts are shown by the green line.

At this stage of the pre-selection, 28'148 events of signal are selected out of 1'225'056 generated events. The efficiency of the selection is $\varepsilon_{sel}^{signal} = (2.30 \pm 0.01)\%$ at this point.

Let us now shortly develop the B/S ratio calculation using $b\bar{b}$ inclusive background (section 3.4).

Background over signal studies

The number of $B_d^0 \to J/\psi K_s^0$ events produced in the spectrometer acceptance, reconstructed and selected per year of data taking, is:

$$S = \mathcal{L}_{int}\, \sigma_{b\bar{b}}\, 2\, f_{B_d}\, BR_{vis}\left(B_d \to J/\psi\left(\mu^+\mu^-\right) K_s^0\left(\pi^+\pi^-\right)\right) \varepsilon_{tot}^{signal} \tag{5.3}$$

with :

- $\mathcal{L}_{int} = 2\text{fb}^{-1}$, the integrate luminosity for one year,
- $\sigma_{b\bar{b}} = 500\,\mu$b, the cross section for $b\bar{b}$ production at $\sqrt{s} = 14$ TeV [96],
- $f_{B_d} = 0.398 \pm 0.012$, the $b\bar{b}$ hadronization factor for B_d^0 production given in [96]. The factor 2 in front of f_{B_d} takes into account the possible production of both B^0 and $\overline{B}^0$ mesons from a $b\bar{b}$ pair,

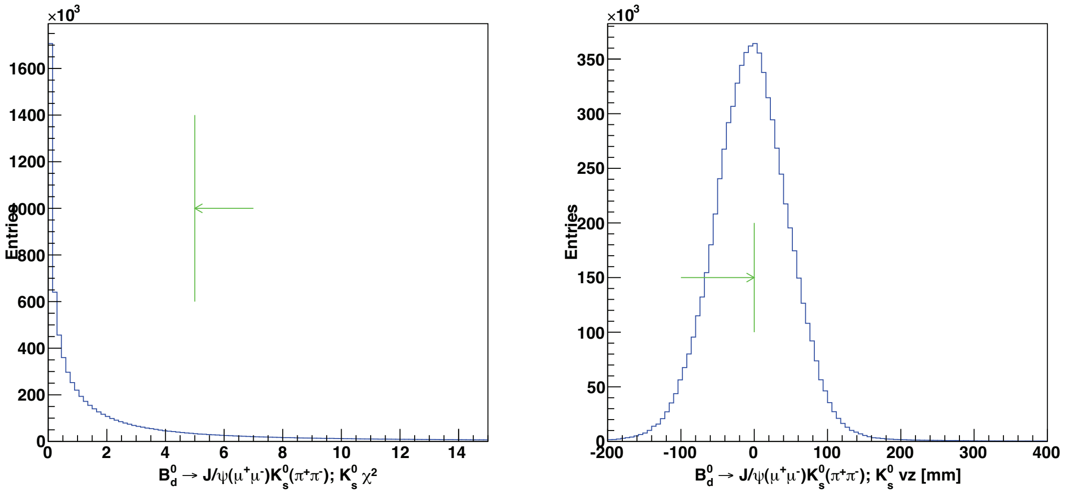

Figure 5.5: Left, $\chi^2/Ndof$ of the vertex fit of the K_s^0 and right, z coordinate of the position of the reconstructed vertex of the K_s^0 in [mm] after the loose pre-selection. The final cuts are shown by the green line.

- $BR_{vis}\left(B_d \to J/\psi\left(\mu^+\mu^-\right)K_s^0\left(\pi^+\pi^-\right)\right) = 17.90 \pm 0.87 \cdot 10^{-6}$, the visible branching ratio given in [15]

The total efficiency of the signal can be written as:

$$\varepsilon_{tot}^{signal} = \varepsilon_{gen}^{signal} \cdot \varepsilon_{sel}^{signal} \cdot \varepsilon_{trig} \tag{5.4}$$

where:

- $\varepsilon_{gen}^{signal} = (20.6 \pm 1.3)\%$ is the generation efficiency of the signal sample in the geometrical acceptance (Section 3.4),
- $\varepsilon_{sel}^{signal} = \dfrac{N_{sel}^{signal}}{N_{gen}^{signal}}$ is the selection cut efficiency with N_{sel}^{signal} the number of selected events over N_{gen}^{signal} the number of generated events,
- ε_{trig} is the trigger efficiency (Section 5.5.1). For the tuning of the cuts we decided to leave aside the trigger efficiency (ε_{trig}) and work only with the selection efficiencies.

For the background estimation, it is worth opening the B_d^0 mass window at maximum, i.e. to $\pm 500\,\mathrm{MeV/c^2}$ around the nominal mass of the B_d^0. The B/S ratio is calculated with the signal yield S (equation 5.3) and the background B using the selected events in the $b\bar{b}$ sample or any other sample in a defined mass window:

$$\frac{B}{S} = \frac{\varepsilon_{gen}^{b\bar{b}} \varepsilon_{sel}^{b\bar{b}}}{2 f_{B_d} \, BR_{vis} \left(B_d \to J/\psi \left(\mu^+ \mu^- \right) K_s^0 \left(\pi^+ \pi^- \right) \right) \epsilon_{gen}^{signal} \epsilon_{sel}^{signal}} \tag{5.5}$$

with :

- $\varepsilon_{gen}^{b\bar{b}} = 43.4 \pm 0.3\%$ is the generation efficiency of the inclusive $b\bar{b}$ sample (Section 3.4),
- $\varepsilon_{sel}^{b\bar{b}} = \dfrac{N_{sel}^{b\bar{b}}}{N_{gen}^{b\bar{b}}}$ is the selection efficiency on the background with $N_{sel}^{b\bar{b}}$ the number of background events that have survived the selection cuts and $N_{gen}^{b\bar{b}}$ the number of generated inclusive $b\bar{b}$ events.

The number of remaining background events in a mass window of $\pm 500\,\mathrm{MeV/c^2}$ around the nominal B_d^0 mass is 58 on 35'120'198 generated $b\bar{b}$ inclusive events. This corresponds to a B/S ratio in a mass window of $\pm 2\sigma$ around the nominal B_d^0 mass (with $\sigma = 17.5\,\mathrm{MeV/c^2}$) of ~ 0.8 (equation 5.5). The B/S ratio must therefore be further improved to reach the percent order.

The strategy is now to optimize the selection of the K_s^0 in order to improve the B/S ratio without significant reduction in efficiency. We will calculate the background over signal ratio starting from the pre-selection cuts described above and varying several specific cuts applied on the K_s^0. We know that the K_s^0 has a large p_T due to the fact that it comes from a heavy particle, and a long lifetime which implies that its decay vertex is far from its production vertex, i.e. the B_d^0 decay vertex. We will first make a cut on the transverse momentum of the K_s^0 at different values between 300 and 2000 MeV/c, and for each value, calculate the B/S ratio in a mass window of $\pm 2\sigma$ around the nominal B_d^0 mass, σ being the B_d^0 mass resolution. After having the best cut for p_T, we apply the same procedure for the minimum flight distance of the K_s^0, varying it between 0 and 20 mm.

Figure 5.6 shows the calculation of the B/S ratio for different values of the p_T cuts. All the standard cuts described above have been applied and only the cut on the K_s^0 p_T varies. The inflection point is reached when the p_T of the K_s^0 is 1300 MeV/c. For this value, the number of remaining background events in a $\pm 500\,\mathrm{MeV/c^2}$ mass window drops to 12 : 79% of the background has been eliminated by this cut. The signal efficiency decrease to $\varepsilon_{sel}^{signal} = (1.60 \pm 0.01)\%$, which corresponds to a loss of 30%. The B/S with the above mentioned pre-selection and a K_s^0 p_T higher than 1300 MeV/c is ~ 0.23.

After fixing the value of the K_s^0 p_T cut to 1300 MeV/c, we removed those K_s^0 decaying too close to the primary vertex. The B/S ratio is calculated using the set of cuts detailed above with different values of the minimum of flight distance (FD) cut between 0 and 20 mm (figure 5.7). B/S decreases a little until the lower limit of FD fixed at 2 mm, then

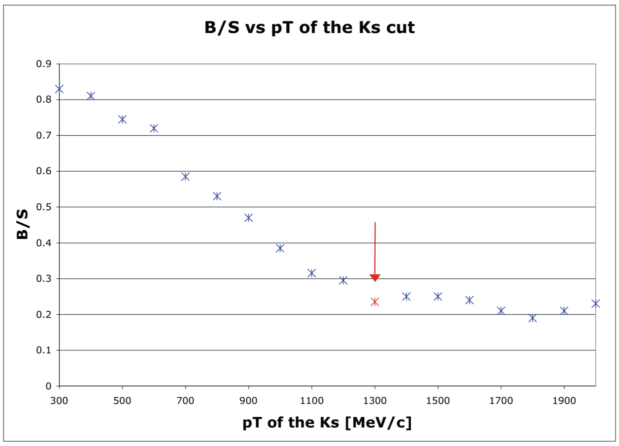

Figure 5.6: B/S ratio versus the transverse momentum cut of the K_s^0 in [MeV/c].

plateaus. At this value, the number of remaining background events decreases from 12 to 9, which represents an improvement of 25% in the elimination of the background. The efficiency is not affected by this cuts and stays at $\varepsilon_{sel}^{signal} = (1.60 \pm 0.01)\%$ and the B/S ratio now drops to ~ 0.19.

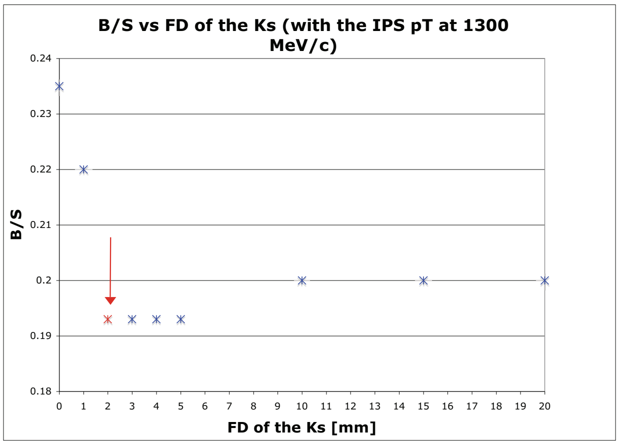

Figure 5.7: B/S ratio versus minimum flight distance cut of the K_s^0 in [mm].

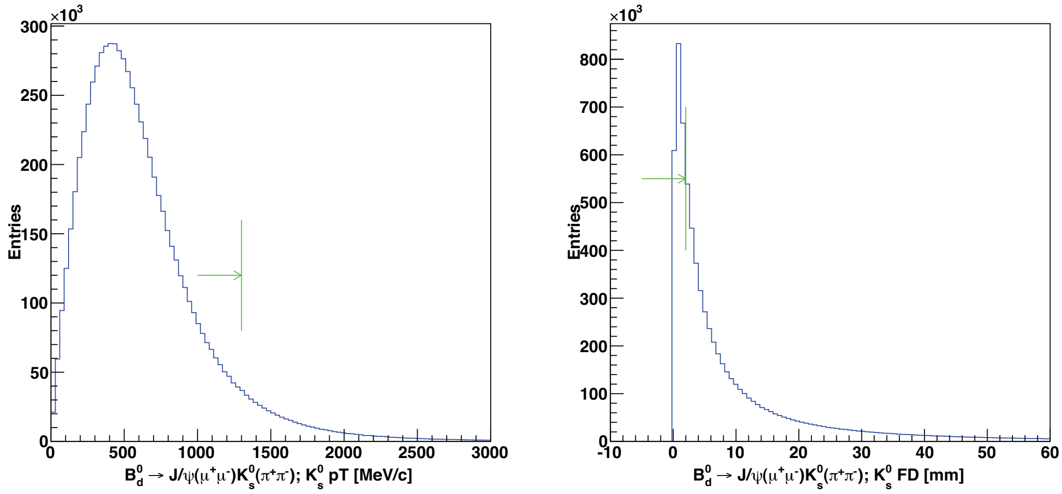

Figure 5.8: Transverse momentum of the K_s^0 in [MeV/c] (left) and flight distance with respect to the primary vertex of the K_s^0 in [mm] (right) after the loose pre-selection. The final cuts are shown by the green line.

Conclusion of the pre-selection

The pre-selection is presented in table 5.2 and its results are given in table 5.3, for the canditates, the events and the associated events. The nomenclature is explained hereafter. Several B_d^0 candidates can be reconstructed in a single event if a "fake particle" passes all the selection cuts. A reconstructed event is called "associated" if it can be associated to a signal event in the MC Truth. The three "associated background events in the wide mass window are three events for which the particles satisfy the MC Truth. They are indeed $B_d^0 \to J/\psi K_s^0$ events and, therefore, will not be considered as "background" in the following.

On Fig 5.9, the reconstructed mass of the B_d^0 is fitted with a single Gaussian, which does not reproduce well the mass distribution but gives an idea of the resolution at this stage of the analysis: $\sigma_{m_{B_d^0}} = (17.09 \pm 0.11)\,\mathrm{MeV/c^2}$. The mean value is $\mu_{m_{B_d^0}} = (5277.5 \pm 0.1)\,\mathrm{MeV/c^2}$, and is biased from the nominal B_d^0 mass by $1.5\,\mathrm{MeV/c^2}$. These results are of course not acceptable for a study of $B_s^0 \to J/\psi K_s^0$ as already mentioned in section 1.6.2.

Pre-selection cuts	**LL-tracks**
muons	StdLooseMuons
J/ψ mass window	$\pm 50\,\mathrm{MeV/c^2}$
χ^2 vertex J/ψ	< 6
DLL(μ/π)	> -1
$\mathrm{p}_T(\mu^\pm)$	$> 500\,\mathrm{MeV/c}$
FSPV of the J/ψ	> 2
pions	StdLoosePions
track quality χ^2/dof	< 20
$p_{\pi^\pm}$	$> 3\,\mathrm{GeV/c}$
IPS$_{\pi^\pm}$ wrt PV	> 10
K_s^0 mass window	$\pm 50\,\mathrm{MeV/c^2}$
χ^2 vertex K_s^0	< 5
z vertex position of K_s^0	$> 0\,\mathrm{mm}$
$\mathrm{p}_T(K_s^0)$	$> 1300\,\mathrm{MeV/c}$
FD of the K_s^0	$> 2\,\mathrm{mm}$
B_d^0 mass window	$\pm 200\,\mathrm{MeV/c^2}$
χ^2 vertex B_d^0	< 20

Table 5.2: Pre-selection cuts used for $B_d^0 \to J/\psi(\mu^+\mu^-)K_s^0(\pi^+\pi^-)$ decay.

Pre-selection	$N_{sel}^{signal}(\pm 200\,\mathrm{MeV/c^2})$	$N_{sel}^{b\_incl}(\pm 500\,\mathrm{MeV/c^2})$
Generated	1'225'056	35'120'198
Candidates	20'560	13
Events	19'623	12
Ass. events	11'445	3
Non ass. events	8'178	9

Table 5.3: Pre-selection results

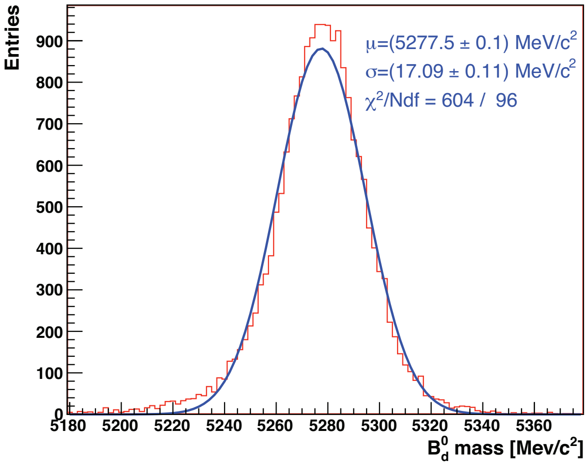

Figure 5.9: Reconstructed mass of the B_d^0 after the pre-selection cuts using the signal sample DC06-stripping-v31. A single Gaussian fit do not reproduce well the mass distribution, nor does it for the peak position.

5.2 Fine selection of the B_d^0

To improve the B/S ratio, we first have to decrease the B_d^0 mass resolution to less than $10\,\mathrm{MeV/c^2}$ as stressed in section 1.6.2.

5.2.1 Improving the B_d^0 mass resolution

To improve the mass resolution, we have performed a new vertex fit constraining J/ψ and K_s^0 masses to their true values [2]. The mass is maintained fixed; this implies that the four momentum of the daughter particles ($\mu^\pm$ for J/ψ and $\pi^\pm$ for K_s^0) are modified. The obtained B_d^0 mass resolution after the B_d^0 daughter masses constrained fit is adjusted with a single Gaussian in Fig. 5.10. The sigma value of the Gaussian is $\sigma_{m_{B_d^0}} = (8.08 \pm 0.06)\,\mathrm{MeV/c^2}$, i.e. an improvement by a factor 2 compared to the previous results (Fig 5.9). The mean value of the mass is now well centered around the true B_d^0 mass.

The number of signal and background ($b\bar{b}$) events passing the pre-selection cuts and the mass constrained fit are given in table 5.4. The signal efficiency $\varepsilon_{sel}^{signal} = 18'548/1'151'051 = (1.61 \pm 0.01)\%$ is not affected. The number of non associated background events increases a little, from 9/35'120'198 to 14/35'586'759, due to statistical effects, but these events

---

[2] The true value corresponds to the Monte Carlo Truth value, i.e. the value used for the generation of the particles.

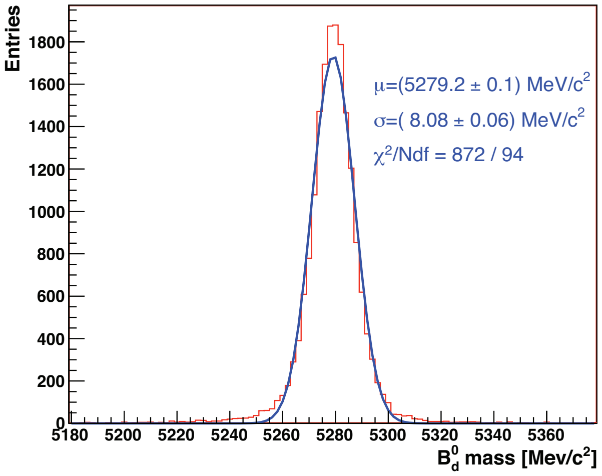

Figure 5.10: Reconstructed mass of the B_d^0 after the pre-selection cuts using the mass constrained fitter. A single Gaussian fit show that the mass resolution is improved by a factor 2 compare to Fig 5.9.

will be removed by the B_d^0 cuts. The B/S value in a $\pm 2\sigma$ mass window around the nominal B_d^0 mass with $\sigma_{m_{B_d^0}} = 8.08\,\mathrm{MeV/c^2}$ is now ~ 0.13.

Pre-selection	$N_{sel}^{signal}(\pm 200\,\mathrm{MeV/c^2})$	$N_{sel}^{b\bar{b}}(\pm 500\,\mathrm{MeV/c^2})$
Generated	1’151’051	35’586’759
Candidates	19’505	18
Events	18’548	17
Ass. events	10’888	3
Non ass. events	7’660	14

Table 5.4: Results of the pre-selection with mass constrained fit. The mass window of the signal selection is left at $\pm 200\,\mathrm{MeV/c^2}$ around the B_d^0 nominal mass. The 3 remaining ”associated events” from $b\bar{b}$ are actually $B_d^0 \to J/\psi K_s^0$ events.

5.2.2 Fine tuning the cuts on B_d^0

The large boost in the LHCb experiment forces the B-mesons to have a large momentum in the z-direction and a measurable flight path before decaying into their final states. The reconstructed B_d^0 is supposed to point to the primary vertex: this implies that the impact parameter significance (IPS) with respect to the PV of the B_d^0 can be required to be small (Fig. 5.11). For the final selection the mass window of the selected B_d^0 is $\pm 50\,\mathrm{MeV/c^2}$ around the true B_d^0 mass. The $\chi^2/Ndof = 20$ cut on the B_d^0 vertex fit is not modified as it has no significant influence on the background supression. As stated above, the $b\bar{b}$ background considered here excludes the "associated events" the number of which is 3 (Table 5.4) after the preselection.

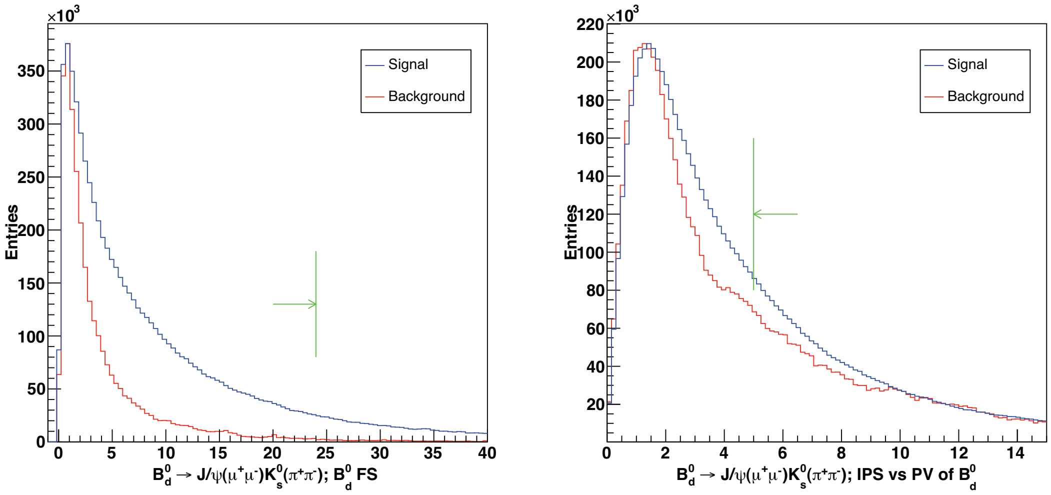

Figure 5.11: Left, the flight distance significance with respect to the primary vertex of the B_d^0 and right, the impact parameter significance with respect to the primary vertex FSPV of the B_d^0 after the loose pre-selection. The associated signal is in blue and the $b\bar{b}$ inclusive background is in red (normalized at thier maximum values). The final cuts are shown by the green line.

The first cut we will explore for the B_d^0 selection will be the lower limit of the flight distance significance with respect to the primary vertex (FSPV), and the second will be the IPS upper limit. The figure 5.11 shows the flight distance significance of the B_d^0 and its IPS after having applied the loose pre-selection (table 5.1) on the signal and $b\bar{b}$ inclusive background. The choice of the value of the minimum flight distance significance (FSPV) will be determined by a compromise between a low B/S ratio and high signal efficiency. The IPS of the B_d^0 has to be limited with a maximum value. The study of this cut will be done once the most efficient cut on the FSPV is found. Here again, the B/S ratio is calculated for each set of cuts (equation 5.5).

When the number of remaining background events is very small (less than 10), we use the unified approach of Feldman and Cousins [97], which gives the unified confidence interval $[\nu_1, \nu_2]$ for a mean of a Poisson variable given n observed events, for different confidence level values. Assuming that the $b\bar{b}$ background is uniformly distributed in an enlarged mass window, we simply multiply the 90% confidence level interval content by the ratio of the two mass windows widths (i.e. $\pm 2\sigma$ interval of the B_d^0 mass over

±500 MeV/c^2).

Table 5.5 presents the results of the calculation of the B/S ratio using the pre-selection cuts (table 5.2), the mass constrained fit and a signal mass window of ±50 MeV/c^2 around the true B_d^0 mass with different lower FSPV limits of the B_d^0. This cut is very powerful: at FSPV> 24, the number of remaining backgrounds events drops from 14 to 2, which represents an elimination of the background of 86%. The signal looses 38% of its efficiency that drops from 1.58% to 0.97%. But this sacrifice leads to a B/S ratio between 0.008 and 0.089 at 90% of confidence. At this stage, we have reached the percent level for our B/S ratio, but the upper limit of this ratio is still too high. To remove the 2 last remaining background events, we added a cut on the upper limit of the IPS of the B_d^0.

FSPV lower cut	B/S min	B/S max	$N_{sel}^{b\bar{b}}$(±500 MeV/c^2)	$\varepsilon_{sel}^{signal}$(±50 MeV/c^2)
no cut	0.072	0.186	14	1.58 ± 0.01
5	0.053	0.160	10	1.50 ± 0.01
10	0.039	0.136	7	1.34 ± 0.01
15	0.018	0.105	4	1.19 ± 0.01
20	0.020	0.118	4	1.06 ± 0.01
24	0.008	0.089	2	0.97 ± 0.01
25	0.008	0.091	2	0.94 ± 0.01
30	0.002	0.074	1	0.85 ± 0.01

Table 5.5: Results of the calculation of the B/S ratios using different values of flight distance significance (FSPV) lower limit of the B_d^0. The background events are those which are not associated to a MC signal events.

The calculation of the B/S ratio, using the same cuts as in the optimization of the FSPV minimum and keeping the FSPV at FSPV> 24, is presented table 5.6 for various IPS values. If we put the IPS upper limit at 5, no background event survives the selection and the efficiency stays the same (0.96%). The B/S ratio at 90% confidence level is in the range [0, 0.037]. Compared to the results quoted in [99], which was B/S= 0.63 in a mass range of ±60 MeV/c^2, our result presents a gain of a factor 4.5 if we scale the number of events down to a mass range of $\pm 2\sigma = \pm 2 \times 8\,\mathrm{MeV/c^2}$ and if we take worse case B/S= 0.037.

The two goals of the selection are now reached: the B/S ratio is at the percent level and the B_d^0 mass resolution is $\sigma_{m_{B_d^0}} = 8\,\mathrm{MeV/c^2}$, which is sufficient to well separate the B_s^0 and B_d^0 peaks. The final selection is detailed in Table 5.7.

IPS upper cut	B/S min	B/S max	$N_{sel}^{b\bar{b}}(\pm 500\,\mathrm{MeV/c^2})$	$\varepsilon_{sel}^{signal}(\pm 50\,\mathrm{MeV/c^2})$
15	0.008	0.089	2	0.97 ± 0.01
10	0.002	0.066	1	0.97 ± 0.01
7	0.002	0.066	1	0.97 ± 0.01
5	0	0.037	0	0.96 ± 0.01

Table 5.6: Results of the calculation of the B/S ratios using different values of impact parameter significance upper limit of the B_d^0. The background events are those which are not associated to a MC signal events.

Selection cuts	**LL-tracks**
muons	StdLooseMuons
J/ψ mass window	$\pm 50\,\mathrm{MeV/c^2}$
χ^2 vertex J/ψ	< 6
DLL(μ/π)	> -1
$\mathrm{p}_T(\mu^\pm)$	$> 500\,\mathrm{MeV/c}$
FSPV of the J/ψ	> 2
mass constrained fit	
pions	StdLoosePions
track quality χ^2/dof	< 20
$p_{\pi^\pm}$	$> 3\,\mathrm{GeV/c}$
IPS$_{\pi^\pm}$ wrt PV	> 10
K_s^0 mass window	$\pm 50\,\mathrm{MeV/c^2}$
χ^2 vertex K_s^0	< 5
z vertex position of K_s^0	$> 0\,\mathrm{mm}$
$\mathrm{p}_T(K_s^0)$	$> 1300\,\mathrm{MeV/c}$
FD of the K_s^0	$> 2\,\mathrm{mm}$
mass constrained fit	
B_d^0 mass window	$\pm 50\,\mathrm{MeV/c^2}$
χ^2 vertex B_d^0	< 20
FSPV of the B_d^0	> 24
IPS$_{B_d^0}$ wrt PV	< 5

Table 5.7: Selection cuts used for $B_d^0 \to J/\psi(\mu^+\mu^-)K_s^0(\pi^+\pi^-)$ decay.

5.3 Final selection results

In this section, we will give the resolutions which are obtained with the MC associated canditates surviving the selection cuts described above. This will give the estimation of the LHCb performances of the reconstruction and analysis algorithms.

5.3.1 Selected events

The selection results are detailed in Table 5.8. The numbers of candidates and events passing the selection differ by about 4%. This means that there are very few multiple candidates per event. The purity, i.e. the number of associated events divided by the number of events is about 60%. For the determination of the resolution, only the associated events are considered. Hence, no $b\bar{b}$ inclusive background event survives after the selection apply on the 35'586'759 $b\bar{b}$ inclusive generated events.

Selection	$N_{sel}^{signal}(\pm 50\,\mathrm{MeV/c^2})$	$N_{sel}^{b\bar{b}}(\pm 500\,\mathrm{MeV/c^2})$
Generated	1'151'051	35'586'759
Candidates	11'600	0
Events	11'064	0
Ass. events	6'658	0
Ass. events (1 cand.)	6'373	0
Non ass. events	4'406	0

Table 5.8: Selection results.

5.3.2 Mass resolutions

We have seen in table 5.8 that more than 95% of associated events have an unique $B_d^0 \to J/\psi K_s^0$ candidate. For an accurate estimation of the mass resolutions, we will only use these 6373 events that are associated to a unique candidate; otherwise, we would have some distortions in the distributions.

The mass spectra of the J/ψ, K_s^0 and B_d^0 are presented in Figures 5.12 and 5.13. The distributions are shown for events passing the selection cuts described above and before any trigger. The J/ψ invariant mass is fitted with single Gaussian. Its mean value $\mu_{m_{J/\psi}} = 3095.4 \pm 0.2\,\mathrm{MeV/c^2}$ is quite close to the generated value and the resolution is $\sigma_{m_{J/\psi}} = 12.66 \pm 0.15\,\mathrm{MeV/c^2}$.

In the case of K_s^0, the resulting width of the mass spectrum is $\sigma_{m_{K_s^0}} = 3.71 \pm 0.05\,\mathrm{MeV/c^2}$, using a single Gaussian fit. Its mean, $\mu_{m_{K_s^0}} = 497.79 \pm 0.05\,\mathrm{MeV/c^2}$, is similar to the generated K_s^0 mass value. The results are compatible with the values quoted in [98], where the resolution for the J/ψ mass is $\sim \sigma_{m_{J/\psi}} = 10\,\mathrm{MeV/c^2}$ and that of K_s^0 mass using Long-Long tracks is $\sigma_{m_{K_s^0}} = 3.6\,\mathrm{MeV/c^2}$.

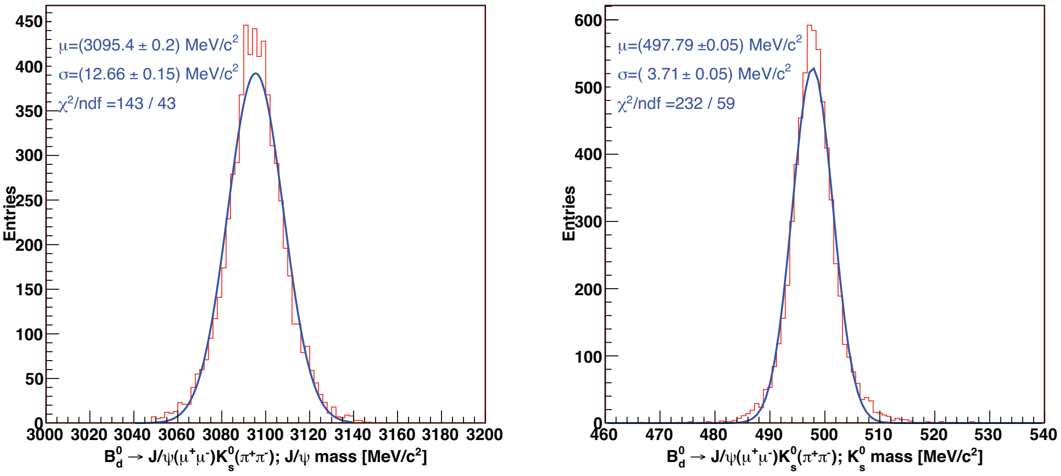

Figure 5.12: Mass distributions for the J/ψ (left) and the K_s^0 (right). The J/ψ mass in the Monte Carlo simulation is $M_{J/\psi} = 3096.916 \pm 0.011\,\mathrm{MeV/c^2}$, and, for the K_s^0, $M_{K_s^0} = 497.648 \pm 0.022\,\mathrm{MeV/c^2}$ as given in the PDG [15]. The mass distributions are fitted with a single Gaussian.

Finally, the reconstructed mass distribution of the B_d^0 is shown on Fig. 5.13. The mean value $\mu_{m_{B_d^0}} = 5279.1 \pm 0.1\,\mathrm{MeV/c^2}$ corresponds to the generate value. A single Gaussian fit gives a resolution of $\sigma_{m_{B_d^0}} = 7.87 \pm 0.09\,\mathrm{MeV/c^2}$ and the double Gaussian fit gives $\sigma_{m_{B_d^0}} = 7.17 \pm 0.14\,\mathrm{MeV/c^2}$ for the core and $\sigma_{m_{B_d^0}} = 17.74 \pm 1.71\,\mathrm{MeV/c^2}$ for the tails. The core Gaussian represents 95.5% of the curve. The results are compatible with the resolution of the mass distribution of $7.7\,\mathrm{MeV/c^2}$ quoted in [99].

To distinguish the B_s^0 from the B_d^0 peak, it is necessary to have a mass resolution of the B_d^0 better than $10\,\mathrm{MeV/c^2}$ for a core Gaussian and a core to tail ratio which is not large. A rapid simulation of these peaks, assuming a B_s^0/B_d^0 ratio of 1/85 shows that the peaks can be separated (Fig. 5.14).

5.3.3 Momentum resolution

The momentum resolution for the B_d^0 candidates is quite important as the momentum enters in the proper time evaluation. Due to the forward boost in LHCb, B_d^0 momentum resolution reflects the resolution on its z component. Fig. 5.15 shows the residuals of the z component of the B_d^0 momentum. The shape of the histogram is due to the fact that

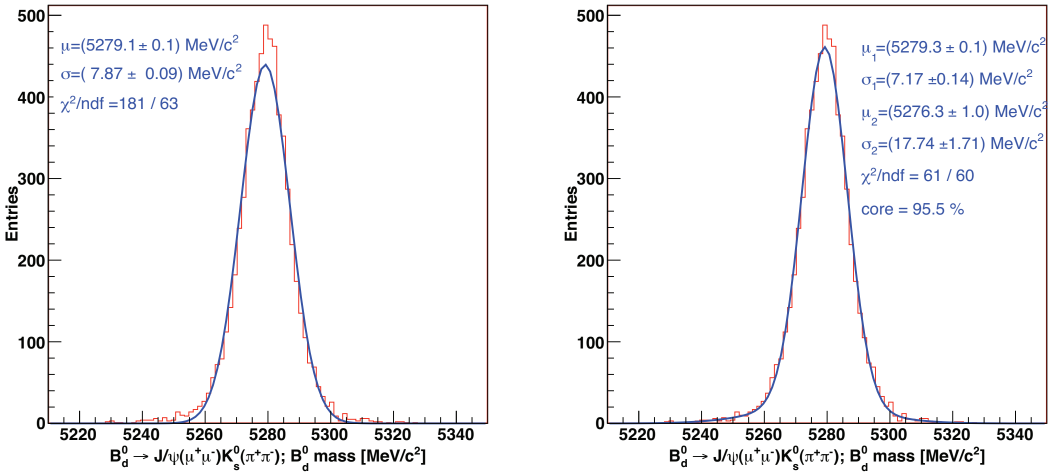

Figure 5.13: Mass distributions for the B_d^0. The mass of the B_d^0 in the Monte Carlo simulations is $M_{B_d^0} = 5279.4 \pm 0.5\,\mathrm{MeV/c^2}$ as given in the PDG [15]. The mass distribution is fitted with a single Gaussian (left) and with a double Gaussian (right).

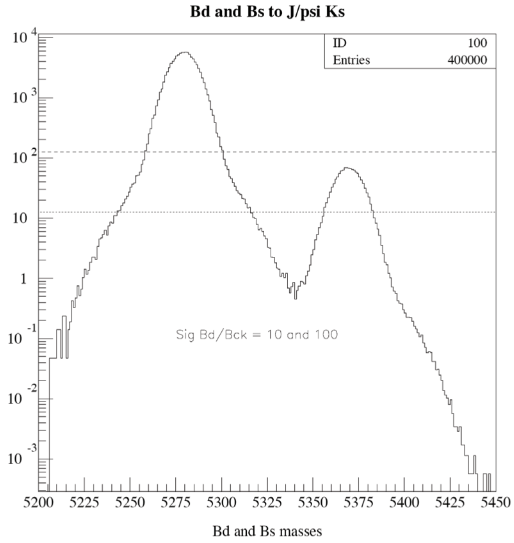

Figure 5.14: Simulation of B_d^0 and B_s^0 mass peaks using a double Gaussian with a resolution of $\sigma_{m_{B_d^0}} = 7.17 \pm 0.14\,\mathrm{MeV/c^2}$ for the core, $\sigma_{m_{B_d^0}} = 17.74 \pm 1.71\,\mathrm{MeV/c^2}$ for the tails, and assuming a B_s^0/B_d^0 ratio of 1/85.

the momentum resolution increases with the daughters particles momenta. The total momentum resolution is also shown on Fig. 5.15: $\sigma(\delta P/P) = (0.218 \pm 0.003)\,\%$, which is quite comparable with previous studies.

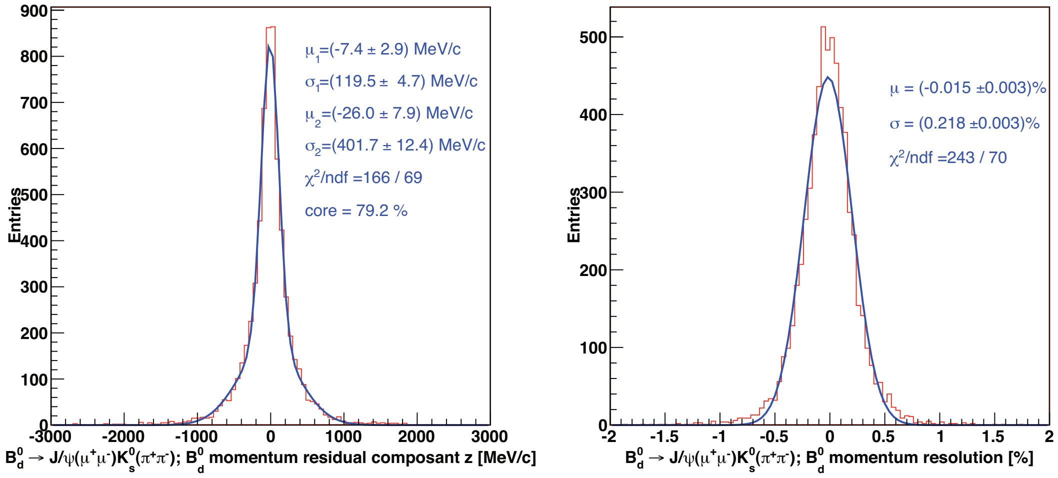

Figure 5.15: Residuals of the z-component of the B_d^0 momenta (left) and momentum resolution of B_d^0 candidates (right).

5.3.4 Vertex resolution

The proper time measurement is obtained using the scalar product of the momentum vector and the flight distance vector of the B_d^0. An accurate vertex resolution is therefore required. Using the MC data sample DC06, the primary vertex resolution was found to be about $59\,\mu$m in the beam direction and 8 and $10\,\mu$m for the x and y axes [100]. The primary vertex is reconstructed prior to our selection and consists of an iterative procedure which excludes the tracks which do not fit to a common point and gives at the end a set of primary vertices.

The primary vertex resolutions and the B_d^0 vertex resolutions are shown on Fig. 5.16, 5.17 and 5.18. The transverse x and y PV resolutions are fitted with double Gaussians and their resolutions are around $9\,\mu$m for the core Gaussian which represents about 96% of the peak area and is in total agreement with the expected values.

The most important source of uncertainties is the secondary vertex determination for which only two tracks and extrapolated K_s^0 track are required. Because of the boost in the beam direction, the worst vertex resolution remains along the beam axis with a core resolution of $\sigma_{v_z} = (125 \pm 5)\,\mu$m and a tail of $\sigma_{v_z} = (337 \pm 10)\,\mu$m. This is to be compared to the primary vertex resolution ($\sigma_z(PV) = (37 \pm 1)\,\mu$m for the core Gaussian). The transversal secondary vertex resolutions are $17\,\mu$m and $16\,\mu$m respectively (Fig. 5.16 and 5.17).

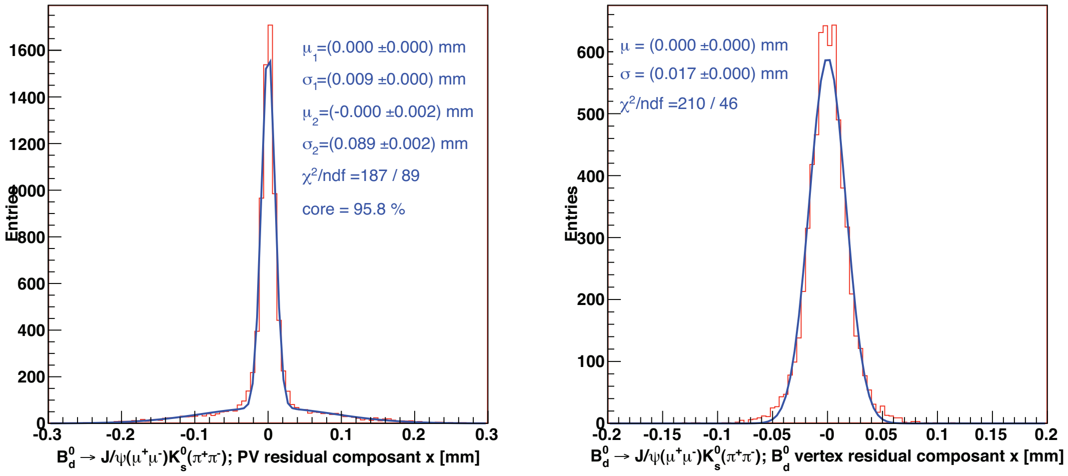

Figure 5.16: x-component position residuals for the reconstructed primary vertex (left) and the B_d^0 decay vertex (right).

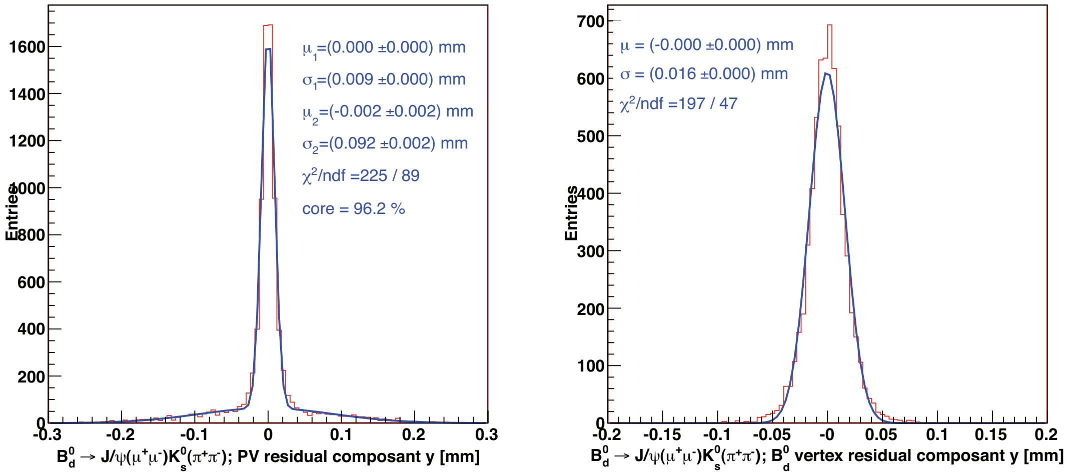

Figure 5.17: y-component position residuals for the reconstructed primary vertex (left) and the B_d^0 decay vertex (right).

5.4 Proper time studies

The proper time of the B_d^0 and its error are very important parameters which will be in the determination of the time dependent CP asymmetry $\mathcal{A}_{CP}(t)$ of the B_s^0 (Chapter 6).

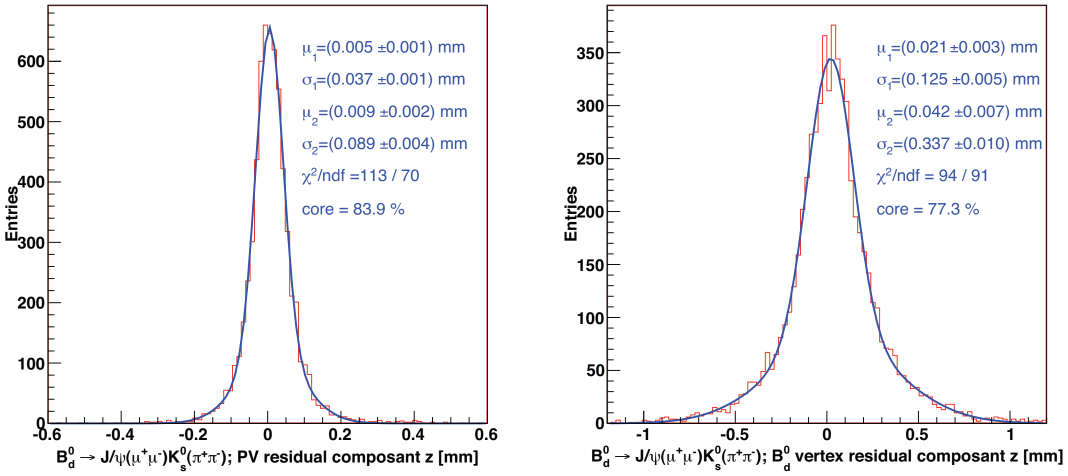

Figure 5.18: z-component position residuals for the reconstructed primary vertex (left) and the B_d^0 decay vertex (right).

The oscillation between the B_s^0 and the $\overline{B}_s^0$ is fast and an excellent proper time resolution is required to access the asymmetry values.
The proper time τ satisfies the relativistic dilatation $\tau = t_{lab}/\gamma$, where t_{lab} is the B meson lifetime in the laboratory and $\gamma = \left(\sqrt{1 - \overrightarrow{\beta}^2}\right)^{-1}$ is the relativistic Lorentz factor for a particle having a speed of $\overrightarrow{\beta} c$. The flight distance of the B meson is given by:

$$\overrightarrow{FD} = \overrightarrow{\beta} c t_{lab} = \overrightarrow{\beta} c \gamma \tau$$

With m the B mass and $\overrightarrow{p} = m \overrightarrow{\beta} c \gamma$ its momentum,

$$\overrightarrow{FD} = \frac{\overrightarrow{p}}{m} \tau \Longleftrightarrow \tau = \frac{\overrightarrow{p} \cdot \overrightarrow{FD}}{|\overrightarrow{p}|^2} \cdot m \tag{5.6}$$

To measure the proper time, we used the $LifeTimeFitter$, which is integrated in DaVinci v19r11. Given a reconstructed particle with its decay vertex, its momentum and its production point, one can determine the propertime τ and its error by a simple χ^2 fit [101]. As we have in total 9 observables (the decay vertex, the momentum and the production vertex) and 7 unknowns (the decay point, the momentum and the proper time) the χ^2 that we obtain must be distributed according to a χ^2 distribution with 2 degrees of freedom, i.e. with its mean equal to 2.

5.4.1 Proper time fit and resolution

The proper time and its error distributions are shown in Fig. 5.19. A decaying exponential fit is applied to the distribution for times $t > 1.2$ ps. The slope of the exponential gives the lifetime $\tau_{rec} = (1.45 \pm 0.02)$ ps, which is compatible to the PDG [15] value $\tau_{B_d^0} = (1.536 \pm 0.014)$ ps.

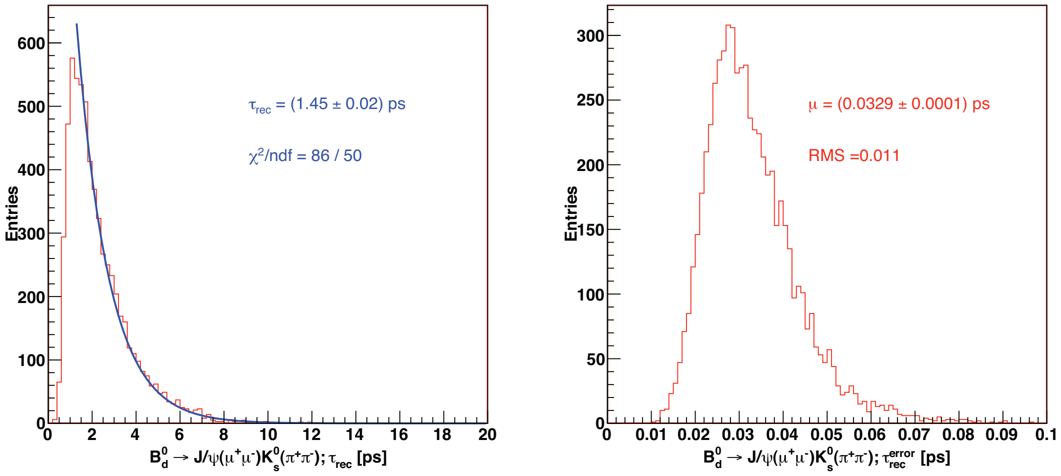

Figure 5.19: Proper time distribution of B_d^0 candidates after selection fitted with an exponential (left) and the proper time errors deduced from the fit of B_d^0 candidates after selection (right).

The error on the proper time determination is deduced from the Least square determination of τ. The spread of the errors might be due to a large spread of kinematical domain of momentum and decay lengths.

The proper time resolution, consisting in the residual of the proper time $\tau_{rec} - \tau_{MC}$, is displayed together with a single Gaussian fit in Fig. 5.20. The width of the single Gaussian is $\sigma_{res}(\tau) = (37.2 \pm 0.4)$ fs and corresponds to the expected proper time resolution for B-decays with only charged tracks. This value is to be compared to the mean of the error distribution $\langle\tau_{err}\rangle = (32.9 \pm 0.1)$ fs : if the latter were correctly estimated, one should have $\langle\tau_{err}\rangle = \sigma_{res}(\tau)$. The difference of 13% can be attributed to an underestimation of the errors, as can be seen in the χ^2 whose mean is 2.91 ± 0.04.

5.4.2 Proper time acceptance

The selection cuts (table 5.7), particularly the flight distance and impact parameter cuts, introduce a bias in the proper time distribution by removing the short lived B_d^0 mesons (Fig. 5.19). Therefore the probability to select the signal events is no longer

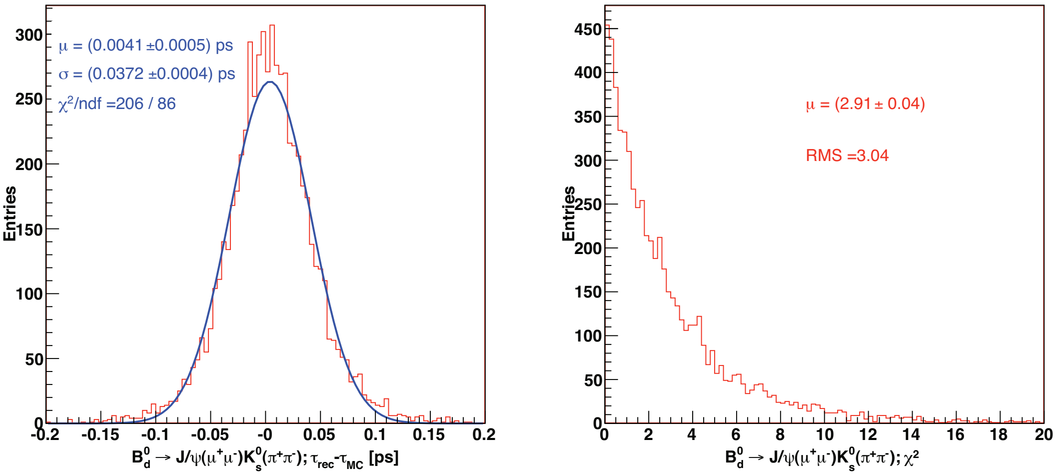

Figure 5.20: Proper time resolution of B_d^0 candidates after selection fitted with a single Gaussian (left) and χ^2 function resulting from the proper time fit (right).

uniform and depends on the proper time value. The acceptance function describes this probability and represents a time-dependent bin-to-bin selection efficiency. To define this acceptance function, the reconstructed proper time τ_{rec} distributions before and after selection are compared. The acceptance function before any trigger, after L0 and after HLT are shown Fig. 5.21 and Fig. 5.22 and can be fitted using a time-dependent efficiency function $\varepsilon_\tau(\tau)$ of the reconstructed proper time τ:

$$\varepsilon_\tau(\tau) = acc_a \cdot \frac{(acc_s \cdot \tau)^3}{1 + (acc_s \cdot \tau)^3} \tag{5.7}$$

where acc_a is a normalization factor and acc_s the slope of the rising part of the function. The results of the fits Fig. 5.21 and Fig. 5.22 are $acc_s = (1.035 \pm 0.011)\,\mathrm{ps}^{-1}$ before any trigger, $acc_s^{L0} = (1.033 \pm 0.020)\,\mathrm{ps}^{-1}$ after L0 and $acc_s^{HLT} = (1.055 \pm 0.023)\,\mathrm{ps}^{-1}$ after HLT. The normalization is arbitrary. The slope is not affected by the L0 trigger. The HLT is not well implemented in DaVinci v11r19, the acceptance function results will therefore not be commented. The resulting slope is 10 times smaller than in [99] ($11.7 \pm 1\,\mathrm{ps}^{-1}$) as the short lifetimes are more strongly removed by our selection. This is explained by the very stringent cuts applied on the flight distance significance and on the impact parameter significance with respect to the primary vertex of the B_d^0.

5.4.3 Proper time pull

The proper time pull distribution, i.e. the residual of the proper time divided by the error of the fit (Fig. 5.19), is shown in Fig. 5.23. The distribution is fitted with a single

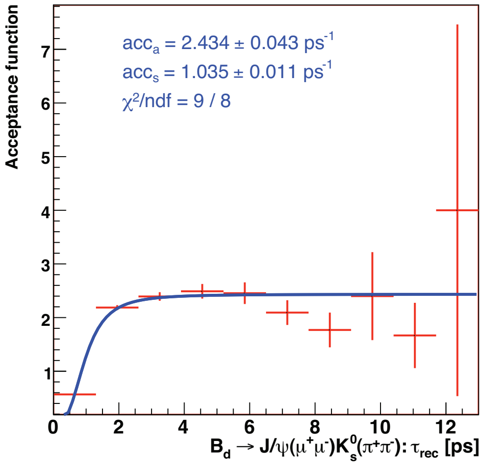

Figure 5.21: Proper time acceptance distribution fitted with the acceptance function after selection cuts.

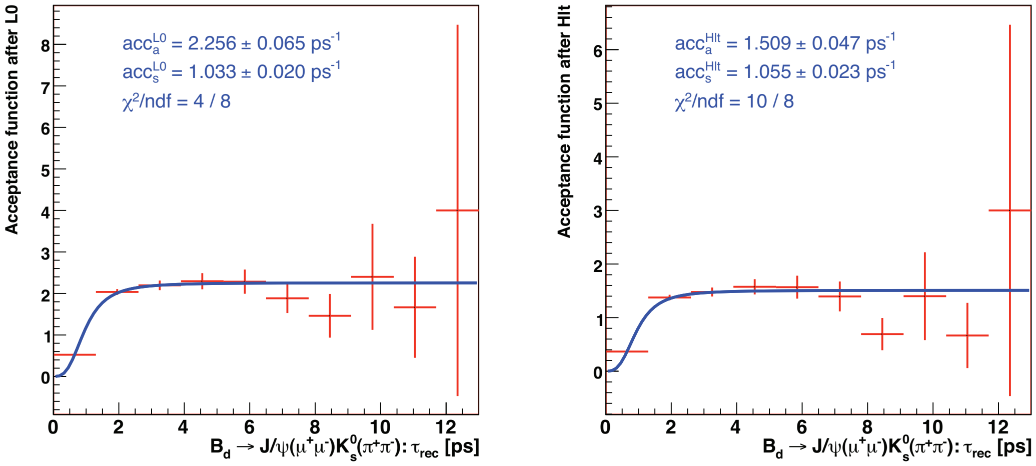

Figure 5.22: Proper time acceptance distribution fitted with the acceptance function after selection cuts and L0 trigger (left) and after HLT trigger (right).

Gaussian and its sigma value is $\sigma_{\tau_{pull}} = 1.177 \pm 0.012$. Again, that means that the errors are somewhat underestimated.

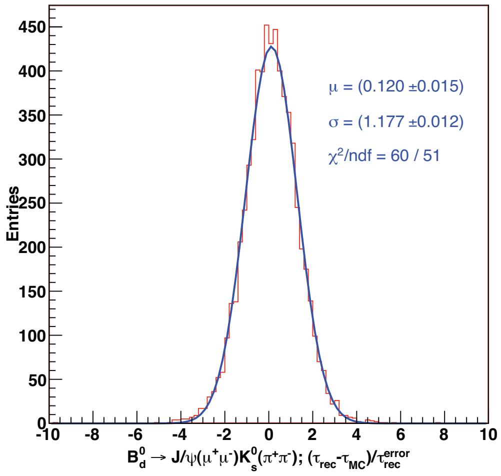

Figure 5.23: Proper time pull distribution of B_d^0 candidates after selection fitted with a single Gaussian.

5.5 Efficiencies and annual signal yields

In this section, we will present the selection efficiencies obtained before and after triggers, show the tagging performances and calculate the signal yield for an integrated luminosity of 2 fb^{-1}. In the last part we will estimate the background-over-signal ratio for different background contributions.

5.5.1 Efficiencies

We recall that the total efficiency ε_{tot} of the selection is composed of different efficiencies:

- $\varepsilon_{gen}^{signal}$, the efficiency of the signal generation in the geometrical acceptance, defined in section 3.4,
- ε_{sel}, the efficiency on the off-line selection corresponding to the number of selected events N_{sel}^{signal} divided by the total number of generated events N_{gen}^{signal} defined in section 3.4,
- and the trigger efficiency $\varepsilon_{trig} = \varepsilon_{L0/sel} \times \varepsilon_{HLT/L0}$, with $\varepsilon_{L0/sel} = N_{L0}/N_{sel}$ corresponding to L0 efficiency on the off-line selected events, and $\varepsilon_{HLT/L0} = N_{HLT}/N_{L0}$ the HLT efficiency on the off-line selected events surviving the L0 trigger.

$$\varepsilon_{tot} = \varepsilon_{gen} \times \varepsilon_{sel} \times \varepsilon_{trig} \tag{5.8}$$

For the signal yield and the background-over-signal ratio calculations, all the selected events, associated to MC or not, are taken into account. With our selection, N_{sel}^{signal} =11'064 and N_{gen}^{signal} =1'151'051 (table 5.8). The total efficiency is then 0.198 ± 0.014% with $\varepsilon_{gen}^{signal} = 20.6 \pm 1.3\%$ and $\varepsilon_{sel}^{signal} = 0.96 \pm 0.01\%$ before any trigger. The errors have been calculated assuming a binomial distribution.

Trigger performances

The trigger contribution is described in table 5.9, and the trigger efficiencies in table 5.10. The HLT efficiency is low and is not fully implemented in the DaVinci v19r11. For the signal yield calculation, we will only take into account the L0 trigger. The total efficiency after L0 trigger becomes $\varepsilon_{tot} = 0.183 \pm 0.004\,\%$.

	N_{sel}	N_{L0}	N_{HLT}
Selected events	11'064	10'240	6'997
Associated events (1 cand.)	6373	5882	4012

Table 5.9: Trigger contribution for our studied decay.

$\varepsilon_{L0/sel}$	$\varepsilon_{HLT/L0}$	ε_{trig}
92.5 ± 0.4	68.3 ± 0.9	63.2 ± 0.7

Table 5.10: Trigger efficiency breakdown for the studied decay.

Tagging performances

The tagging performances for $B_d^0 \to J/\psi K_s^0$ are shown table 5.11. The tagging efficiency ε_{tag} (equation 3.1), the wrong tag fraction ω_{tag} (equation 3.2) and the effective combined tagging efficiency $\varepsilon_{eff} = \varepsilon_{tag}(1-2\omega_{tag})^2$ (equation 3.5) are given before any trigger, after L0 trigger and HLT trigger for the associated candidates using the analysis program. The tagging efficiency is better after the L0 trigger as clean events have been reconstructed and selected, which are therefore easier to tag. For the $B_s^0 \to J/\psi K_s^0$ decay analysis (Chapter 6), we will take the tagging factors obtained after L0.

	before trigger [%]	after L0 [%]	after HLT [%]
ε_{tag}	61.45 ± 0.61	62.07 ± 0.63	63.86 ± 0.76
ω_{tag}	39.30 ± 0.78	39.25 ± 0.81	39.66 ± 0.97
ε_{eff}	2.81 ± 0.78	2.87 ± 0.82	2.73 ± 1.01

Table 5.11: Tagging performances before and after trigger.

These results are similar to the tagging results of the selection of $B_d^0 \to J/\psi K_s^0$ quoted in [102] where the figures are $\omega_{tag} = 39.10 \pm 0.27\%$ and $\varepsilon_{eff} = 2.73 \pm 0.13\%$ after the L0 trigger. The tagging of the B_s^0 for similar decays like $B_s^0 \to J/\psi\eta$ in [104] or $B_s^0 \to J/\psi\eta'$ in [103] is more efficient: $\varepsilon_{eff} = 8.5 \pm 1.9\%$ for $B_s^0 \to J/\psi\eta(\pi^+\pi^-\pi^0)$ and $\varepsilon_{eff} = 8.7 \pm 2.0\%$ for $B_s^0 \to J/\psi\eta'$. This is mostly due to a smaller wrong tag fraction

($\omega_{tag} = 30.1 \pm 1.6\%$ and $\omega_{tag} = 31.4 \pm 1.7\%$ respectively).

For our sensitivity analysis, we have decided to keep the tagging results (ε_{tag} and ω_{tag}) of our B_d^0 selection to simulate the $B_s^0 \to J/\psi K_s^0$ knowing that the wrong tag fraction is underestimated for a B_s^0.

5.5.2 Untagged signal yields

The $2\,\mathrm{fb}^{-1}$ untagged signal yield is the number of selected, reconstructed and triggered events in one year of running. This number is calculated with equation 5.3 for the B_d^0 events. For the B_s^0 estimation, we use the same formula with the hadronization factor for B_s^0, $f_{B_s} = 0.103 \pm 0.014$ given in [96] and the visible branching ratio $BR_{vis}\left(B_s^0 \to J/\psi\,(\mu^+\mu^-)\,K_s^0\,(\pi^+\pi^-)\right) \simeq (8.21 \pm 0.45) \times 10^{-7}$, given in [29]. The signal yields are detailed table 5.12. The difference of 7.7% between the signal yield in a $\pm 50\,\mathrm{MeV/c^2}$ and in a $\pm 2\sigma$ mass window is essentially due to the wrong associated signal events arriving in the large mass window; this difference is about 5% between the $\pm 3\sigma$ and the $\pm 2\sigma$ mass windows, which corresponds to the expected difference for a gaussian distribution. The errors quoted in Table 5.12 results from the individual errors on the factors entering in equation 5.3.

	$\pm 50\,\mathrm{MeV/c^2}$ mass window	$\pm 3\sigma$ mass window	$\pm 2\sigma$ mass window
S(B_d^0)	$26'112 \pm 3'963$	$25'393 \pm 3'857$	$24'092 \pm 3'666$
S(B_s^0)	310 ± 82	301 ± 80	286 ± 76

Table 5.12: Signal yield in number of events per year with $2\,\mathrm{fb}^{-1}$ for $B_{d,s}^0 \to J/\psi\,(\mu^+\mu^-)\,K_s^0\,(\pi^+\pi^-)$ after L0.

5.6 Background contributions

Four different sources of background which can mimic the selected signal have been passed through the selection criteria and are listed in table 5.7. The results are given in table 5.13. From these results the B/S ratio will be calculated.

$\boldsymbol{B_d^0 \to J/\psi\,(\mu^+\mu^-)\,K_s^0\,(\pi^+\pi^-)}$	$\boldsymbol{N_{gen}}$	$\boldsymbol{N_{sel}}$	$\boldsymbol{N_{sel}^{L0}}$	$\boldsymbol{N_{sel}^{HLT}}$
inclusive $b\bar{b}$	35’586’759	0	0	0
inclusive J/ψ	1’935’235	0	0	0
$B_u^+ \to J/\psi K^+$	1’753’742	3.6 ± 0.7	3.4 ± 0.7	2.8 ± 0.7
$\Lambda_b \to J/\psi \Lambda$	138’723	12.0 ± 1.4	11.4 ± 1.4	7.8 ± 1.1

Table 5.13: Background events after the final selection in mass window of $\pm 2\sigma$.

5.6.1 Inclusive $b\bar{b}$ background levels

The inclusive $b\bar{b}$ background contribution, as we have already seen in section 5.1.2, can be estimated with the following equation:

$$\left(\frac{B}{S}\right)_{B_d^0}^{b\bar{b}} = \frac{\varepsilon_{gen}^{b\bar{b}} \varepsilon_{sel}^{b\bar{b}}}{2 f_{B_d} BR_{vis} \left(B_d \rightarrow J/\psi \left(\mu^+\mu^-\right) K_s^0 \left(\pi^+\pi^-\right)\right) \varepsilon_{gen}^{signal} \varepsilon_{sel}^{signal}} \tag{5.9}$$

with:

- $\varepsilon_{gen}^{b\bar{b}} = 43.4\%$ (section 3.4), the 400 mrad acceptance cut for the $b\bar{b}$ events.
- $\varepsilon_{sel}^{b\bar{b}} = \frac{N_{sel}^{b\bar{b}}}{N_{gen}^{b\bar{b}}}$, the selection efficiency of the $b\bar{b}$ events.

The other parameters have been detailed in section 5.1.2. The number of selected background events $N_{sel}^{b\bar{b}}$ is null in a mass window of $\pm 500\text{MeV/c}^2$ using a sample of 35'586'759 inclusive $b\bar{b}$ background generated events (table 5.13). Therefore, we have to use the unified approach of Feldman and Cousins [97] (see section 5.2.2). The results is that number of selected events in the large mass window should be in the interval of $[0, 2.44]$ at 90% confidence level. This corresponds to a maximum of $b\bar{b}$ selected events falling in a $\pm 2\sigma$ mass window of 0.078. Using equation 5.9, the B/S ratio for inclusive $b\bar{b}$ events after the L0 trigger is at maximum 0.039 (Table 5.14).

$B_d^0 \rightarrow J/\psi K_s^0$	B/S no trigger	B/S after L0	B/S after HLT
$b\bar{b}$ background	[0,0.037]	[0,0.039]	[0,0.058]
$B_u^+ \rightarrow J/\psi K^+$	0.0007 ± 0.0005	0.0007 ± 0.0005	0.0008 ± 0.0007
$\Lambda_b \rightarrow J/\psi \Lambda$	0.004 ± 0.003	0.004 ± 0.003	0.004 ± 0.003

Table 5.14: Background over signal ratios for the B_d^0 before and after triggers using the final selection. The mass window is $\pm 2\sigma$ around the B_d^0 mass value.

5.6.2 Inclusive J/ψ background studies

J/ψ are copiously produced in LHCb via gluon fusions which populate high level $c\bar{c}$ states $\chi_{c0}(1P)$, $\chi_{c1}(1P)$ and $\chi_{c2}(1P)$ decaying to J/ψ. The gluon process can also gives J/ψ directly. J/ψ can also come from decays of beauty hadrons. The cross section used in the simulation is $\sigma_{J/\psi\_\text{incl}} = (286 \pm 2)\,\mu\text{b}$ [96] out of which $(92.9 \pm 2.5)\%$ are prompt J/ψ and $(7.1 \pm 2.5)\%$ come from beauty hadron decays. With such a high inclusive production cross section, the rate of prompt J/ψ will be very high and a high statistics study of this specific background is needed. However, out of the 1'935'235 events which have been generated, none have survived the cuts in the mass interval of $\pm 2\sigma$ around the B_d^0 mass. We are quite confident in the fact that this type of background can be easily removed with a more stringent cut on the flight distance or on the impact parameter of the J/ψ. Other studies for $B_s^0 \rightarrow J/\psi\eta$ and $B_s^0 \rightarrow J/\psi\eta'$ decays have also shown that background from J/ψ does not represent a harmful noise to our study. Therefore we will not consider prompt J/ψ as a source of background.

J/ψ from beauty hadron decays

This background is a part of the inclusive $b\bar{b}$ background. The statistics for the latter is much higher than any of the exclusive channels that we have considered. The B/S estimation will therefore be obtained from $b\bar{b}$ inclusive events. For sake of completeness, however, we have studied the two exclusive channels, $B_u^+ \rightarrow J/\psi K^+$ and $\Lambda_b \rightarrow J/\psi\Lambda$.

5.6.3 Backgrounds from specific *b*-hadron decays

Two specific background contributions are described in this section: $B_u^+ \rightarrow J/\psi K^+$ and $\Lambda_b \rightarrow J/\psi\Lambda$ channels.

$B_u^+ \rightarrow J/\psi K^+$

The presence of muons from J/ψ decays and of the K^+ which can be mistaken as a π^+ and be associated to a π^- can mimic a B_d^0 decay. Moreover, the B_u^+ has almost the same mass ($5279.13 \pm 0.31\,\mathrm{MeV/c^2}$) as the B_d ($5279.50 \pm 0.33\,\mathrm{MeV/c^2}$) [15]. Therefore, this channel is a potential source of background for $B_d^0 \rightarrow J/\psi K_s^0$. The calculation of the B/S ratio is given by:

$$\left(\frac{B}{S}\right)^{B_u^+\rightarrow J/\psi K^+} = \frac{f_{B_u}\, BR_{vis}\left(B_u \rightarrow J/\psi\left(\mu^+\mu^-\right)K^+\right)\, \varepsilon_{gen}^{B_u\rightarrow J/\psi K^+}\varepsilon_{sel}^{B_u\rightarrow J/\psi K^+}}{f_{B_d}\, BR_{vis}\left(B_d \rightarrow J/\psi\left(\mu^+\mu^-\right)K_s^0\left(\pi^+\pi^-\right)\right)\, \varepsilon_{gen}^{signal}\varepsilon_{sel}^{signal}} \tag{5.10}$$

with the hadronization factor $f_{B_u} = 0.398 \pm 0.012$, and a visible branching ratio of $BR_{vis}\left(B_u \rightarrow J/\psi\left(\mu^+\mu^-\right)K^+\right) = (59.71 \pm 0.81)\cdot 10^{-6}$ and $\varepsilon_{gen}^{B_u\rightarrow J/\psi K^+} = (17.89 \pm 0.03)\%$. The B/S ratio in a mass window of $\pm 2\sigma$ around the invariant mass of the B_d^0 is 0.0007 ± 0.0005 after the L0 trigger.

$\Lambda_b \rightarrow J/\psi\Lambda$

In this channel, the Λ decays into a proton and a π^-. The proton can be reconstructed as a pion and thus mimic a $B_d^0 \rightarrow J/\psi K_s^0$ decay. The mass distribution is however displaced to high masses. The background over signal ratio for this particular channel is detailed hereafter.

$$\left(\frac{B}{S}\right)^{\Lambda_b\rightarrow J/\psi\Lambda} = \frac{f_{\Lambda_b}\, BR_{vis}\left(\Lambda_b \rightarrow J/\psi\left(\mu^+\mu^-\right)\Lambda\right)\, \varepsilon_{gen}^{\Lambda_b\rightarrow J/\psi\left(\mu^+\mu^-\right)\Lambda}\varepsilon_{sel}^{\Lambda_b\rightarrow J/\psi\left(\mu^+\mu^-\right)\Lambda}}{f_{B_d}\, BR_{vis}\left(B_d \rightarrow J/\psi\left(\mu^+\mu^-\right)K_s^0\left(\pi^+\pi^-\right)\right)\, \varepsilon_{gen}^{signal}\varepsilon_{sel}^{signal}} \tag{5.11}$$

with the hadronization factor $f_{\Lambda_b} = 0.10 \pm 0.02$, and a visible branching ratio of $BR_{vis}\left(\Lambda_b \rightarrow J/\psi\left(\mu^+\mu^-\right)\Lambda\right) = (2.79{\pm}1.69){\cdot}10^{-5}$ and $\varepsilon_{gen}^{\Lambda_b \rightarrow J/\psi\left(\mu^+\mu^-\right)\Lambda} = (20.76{\pm}0.05)\%$. The B/S ratio in a mass range of $\pm 2\sigma$ around the B_d^0 is again very low (0.004 ± 0.003).

5.7 Annual yield of $B_s^0 \rightarrow J/\psi K_s^0$ at LHCb

The signal yield of B_s^0 decaying into $J/\psi K_s^0$ has been given in table 5.12. With an integrated luminosity of $2\,\mathrm{fb}^{-1}$ we will observe around 300 events of $B_s^0 \rightarrow J/\psi K_s^0$ in a year of data taking. The B/S ratios are detailed in table 5.15. The B/S ratios have been obtained from those ratios for $B_d^0 \rightarrow J/\psi K_s^0$: in the mass window of $\pm 50\,\mathrm{MeV/c^2}$, the B/S ratio should vary between 0 and 9.60, whereas in a $\pm 2\sigma$ mass window, it will be between 0 and 3.33. Figure 5.24 gives the figure that we can expect for the mass distribution. The figure accounts for the worse B/S ratio and a resolution of $8\,\mathrm{MeV/c^2}$ for the peaks. No tails have been included. We are confident in the possibility of extracting the $B_s^0 \rightarrow J/\psi K_s^0$ signal.

$\boldsymbol{B_s^0 \rightarrow J/\psi K_s^0}$	B/S no trigger	B/S after L0	B/S after HLT
$b\bar{b}$ background	[0, 3.09]	[0, 3.33]	[0, 4.88]
$B_u^+ \rightarrow J/\psi K^+$	0.056 ± 0.047	0.057 ± 0.049	0.071 ± 0.064
$\Lambda_b \rightarrow J/\psi\Lambda$	0.32 ± 0.28	0.33 ± 0.29	0.33 ± 0.29

Table 5.15: B/S ratios for the B_s^0 before and after triggers using the final selection and in mass window of $\pm 2\sigma$.

In the next chapter, we will use the results presented here to simulate the B_s^0 signal and estimate the sensitivity of the LHCb experiment to the parameters a and θ (see section 1).

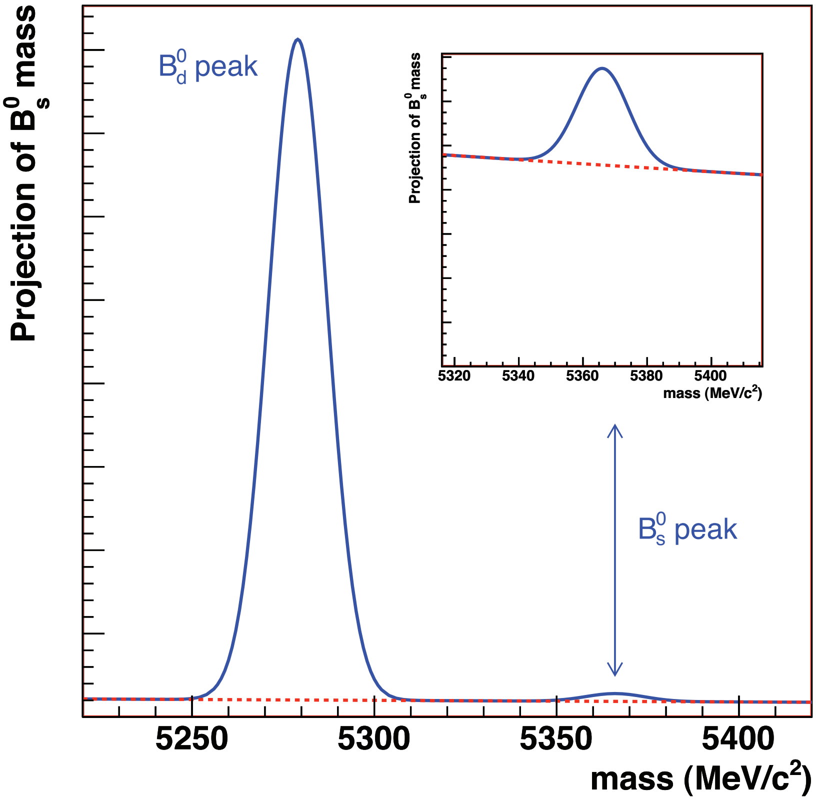

Figure 5.24: Mass distributions of B_d^0 and B_s^0 after one year of run at 2 fb^{-1}. The B/S ratio considered here is 3.33 in a mass window of $\pm 2\sigma$ around the B_s^0 nominal mass after the L0 trigger. The red dashed line corresponds to the $b\bar{b}$ background level.

Chapter 6

LHCb sensitivity to the penguin contribution in the determination of $\sin 2\beta$

In this chapter, we will present the method that we used to determine the sensitivity of LHCb to the parameters a and θ, i.e. the sensitivity to the penguin contribution in the $B_s^0 \to J/\psi K_s^0$ decays given the CKM γ angle (see section 1.5.5). We will access these parameters via the time-dependent asymmetry:

$$\mathcal{A}_{CP}(t) = -\frac{\mathcal{A}_{CP}^{dir}\cos(\Delta M_s t) + \mathcal{A}_{CP}^{mix-ind}\sin(\Delta M_s t)}{\cosh\left(\Delta\Gamma_s t/2\right) + \mathcal{A}_{\Delta\Gamma}\sinh(\Delta\Gamma_s t/2)}$$

The $\mathcal{A}_{CP}^{dir}$, $\mathcal{A}_{CP}^{mix-ind}$ and $\mathcal{A}_{\Delta\Gamma}$ can be written as functions of a and θ [29] (see section 1.5.5 for details):

$$\begin{aligned}
\mathcal{A}_{CP}^{dir} &= \frac{2a\sin\theta\sin\gamma}{1-2a\cos\theta\cos\gamma+a^2} \\
\mathcal{A}_{CP}^{mix-ind} &= \eta_{CP}\left[\frac{\sin\phi_s - 2a\cos\theta\sin\left(\phi_s+\gamma\right) + a^2\sin\left(\phi_s+2\gamma\right)}{1-2a\cos\theta\cos\gamma+a^2}\right] \\
\mathcal{A}_{\Delta\Gamma} &= -\eta_{CP}\left[\frac{\cos\phi_s - 2a\cos\theta\cos\left(\phi_s+\gamma\right) + a^2\cos\left(\phi_s+2\gamma\right)}{1-2a\cos\theta\cos\gamma+a^2}\right]
\end{aligned}$$

We recall that the parameters a (a') and θ (θ') are related to the ratios of amplitudes by (equation 1.45):

$$a \cdot e^{i\theta} = a' \cdot e^{i\theta'} = R_B\left(1-\frac{\lambda^2}{2}\right)\cdot\left(\frac{P'_{ut}}{A'_T + P'_{ct}}\right)$$

$R_B \equiv \frac{1}{\lambda}\left|\frac{V_{ub}}{V_{cb}}\right| = 0.41 \pm 0.07$, $\lambda = |V_{us}| = 0.22$, $P'_{ut} = P'_u - P'_t$ and $P'_{ct} = P'_c - P'_t$.

Neglecting the penguin process with c and u quarks, one gets:

$$a \cdot e^{i\theta} = a' \cdot e^{i\theta'} = R_B\left(1 - \frac{\lambda^2}{2}\right) \cdot \left(\frac{-P'_t}{A'_T - P'_t}\right)$$

Two arguments can be brought here to assess the a factor:

1. the weak phase between the tree amplitude ($\propto V_{cs}V^*_{cb}A_T$) and the penguin amplitude ($\propto V_{ts}V^*_{tb}P_t$) is proportional to λ^2 in SM,
2. the penguin diagram is higher order than the tree one.

As the weak phase is small, the above equation shows that a is proportionnal to the ratio of the penguin amplitude to the total amplitude.

The results of the selection, tuned for the decay $B^0_d \rightarrow J/\psi K^0_s$ with the full Monte Carlo, will be used for the analysis of the decay $B^0_s \rightarrow J/\psi K^0_s$.

6.1 Method to extract the parameters a and θ

The number of events $B^0_s \rightarrow J/\psi K^0_s$ that one can generate in a full Monte Carlo simulation is too low due to CPU and storage limitations if one also wants to have a comparable sample of background events. Therefore, such a simulation will not allow us to determine the sensitivity of the experiment to the physics parameters we are looking for. Instead, we use a "toy Monte Carlo"[1] which simulates the results of around 200 "experiments" with a statistics corresponding to $10\,\mathrm{fb}^{-1}$, $50\,\mathrm{fb}^{-1}$ and $100\,\mathrm{fb}^{-1}$ per experiment[2] in our case (with an integrated luminosity of $2\,\mathrm{fb}^{-1}$, the statistics for our channel is too low). The resolutions, the B/S ratio and the acceptance function of LHCb deduced from the full simulation serve as inputs to the toy Monte Carlo. The generation of Monte Carlo events is performed by a toolkit for data modelling, RooFit [105]. MINUIT [106] is used for the fitting part and ROOT [107] for the data analysis.

For each event, the mass of the B^0_s and its proper time are generated using a probability density function that we will described hereafter. When the number of events has been reached for a given integrated luminosity, the "experiment" is considered to be over and the distributions are fitted according to an extended likelihood function maximization which includes the physics parameters that we want to determine as free parameters. For each experiment, we obtain a mean value and an error for each of our physical free

---

[1] The toy Monte Carlo have been developped in C++, using the RooFit v2.07 libraries and interfaced to ROOT v5.10 in our analysis.

[2] $100\,\mathrm{fb}^{-1}$ corresponds to the maximum integrated luminosity of the upgraded LHCb after 5 years [108] and [109] (50, corresponds to 2.5 years of run with the upgraded LHCb).

parameters. The distributions of the errors of the 200 experiments have a mean value which corresponds to the sensitivity. Indeed, the sensitivity to a parameter is defined as the average value of the errors distribution when the experiment is repeated a great number of times.

6.2 Extended likelihood description

In this section we will describe how the signal and the background are modelled using a "probability density function" (PDF). First, the PDF of the B_s^0 mass distribution and the background is constructed using the mass resolution and the B/S ratio deduced from the Monte Carlo studies, and, second, the time dependent decay rates of the B_s^0 and $\overline{B}_s^0$ are modelled with their background taking into account the time resolution, the acceptance and the tagging results calculated in chapter 5.
The background slopes are determined by the full MC studies and are described as decreasing exponentials for the mass and decay rate distributions. Two mass regions are defined in our analysis, the *loose mass window* corresponding to $\pm 50\,\mathrm{MeV/c^2}$ around the mass of the B_s^0 and the *tight mass window* which reprensents de region of $\pm 2\sigma$ around the nominal mass of the B_s^0.

6.2.1 Modeling the B_s^0 mass

The probability density functions used to fit and generate the mass distribution consist of:

- a Gaussian (G) for the signal with a mean value $m_{B_s^0}$ equal to the mass of the B_s^0 and a resolution of $\sigma_{B_s^0} = 8\,\mathrm{MeV/c^2}$.
- an Exponential (E) for the background.

The mass PDF consists of a sum of two extended likelihood [110] given by [3]:

$$\begin{aligned}
\mathcal{L}_m^{sig}(m_i; N_{sig}, m_{B_s^0}, \sigma_{B_s^0}) &\propto (N_{sig})^{(N_{sig}+N_{bkg})} e^{-N_{sig}} G(m_i; m_{B_s^0}, \sigma_{B_s^0}) \\
\mathcal{L}_m^{bkg}(m_i; N_{bkg}, \kappa_{bkg}) &\propto (N_{bkg})^{(N_{sig}+N_{bkg})} e^{-N_{bkg}} E(m_i; \kappa_{bkg}) \qquad (6.1)
\end{aligned}$$

where:

- m_i is the generated and fitted mass for the experiment i,
- N_{sig} is the number of signal events in the $\pm 2\sigma$ mass window ,
- $m_{B_s^0} = 5366.1\,\mathrm{MeV/c^2}$ is the mass of the B_s^0,

---

[3] The Poisson distributions in front of the gaussian and exponential functions insure that we have the correct B/S ratio in the tight mass window.

- $\sigma_{B_s^0}$ is the B_s^0 mass resolution,
- $N_{bkg} = N_{sig} \times B/S$ is the number of background events in the $\pm 2\sigma$ mass window with B/S the background-over-signal ratio in this mass window,
- $\kappa_{bkg} = -1.0\,(\mathrm{MeV/c^2})^{-1}$ is the slope of the background exponential resulting from a guess.

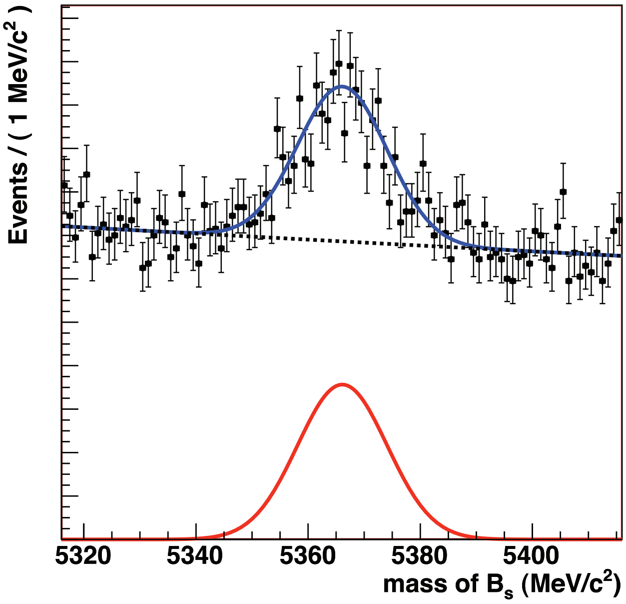

Figure 6.1: Projection of the mass PDF for $B_s^0 \to J/\psi K_s^0$ channel. The background is the dashed black line, the signal is the red line and the sum of the two contributions is in blue. The dots are toy MC generated events.

The projection of the mass PDF is shown Fig 6.1. The parameters of the fit are $\sigma_{B_s^0} = 8\,\mathrm{MeV/c^2}$, $N_{sig} = 1430$ corresponding to the number of B_s^0 events after five years of data taking ($10\,\mathrm{fb^{-1}}$) and $B/S = 3.33$ in the tight mass window (see Table 5.15).

6.2.2 Modeling the proper time

For a decay to pure CP-odd ($\eta_{CP} = -1$) eigenstate, like the $B_s^0 \to J/\psi K_s^0$ decay, the observed decay rates, assuming a perfect resolution, are defined as:

$$\begin{aligned} R(B_s^0 \to f) &= (1-\omega_{tag}) \times \Gamma(B_s^0 \to f) + \omega_{tag} \times \Gamma(\overline{B}_s^0 \to f) \\ R(\overline{B}_s^0 \to f) &= (1-\omega_{tag}) \times \Gamma(\overline{B}_s^0 \to f) + \omega_{tag} \times \Gamma(B_s^0 \to f) \end{aligned}$$

where $\Gamma(B_s^0 \rightarrow f)$ and $\Gamma(\overline{B}_s^0 \rightarrow f)$ are the decay rates defined in the chapter 1.4.4 equation 1.34 and ω_{tag} is the wrong tag fraction defined in chapter 3.3. These decay rates can be express as functions of physics parameters like $\Delta\Gamma_s$, ΔM_s, and the CP asymmetries $\mathcal{A}_{CP}^{dir}$, $\mathcal{A}_{CP}^{mix-ind}$ and $\mathcal{A}_{\Delta\Gamma}$ [4]:

$$
\begin{aligned}
R(B_s^0(t) \rightarrow f) &= |A_f(0)|^2 \cdot e^{-\Gamma_s t}\Bigg\{ \cosh\left(\frac{\Delta\Gamma_s t}{2}\right) + \mathcal{A}_{\Delta\Gamma}\sinh\left(\frac{\Delta\Gamma_s t}{2}\right) \\
&\quad + D\mathcal{A}_{CP}^{dir}\cos(\Delta M_s t) + D\mathcal{A}_{CP}^{mix-ind}\sin(\Delta M_s t)\Bigg\} \\
R(\overline{B}_q^0(t) \rightarrow f) &= |A_f(0)|^2 \cdot e^{-\Gamma_s t}\Bigg\{ \cosh\left(\frac{\Delta\Gamma_s t}{2}\right) + \mathcal{A}_{\Delta\Gamma}\sinh\left(\frac{\Delta\Gamma_s t}{2}\right) \\
&\quad - D\mathcal{A}_{CP}^{dir}\cos(\Delta M_s t) - D\mathcal{A}_{CP}^{mix-ind}\sin(\Delta M_s t)\Bigg\} \qquad (6.2)
\end{aligned}
$$

where $D = (1 - 2\cdot\omega_{tag})$ is the tagging dilution factor defined chapter 3.3. By introducing the tagging categories q_i, the equation 6.2 can be reduced to one equation, which combines the two decay rates defined above. The tagging results, presented in chapter 5.5.1, can be easily integrated as $q_i = \{+1, -1, 0\}$ whether the signal is tagged at the production step as B_s^0 when $q_i = 1$, $\overline{B}_s^0$ when $q_i = -1$, and not tagged when $q_i = 0$. The decay rate becomes:

$$
\begin{aligned}
R_f(t_i^{true}, q_i; \omega_{tag}, \overrightarrow{\alpha}) &\propto e^{-\Gamma_s t_i^{true}} \times \Bigg\{ \cosh\left(\frac{\Delta\Gamma_s t_i^{true}}{2}\right) + \mathcal{A}_{\Delta\Gamma}\sinh\left(\frac{\Delta\Gamma_s t_i^{true}}{2}\right) \\
&\quad + q_i D\left(\mathcal{A}_{CP}^{dir}\cos(\Delta M_s t_i^{true}) + \mathcal{A}_{CP}^{mix-ind}\sin(\Delta M_s t_i^{true})\right)\Bigg\} \qquad (6.3)
\end{aligned}
$$

where $\overrightarrow{\alpha} = (\Gamma_s, \Delta\Gamma_s, \Delta M_s, \phi_s, \tau_s, a, \theta)$ is the physics parameters vector and t_i^{true} the true proper time used for the generation.

The decay rate described above is the "ideal" physical decay rate; to reproduce the experimental results, we have to consider the effects of the time resolution and of the selection cuts on the proper time. In the section 5.4, we have determined the proper time resolution and the acceptance efficiency function for the B_d^0 selection. We use these resolution and acceptance functions to define our proper time PDF:

$$
\begin{aligned}
\mathcal{L}_t^{sig}(t_i^{rec}, t_i^{true}, q_i, \sigma_{t_i^{rec}}; acc_s, \omega_{tag}, \overrightarrow{\alpha}, S) &\propto A(t_i^{rec}; acc_s) \times R_f(t_i^{true}, q_i; \omega_{tag}, \overrightarrow{\alpha}) \\
&\quad \otimes G(t_i^{rec} - t_i^{true}, \sigma_{t_i^{rec}}; S) \qquad (6.4)
\end{aligned}
$$

---

[4] The asymmetry due to $\Delta\Gamma$ is not affected by the dilution factor: indeed, in the two rates mentioned in equations 6.2, this asymmetry appears with the same sign for both decays.

where:

- $A(t_i^{rec}; acc_s)$ is the time dependent acceptance efficiency function with t_i^{rec} the reconstructed proper time and acc_s the acceptance coefficient defined by the full MC selection. It multiplies this decay rates [5].
- $G(t_i^{rec} - t_i^{true}; \sigma_{t_i^{rec}} S)$ is the Gaussian resolution function. It depends of the reconstructed proper time error $\sigma_{t_i^{rec}}$ multiplied by a scale factor S. This factor accounts for the underestimation of errors. The decay rates (6.3) is convoluted with this resolution function.

The proper time background contribution PDF is parametrized by a simple exponential lifetime multiplied by the acceptance function to simulate the experimental effects :

$$\mathcal{L}_t^{bkg}(t_i^{rec}, t_i^{true}; acc_s, \tau_{bkg}) \propto A(t_i^{rec}; acc_s) \times E(t_i^{true}; \tau_{bkg}) \otimes \delta(t_i^{rec} - t_i^{true}) \qquad (6.5)$$

with $E(t_i^{true}; \tau_{bkg})$ being the exponential model for the proper time background and $\tau_{bkg} = 1.0\,\mathrm{ps}^{-1}$ the slope of the exponential.
The behaviour of the observed signal B_s^0 and $\overline{B}_s^0$ decay rates are illustrated in Fig 6.2 and 6.3. First, we draw the analytical rates using the experimental values as input parameters:

- $\Delta\Gamma_s = 0.084\,\mathrm{ps}^{-1}$ [15]
- $\tau_s = 1.437\,\mathrm{ps}$ [15]
- $\Delta M_s = 17.77\,\mathrm{ps}^{-1}$ [15]
- $\phi_s = 2^\circ$ [23]
- $\gamma = 76.8^\circ$ [23]
- $a = 0.2$ [29]
- $\theta = 30^\circ$ [29]

The wrong tag fraction was determined in the full selection of the B_d^0 (section 5.5.1): $\omega_{tag} = 39.25\,\%$ (after L0 trigger). The dilution factor is then $D = (1 - 2 \cdot \omega_{tag}) = 0.215$. The two physical parameters a and θ in which we are interested are fixed at $a = 0.2$ and $\theta = 30^\circ$ as proposed by Fleischer [29]. They will be free parameters in the final fit.

Figure 6.2 shows the analytical rate diluted by the wrong tag fraction and the effect of the convolution with the proper time resolution (see section 5.4). One could have thought of extracting the proper time resolution by unfolding the proper time distribution. Unfortunately, we have to take into account this acceptance function which remove the short-lived events, making this determination quite difficult if not impossible.

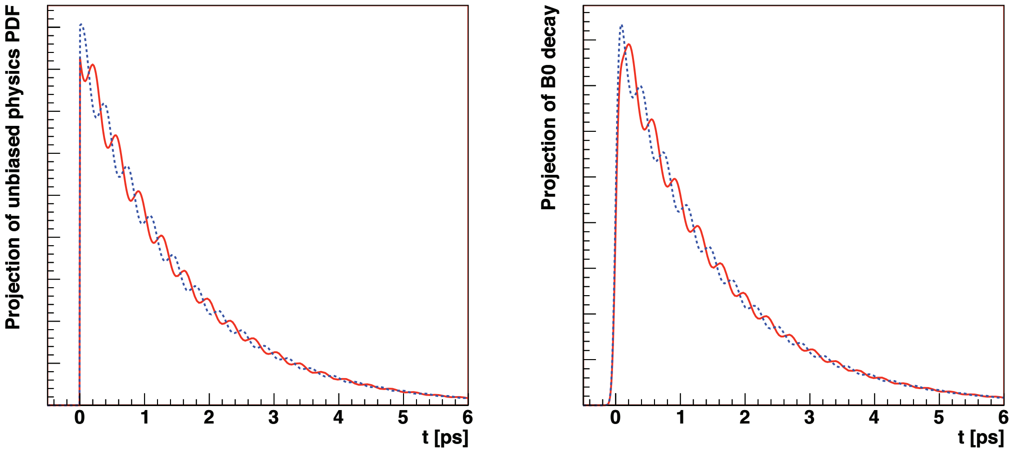

Figure 6.2: Signal decay rates for $B_s^0 \to J/\psi K_s^0$ to pure CP odd eigenstates as a function of the meson proper time (arbitrary units). The red solid line indicates the expected rates for an initially tagged B_s^0 meson, whereas the blue dashed line shows the time dependent rate for a meson initially tagged as $\overline{B}_s^0$. The analytical rates are shown on the left figure and the same decay rates convoluted with the proper time resolution is on the right figure.

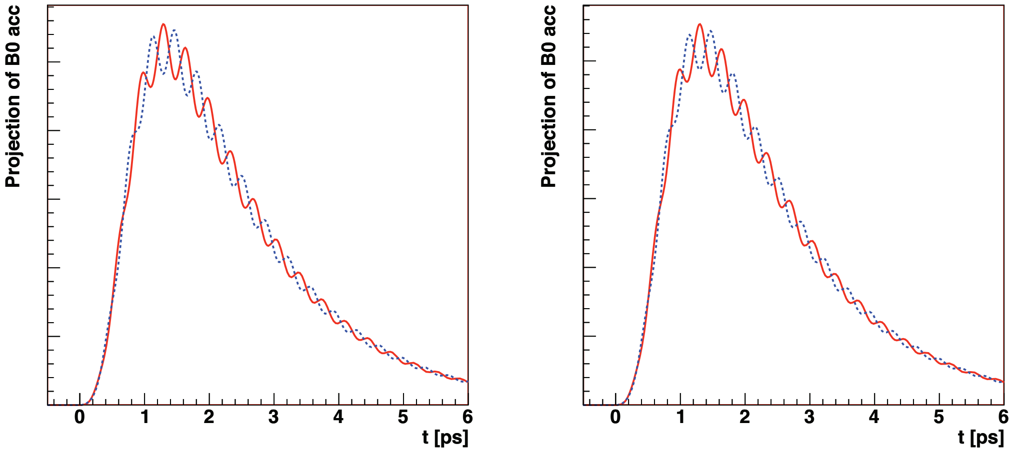

Figure 6.3: Signal decay rates for $B_s^0 \to J/\psi K_s^0$ to pure CP odd eigenstates (arbitrary units). On the left figure, the analytical rates diluted with the wrong tag fraction is multiplied by the acceptance function and on the right figure, the proper time resolution is also added.

The challenge is now to extract the physical parameters from a likelihood fit including the background. The background level in our analysis is very high (B/S $\in [0\,,3.33]$ after L0 trigger (see section 5.7)) and the statistic is quite low (~ 300 events/year at nominal luminosity ($2\,\mathrm{fb}^{-1}$)). Adding the proper time uncertainties and the tagging effects, the extraction of the physical parameters from the likelihood fit is very difficult.

To illustrate this challenge, the projection of the likelihood function onto the proper time with B/S$= 3.33$ for a luminosity of $10\,\mathrm{fb}^{-1}$ is shown in figure 6.4. We have used the nominal full MC results and the PDG's physics parameters described above. The figure shows that the oscillations of the initially tagged B_s^0 signal in the tight mass window is quite difficult to see because of the high level of background, which tends to flatten out the B_s^0 oscillations.

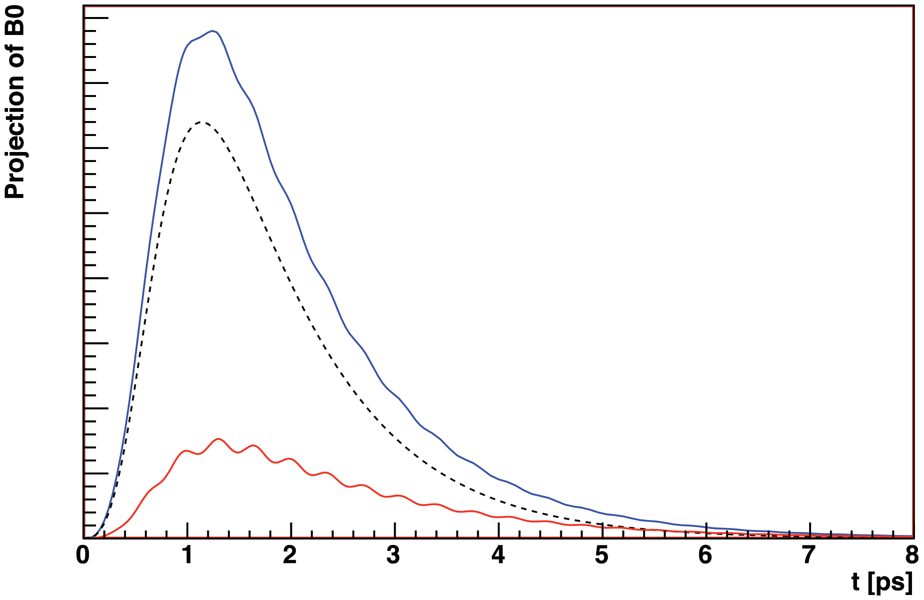

Figure 6.4: Projection of the likelihood onto the proper time for B_s^0 selected in the tight mass window ($\pm 2\sigma$) and for a luminosity of $10\,\mathrm{fb}^{-1}$ (arbitrary units). The red line is the projection of the signal initially tagged as B_s^0 contribution, the dashed black line corresponds to the background and the blue line is the projection of the sum of the signal initially tagged as B_s^0 and the background contribution.

---

[5] We used here $acc_s = 1.036$, well compatible with the value measured in the full selection of the B_d^0 after L0 trigger : $acc_s = 1.033 \pm 0.020$.

6.2.3 Generation and fit procedure

Total likelihood

The total likelihood (signal and background) used to both generate and fit the events is:

$$\mathcal{L}_{tot} = \prod_{i \in B_s^0 \to f} \mathcal{L}_i(m_i, t_i^{rec}, q_i, \sigma_{t_i^{rec}})$$

where $\mathcal{L}_i$ is the combination of the mass and the proper time terms defined above.

$$\begin{aligned} \mathcal{L}_i(m_i, t_i^{rec}, q_i, \sigma_{t_i^{rec}}) &= \mathcal{L}_m^{sig}(m_i) \cdot \mathcal{L}_t^{sig}(t_i^{rec}, q_i, \sigma_{t_i^{rec}}) + \\ & \quad \mathcal{L}_m^{bkg}(m_i) \cdot \mathcal{L}_t^{bkg}(t_i^{rec}) \end{aligned} \tag{6.6}$$

Tagging simulation

In our analysis, the tagging q_i is defined using a sample of data generated with proportions of initially tagged B_s^0, tagged $\overline{B}_s^0$ and untagged events. The tagging efficiency $\varepsilon_{tag} = 0.62$ is defined by the tagging performances of the full MC selection of the B_d^0 (section 5.5.1):

- initially tagged as B_s^0 events ($q_i = -1$) with a proportion of $0.5 \cdot \varepsilon_{tag}$,
- initially tagged as $\overline{B}_s^0$ events($q_i = 1$) with a proportion of $0.5 \cdot \varepsilon_{tag}$,
- untagged events ($q_i = 0$) with a proportion of $1 - \varepsilon_{tag}$.

Fitting procedure

In the fit we will only determine the parameters a and θ, leaving the other physics parameters fixed at their nominal values. The mass window is defined to be $\pm 50\,\mathrm{MeV/c^2}$ around the nominal B_s^0 mass : in this window the B/S ratio is 9.6 whereas in the tight window of $\pm 2\sigma$ around the B_s^0 mass, B/S is 3.33 (see Section 5.7). As only four parameters are to be fitted (N_{sig}, N_{bkg}, a and θ), we can afford to fit both the mass and the time distributions at the same time.

Monte Carlo inputs

The table 6.1 summarizes the inputs used to extract the two physical parameters a and θ. The fit is quite difficult to do because of the poor statistics and the high level of background. This is the reason why only four parameters are let free in this fit: the number of signal N_{sig} and background N_{bkg} events, and the two physics parameters a and θ. The nominal (starting) values for a and θ are 0.2 and 30° respectively as proposed in [29]. In the fit, they are allowed to vary in the domain $a \in [0,1]$ and $\theta \in [0,90°]$.

The sensitivity will be estimated for different luminosities and B/S values. The number of signal events used for this analysis is summarized in table 6.2. For each integrated luminosity, the sensitivity is measured first without background to get the best possible sensitivity and then for B/S= 3.33, corresponding to the maximum B/S in the tight mass window (section 5.7). To have another estimation, the sensitivity is also determined for B/S= 1.

	Physical parameter	value in MC
Mass	$m_{B_s^0}$	$5366.1\,\mathrm{MeV/c^2}$
	$\sigma_{B_s^0}$	$8\,\mathrm{MeV/c^2}$
Time resolution	$< \sigma_{t_i^{rec}} >$	0.037ps
	S	1.177
Time acceptance	acc_s	1.036
Time decay	$\Delta\Gamma_s$	$0.084\,\mathrm{ps}^{-1}$
	τ_s	1.437 ps
	ΔM_s	17.77 ps^{-1}
	ϕ_s	2°
	γ	76.8°
Background	κ_{bkg}	-1 $(\mathrm{MeV/c^2})^{-1}$
	τ_{bkg}	$1.0\,\mathrm{ps}^{-1}$
Tagging	ω_{tag}	39.25%
	ε_{tag}	62%

Table 6.1: Input used in the toy MC to extract the sensitivity to the physical parameters. All these parameters are fixed in the fit.

Luminosity	N_{sig}	Nb. of years of data taking
$10\,\mathrm{fb}^{-1}$	1430	5 years of LHCb
$50\,\mathrm{fb}^{-1}$	7150	2.5 years of upgraded LHCb
$100\,\mathrm{fb}^{-1}$	14300	5 years of upgraded LHCb

Table 6.2: Number of signal events used for the toy MC. The annual yield of $B_s^0 \to J/\psi(\mu^+\mu^-)K_s^0(\pi^+\pi^-)$ events is 286 in the tight mass window around the B_s^0 mass for $\mathcal{L}_{int} = 2\,\mathrm{fb}^{-1}$. With the LHCb upgrade, the statistics is estimated to be 10 times higher [108].

6.3 Likelihood fit results

We have produced data samples corresponding to the different luminosities listed in table 6.2 and to different background levels. In order to determine the sensitivity of the experiment to a and θ, we will fix the B/S ratio to 0, 1 and 3.33 for each luminosity.
In the following, we will first study the correlation between the two physics parameters.

Then the sensitivity to a and θ will be presented for each luminosity and B/S ratio.

6.3.1 Correlation studies

For a given luminosity and a B/S ratio, we have simulated 200 "experiments" and fitted the two physics parameters a and θ. For each of these 200 experiments, the correlation coefficient[6] between a and θ is measured.

Global correlation studies are shown in Fig 6.5. On these figures, most of the experiments show no correlations. For a few of them however, especially when the background is added in the simulation, the fit does not converge to the generated values and the correlations between the free parameters increase. This is particularly noticeable in cases where the statistics is poor and a high background level is added. For all integrated luminosities, the samples containing only signal give no correlations between a and θ. When statistics increases, the number of experiments with significant correlation between a and θ decreases. Hereafter, we will consider that there is not any correlation between a and θ.

6.3.2 Sensitivity to the physics parameters a and θ

We have very quickly noticed that the statistics is an important issue in the determination of the sensitivity. With a total integrated luminosity of $10\,\mathrm{fb}^{-1}$, i.e. after 5 years of data taking at nominal LHCb luminosity, the determination of θ is still impossible. The sensitivity to a is however reachable and is (0.172 ± 0.004) provided that the B/S ratio is kept to a very low level. Adding a noise level rapidly deteriorates the results for a: the errors spread out due to the fact that for some of the "experiments" the fit does not converge. The parameter θ, being not measurable at B/S$= 0$, remains *a fortiori* not accessible when a noise level is added.

We then tried to increase the integrated luminosities to $50\,\mathrm{fb}^{-1}$ and $100\,\mathrm{fb}^{-1}$; this corresponds to 2.5 years and 5 years of data taking with the upgraded LHCb which is expected to come in the years 2015. We keep the B/S at the same level as obtained in this work. This might be somewhat adventurous as quite new trigger schemes and detectors will be implemented. The situation about the penguin contribution in the determination of the CKM angle β might also have improved substantially, rending this kind of study obselete. We did it howerver for sake of completeness.

---

[6] The correlation coefficient for two independent random variable X and Y is defined as:

$$\rho = \frac{Cov[X,Y]}{\sqrt{Var[X]Var[Y]}}$$

where $Cov[X,Y] = E[X,Y] - E[X]E[Y]$ is the covariance of X and Y, $E[X] = \sum_x xf(x)$ the expectation with $f(x)$ the probability function, and $Var[X] = E[X^2] - E[X]^2$ the variance. The diagonal elements of the correlation matrix are equal to 1, as $Cov[X,X] = Var[X]$. The off-diagonal terms give prominence to the parameters that cannot be determined simultaneously.

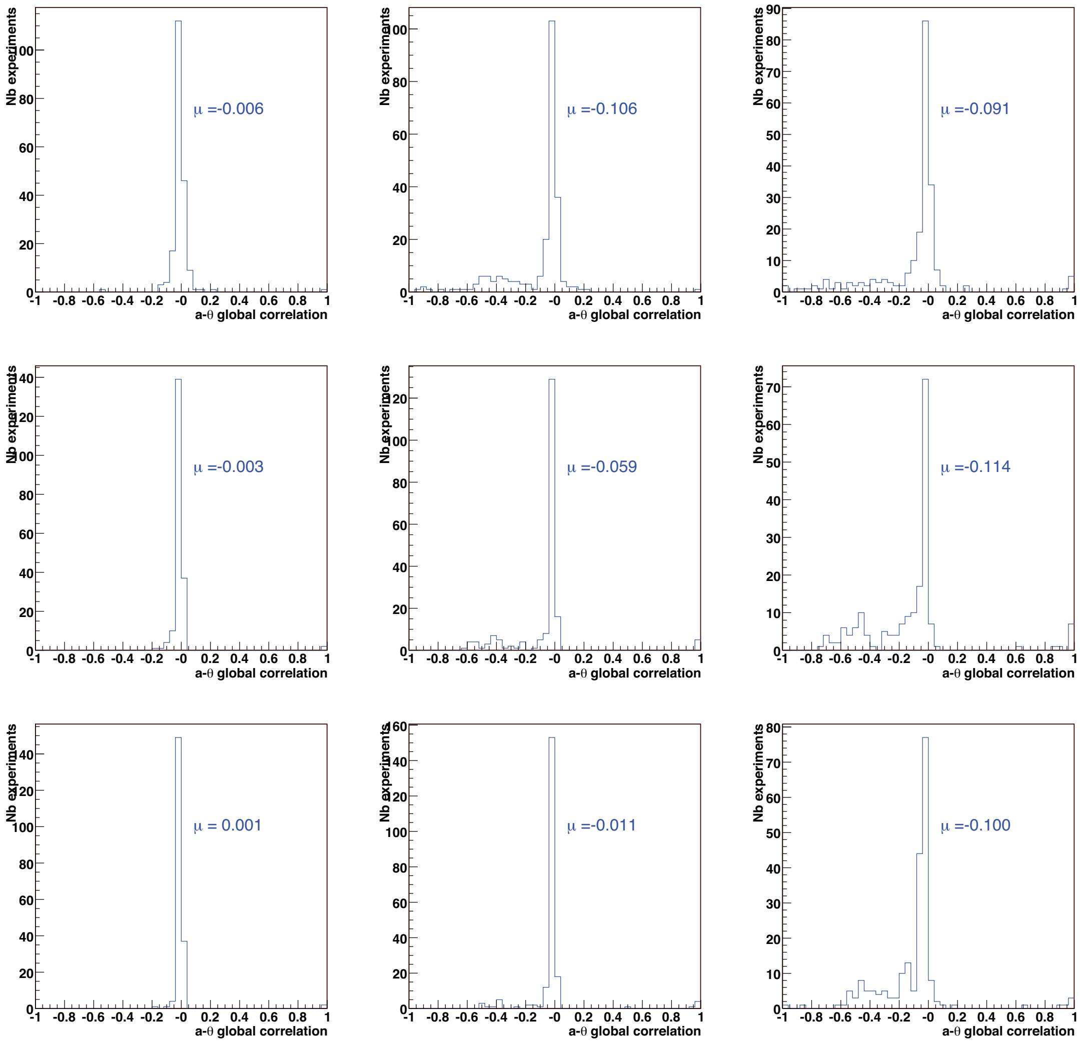

Figure 6.5: Correlation between a and θ with a luminosity of $10\,\mathrm{fb}^{-1}$ (top), $50\,\mathrm{fb}^{-1}$ (middle) and $100\,\mathrm{fb}^{-1}$ (bottom) and B/S=0 (left), B/S=1 (middle) and B/S=3.33 (right) in a mass window of $\pm 2\sigma$ around the nominal B_s^0 mass (μ indicates the mean value).

For higher luminosities ($\mathcal{L}_{int} = 50\,\mathrm{fb}^{-1}$ and $\mathcal{L}_{int} = 100\,\mathrm{fb}^{-1}$) the sensitivity to a indeed improves from $(7.2 \pm 0.1)\%$ to $(5.0 \pm 0.1)\%$ for B/S= 0 and from $(12.5 \pm 0.3)\%$ to $(8.9 \pm 0.2)\%$ for B/S= 3.33. The fit for θ now becomes acceptable, yielding a sensitivity of 22.6° for B/S=1 and $\mathcal{L}_{int} = 50\,\mathrm{fb}^{-1}$ and a sensitivity to θ ranging from 14.6° and 25.0° at $\mathcal{L}_{int} = 100\,\mathrm{fb}^{-1}$.
A general remark however: except for a clean signal, i.e. B/S= 0, in some cases among the "experiments", one encounters bad fits which result in a dispersion of the errors and pull distributions which are far from being normally distributed.

Table 6.3 and Appendix B show the details of our studies. In this table, we have only reported the cases for which the parameters given by the fit are reasonably distributed around the nominal values.

Parameter	Luminosities [fb^{-1}]	B/S = 0	B/S = 1	B/S = 3.33
a	10	0.172 ± 0.004	-	-
a	50	0.072 ± 0.001	0.096 ± 0.003	-
a	100	0.050 ± 0.001	0.065 ± 0.001	0.089 ± 0.002
θ	10	-	-	-
θ	50	$(21.6 \pm 1.0)^\circ$	$(22.6 \pm 0.8)^\circ$	-
θ	100	$(14.6 \pm 0.4)^\circ$	$(18.3 \pm 0.5)^\circ$	$(25.0 \pm 0.9)^\circ$

Table 6.3: Sensitivity to a and θ with different luminosity values and B/S ratios. All the detailled results are described in Appendix B.

Using the fact that two parameters a and θ do not show any correlation, we have also performed the fits fixing θ to various values from 10° to 50° and letting the sole physics parameter a to vary freely in the interval [0, 1]. The sensitivity that we obtain for a is here 0.169, in agreement with the previous result where both parameters were let free. The results are detailled in Appendix B and are in agreement with the results obtained when allowing the two parameters to vary.

Conclusion

In 5 years of nominal running, LHCb will be able to determine the parameter a with a sensitivity of (0.172 ± 0.004) when the background level is shrinked to zero. With an increased level of background, the determination of a can still be possible, provided that the value of θ is known. In this case, the sensitivity to a ranges from 0.169 to 0.374 as B/S is increased from 0 to 3.33, but many fits do not congerve. Although it might be premature to study the sensitivity of the upgraded LHCb to a and θ, as the detectors, the trigger and the selection schemes will be renewed, we have studied the sensitivity of upgraded LHCb to a and θ. As expected, the situation is better there and allows the determination of both parameters with reasonable sensitivities.

Conclusion

The studies presented in this dissertation can be divided into three parts: the contributions to the Inner Tracker design and production, the selection of the $B_d^0 \rightarrow J/\psi(\mu^+\mu^-)K_s^0(\pi^+\pi^-)$ events, and the study of the sensitivity to the penguin contributions in the $\sin 2\beta$ measurement of the LHCb experiment based on a fast simulation of the U-spin related $B_s^0 \rightarrow J/\psi K_s^0$ decay. We outline hereafter the main results obtained in these studies.

The cooling system of the Inner Tracker detector boxes has been designed, tested and produced in our lab. The cooling tests show that with an external air temperature of 22°C, the cooling ability of our detector is sufficient. The expected temperature on the hottest sensors which have been in operation for ten years is 7°C, while the critical temperature above which thermal runaway might occur is estimated to be above 10°C. The cooling circuit has been leak-tested at 2.5 bars. The turbulent flow of the coolant in the cooling rod does not create unacceptable vibration. The production and the installation are now completed and the detector was successfully tested for the cooling in the experimental hall.

The selection of the $B_d^0 \rightarrow J/\psi K_s^0$ channel developed in the present work is based on the standard tight selection of the daughter particles, mainly on the K_s^0 transverse momentum, on the K_s^0 flight distance and on the topological and kinetic characteristics of the B-meson decay which are its impact parameters and its flight distance. This selection has been optimized to achieve the highest efficiency for the signal while reducing at the percent level the contribution of background events and to reach a mass resolution less than $10\,\mathrm{MeV/c^2}$ in order to separate the B_d^0 and B_s^0 peaks. The mass resolution has been reduced to $8\,\mathrm{MeV/c^2}$. The background contributions, composed of inclusive $b\bar{b}$, specific $H_b \rightarrow J/\psi X$ channels and inclusive J/ψ events, were taken into account for this analysis. The analysis shows that the inclusive $b\bar{b}$ is the only remaining background. The background-over-signal ratio has been estimated to be [0, 0.039] at 90% CL after L0 trigger and in a mass window of 2σ around the B_d^0 mass. The proper time resolution is 37.2 fs. Nevertheless the pull distribution after the mass constrain fit shows an underestimation of the errors of 13%. A good separation of the B_d^0 and B_s^0 peaks is ensured by this selection and the percent level of B/S ratio allows the extraction of the B_s^0 peak from the background. The B/S ratio for the $B_s^0 \rightarrow J/\psi K_s^0$ channel is estimated to be

[0, 3.33] at 90% CL after L0 trigger and in a mass window of $\pm 2\sigma$ around the B_s^0 mass. With $2\,\text{fb}^{-1}$ of integrated luminosity, the signal yield of $B_s^0 \to J/\psi K_s^0$ is estimated to be about 300 events per year after the L0 trigger.

These results have been then used in a toy Monte Carlo study to assess the sensitivity of the LHCb experiment to the penguin contributions in the extraction of the $\sin 2\beta$ in the $B_d^0 \to J/\psi K_s^0$ decay. For this analysis, the simulation of the $B_s^0 \to J/\psi K_s^0$ signal was made using the parametrization proposed by R. Fleischer [29]. The two important physics parameters, the amplitude a and the strong phase difference θ, have been implemented in the time-dependent decay rates and are extracted by a fit. The simulation takes into account in an event-by-event basis the proper time error measurements, the B/S ratio, the selection efficiency of the signal as a function of the B_s^0 proper time and the tagging efficiencies. The sensitivity to a and θ has first been studied for five years of nominal operation of LHCb, i.e. for an integrated luminosity of $10\,\text{fb}^{-1}$. The B/S ratio has been varied. The low statistics and the high background level do not allow a good measurement of the physics parameters. Similar studies have been performed for the future upgrade of LHCb, assuming the same performances of the detectors and of the analysis. We have considered integrated luminosities corresponding to 2.5 and 5 years of operations of the upgraded LHCb. In the first case, the measurement of a and θ is possible with a sensitivity of ~ 0.1 and $\sim 23^\circ$ respectively if the B/S ratio is about 1. In the case of an integrated luminosity of $100\,\text{fb}^{-1}$, the measurement of a and θ gives a sensitivity to parameter a between 0.05 and 0.09, and to parameter θ between 15° and 25° depending the background level.

Appendix A

Material budget of Inner Tracker for DC06

The LHCb Inner Tracker, located just behind the bending magnet, covers the region closest to the beam pipe. Each of the three stations consists of 4 detector boxes each having four layers of silicon sensors. Electrical signal cables connect the detector boxes to the service boxes which are outside the acceptance. Most of these cables, as well as the cables containing the cooling fluid are however in the LHCb acceptance.
An important issue to understand the data is the interaction of the studied particles with the material which is in the acceptance. This will be simulated in Monte Carlo programs. Charged particles traversing a material loose a part of their energy and undergo multiple scattering. They can also interact in the material and produce secondary particles. Therefore, a precise description of the detector geometry is mandatory. A precise placement of the sensors in this description is also of great importance as it will be used in the track reconstruction.
The material implementation of the detector description is done in different steps. First a detailed list of all the different materials of the whole detector, including the supports, the cables, the cooling pipes etc..., is made. Then the detector is divided into "logical volumes" to which a single type of material is assigned and implemented in GEANT4 using the XML (eXtensible Markup Language). My part consisted in the first part of this implementation. The second part is developped in the note [92].

A.1 Detector description

The Inner Tracker is composed of 3 stations placed behind the magnet and before second RICH detector. Each station consists of 4 individual detector boxes, which are arranged around the beam pipe. The boxes placed at the sides of the beampipe host modules built out of two silicon sensors bonded together to form a 22 cm long detector, while the modules above and below the beam pipe consist of one single sensor only. Each box houses 28 modules which are placed in 4 layers allowing x,u,v,x coordinate measurements. The u and v layers are being tilted along the y axis by -5° and +5° respectively (see Fig. A.1).

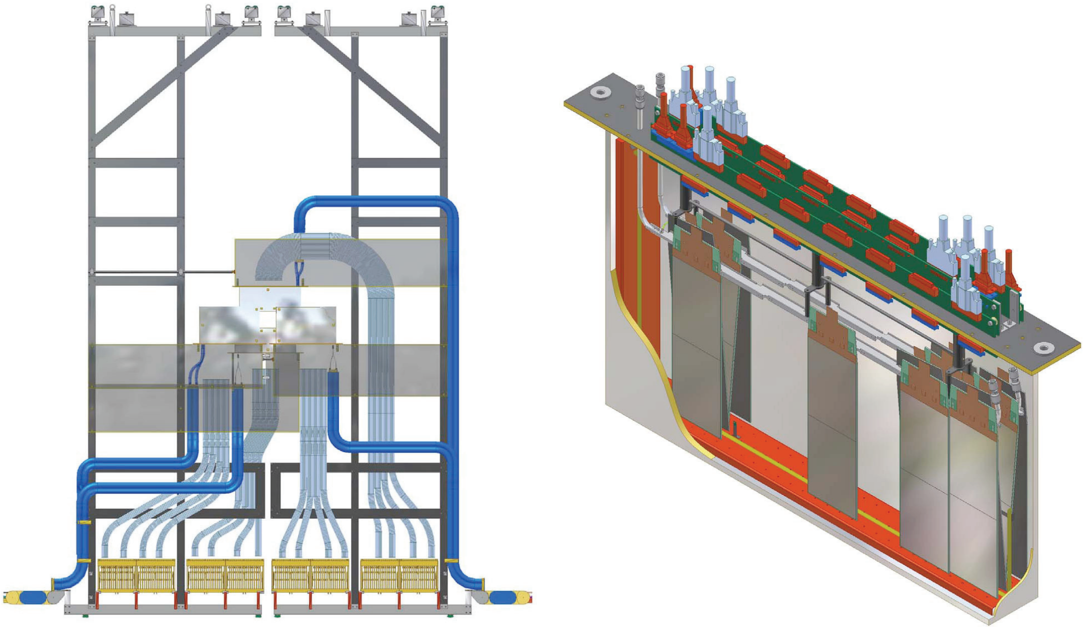

Figure A.1: The Inner Tracker design : Station T1 (left) and a side detector box (right).

To implement the Inner Tracker in the LHCb software, we have divided the detector in different "logical volumes". A logical volume is a three-dimensional volume which has a width (corresponding to the LHCb x-coordinate), a height (y) and a thickness (z) and contains the information about its shape (rectangular box, cylinder...). Each logical volume is a mixture of different materials characterised by the relative amount of elements included, given in percentage of the mass, and has an average density.

For each logical volume, which is a sort of an envelope around the little pieces of material that are not simulated individually, we have calculated the exact material composition and found a real mass and a real volume. The "real" mass (volume) is the sum of the masses (volumes) of all the elements contained in the area defined by the logical volume. The "density" of a logical volume is the real mass divided by the real volume. The width or the height of a logical volume is taken as the largest width or height of the elements contained in this volume. Hence, its thickness is an average given by the real volume divided by a maximized width times height. In some cases, the thickness is fixed to the real thickness and the density is averaged, as done for example for the box walls (see Section A.1.2).

In this section we will describe the different logical volumes which compose the Inner Tracker. All the volumes and calculations are available at:
http://lphe.epfl.ch/∼lhcb/itproduction/Materialbudget.

A.1.1 Sensor modules

Silicon sensors are glued on a sandwich made up by 4 layers: 25μm of kapton [75] used here for electrical insulation purposes, 200μm of heat conducting carbon fibre (Mitsubishi K13D2U [76]), 1 mm of foam (Airex R82 [78]) and once more 200μm of carbon fibre. The ensemble which constitues a module is also called "ladder". The front-end electronics, i.e. the three Beetle chips, resistors and capacitors, are mounted on an hybrid circuit which is glued on an aluminium piece called "balcony". This balcony, whose width is 10 mm less than the ladder's one, is inserted in the sandwich support and glued to the carbon layers with heat-conducting silver glue.

Figure A.2: Logical volumes of an IT ladder

In the detector description each module is described with 4 logical volumes (see Fig A.2 and table A.1):

- *LadderTop*: composed of the kapton-hybrid with its SMD components, solders, the silver glue and the sandwich support. Its width is defined by the minimum width of the ladder, its height is the distance between the top of the ladder and the balcony, and its thickness is averaged.
- *Balcony*: composed of the aluminium balcony itself, the hybrid part where the readout chips are located, the sandwich support, the pitch adaptor and the silver

glue. The width of this volume is given by the width of the balcony, the height is the height of the balcony plus the pitch adaptor and its thickness is an average one.

- *LongSupport* and *ShortSupport*: composed of the rest of the sandwich support, the sensor glue and the wire bonds. Width and height are defined by the rest of the ladder support and the thickness is averaged.
- *LongSensor* and *ShortSensor*: composed of the silicon sensors. The dimensions are the ones of the silicon sensors, plus 150μm in the case of the long ladders.

Volume	Height [cm]	Width [cm]	Thickness [cm]	Density [g/cm^3]
LadderTop	1.8500	7.2000	0.1725	1.0390
Balcony	2.4500	7.0000	0.1852	2.3946
LongSupport	22.2000	8.0000	0.1474	0.5153
ShortSupport	11.1000	8.000	0.1474	0.5152
LongSensor	22.0150	7.8000	0.0410	2.3284
ShortSensor	11.0000	7.8000	0.0320	2.3300

Table A.1: Dimensions of the logical volumes composing an IT ladder.

A.1.2 Detector box

In the detector box (see Fig. A.1), we have four layers of 7 modules (named ladders in XML code) attached to two cooling rods. The purpose of the cooling rods is to cool the front-end electronics and the sensors. The signals as well as the HV, LV supplies are brought in/out to the modules through kapton tails and four PCBs with connectors. The cooling rods are maintained by carbon columns. A cover and the walls of the box complete the description of the detector box. In the XML code, these parts of the box form individual volumes.

Cooling rods

The two cooling rods are two aluminium pieces with a complicated shape (see Fig. A.3). On each rod a 6 mm outer-diameter aluminium pipe (thickness 0.4 mm) is glued with silver and aluminium glue. In LHCb, the cooling fluid will be C_6F_{14} [82]. In the XML description, the cooling rods have a parallelepipedal shape. The width of this logical volume corresponds to the maximum width of the real rod and its thickness is the minimum distance between the two module layers. The height is the average height, i.e. real volume divided by the width times the thickness. Each logical volume for the cooling rod contains aluminium, screws, glue, aluminium pipe and coolant. These volumes are called *CoolingRodSide* for a side box and *CoolingRodCenter* for a center box (see Table A.2).

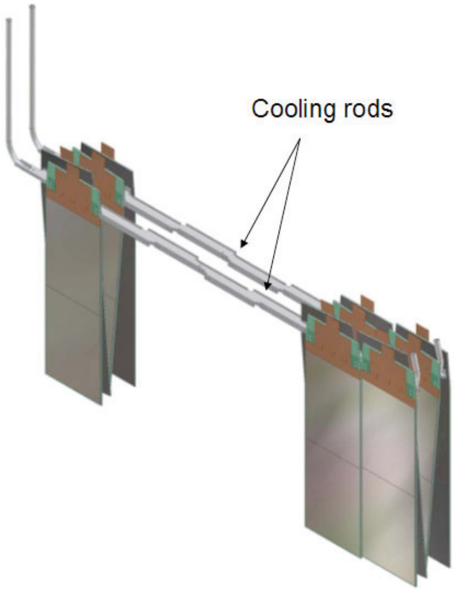

Figure A.3: Design of the cooling rods.

The two pipes glued on the cooling rods are exiting the box on the same side. They are represented by 2 vertical cylinders composed of a mixture of aluminium and C_6F_{14}. Their height is given by design and their diameter is 6 mm. The name of those logical volumes is *Pipe*.

Volume	Height [cm]	Width [cm]	Thickness [cm]	Density [g/cm^3]
CoolingRodSide	0.7320	57.0000	0.9000	2.3290
CoolingRodCenter	0.7283	57.5000	0.9000	2.3275

Table A.2: Dimensions of the logical volumes of the cooling rods.

Printed Circuit Boards (PCBs)

The signals and supplies are brought to and from the hybrids through a single PCB for each detector plane. These PCBs will have connectors to the kapton tails and to the signal cables outside the detector boxes. Due to limited space, the heights of the PCBs have to be different to accomodate the connectors on the signal cables side. There are two type of PCBs: 2 “long” ones (70 mm height) in the middle of the cover and two “short” ones (50 mm height) on both sides. A single Amphenol connector allows to bring individually HV to the sensors. To describe this structure in the XML code, the long and short PCBs are divided into 3 and 4 logical volumes respectively (see Fig. A.4 and Table A.3).

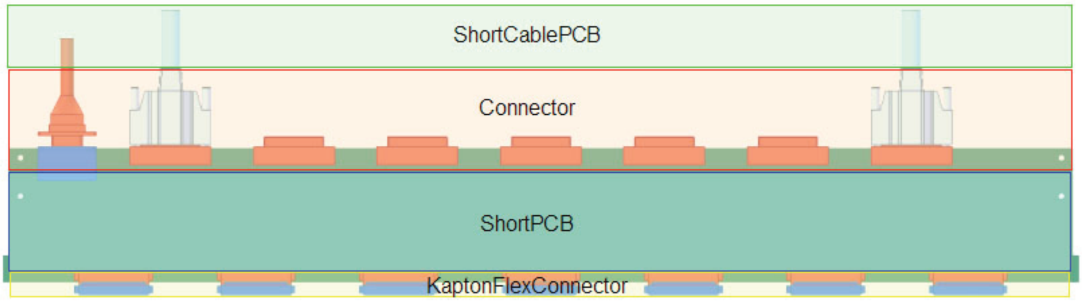

Figure A.4: Logical volumes of a short PCB.

- *KaptonFlexConnector*: this is composed of the 7 male and female connectors inside the box and between the PCB and the modules, in addition to the PCB material. The width is the real width of the PCB and the height is defined by the dimensions of the connectors.

- *ShortPCB* or *LongPCB*: between the inner and outer connectors, there is the PCB part which is only of PCB material. The dimensions are the real width of the PCB and the vertical distance between the 2 connectors. This height is different for long and short PCBs. The thickness is again given by the real volume of material divided by the width times the height.

- *Connector*: the connector zone is composed of the 7 connectors for signal cables (male and female), one HV connector (male and female) and the PCB material which is essentially epoxy, glass fiber, and copper traces. Its width is defined by the width of the PCB, its height is the distance between the top of the signal connectors and the bottom of the female connectors which are fixed on the PCB. The thickness is an average thickness.

- *ShortCablePCB*: for the short PCBs, a volume was added above the connector volume outside the box, which is composed of 7 signal cables and one HV cable[1] (see Section A.1.4). The width corresponds to the width of the PCB, the height is the height difference between long and short PCBs, and the thickness is averaged.

Kapton flex part

Each module is connected to its PCB by a kapton tail. In this region, there is no other material but 28 kapton tails (kapton and copper traces), the carbon columns maintaining the cooling rods and the connection between the 2 cooling rods (see Fig. A.5). To simplify the XML description, only one logical volume, *KaptonFlexCenter* for the center boxes

---

[1] In the March 2006 version, the material used for the cables in this logical volume has not the correct density as the empty space inside the cable is not included (see Section A.1.4).

Volume	Height [cm]	Width [cm]	Thickness [cm]	Density [g/cm^3]
Connector	5.1000	50.6000	0.2833	2.5206
ShortPCB	3.5500	50.6000	0.1600	3.0650
LongPCB	5.5500	50.6000	0.2779	2.9475
KaptonFlexConnector	1.2000	50.6000	0.2700	2.0733
ShortCablePCB	2.0000	50.6000	0.1125	2.3976

Table A.3: Dimensions of the logical volumes of the PCBs.

and *KaptonFlexSide* for the side ones (see Table A.4), with fixed dimension and an average density was defined.

Volume	Height [cm]	Width [cm]	Thickness [cm]	Density [g/cm^3]
KaptonFlexCenter	6.6400	50.6000	6.4000	0.0396
KaptonFlexSide	6.6400	50.6000	6.4000	0.0396

Table A.4: Dimensions of the “kaptonflex” volumes.

Box walls and Cover

All the elements in the box (cooling rods, PCBs, ...) are attached to the cover which in turn is attached to the IT support. The cover is a sandwich of two 200 μm layers of carbon fiber tissue glued with standard Araldite on either side of a 12 mm slice of Airex R82 foam [78]. Stesalite inserts are glued on this cover plate to allow its mounting to the detector box. Side and center covers have different sizes. The design of the cover is complex as the PCBs and cooling pipes are fed through it. To simplify the description, one material for each cover type (side and center) is defined as a mixture of all the contributing materials. The cover is divided in 4 parts (see Fig. A.6 and Table A.5) which are composed of those specific materials. Dimensions and densities are fixed in those logical volumes to avoid any overlap in the XML code.

Volume	Height [cm]	Width [cm]	Thickness [cm]	Density [g/cm^3]
SideCover1	0.6500	7.7000	8.0000	0.2243
SideCover2	0.6500	58.7500	1.8100	0.2243
SideCover3Pipe	0.6500	9.7500	8.0000	0.2243
CenterCover1	0.6500	9.0000	8.0000	0.2233
CenterCover2	0.6500	59.3500	1.8100	0.2233
CenterCover3Pipe	0.6500	10.6500	8.0000	0.2233

Table A.5: Dimensions of the logical volumes of the side cover.

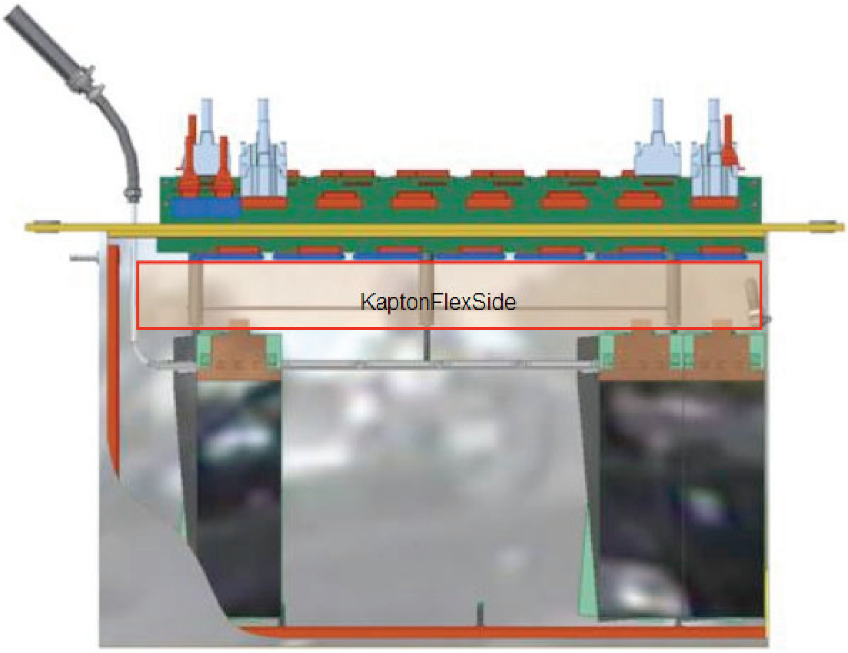

Figure A.5: The *KaptonFlexSide* volume.

Figure A.6: Logical volumes of a cover.

The box wall is a sandwich of glass fiber on either side of a 8 mm of polyisocyanurate (PIR [85]) foam (3 mm on the beam side). The electromagnetic noise shielding is ensured by 2 foils of 25 μm aluminium. The side and center boxes are each divided into 5 logical volumes: the four sides and the bottom[2] (see Fig. A.7 and Table A.6). A gas channel made of glass fiber has been included in the box wall. The dimensions of all the logical volumes of the box wall are fixed and their density is an average.

A.1.3 Support

Each station is built as separate left and right sides. Each side is composed of two 6 m carbon and glass fiber pillars, 2 large plates with a 1 m^2 sandwich structure composed

---

[2] The bottom of the box is defined as the part opposite to the cover.

[3] The name of this volume is not consistent with our nomenclature. It will be change to *CenterBox3* in a future version.

Volume	Height [cm]	Width [cm]	Thickness [cm]	Density [g/cm^3]
SideBox1	38.7000	62.4000	0.8000	0.1027
SideBoxBeam	37.9000	0.3000	6.4000	0.2244
SideBox4	37.9000	0.8000	6.4000	0.2055
SideBoxBottom	0.8000	62.4000	6.4000	0.1835
CenterBox1	25.6500	63.9000	0.8000	0.1027
CenterBox4	25.3500	0.8000	6.4000	0.2172
CenterBoxBeam	0.3000	63.9000	6.4000	0.2468
CenterBoxBottom[3]	25.3500	0.8000	6.4000	0.1100

Table A.6: Dimensions of the logical volumes of the box walls.

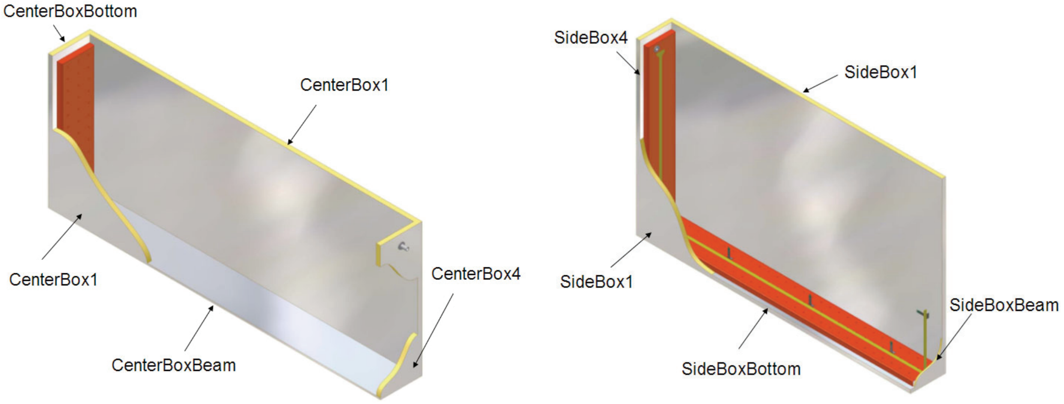

Figure A.7: Logical volumes of the center box (left), of the side box (right).

of a 8 mm honeycomb [111] layer and two 0.5 mm carbon fiber layers which hold two detector boxes, and several short CF-sandwich bars[4] to reinforce the whole structure (see Fig. A.1). Signal cables, HV cables and cooling lines are attached on this structure. As we have only introduce the part which is in the LHCb acceptance, in this description the external dimensions are different for each station. To simplify the XML code, each station is divided in 3 parts:

- the area between the 2 pillars of the right part,
- the area between the 2 pillars of the left part,
- the area in the middle of the structure, where the detector boxes are positionned.

Each pillar consists of one logical volume with fixed dimensions: the height is the height in the acceptance, the width and the thickness are 76 mm and the density is an

---

[4] The bars at 50° on the top of the structure (see Fig. A.8) were not implemented in the XML code.

average[5]. The small CF-sandwich bars are considered as a logical volume as they fit into the area defined by the two pillars. Their height and width are fixed by the real design while the thickness is an average. The large plates have to be divided in a part between the two pillars and another in the center part. Their dimensions are fixed to the geometrical dimension except for the thickness which is an average. Cables and cooling lines are distributed in different layers and divided into many logical volumes.

A.1.4 Cables and cooling lines

The signal cables and the cooling tubes are connected to the detector boxes and passed through the acceptance of the experiment. They represent an important amount of material because of the large number of signal cables. The design has been made to minimize the length of the cables and to avoid "hot spots" due to overlapping cables within a station. Twenty eight signal cables [112], one HV cable, one cable for the temperature probes in the box and two different cooling lines (inlet 9 mm inner diameter, outlet 14 mm inner diameter) are connected to a detector box. The 28 signal cables and the temperature cable are grouped together, while the cooling lines and the HV cable form an other group. The cooling lines are composed of reinforced nitril rubber tubes [86] with Armaflex insulation [87] and C_6F_{14} coolant liquid.

The definition of the cable logical volumes is done in two steps: first, the material is defined via the density and atomic composition of the various materials of a cable. Second, the logical volume is definited, where the previously defined material is used. The same strategy applies for the cooling lines.

As these cables represent an important amount of material, the description of the logical volumes must be very precise. An important effort was put to reduce the amount of material, which has caused frequent design changes. The last version that was released in March 2006 accounts for all the efforts done so far. Two versions will be presented in this Section:

- the "March 2006 version"[6] uses a simple factor, to account for the thickness of the cables.

- the "future version", which will possibly be released in summer 2006, will include a precise positionning of the cables on the support and a more precise description of material of the cables [7].

The thickness in term of radiation length is expected to be very similar in the two versions.

---

[5] The pillar logical volumes will be changed to a square tube with the real density to be more realistic in the future version

[6] The March 2006 version complies to the v30r1 of DDDB.

[7] The position of the cables will be measured during the installation of the detector and a sample of the latest version of the signal cable will be then weighted to adjust the amount of material.

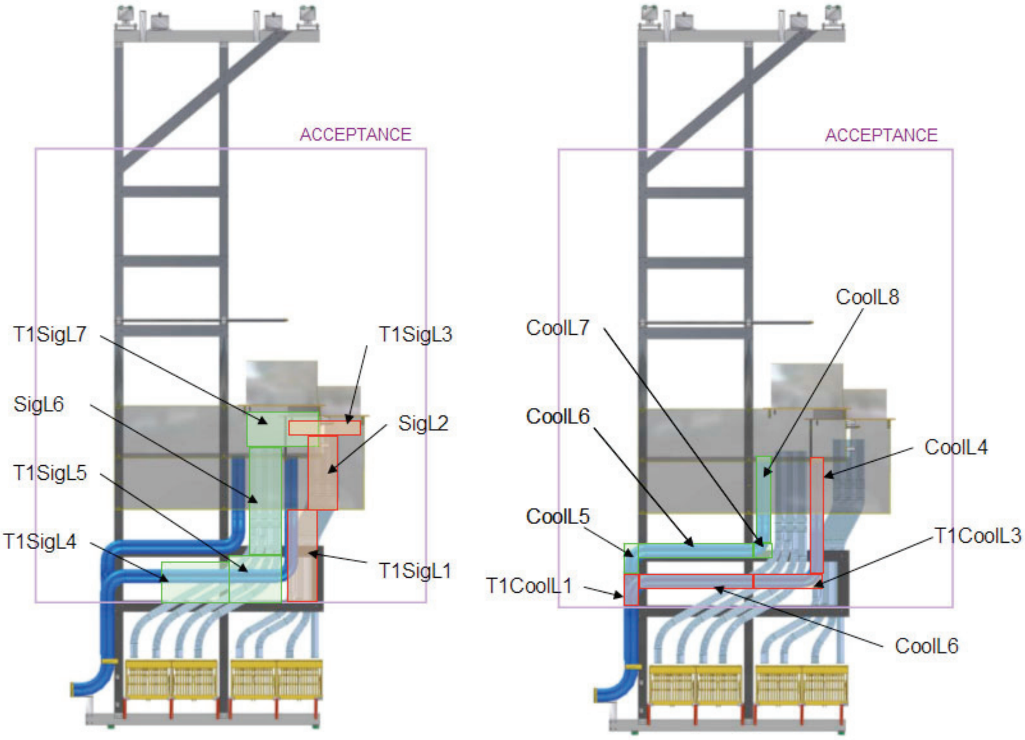

Figure A.8: Station T1 left version March 2006: description of the *ElecCable* volumes (left), description of the *CoolingCable* volume (right).

March 2006 version

a) The material definition

The signal cable is described with 68 copper conductors (AWG30) insulated in a halogen-free plastic, a thin aluminium shielding and an external halogen-free plastic insulation. The thickness of this insulation was estimated to be 0.75 mm and the total diameter to be 8 mm. The actual cable volumes are not completely filled with material, but contains about 30% of empty space between individual conductors. This has been taken into account in the volume definition.

For the HV cable, the temperature sensor cable and the cooling lines, the calculations are done in the same way.

b) The volume definition

The *ElecCable* logical volumes contain 28 signal cables and the cable for the temperature sensors (see Fig. A.8). Each *ElecCable* volume contain twenty eight 8 mm diameter cylinders for the signal cable material and one 5 mm diameter cylinder for the temperature sensor cable. Its height is defined by the design, its width corresponds to the total width of the 29 cylinders (22.9 cm). Depending upon the position in the acceptance, width and height can be exchanged. The thickness is fixed (corresponding to an old version of the cable). The average parameter is the density. The empty space inside the cables is accounted for this density parameter.

The inlet and outlet cooling tubes and the HV cable compose the *CoolingCable* logical volumes (see Fig. A.8). Like *ElecCable*, each line and cable is treated as a cylinder. The height and the width of this type of logical volume are given by the design, width or height, depending on the position in the acceptance, is the sum of the inlet and outlet cylinder diameter (11.5 cm in total). The HV cable is placed between the two cooling lines. Its thickness is fixed and the density is averaged. The empty spaces represent 2% inside cooling lines and 20% inside a single HV cable.

The position of each *ElecCable* volume and *CoolingCable* volume is defined by the design of the detector. Their exact positions will only be known after the final installation in the pit.

Next version

a) The material definition

In the next version and in order to obtain a precise description of the final signal cables [112], we will dismantle a piece of the cable and determine the mass of the individual components. The cable for the temperature sensor will be more realistic with less material than in the present version. We will also account for the empty spaces in the definition of the densities of the cables and tubes.

b) The volume definition

The final position of the cables and cooling lines will be measured on the detector support in the pit. The new *ElecCable* logical volumes position will be more realistic. The way to define the logical volumes will be simpler: the heigth/width will be defined by the measurements, and adjusted to the new cables diameters, and their thickness averaged. The density will be defined as previously.

c) Additional modifications

In next versions, the connection between the cooling pipe from the detector box and the nitril rubber tubes will be added. It represents a substantial amount of material. The glue in the ladder support will be changed, leading to an adjustment of the density of this logical volume. The density of *KaptonFlexCenter* and *KaptonFlexSide* volumes will also be changed due to the modification of the cooling connectors. The connectors parts in the PCBs, i.e. *KaptonFlexConnector* and *Connector*, will have their dimensions fixed by the March 2006 version and the density averaged according to their material composition.

The aluminium inserts and the screws on the support are not implemented in our material budget. They might represent locally some amount of material, but their implementation is too complicated to be done in a realistic way. An estimation of the material outside the acceptance (support fixations on the rails, service boxes, cable chain ...) is performed however, not implementated yet.

A version for 2008 is implemented. All the corrections described above has been done and some details were added. A note will be written to describe in details the new version.

Appendix B

Sensitivity to the physics parameters.

B.1 Studies for a luminosity of $10\,\mathrm{fb}^{-1}$

In this appendix we will first present the sensitivity of LHCb to the parameters a and θ after five years of data taking at $\mathcal{L}_{int/year} = 2\,\mathrm{fb}^{-1}$. The mean values, the errors and the pull distributions from a set of $\sim$ 200 experiments, each representing data at $\mathcal{L}_{int} = 10\,\mathrm{fb}^{-1}$, are shown using a B/S ratio of 0, 1 and 3.33 in a mass window of $\pm 2\sigma$ around the true B_s^0 mass. The physics parameters' values used in the fit are those listed in table 6.1. The fit results are considered as not sensitive when the distribution of the reconstructed values has no structure and when the pull distribution is biased by bad fits or large errors. The boundary values of a (0, 1) and θ (0 and $\pi/2$) are excluded in the error distribution in order to avoid any bias in the sensitivity determination.

Signal only

We first determine the sensitivity to a and θ using only signal (B/S=0) to see whether LHCb is sensitive to these parameters after 5 years of data taking.
Figure B.1 reports the results:

- a is quite well reproduced by the fit, the mean value $\mu = 0.268 \pm 0.012$ has a bias [1] with respect to the starting value of $+0.068$ which is due in part to the lower bound of the fit range (see Figure B.1). The errors are well distributed but the pull is biased for the reason mentioned before. The sensitivity to a in this case is of order 0.2.

- it is difficult to measure θ (no peak observed at the generated value and no structure in the distribution). Large errors do not allow a determination of the sensitivity to θ. The pull is well behaved ($\mu = 0.036, \sigma = 1.009$) as the large differences between the fit value and the nominal value of θ are compensated by the large errors.

---

[1] The bias is defined here as the difference between the fitted value and the generated one.

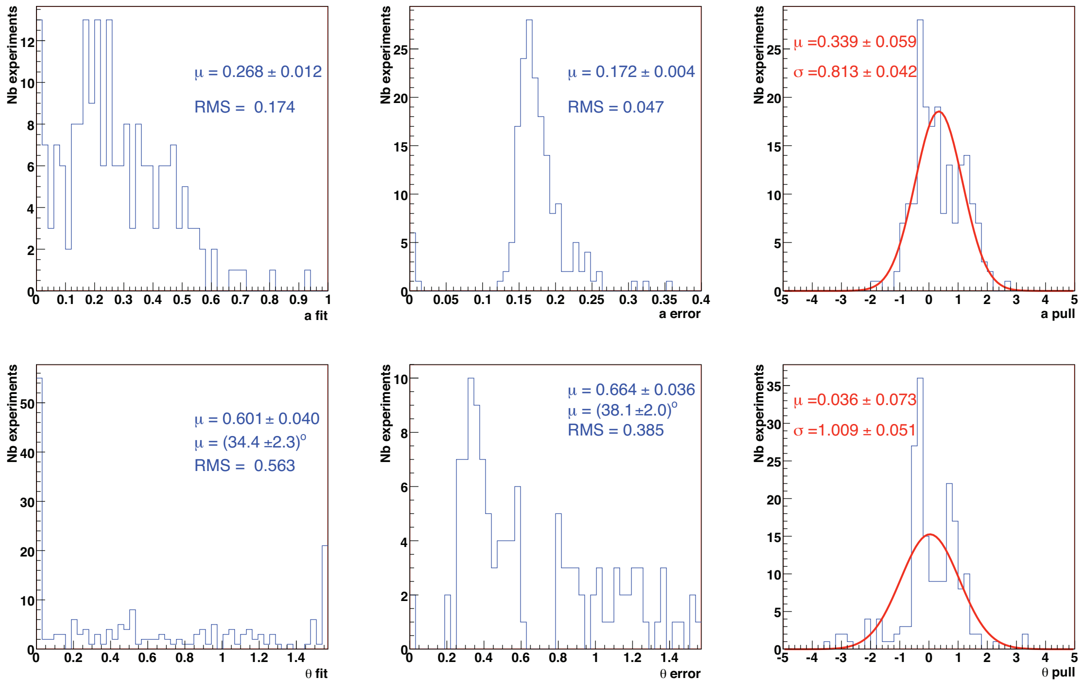

Figure B.1: a (top) and θ (bottom) likelihood fit output, error and pull distributions for 200 experiments using a luminosity of $10\,\mathrm{fb}^{-1}$ and B/S=0. The pull distribution is fitted with a single Gaussian.

Adding the noise

With five years of data taking in LHCb at nominal luminosity and without background, the fit is not sensitive to θ and we have only a poor sensitivity to a. Adding a background level degrades the sensitivity to a even further. With B/S=1 (Fig B.2), the output fit for a is biased by $+0.123$ and large fit errors appear. The θ results doesn't allow to determine any sensitivity. For a higher background level (Fig B.3), the sensitivity to a vanishes.

Studies with the parameter θ fixed

We have seen that the parameters a and θ are not correlated (section 6.3.1) and the fit has some sensitivity to a. For an integrated luminosity of $10\,\mathrm{fb}^{-1}$, we have also left the parameter a free to vary and have fixed the parameter θ to various values ($10^\circ, 20^\circ, 30^\circ$ and 50°) in the fit.

The mean values, errors and pulls are shown Fig. B.4, Fig. B.5 and Fig. B.6

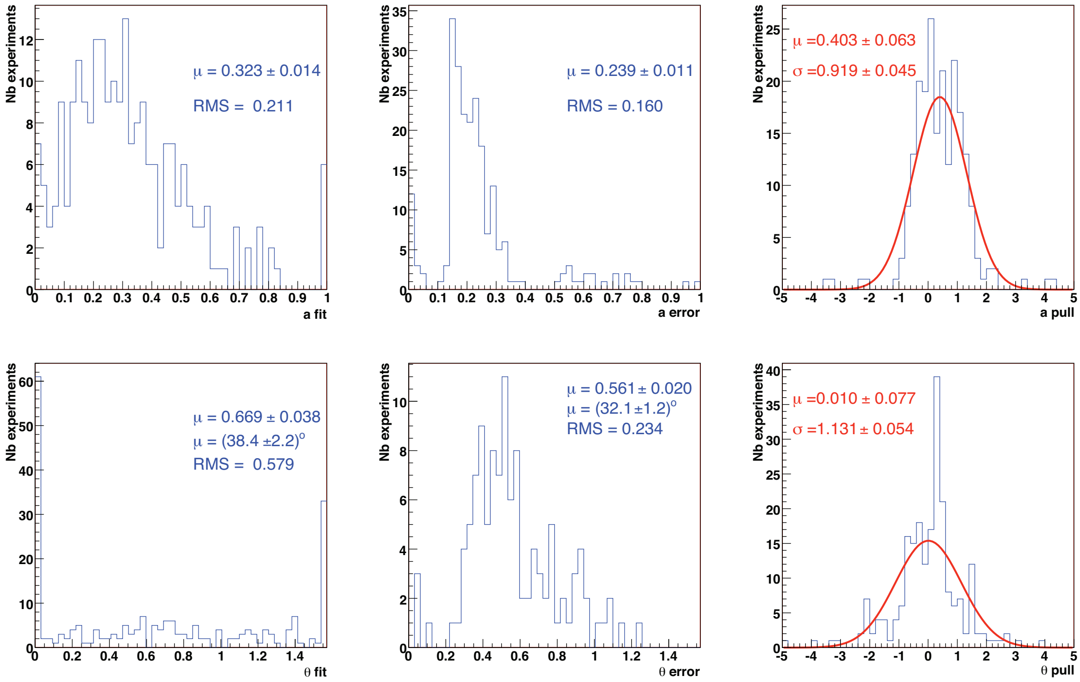

Figure B.2: a (top) and θ (bottom) likelihood fit output, error and pull distributions for 200 experiments using a luminosity of 10 fb^{-1} and B/S=1. The pull distribution is fitted with a single Gaussian.

θ fixed to	a fit value (B/S=0)	a fit value (B/S=1)	a fit value (B/S=3.33)
10°	0.215	0.241	0.299
20°	0.228	0.253	0.283
30°	0.205	0.240	0.273
50°	0.189	0.237	0.293
mean	0.209	0.243	0.287
RMS	0.014	0.006	0.010

Table B.1: Means of the fit value of a for different θ and B/S ratios at a luminosity of 10 fb^{-1}.

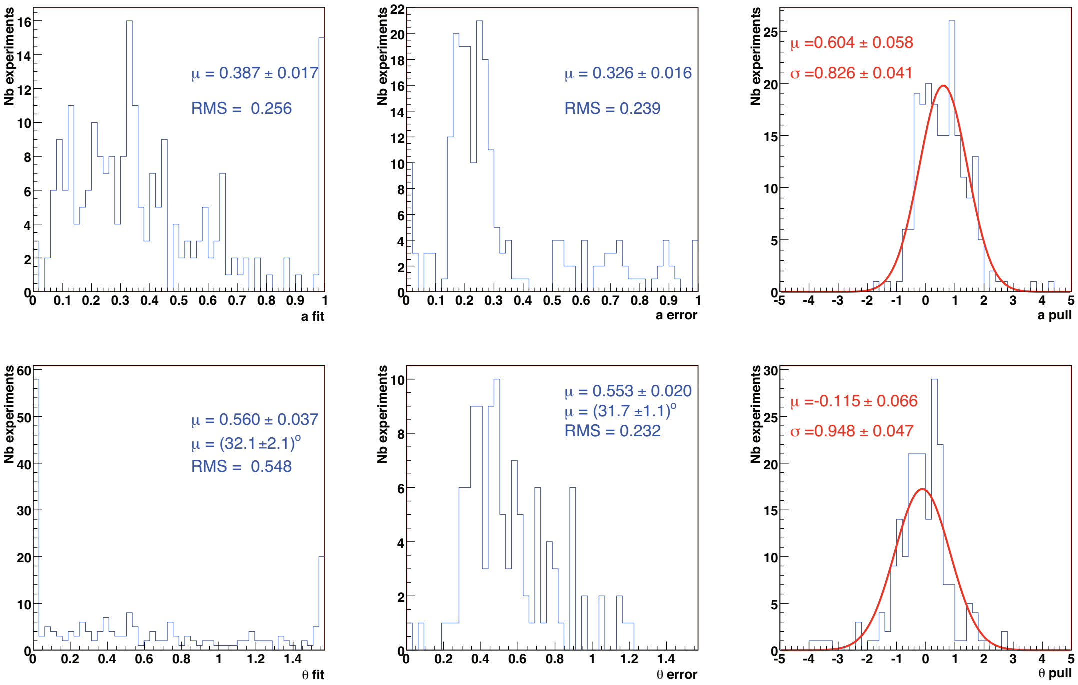

Figure B.3: a (top) and θ (bottom) likelihood fit output, error and pull distributions for 200 experiments using a luminosity of $10\,\mathrm{fb}^{-1}$ and B/S=3.33. The pull distribution is fitted with a single Gaussian.

θ fit value	a sensitivity (B/S=0)	a sensitivity (B/S=1)	a sensitivity (B/S=3.33)
10°	0.167	0.301	0.342
20°	0.168	0.252	0.394
30°	0.171	0.242	0.328
50°	0.169	0.244	0.430
mean sensitivity	0.169	0.260	0.374
RMS	0.001	0.024	0.041

Table B.2: Sensitivity of LHCb to the physics parameter a for different θ and B/S ratios at a luminosity of $10\,\mathrm{fb}^{-1}$. The boundary values of a (0, 1) and θ (0 and $\pi/2$) are excluded in the error distribution in order to avoid any bias in the sensitivity determination.

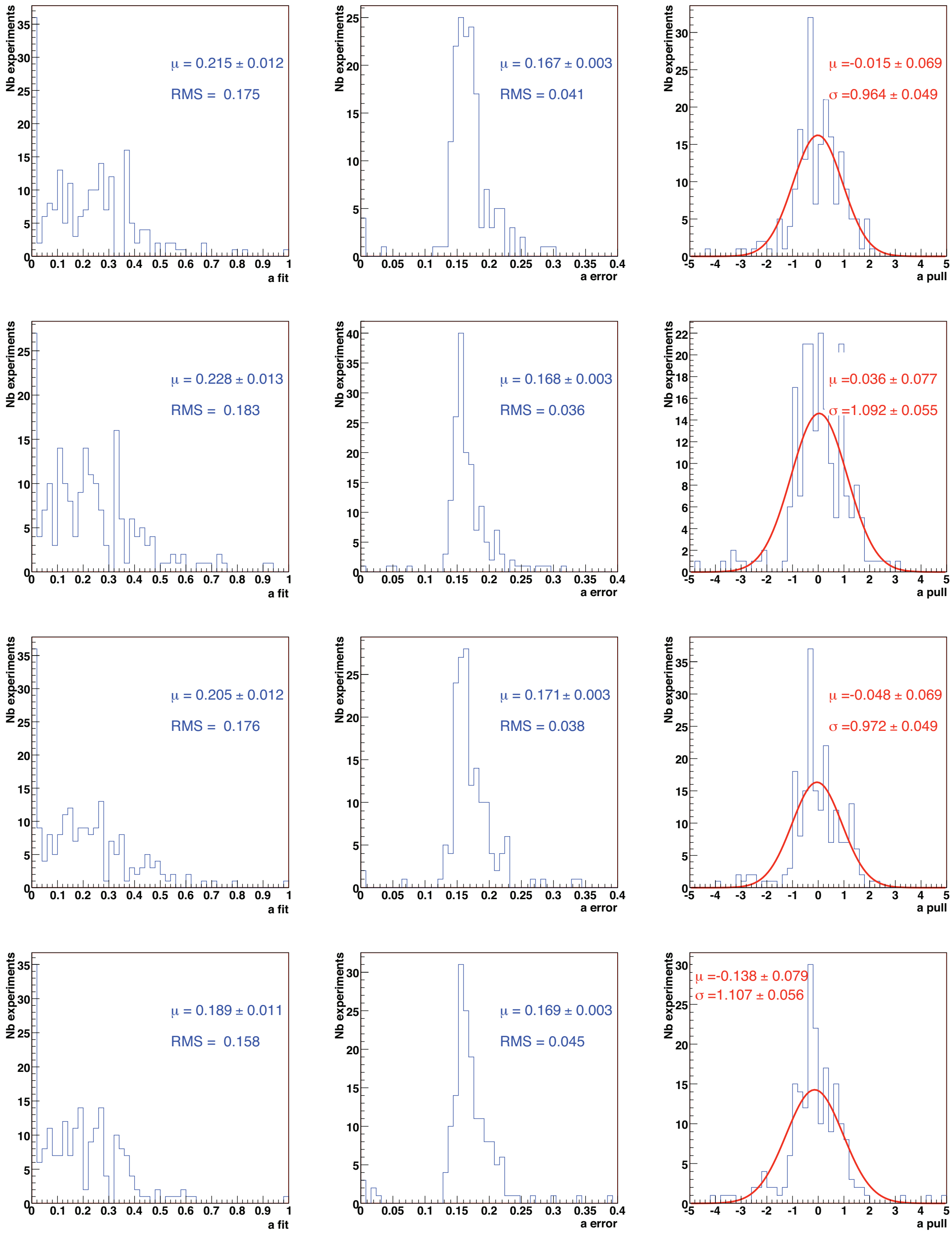

Figure B.4: a likelihood fit output, error and pull distributions for 200 experiments using a luminosity of $10\,\mathrm{fb}^{-1}$, B/S=0 and fixing θ at 10° (first row) 20° (second row), 30° (third row) and 50° (fourth row). The pull distribution is fitted with a single Gaussian.

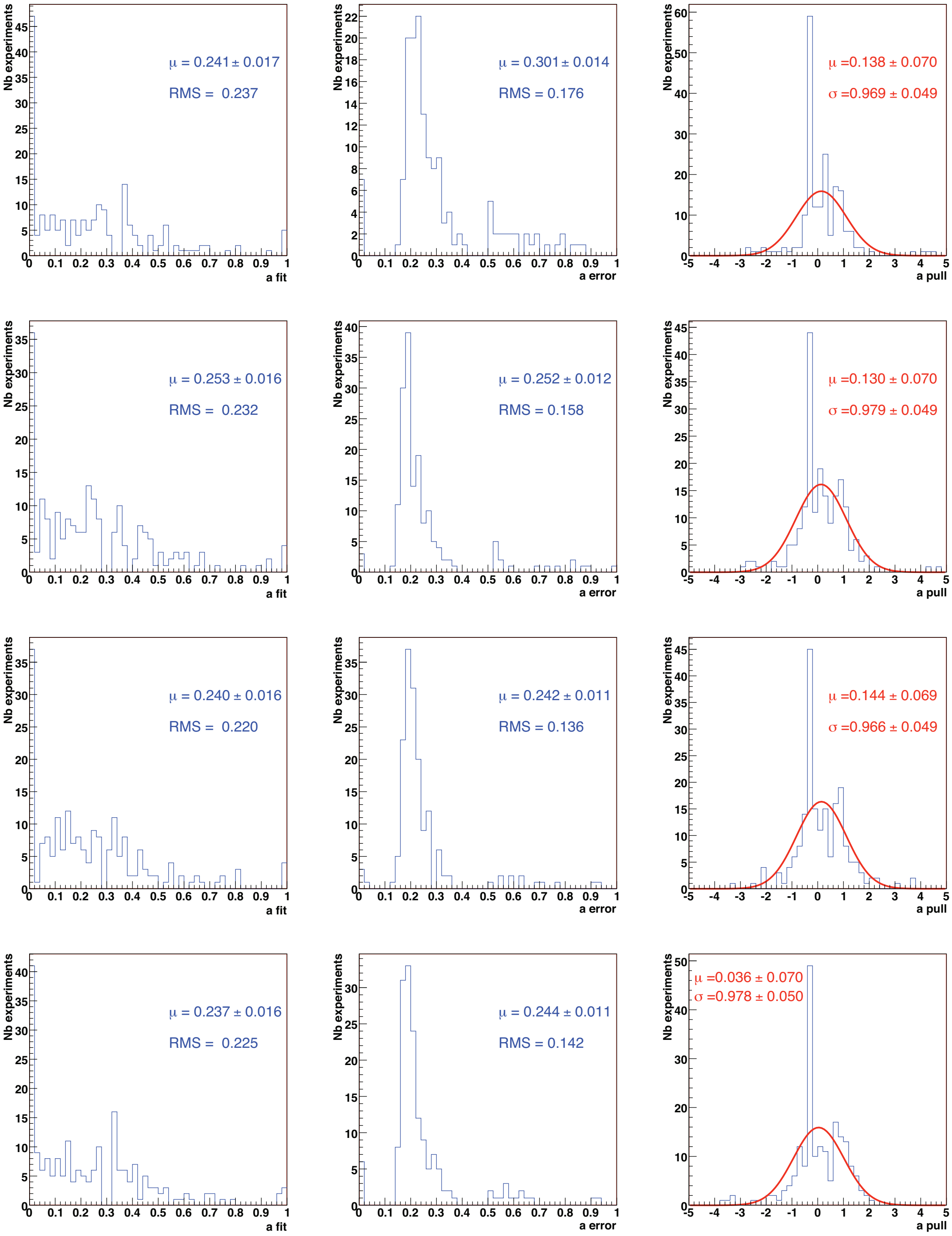

Figure B.5: *a* likelihood fit output, error and pull distributions for 200 experiments using a luminosity of 10 fb^{-1}, B/S=1 and fixing θ at 10° (first row) 20° (second row), 30° (third row) and 50° (fourth row). The pull distribution is fitted with a single Gaussian.

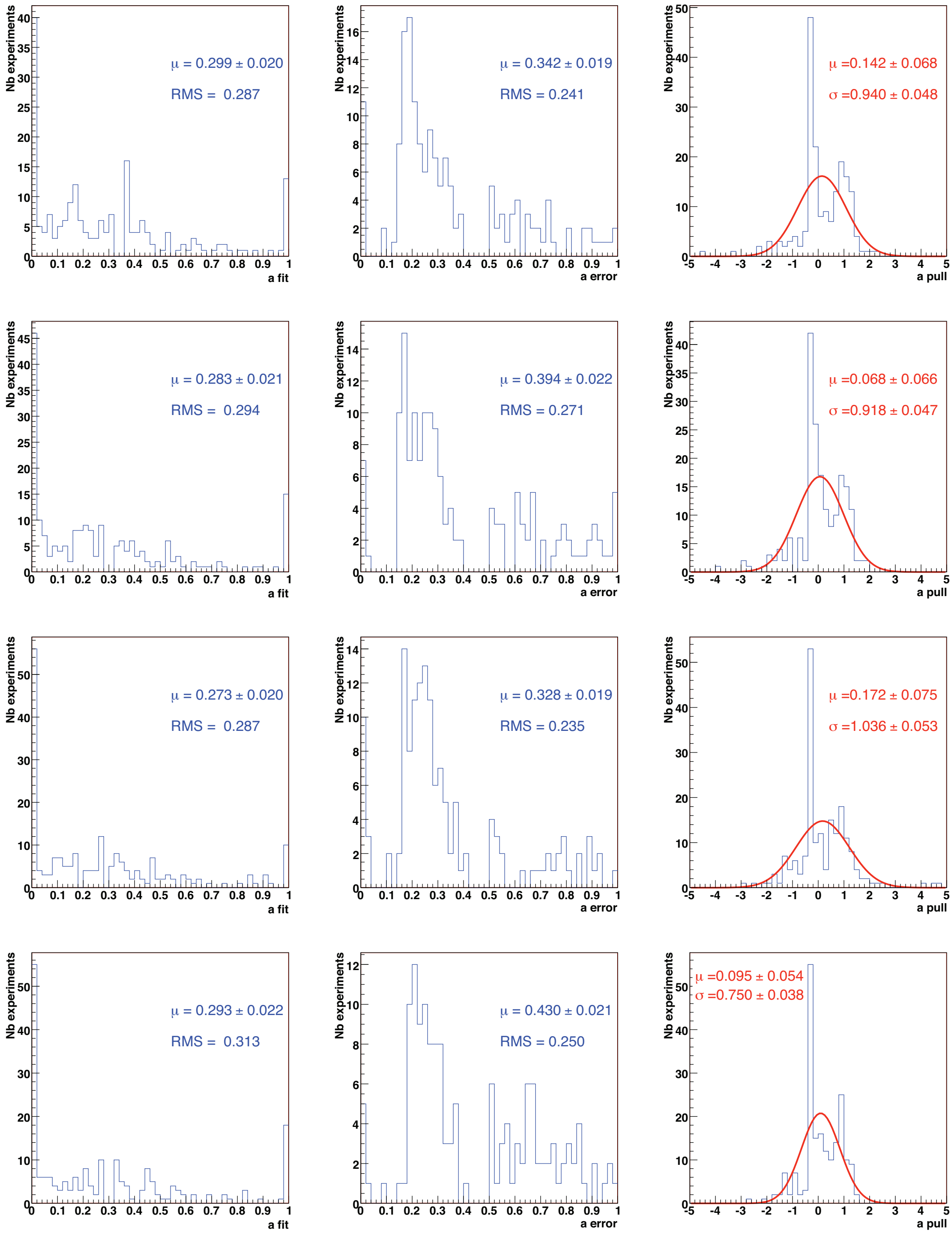

Figure B.6: a likelihood fit output, error and pull distributions for 200 experiments using a luminosity of 10 fb^{-1}, B/S=3.33 and fixing θ at 10° (first row) 20° (second row), 30° (third row) and 50° (fourth row). The pull distribution is fitted with a single Gaussian.

In table B.1 are detailed the likelihood fit output of a for different values of θ and B/S ratios and the sensitivity to a is presented in table B.2. Without background, the pull distributions of the 200 experiments are centered on zero and indicate that errors estimated by the likelihood fits does represent the variance of the results. The mean fitted value is ~ 0.209 and the sensitivity is ~ 0.169. The RMS of the different mean values of a in table B.1 gives an idea of the systematics error due to the undefined θ value: $\sigma_{sys}^{B/S=0} \simeq 0.014$. a can be measured as $0.209 \pm 0.169_{stat} \pm 0.014^{\theta}_{sys}$ without background for a fixed value of θ. The errors are dominated by the statistics and the systematics errors can be neglected.

By adding a background, the sensitivity decreases (see table B.2 in section 6.3.2): the fits of the 200 experiments give a non gaussian distribution around the nominal value of a and large errors appear in the error distributions. The pull are biased by the bad convergence of fits. No sensitivity to a can be obtained at $\mathcal{L} = 10\,\text{fb}^{-1}$ whwn background is present.

Conclusions

The sensitivity of the experiment to both a and θ is not easily accessible with a luminosity $\mathcal{L}_{int} = 10\,\text{fb}^{-1}$. As expected, the more the background, the more the number of experiments with a bad fit. The LHCb is not sensitive to both θ and a with this "poor" integrated luminosity, but fixing the value of θ in the fit and having a very low background level, the sensitivity of a is about 0.169 and the "systematics error" due to the unknown value is θ of 0.014. This result has to be compared to the sensitivity of a in the case where θ is let free, which is 0.172 ± 0.004. The sensitivity is not really improved by fixing θ but the bias from the input value of a and the pull distribution is better.

B.2 Studies for a luminosity of $50\,\text{fb}^{-1}$

We increase the statistics by a factor five, i.e. we jump to a luminosity of $50\,\text{fb}^{-1}$, which corresponds to the integrated luminosity for the upgraded LHCb after 2.5 years of data taking [108]. The mean values, the errors and the pull distributions for a set of ~ 200 experiments, each representing data at $\mathcal{L}_{int} = 50\,\text{fb}^{-1}$, are shown for B/S ratios of 0, 1 and 3.33 in a mass window of $\pm 2\sigma$ around the true B_s^0 mass on figures B.7, B.8 and B.9.

Signal only

Again, the case of signal without background is first presented. Figure B.7 shows the results of the fit of 200 experiments for a and θ with no background. The fit value of a is well distributed and its mean value, $\mu = 0.210 \pm 0.005$ is only $+0.01$ biased from the input value. The errors distribution gives a senstivity of LHCb to a of 0.072 ± 0.001 and the pull well distributed. For θ, the distributions indicate that the results can be used.

A peak shows up in the θ errors distribution and gives a sensitivity of $(21.6 \pm 1.0)^\circ$ to the parameter θ.

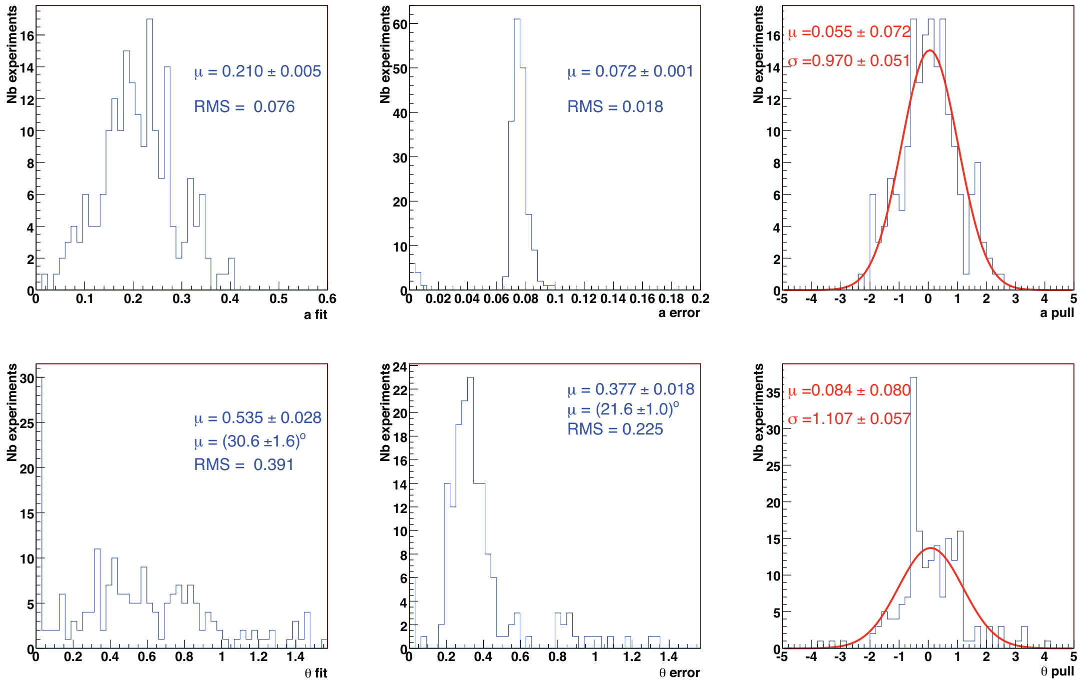

Figure B.7: a (top) and θ (bottom) likelihood fit output, error and pull distributions for 200 experiments using a luminosity of 50 fb^{-1} and B/S=0. The pull distribution is fitted with a single Gaussian.

Adding the noise

Increasing the background over signal ratio to 1 in a 2σ mass window around the B_s^0 mass degrades the sensitivity to the physics parameters. For a (Fig. B.8) the 200 experiment fit outputs mean is $\mu = 0.241 \pm 0.007$, corresponding to a bias from the generated value of $+0.041$. Very small errors appear in the error distribution and show that 5% fits doesn't converge and bias the pull distribution. The results are still usable and give a sensitivity to a of 0.096 ± 0.003. The θ outputs is usable too (Fig. B.8), the mean value is $(32.4 \pm 1.7)^\circ$, i.e. only 2.4° different from the input value. The experiments are less sensitive to θ than without background with an error mean value of $(22.6 \pm 0.8)^\circ$.

In the case of B/S=3.33, the distribution of the output of the fits for θ is no more gaussian and the pull distribution behaviour for a shows that too many experiments cannot be fitted. Around 16% of the 200 experiments give a small error in the a error distribution and 27% give a value for θ which butts against the θ lower/upper limit. For our highest background level, 2.5 years of data taking with upgraded LHCb are not sufficient to access the sensitivity of a and θ.

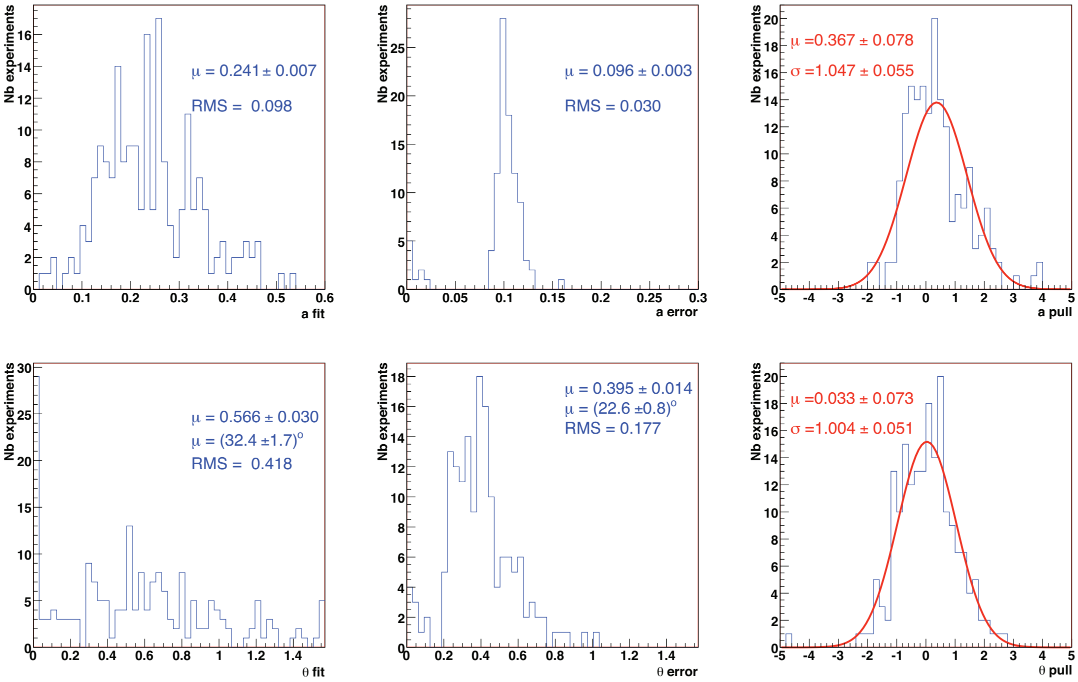

Figure B.8: a (top) and θ (bottom) likelihood fit output, error and pull distributions for 200 experiments using a luminosity of $50\,\mathrm{fb}^{-1}$ and B/S=1. The pull distribution is fitted with a single Gaussian.

Again, the experiment is more sensitive to the parameter a than to θ (Fig. 6.5). For a high B/S ratio, we fitted 200 experiments allowing the parameter a to vary and fixing θ to different values ($10°, 20°, 30°$ and $50°$) (see Fig. B.10 and table B.3 lists the results of the fit and the sensitivities for each set of 200 experiements described above). The results give a sensitivity to a at 0.107. The dispersion due to the unknow value of θ is very small and can be neglected. The measurement of a gives $a = 0.206 \pm 0.107_{stat} \pm 0.001^{\theta}_{sys}$ and the pull distributions have acceptable behaviours. With θ free, the determination of a is less precise ($a = 0.245 \pm 0.125_{stat}$).

Conclusions

With a very low background level and a luminosity of $\mathcal{L}_{int} = 50\,\mathrm{fb}^{-1}$, LHCb is quite sensitive to a (sensitivity = 0.072) and starts to be sensitive to θ (θ sensitivity = 21.6°). With a B/S ratio of around 1, we can still measure a and θ with some difficulty however; the sensitivity to a is 0.096 and 22.6° for θ. With a higher B/S ratio, the measure of a and θ is quite difficult. We can still measure a with a sensitivity of 0.107 if the value of θ is maintained fixed.

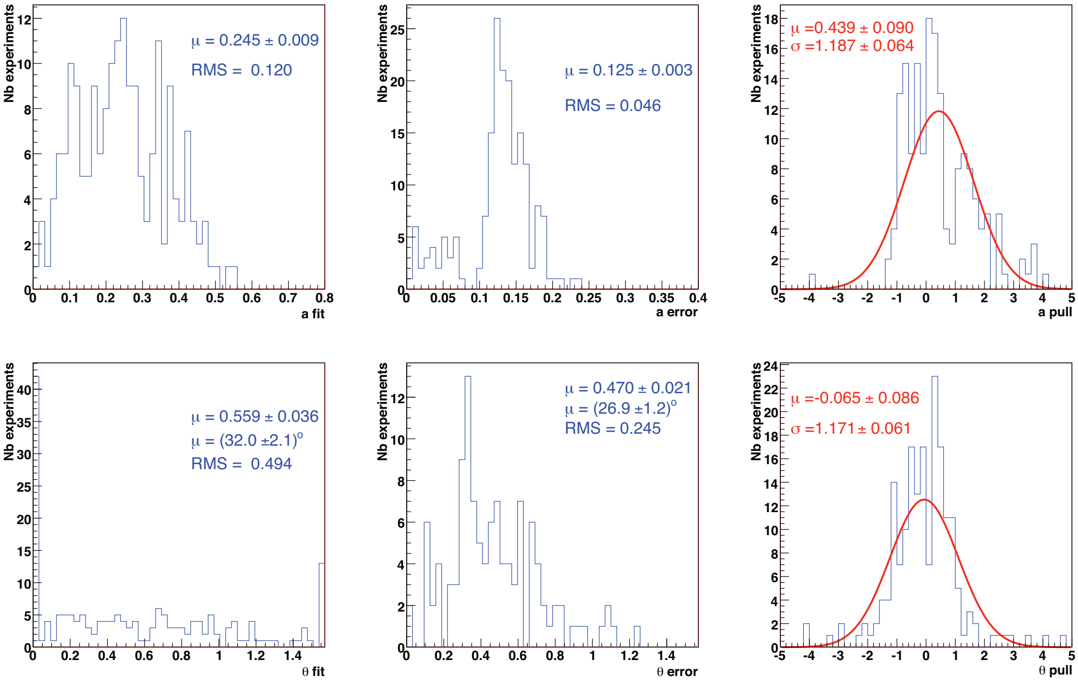

Figure B.9: a (top) and θ (bottom) likelihood fit output, error and pull distributions for 200 experiments using a luminosity of 50 fb^{-1} and B/S=3.33. The pull distribution is fitted with a single Gaussian.

θ fit value	a fit value	a sensitivity
10°	0.206	0.106
20°	0.202	0.107
30°	0.209	0.102
50°	0.205	0.107
mean value	0.206	0.107
RMS	0.002	0.001

Table B.3: Means of the fit value and sensitivity of a for different θ fit values and a B/S ratio of 3.33 at a luminosity of 50 fb^{-1}.

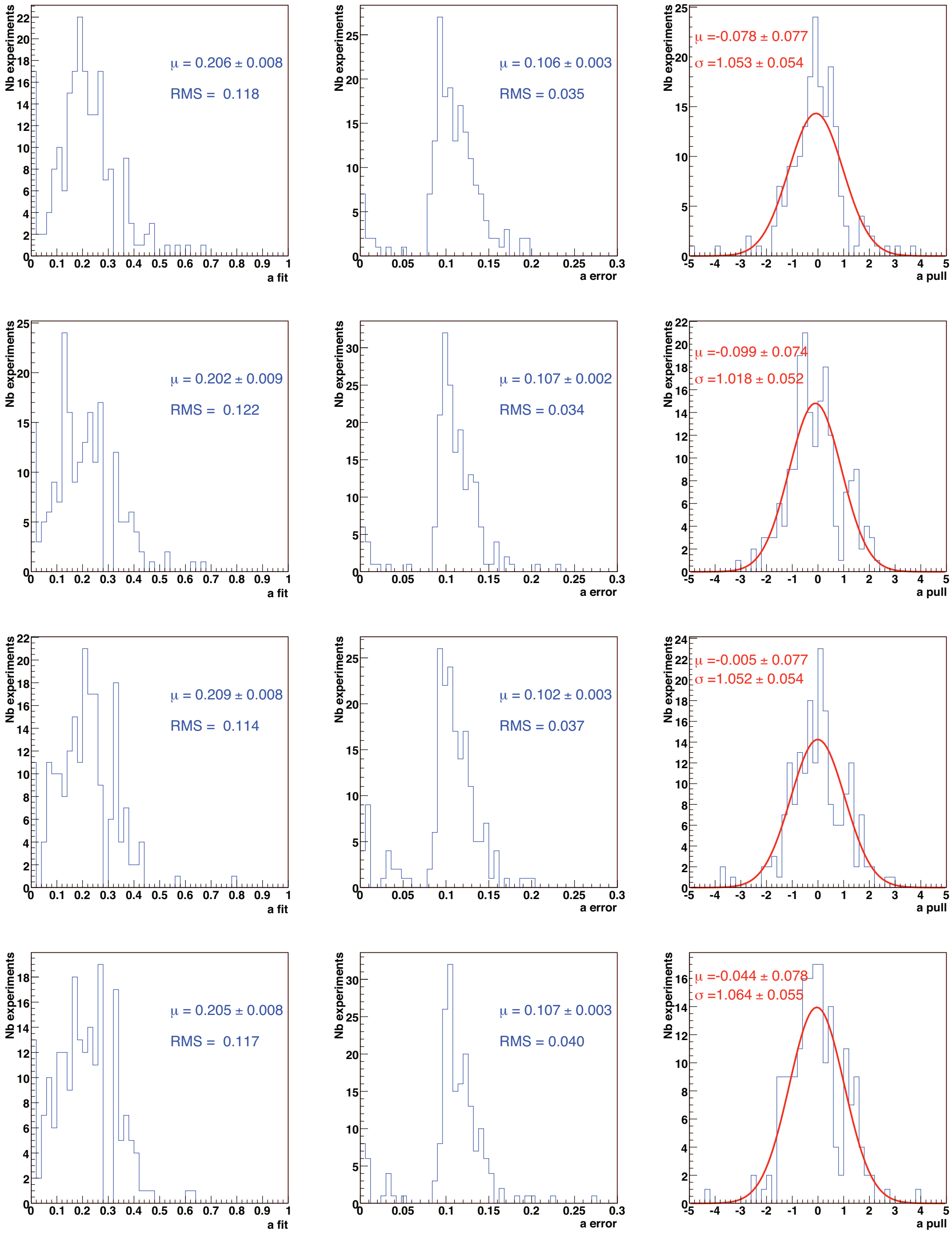

Figure B.10: a likelihood fit output, error and pull distributions for 200 experiments using a luminosity of $50\,\text{fb}^{-1}$, B/S=3.33 and fixing θ at 10° (first row) 20° (second row), 30° (third row) and 50° (fourth row). The pull distribution is fitted with a single Gaussian.

B.3 Studies for a luminosity of 100 fb^{-1}

After five years of data taking with the upgraded LHCb, the integrated luminosity will be about 100 fb^{-1}. In the last part of this analysis we have determined a and θ with different B/S ratios at the luminosity of 100 fb^{-1}. Again, the mean values, the errors and the pull distributions for a set of ~ 200 experiments are shown using a B/S ratio of 0, 1 and 3.33 in a mass window of $\pm 2\sigma$ around the true B_s^0 mass.

Signal only

The results of the fit of the 200 experiments at 100 fb^{-1} without background are presented in Fig. B.11. The distribution of a is well centered around the nominal value with a mean value of 0.207 ± 0.004 and the pull distribution confirm the measurement is indeed possible. The sensitivity to a is of 0.050 ± 0.001. The results for θ is quite improved compared with the ones obtained for $\mathcal{L}_{int} = 50\,\mathrm{fb}^{-1}$: the ouput fit distribution is well behaved despite a small bias due in part to a few bad fits giving $\theta = 0$; this bias also reflects itself in the displacement of the pull distribution. The sensitivity is $(14.6 \pm 0.4)^\circ$ for $\theta = 30^\circ$.

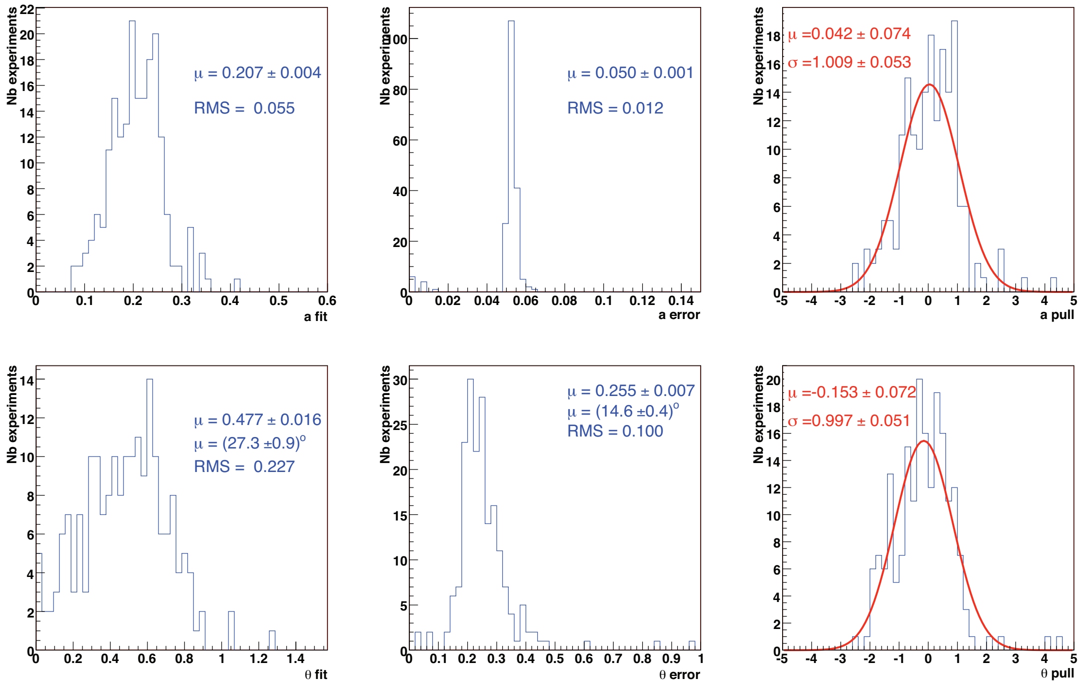

Figure B.11: a (top) and θ (bottom) likelihood fit output, error and pull distributions for 200 experiments using a luminosity of 100 fb^{-1} and B/S=0. The pull distribution is fitted with a single Gaussian.

Adding the noise

With a B/S ratio at 1 in the 2σ mass window around B_s^0 mass, the determination of a and θ will more difficult: in Fig.B.12, the parameter a is biased from its nominal value by $+0.018$ and some very small errors, corresponding to bad fits, appear in the error distribution. This induces a bias in the pull distribution. But determination of a is quite possible with a sensitivity of 0.065 ± 0.001. The distribution of the fit ouputs for θ gives a mean value of $(31.7 \pm 1.2)^\circ$ (Fig. B.12). The shape of this distribution is still gaussian but a bias of $+1.7^\circ$ appears. A tail of higher errors in the error distribution compensate the overestimation of θ and give a good pull distribution in the end. The sensitivity of θ is $(18.3 \pm 0.5)^\circ$, given the nominal value of $\theta = 30^\circ$.

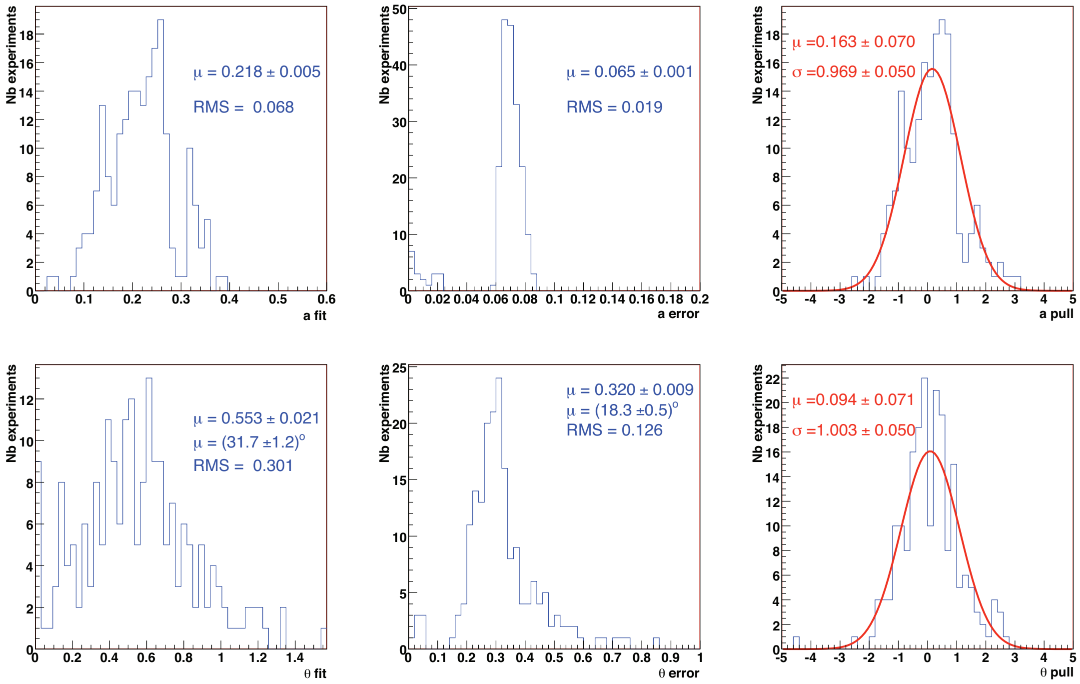

Figure B.12: a (top) and θ (bottom) likelihood fit output, error and pull distributions for 200 experiments using a luminosity of $100\,\text{fb}^{-1}$ and B/S=1. The pull distribution is fitted with a single Gaussian.

With our maximum estimated value of background level, the bias in the determination of a increases to $+0.023$ (Fig B.13) and the number of bad fits giving a small errors become higher (8 to 18% of the 200 experiments between B/S=1 and 3.33). The bias in the pull distribution is multiplied by a factor 2 with respect to the case of B/S=1. The sensitivity to a parameter is of 0.089 ± 0.002 and still allows a measurement of $a \sim 0.2$. For θ (Fig B.13), the measurement is more difficult: the bias in the fit output distribution is of 4.5° and 18% of the fits give values which go to the limits of the allowed domain for θ. The pull distribution of θ for B/S ratio at 3.33 is well behaved as the errors compensate the bad fit values. The sensitivity is for θ of $(25.0 \pm 0.9)^\circ$.

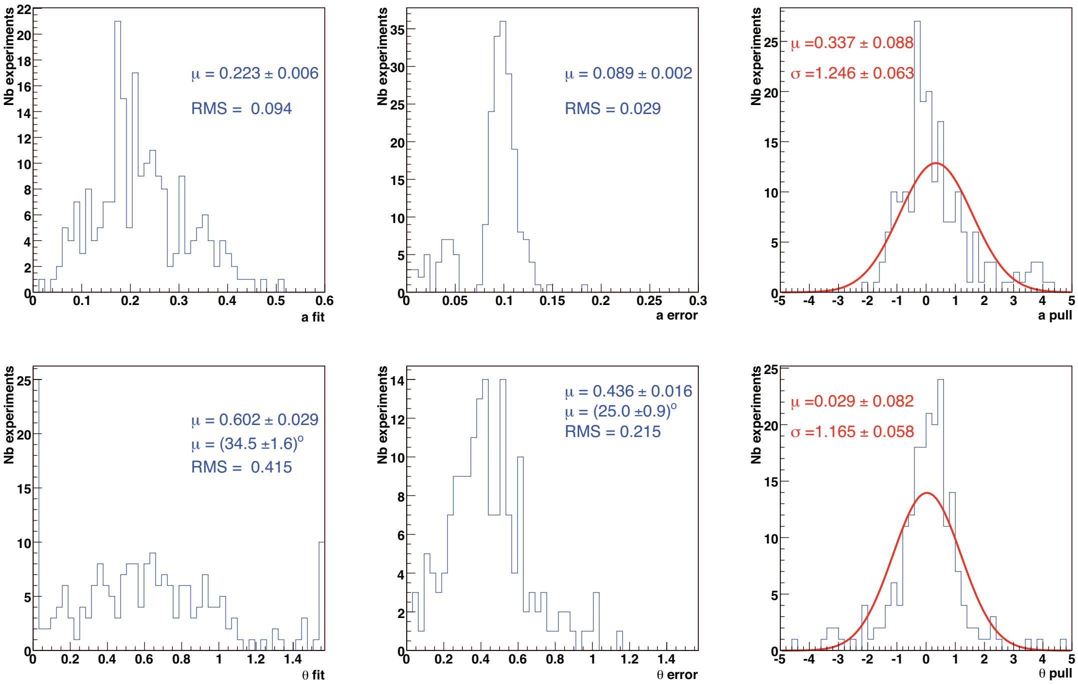

Figure B.13: a (top) and θ (bottom) likelihood fit output, error and pull distributions for 200 experiments using a luminosity of 100 fb^{-1} and B/S=3.33. The pull distribution is fitted with a single Gaussian.

Conclusions

After five years of taking data with the upgraded version of the LHCb experiment and with a selection comparable to the one described in section 6, we can measure the two parameters a and θ with a sensitivity better than 0.1 for a and $\sim 30^\circ$ for θ. If the background is very low (B/S$\sim$ 0), we can measure the parameter a with a sensitivity of 0.05 and θ with a precision of $\sim 15^\circ$. By increasing B/S ratio to one, 8% of the fits do not converge and induce a bias in the a and θ results, but the determination is still possible with a sensitivity of 0.065 for a and $\sim 18^\circ$ for θ. At the maximum foreseen background level, the number of bad fits increases to 18% and the sensitivity for a is ~ 0.09 and $\sim 25^\circ$ for θ.

Bibliography

[1] J. H. CHRISTENSON, J. W. CRONIN, V. L. FITCH, AND R. TURLAY. *Evidence for the 2π decay of the* K_2^0 *meson.* Phys. Rev. Lett. 13 (1964) 138-140.

[2] A. D. SAKHAROV, *Violation of CP invariance, C asymmetry and baryon asymmetry of the Universe*, Sov. Physics Journal of Exp. and Theo. Physics (JETP) 5 (1967) 24-27.

[3] M. KOBAYASHI AND T. MASKAWA. *CP violation in the renormalizable theory of weak interaction.* Prog. Theor. Phys., 49:652657, 1973.

[4] N. CABIBBO. *Unitary symmetry and leptonic decays.* Phys. Rev. Lett., 10:531532, 1963.

[5] B. AUBERT ET AL. *Observation of CP violation in the* B^0 *meson system.* Phys. Rev. Lett., 87:091801, 2001, hep-ex/0107013.

[6] B. AUBERT ET AL. *Measurement of CP violating asymmetries in* B^0 *decays to CP eigenstates.* Phys. Rev. Lett., 86, 2515-2522 , 2001.

[7] K. ABE ET AL. *Observation of large CP violation in the neutral B meson system.* Phys. Rev. Lett., 87:091802, 2001, hep-ex/0107061.

[8] ROBERT FLEISCHER. *Flavour physics and CP violation.* 2004, hep-ph/0405091.

[9] P. BALL ET AL. *B decays at the LHC.* 2000, hep-ph/0003238.

[10] JOAO P. SILVA. *Phenomenological aspects of CP violation.* 2004, hep-ph/0410351

[11] ANDRZEJ J. BURAS. *Flavor dynamics: CP violation and rare decays.* 2001, hep-ph/0101336.

[12] ANDRZEJ J. BURAS AND ROBERT FLEISCHER. *Quark mixing, CP violation and rare decays after the top quark discovery.* Adv. Ser. Direct. High Energy Phys., 15:65238, 1998, hep-ph/9704376.

[13] G. C. BRANCO, L. LAVOURA, J. P. SILVA. *CP violation*, Oxford Science Publication, 1999.

[14] S. L. GLASHOW, J. ILIOPOULOS, AND L. MAIANI. *Weak interactions with lepton hadron symmetry.* Phys. Rev., D2:12851292, 1970.

[15] W.-M. YAO et al. *The Review of Particle Physics* , Journal of Physics, G 33, 1 (2006) and 2007 partial update for 2008. http://pdg.lbl.gov/

[16] LING-LIE CHAU AND WAI-YEE KEUNG. *Comments on the parametrization of the Kobayashi-Maskawa matrix.* Phys. Rev. Lett., 53:1802, 1984.

[17] LINCOLN WOLFENSTEIN. *Parametrization of the Kobayashi-Maskawa matrix.* Phys. Rev. Lett., 51:1945, 1983.

[18] C. JARLSKOG. *A Basis independent formulation of the connection between quark mass matrices, CP violation and experiment.* Z. Phys., C29:491497, 1985.

[19] K. CHADWICK et al., *Decay of b flavored hadrons to single muon and dimuon*, Phys. Rev. Lett. 46 (1981) 88.

[20] L. SPENCER et al., *Measurement of B-Meson Semileptonic Decay*, Phys. Rev. Lett. 47 (1981) 771.

[21] A. ABULENCIA et al. (CDF collaboration), *Observation of* B_s-$\overline{B}_s$ *oscillations*, P.R.L 97(2006)

[22] V. M. ABAZOV (D0 collaboration), *Measurement of* B_s^0 *mixing parameters from the flavor-tagged decay*, hep-ex 0802.2255 (2008)

[23] J. CHARLES et al. *CP Violation and the CKM Matrix: Assessing the Impact of the Asymmetric B Factories* hep-ph/0406184v39 and http://ckmfitter.in2p3.fr/ for updates

[24] H. ALBRECHT et al., *Observation of* B^0-$\overline{B}^0$ *mixing*, Phys. Lett. B192 (1987) 245.

[25] Lepton-Photon 2007 conference : talk given by DAVID BROWN (Lawrence Berkeley National Lab) *CKM phase and CP Violation in B Decays*, http://chep.knu.ac.kr/lp07/htm/s11_01_01.htm.

[26] BELLE collaboration. K.-F. CHEN EL et al., *Observation of Time-Dependent CP Violation in* $B^0 \rightarrow \eta' K^0$ *Decays and Improved Measurements of CP Asymmetries in* $B^0 \rightarrow \phi K^0, K_s K_s K_s$ *and* $B^0 \rightarrow J/\psi K^0$ *Decays* Phys.Rev.Lett.98, 031802 (2007).

[27] BABAR collaboration. B. ALBERT et al. *Improved Measurement of CP Violation in Neutral B Decays to* $c\bar{c}s$, hep-ex/0703021

[28] JOAO P. SILVA et al., *Phenomenological aspects of CP violation*, hep-ph/0410351

[29] R. FLEISCHER et al., *Extracting* γ *from* $B_{s(d)} \to J/\psi K_s$ *and* $B_{d(s)} \to D^+_{d(s)} D^-_{d(s)}$, Eur. Phys J. C10 (1999) 299-306

[30] R. FLEISCHER, *CP Violation in the B System and Relations to* $K \to \pi\nu\bar{\nu}$ *Decays*, Phys. Report 370 (2002) 537-680

[31] P. BALL, R. FLEISCHER et al., *B decays at the LHC*, CERN-TH 2000-101.

[32] S. COHEN et al., $\gamma + \phi_s$ *sensitivity studies from combined* $B^0_s \to D^-_s \pi^+$ *and* $B^0_s \to D^{\mp}_s K^{\pm}$ *is* $\sim 10^\circ$ *samples at LHCb.* LHCb-note 2007-041

[33] CERN public web page. http://public.web.cern.ch

[34] P. LEFEVRE and T. PETTERSON, *The Large Hadron Collider: conceptual design*, CERN-AC-95-05-LHC, 1995.

[35] T. NAKADA, O. SCHNEIDER, *LHCb Trigger*, Proceedings of the 4th International Workshop on B physics and CP violation, February 19-23, 2001, Ise-Shima, Japan, IPHE, 2001.

[36] S. AMATO ET AL. *LHCb technical proposal*, CERN-LHCC-98-4.

[37] LHCb. *LHCb technical design report: Reoptimized detector design and performance*, CERN-LHCC-2003-030.

[38] LHCb. *LHCb VELO TDR: Vertex locator. Technical design report*, CERN-LHCC-2001-011.

[39] J. GASSNER, F. LEHNER, F. STEINER, *The mechanical design of the LHCb silicon Trigger Tracker*, CERN-LHCB-2004-110.

[40] *The Beetle Reference Manual for Beetle version 1.3 / 1.4 / 1.5*, LHCb-2005-105.

[41] *LHCb : Inner tracker technical design report*, CERN-LHCC-2002-029.

[42] *LHCb magnet: Technical design report*, CERN-LHCC-2000-007.

[43] L. B. A. HOMMELS. *The LHCb outer tracker detector design and production*, CERN- THESIS-2005-035.

[44] *LHCb : RICH technical design report*, CERN-LHCC-2000-037.

[45] RICH webpage. http://lhcb-rich.web.cern.ch/lhcb-rich/

[46] *LHCb calorimeters: Technical design report*, CERN-LHCC-2000-036.

[47] *LHCb muon system technical design report*, CERN-LHCC-2001-010.

[48] *LHCb trigger system technical design report*, CERN-LHCC-2003-031.

[49] E. RODRIGUES, *The LHCb Trigger System*, LHCb-2006-065.

[50] L. FERNANDEZ and P. KOPPENBURG. *Exclusive HLT Performance.* CERNLHCb-2005-047, revised version 2006-08-09.

[51] ANTUNES-NOBREGA ET AL. *LHCb computing Technical Design Report.* Submitted on 11 May 2005.

[52] M. CATTANEO ET AL. *The GAUDI project.* http://proj-gaudi.web.cern.ch/proj-gaudi/, 2001.

[53] G. BARRAND ET AL. GAUDI *The software architecture and framework for building LHCb data processing applications.* Published in CHEP 2000, Computing in high energy and nuclear physics 92-95, 2000.

[54] GAUSS webpage.
http://lhcb-release-area.web.cern.ch/LHCb-release-area/DOC/gauss/

[55] BABAR. *The EVTGEN package home page.*
http://www.slac.stanford.edu/ lange/EvtGen/.

[56] GEANT4 webpage.
http://geant4.web.cern.ch/geant4/

[57] BOOLE webpage.
http://lhcb-release-area.web.cern.ch/LHCb-release-area/DOC/boole/

[58] BRUNEL webpage.
http://lhcb-release-area.web.cern.ch/LHCb-release-area/DOC/brunel/

[59] DaVinci webpage.
http://lhcb-release-area.web.cern.ch/LHCb-release-area/DOC/davinci/

[60] PANORAMIX webpage.
http://lhcb-release-area.web.cern.ch/LHCb-release-area/DOC/panoramix/

[61] Moore webpage.
http://lhcb-release-area.web.cern.ch/LHCb-release-area/DOC/moore/

[62] Bender webpage.
http://lhcb-release-area.web.cern.ch/LHCb-release-area/DOC/bender/

[63] Orwell webpage.
http://lhcb-release-area.web.cern.ch/LHCb-release-area/DOC/orwell/

[64] X. XIE. *Short track reconstruction with VELO and TT*, 2003. CERN-LHCb-2003-100.

[65] R. HIERCK. *Track following in LHCb*, CERN-LHCb-2001-112.

[66] M. BENAYOUN AND O. CALLOT. *The forward tracking, an optical model method*, CERN-LHCb-2003-008.

[67] R. HIERCK ET AL. *Performance of the LHCb OO track-fitting software.* 2000.CERN-LHCb-2000-086.

[68] TrackStateWeb. https://twiki.cern.ch/twiki/bin/view/LHCb/TrackState, 2004.

[69] FLAVOUR TAGGING WORKING GROUP. *Performances on a few channels*, https://twiki.cern.ch/twiki/bin/view/LHCb/FlavourTagging

[70] Bookeeping webpage. http://lhcbbk.cern.ch/BkkWeb/Bkk/welcome.htm

[71] Composite Design S.A. http://www.compositedesign.ch/

[72] P. FAULEND et al. *The Inner Tracker module production.* LHCb draft note 2007.

[73] http://lphe.epfl.ch/ lhcb/itproduction/

[74] H. VOSS, S. KOESTNER et al. *Radiation Damage and Cooling Requirements for the LHCb Inner Tracker*, LHCb-note 2004-106 (draft note).

[75] Polyimide film 0.025 mm: http://www2.dupont.com/Kapton/en_US/index.html

[76] Mitsubishi K13D2U: www.m-chem.com/DataSheets/CarbonFiber/PD%20K13D2U.pdf

[77] R. FREI et al., *Thermal and mechanical studies of U-shaped carbon fibre support for the LHCb Inner Tracker detector's ladder*, LHCb note 2002-060

[78] AIREX R82: http://www.baltek.com/products/airex/airexR82.html

[79] Epo-Tek EE129-4: http://www.epotek.com/SSCDocs/datasheets/EE129-4%20CFDS.PDF

[80] Epo-Tek H20E: http://www.epotek.com/SSCDocs/datasheets/H20E.PDF

[81] Plastic Metal: http://www.weicon.de/de/produkte/2k-klebstoffe/plastik-stahl/weicon-f.php

[82] C_6F_{14}: http://minos.phy.bnl.gov/ diwan/APD/previous/c6f14.pdf

[83] Artic Silver 5 paste: http://www.arcticsilver.com/

[84] Legris connectors n°3106 06 00: http://www.legris.com

[85] Polyisocyanurate PIR: http://www.dyplastproducts.com/index.htm

[86] Nitrile rubber: SILVERPRESS basse pression type GC http://www.angst-pfister.com

[87] Armaflex NH: http://www.armacell.com

[88] Union simples Legris n°3101 08 13: http://www.legris.com

[89] Legris PU tube n°1025U08 01: http://www.legris.com

[90] Legris connectors n°3106 06 08: http://www.legris.com

[91] BOSIGER, LEHNER, STEINER and STRASSLE, *Design, Construction and Thermal Measurements on a Detector Box for the Inner Tracker of the LHCb Experiment*, LHCb 2002-059

[92] A. PERRIN and K. VERVINK, *The Inner Tracker detector description and implementation in the XML database*, LHCb note 2006-018

[93] Dallas Semiconductor DS18S20: http://www.maxim-ic.com

[94] J.M. AMORAAL, *The* $J/\psi \to \mu^1\mu^-$ *selection.* CERN-LHCb-2007-052

[95] G. LANFRANCHI, *Standard* K_s^0 *selection in DC06*, presentation at T-Rec Meeting, January 15th, 2007: http://lhcb.web.cern.ch/lhcb/

[96] Production samples informations: http://lhcb-phys.web.cern.ch/lhcb-phys/DC06_ MC_ samples/

[97] GARY J. FELDMAN, ROBERT D. COUSINS, *A Unified Approach to the Classical Statistical Analysis of Small Signals*, Phys.Rev. D57 (1998) 3873-3889

[98] S. AMATO, J. R. T. de MELLO NETO, C. NUNES, *The LHCb sensitivity to* $\sin 2\beta$ *from* $B_d^0 \to J/\psi K_s^0$ *asymmetry* , CERN-LHCb 2003-107

[99] S. AMATO, M. GANDELMAN, C. GOBEL and L. de PAULA, *Update to the LHCb sensitivity to* $\sin 2\beta$ *from the CP-asymmetry in* $B_d^0 \to J/\psi K_s^0$ *decays*, CERN-LHCb 2007-045

[100] M. KRASOWSKI, M. KUCHARCZY, W. MANNER, G. POLOK, M. WITEK, *Primary vertex reconstruction*, CERN-LHCb-2007-011

[101] G. RAVEN, *B decays at the LHC*, LHCb-2003-118

[102] N. MANGIAFAVE, *Measurements of* $\sin 2\beta$ *from* $B_d^0 \to J/\psi K_s^0$ *with the LHCb detector*, CERN-THESIS-2008-041

[103] S. JIMENEZ, $B_s^0 \to J/\psi\eta'$ *decay and sensitivity to the* B_s^0 *mixing phase at LHCb*, IPHE-THESIS, 2007.

[104] B. CARRON, $B_s^0 \to J/\psi\eta$ *decay and sensitivity to the* B_s^0 *mixing phase at LHCb*, IPHE-THESIS, 2005.

[105] D.KIRBY W.VERKERKE. *The RooFit toolkit for Data Modelling.* http://roofit.sourceforge.net/

[106] FRED JAMES, MINUIT. http://wwwasdoc.web.cern.ch/wwwasdoc/minuit/

[107] REN BRUN and FONS RADEMAKERS, *ROOT : An Object-Oriented Data Analysis framework.* http://root.cern.ch/

[108] F. MUHEIM, *LHCb Upgrade Plans*, Beauty 2006 - Oxford, 2006, web2k07.physics.ox.ac.uk/conferences/beauty2006/Talks/Franz_Muheim_Beauty-lhcb-upgrade.ppt

[109] G. WILKINSON, *Performance of LHCb with very high statistics*, 1st LHCb Collaboration Upgrade Workshop 2007,
http://indico.cern.ch/conferenceDisplay.py?confId=8351

[110] G. COWAN, *Statistical data analysis.* 1998. Oxford, UK Clarendon (1998) 197p.

[111] Honeycomb: Aramid Weberplatte n°213.0008 www.swiss-composite.ch

[112] Madison Cable SCSI Differential Cable AWG30 34 pairs:
http://www.madisoncable.com/

Aurélie Perrin

High Energy Physics Laboratory (LPHE)
Swiss Federal Institute of Technology (EPFL)
CH-1015 Lausanne-Dorigny
Married, one child

Born on April 21th 1980,
in Dole, France

Education

2008	PhD thesis in high energy physics on *Contribution to the Inner Tracker design and penguin sensitivity studies for the measurement of* $\sin 2\beta$ *in LHCb*, at the LPHE, EPFL Supervisor: Dr. Minh-Tâm Tran
2004	Master of Physics thesis on *Etude d'un type de refroidissement des détecteurs "Inner Tracker" de l'expérience LHCb*, at the LPHE, EPFL Supervisor: Dr. Minh-Tâm Tran
2003	Stage at the experiment ATHENA *Study of the output signal of a scintillation crystal (BGO) coupled with an avalanche photodiode (APD)*, Summer 2003 at CERN
1998	"Baccalauréat scientifique option physique chimie", (Dole-France), mention bien

Previous work experience

2004–2008	PhD thesis work in high energy physics on the LHCb experiment at CERN, Geneva
2006-2008	Collaboration in the physics group of the LHCb experiment at CERN
2004-2008	Teaching assistant (practical training and laboratories for senior undergraduate students in Physics and Biology), University of Lausanne
2004-2006	Research and development of the silicon Inner Tracker of the LHCb experiment at CERN
2002–2004	Teaching assistant at the Physics Department (practical training and laboratories for undergraduate physics students), EPFL